

University of Nottingham
UK | CHINA | MALAYSIA

Uncovering the Molecular Compositions, Origins and Formation Pathways of Engine Deposits using OrbiSIMS

Max Kendall Edney

Submitted to the University of Nottingham as a thesis by publication for the award of Doctorate in Engineering

August 2022

Abstract

Internal combustion powered vehicles will be used in road, rail, marine and aviation applications for the foreseeable future, particularly in developing nations. Formation of insoluble deposits on key engine components, such as fuel injectors and filters, affect all these vehicle types to cause increased emissions and fuel consumption. Despite years of research, little is known of the molecular composition, origin of contributing species and formation pathways of deposits, especially of their carbonaceous matrix. This is due to their insolubility and layered nature, meaning traditional solvent-based analysis techniques are unsuited to probe their composition and structure.

This thesis first details previous attempts of characterizing deposits and shows the need for high resolution mass spectrometry (MS) techniques to analyse deposits *in-situ* (*i.e.*, on the component itself). To address this knowledge gap, 3D Orbitrap secondary ion mass spectrometry (3D OrbiSIMS) Ar_{3000}^{+} gas cluster ion beam (GCIB) depth profiling and chemical imaging is applied to deposits from gasoline and diesel vehicles. Molecular species are accurately identified and confirmed using MS/MS for the first time, with supporting X-ray photoelectron spectroscopy (XPS) data. Key species identified include trace levels of lubricating oil derived alkyl benzyl sulfonates, inorganic salts (up to 16 %) in diesel samples and nitrogen containing species (up to 5 %) in the gasoline deposit. Finally, high amounts (> 80 %) of carbon in all samples, which are attributed to polycyclic aromatic hydrocarbon (PAH) type species, previously only speculated to exist in deposits.

Owing to the complexity of the datasets acquired, a method is developed to filter 3D OrbiSIMS data using molecular formula prediction and structural categorization by double bond equivalence measures. Chemistries in complex mixtures are rapidly discerned such as lubricating oil, residual fuel and oxygenated species (including carboxylic acids) in deposits. Multivariate analysis on filtered ions provided more distinct data separation than on the unfiltered data. The approach has utility in areas beyond deposit analysis, for example in complex biological systems, e.g., separating protein fragments and lipids in human serum.

Finally, 16 deposits were grown in an engine testing rig using different precursor fuels and then interrogated with 3D OrbiSIMS GCIB depth profiling and chemical filtering. Their carbonaceous matrix both comprised of planar and curved PAHs and nitrogen containing PAHs (N-PAHs). GCIB depth profiles from both 3D OrbiSIMS and XPS unveiled possible growth mechanisms of PAHs and N-PAHs over time through alkyl scission, cyclisation of aliphatic groups and hydrogen abstraction C_2H_2 addition. A comparison to atmospheric pressure matrix assisted laser desorption ionization (MALDI) MS data shows comparable maximum masses of ions.

Work presented in this thesis has uniquely shown the comprehensive molecular composition and origin of deposits from various sources and developed a novel approach to elucidate plausible formation mechanisms. This insight will aid industrial efforts to mitigate deposits by developing new solubilizing fuel additives, thereby helping to reduce global emissions and fuel consumption, benefiting environmental quality and human health.

Declaration

I hereby declare that all work presented in this thesis, unless explicitly stated, was conducted by myself. This thesis is submitted as a collection of published works written by myself as first author. This project was conducted at the Centre for Doctoral Training for Carbon Capture and Storage and Cleaner Fossil Energy and was funded by the EPSRC (grant number EP/L016362/1) and Innospec Ltd.

This doctoral dissertation was conducted under the supervision of:

Dr David Scurr, Principal Research Fellow at the School of Pharmacy at the University of Nottingham, UK.

Prof. Colin Snape, Professor at the University of Nottingham, UK.

Dr Jim Barker, Senior Research Fellow at Innospec Ltd, UK.



Max Edney MChem.

Acknowledgments

This PhD has by no means been a solo effort and I have many people to thank for their unwavering support along the way, so here goes. Firstly, to my supervision team, Jim, Colin and David for their constant guidance, well placed criticism and constructive feedback. Particularly to David for being someone I could always call with a problem which would always be fixed (often with a pint). To my collaborators including Ed and Jacquie at Innospec; the '3D OrbiSIMS team': Morgan, Julie, Anna, Rian, Wenshi and Mo, thank you for your useful insights and help on my work.

Next, I want to thank my Nottingham 'work' friends, Ieuan, Tesh, Aoife, Claire, Dan and Lizzie, for making the PhD environment fun. To my 'non-work' friends, including Luke, Jem, Tim and Ruth, and countless others. You all made life enjoyable when I needed it most. To Rob and Dan, who got me through the worst times. To Tim and Beth, without your open-house policy, good conversations, life guidance, running partnerships and all things in between I would have dropped out long ago and would have not been the person I am today. To Mum and Dad, for always being there to take my panicked phone calls and calming me down, as well as being a source of strength, encouragement and fun - all my success stem from you both. To Emily and James, for simply being my goofy siblings and making 'home' a good place to come back to, particularly during COVID! Finally, to Becky, your impact on me and my work has been enormous, I promise to continue to work hard for you and for our future.

Table of Contents

1. Introduction

1.1. Abstract.....15

1.2. Introduction to fuels and fuel injection.....16

1.3. Effects of deposit formation.....19

1.4. Known causes and mechanisms of deposit formation.....20

1.5. Analytical techniques used to analyse deposits.....23

1.5.1. Scanning electron microscopy.....23

1.5.2. X-ray photoelectron spectroscopy.....26

1.5.3. Transmission electron microscopy.....27

1.5.4. X-ray diffraction.....28

1.5.5. Fourier-transformed infra-red spectroscopy.....29

1.5.6. Raman spectroscopy.....30

1.5.7. Thermal analysis of injector deposits

1.5.7.1. Thermogravimetric analysis.....32

1.5.7.2. Temperature programmed oxidation.....33

1.5.8. Hydrogen pyrolysis.....34

1.5.9. Topographical analysis of deposits.....34

1.5.10. Mass spectrometry.....35

1.5.10.1. Gas chromatography mass spectrometry.....36

1.5.10.2. Time of flight secondary ion mass spectrometry.....37

1.6. Summary of previous capabilities for analyzing deposits.....39

1.7. Introduction to SIMS and 3D OrbiSIMS

1.7.1. The SIMS emission principle.....41

1.7.2. Primary ion sources.....44
1.7.3. Modes of analysis.....45
1.7.4. The Orbitrap mass analyser.....46
1.7.5. The use of high mass resolving power MS in petroleomics....49
1.7.6. The 3D OrbiSIMS technique.....50
1.8. Aims and Objectives of this Thesis
1.8.1. Existing knowledge and challenges for the field.....53
1.8.2. Thesis aims.....54
1.8.3. Thesis objectives.....54
2. Comparing the Molecular Compositions of Internal and External Gasoline and Diesel Deposits.....56
2.1. Chapter 2 objectives.....57
2.2. Part one.....58
2.2.1. Abstract.....59
2.2.2. Introduction.....60
2.2.3. Results and discussion.....63
2.2.3.1. Identification of molecular species.....63
2.2.3.2. Relative contributions of key molecular species.....67
2.2.3.3. Polycyclic aromatic hydrocarbons.....69
2.2.3.4. Quantified elemental surface analysis.....72
2.2.3.5. Combining 3D OrbiSIMS depth profiling & chemical imaging.....75
2.2.4. Part one conclusions.....79
2.3. Part two
2.3.1. Abstract.....80

2.3.2. Introduction.....81
2.3.3. Results and discussion
2.3.3.1. Visual and elemental analysis of deposits.....85
2.3.3.2. Identifying molecular species.....89
2.3.3.4. Carbonaceous species.....92
2.3.3.5. Combined 3D OrbiSIMS depth profiling and chemical imaging on internal deposits.....94
2.3.4. Part two conclusions.....96
2.4. Chapter 2 materials and methods
2.4.1. Materials.....97
2.4.2. 3D OrbiSIMS
2.4.2.1. Instrumental setup.....98
2.4.2.2. Depth profiles.....99
2.4.2.3. Chemical images.....100
2.4.2.4. MS/MS.....100
2.4.3. X-ray photoelectron spectroscopy.....100
2.4.4. Profilometry.....102
2.4.5. Scanning electron microscopy.....102
2.4.6. Optical microscopy.....102
2.4.7. Miscellaneous.....102
2.5. Comments on Chapter 2.....103
3. The Application of Molecular Formula Prediction for Chemical Filtering of 3D OrbiSIMS Dataset.....104
3.1. Abstract.....105
3.2. Chapter 3 objectives.....106

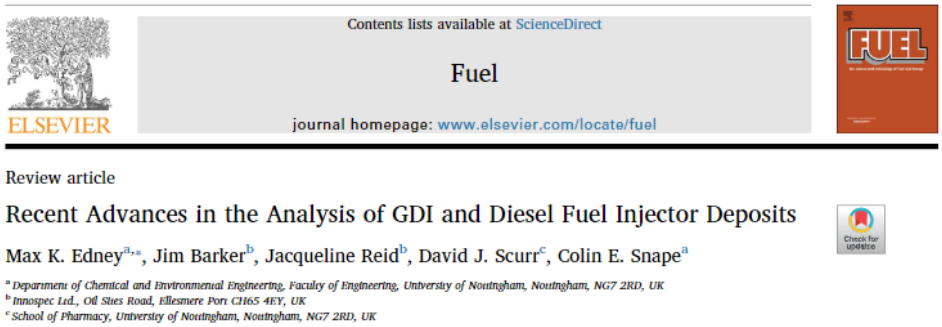
3.3. Introduction.....106
3.4. Results and discussion
3.4.1. Differentiation of contaminant overlayer and aluminium foil substrate.....110
3.4.2. Distinguishing proteins and lipids in a human serum.....113
3.4.3. Using Chemical filtering as a pre-filtering tool to MVA techniques on 3D OrbiSIMS data from carbonaceous engine deposits.....117
3.5. Relevant work not included in the publication
3.5.1. Application of chemical filtering to identify complex additive species in deposits.....125
3.6. Chapter 3 conclusions.....130
3.7. Comments on Chapter 3.....131
3.8. Chapter 3 materials and methods
3.8.1. Materials
3.8.1.1. Aluminium foil.....132
3.8.1.2. Engine deposits.....132
3.8.1.3. Model protein samples and human serum.....132
3.8.2 Methods
3.8.2.1. 3D OrbiSIMS.....133
3.8.2.2. DBE calculations.....134
3.8.2.3. Data interpretation.....134
4. Time Resolved Growth of (N)-Polycyclic Aromatic Hydrocarbons in Engine Deposits Uncovered with OrbiSIMS Depth Profiling.....136
4.1. Abstract.....137

4.2. Chapter 4 objectives.....138
4.3. Introduction.....139
4.4. Results and discussion
4.4.1. Time resolved growth of flat and curved PAHs.....141
4.4.2. Formation of aromatic nitrogen species in deposits.....150
4.4.3. Analysis of thin-film deposits to probe early stages of deposit formation.....156
4.5. Chapter 4 conclusions.....159
4.6. Comments on Chapter 4.....160
4.7. Chapter 4 materials and methods
4.7.1. Engine testing bed.....161
4.7.2. Fuels.....161
4.7.3. 3D OrbiSIMS.....162
4.7.4. Chemical filtering.....164
4.7.5. AP-MALDI.....164
4.7.6. XPS.....166
4.7.7. Miscellaneous.....166
5. Concluding Remarks and Future Perspectives
5.1. Concluding remarks.....167
5.2. Future perspectives.....169
6. Supporting Information for Results Chapters
6.1. Supporting information for Chapter 2.....172
6.2. Supporting information for Chapter 3.....183
6.3. Supporting information for Chapter 4.....191
7. References.....246

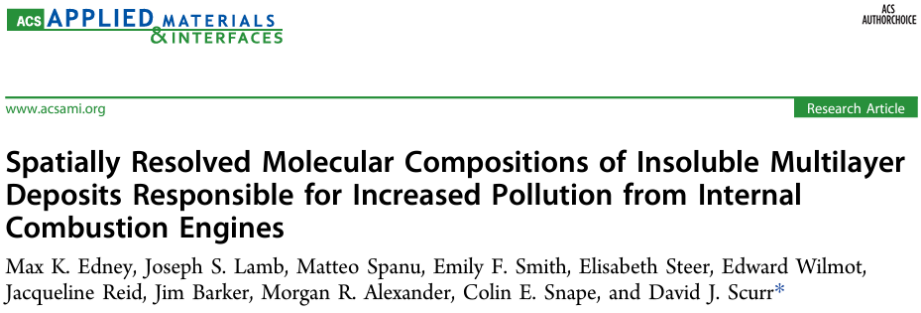
Publications

Peer reviewed publications related to this thesis

1. **M. K. Edney**, J. Barker, J. Reid, D. J. Scurr and C. E. Snape, Recent Advances in the Analysis of GDI and Diesel Fuel Injector Deposits, *Fuel*, 2020, **272**, 117682. (**Chapter 1**).

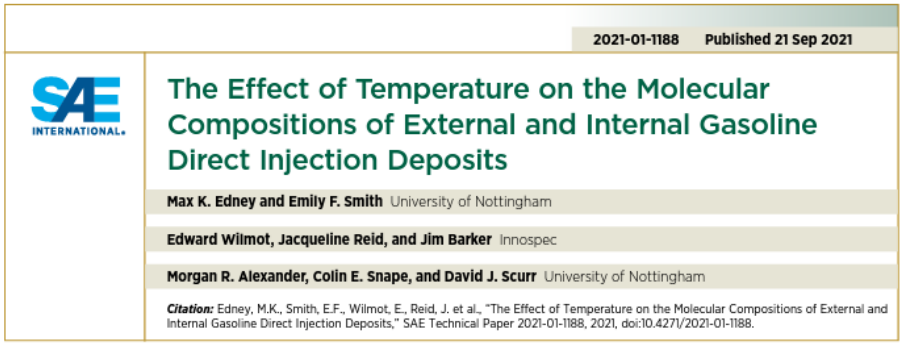


2. **M. K. Edney**, J. Lamb, M. Spanu, E. Smith, E. Steer, E. Wilmot, J. Reid, J. Barker, M. Alexander, C. Snape and D. Scurr, Spatially Resolved Molecular Compositions of Insoluble Multilayer Deposits Responsible for Increased Pollution from Internal Combustion Engines, *ACS Applied Materials & Interfaces*, 2020, **12**, 51026–51035. (**Chapter 2, part 1**).



3. **M. K. Edney**, E. Smith, E. Wilmot, J. Reid, J. Barker, M. Alexander, Colin. E. Snape and D. J. Scurr, The Effect of Temperature on the Molecular

Compositions of External and Internal Gasoline Direct Injection Deposits, *Society of Automotive Engineering*, 2021-01–1188. (**Chapter 2, part 2**).


2021-01-1188 Published 21 Sep 2021

SAE INTERNATIONAL

The Effect of Temperature on the Molecular Compositions of External and Internal Gasoline Direct Injection Deposits

Max K. Edney and Emily F. Smith University of Nottingham

Edward Wilmot, Jacqueline Reid, and Jim Barker Innospec

Morgan R. Alexander, Colin E. Snape, and David J. Scurr University of Nottingham

Citation: Edney, M.K., Smith, E.F., Wilmot, E., Reid, J. et al., "The Effect of Temperature on the Molecular Compositions of External and Internal Gasoline Direct Injection Deposits," SAE Technical Paper 2021-01-1188, 2021, doi:10.4271/2021-01-1188.

4. **M. K. Edney**, A. M. Kotowska, M. Spanu, G. F. Trindade, E. Wilmot, J. Reid, J. Barker, J. W. Aylott, A. G. Shard, M. R. Alexander, C. E. Snape and D. J. Scurr, Molecular Formula Prediction for Chemical Filtering of 3D OrbiSIMS Datasets, *Analytical Chemistry*, 2022, **94**, 4703–4711. (**Chapter 3**).

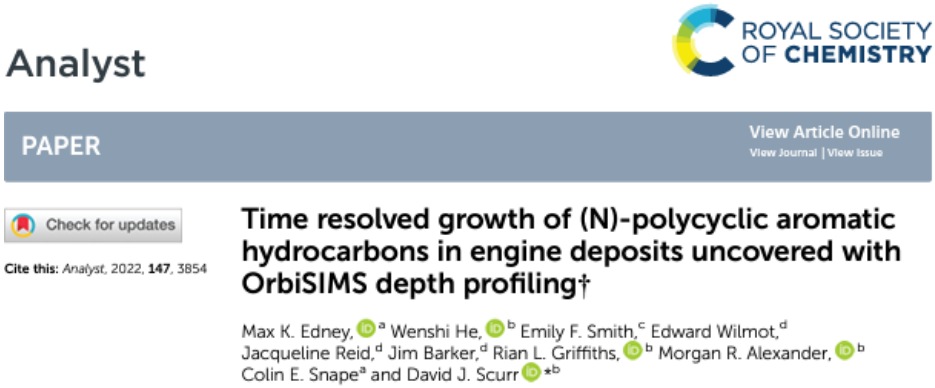

analytical chemistry

pubs.acs.org/ac Article

Molecular Formula Prediction for Chemical Filtering of 3D OrbiSIMS Datasets

Max K. Edney, Anna M. Kotowska, Matteo Spanu, Gustavo F. Trindade, Edward Wilmot, Jacqueline Reid, Jim Barker, Jonathan W. Aylott, Alexander G. Shard, Morgan R. Alexander, Colin E. Snape, and David J. Scurr*

5. **M. K. Edney**, W. He, E. F. Smith, E. Wilmot, J. Reid, J. Barker, R. L. Griffiths, M. R. Alexander, C. E. Snape and D. J. Scurr, Time resolved growth of (N)-polycyclic aromatic hydrocarbons in engine deposits uncovered with OrbiSIMS depth profiling, *Analyst*, 2022, **147**, 3854-3866. (**Chapter 4**).


Analyst

ROYAL SOCIETY OF CHEMISTRY

PAPER

View Article Online
View Journal | View Issue

Check for updates

Cite this: *Analyst*, 2022, **147**, 3854

Time resolved growth of (N)-polycyclic aromatic hydrocarbons in engine deposits uncovered with OrbiSIMS depth profiling†

Max K. Edney,[a] Wenshi He,[b] Emily F. Smith,[c] Edward Wilmot,[d] Jacqueline Reid,[d] Jim Barker,[d] Rian L. Griffiths,[b] Morgan R. Alexander,[b] Colin E. Snape[a] and David J. Scurr*[b]

Peer reviewed collaborative publications

1. N. J. Starr, M. H. Khan, **M. K. Edney**, G. F. Trindade, S. Kern, A. Pirkl, M. Kleine-Boymann, C. Elms, M. M. O'Mahony, M. Bell, M. R. Alexander and D. J. Scurr, Elucidating the molecular landscape of the stratum corneum, *Proceedings of the National Academy of Sciences*, 2022, **119**, e2114380119.


PNAS

RESEARCH ARTICLE | APPLIED BIOLOGICAL SCIENCES BIOPHYSICS AND COMPUTATIONAL BIOLOGY

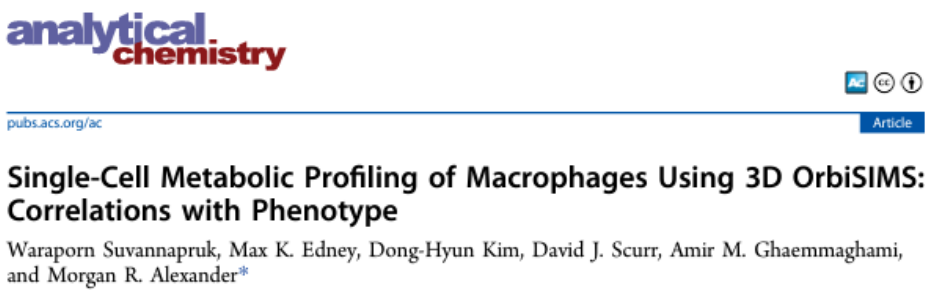
OPEN ACCESS

Check for updates

Elucidating the molecular landscape of the stratum corneum

Nichola J. Starr[a], Mohammed H. Khan[a], Max K. Edney[b], Gustavo F. Trindade[a,c], Stefanie Kern[a] Alexander Pirkl[d], Matthias Kleine-Boymann[d], Christopher Elms[e], Mark M. O'Mahony[e], Mike Bell[e], Morgan R. Alexander[a], and David J. Scurr[a,1]

2. W. Suvannapruk, **M. K. Edney**, D.-H. Kim, D. J. Scurr, A. M. Ghaemmaghami and M. R. Alexander, Single-Cell Metabolic Profiling of Macrophages Using 3D OrbiSIMS: Correlations with Phenotype, *Analytical Chemistry*, 2022, **94**, 9389-9398.


analytical chemistry

pubs.acs.org/ac

Article

Single-Cell Metabolic Profiling of Macrophages Using 3D OrbiSIMS: Correlations with Phenotype

Waraporn Suvannapruk, Max K. Edney, Dong-Hyun Kim, David J. Scurr, Amir M. Ghaemmaghami, and Morgan R. Alexander*

Conference Presentations

UK Surface Analysis Forum (July 2022) – oral and poster presentation and Young Surface Analyst prize finalist

British Mass Spectrometry Society (Sep 2021) – oral presentation

Society of Automotive Engineering (Sep 2021) – oral presentation and publication

2021 Rice University SIMS Workshop – oral presentation

Fuel and Energy Research Forum (Sep 2021) – oral presentation

UK Surface Analysis Forum (Jan 2021) – ***invited oral presentation***

UK Surface Analysis Forum (Jan 2020) – poster presentation

Awards

Best presentation and contribution to SIMS 2020 – Chemical and Bimolecular Engineering category winner at the Rice University international conference on SIMS.

Best research paper of 2020 in the University of Nottingham's Faculty of Engineering (ACS Appl. Mat. 2020 – first author).

Featured up and coming early career researcher in 'The Analytical Science' (Oct 2021).

Finalist for the UK Surface Analysis Forum's Young Surface Analyst Prize (July 2022).

Chapter 1

Part one (published)

Recent Advances in the Analysis of GDI and Diesel Fuel Injector Deposits

Max Edney[a], Jim Barker[b], Jacqueline Reid[b], David Scurr[c], Colin Snape[a]

[a] *Department of Chemical and Environmental Engineering, Faculty of Engineering, University of Nottingham, Nottingham, NG7 2RD, UK*

[b] *Innospec Inc., Oil Sites Road, Ellesmere Port, CH65 4HB, UK*

[c] *School of Pharmacy, University of Nottingham, Nottingham, NG7 2RD, UK*

Published in *Fuel* in 2020 *(DOI: 10.1016/j.fuel.2020.117682)*

Author contributions

M.K.E wrote the manuscript and all authors aided in its edits.

1.1. Abstract

Formation of insoluble fuel deposits in external and internal parts of fuel injectors is a major issue globally for diesel and, more recently, gasoline direct injection (GDI) based engines. Deposit formation reduces fuel economy and

increases emissions of every type of pollutant. Many potential causes exist such as general contamination, the operating conditions or the fuel composition itself. It is expected that as we move toward increased injection pressures to meet emission targets, the occurrence and severity of deposits will increase. It is widely accepted that a necessary step to mitigating deposit formation is to understand their chemistry and structure to gain a deeper understanding into the formation mechanism. An array of analytical techniques have been applied for this endeavor to afford chemical, topographical and structural information on diesel deposits. This has extended into GDI deposits more recently. This literature review summarizes the findings from studies into characterisation of both types of deposits and proposes that further work is required. Emphasis is also placed on the type of information offered by each analytical technique to aid researchers working in this field.

1.2. Introduction to fuels and fuel injection

Gasoline is a complex mixture of hydrocarbons consisting of alkanes, olefins, cycloalkanes, aromatic compounds and oxygenated species.[1] Because of the diverse range of refining techniques, the exact chemical composition of gasoline will vary, hence, strict fuel specifications are put in place to regulate the fuel, usually by wt. % of each 'compound class' in the total blend but this does vary from batch to batch within the specification and as such each fuel batch will have a slightly different composition. Diesel fuel consists of longer, heavier hydrocarbons than gasoline with a higher boiling range. Diesel fuel does not require spark-ignition and is ignited with highly compressed air in the combustion chamber, some advanced piezoelectric systems can operate at pressures up to 2,700 bar.[2] However, the high pressure can lead to deposit

formation being more prevalent in diesel injectors than in traditional gasoline injection, this will be discussed in a later section. The sheers number of internal combustion powered vehicles on the road, particularly in developing nations, which are predicted to see the largest growth in demand for primary energy to 2040,[3,4] means we must continue to partly rely on fossil-fuel based transportation. But this does not mean that efficiency of vehicles cannot be optimized to mitigate emissions of CO_2 and other pollutants. Indeed, this is reflected in modern engine and component design.

Fuel injection is a fundamental process in internal combustion engines. Until recently diesel and gasoline injection systems were very different. With diesel utilizing direct injection (DI) into the combustion chamber at high-pressures and gasoline engines using indirect port-fuel injection (PFI). The need for vehicle engines to give higher fuel efficiencies and meet stricter legislation on emissions saw the development of GDI systems and was first seen in production cars in the 1990's. It is estimated that by 2020 the sale of cars with GDI will overtake the sale of cars with PFI injection.[5] GDI uses the same DI principle as diesel with fuel coming from a high-pressure common-rail, a comparison of the injection systems and a schematic of a GDI injector is given in **Figure 1.1**. In this thesis we will examine GDI injector tip and injector needle components which are from here referred to as either 'GDI deposits' or simply as 'gasoline deposits'.

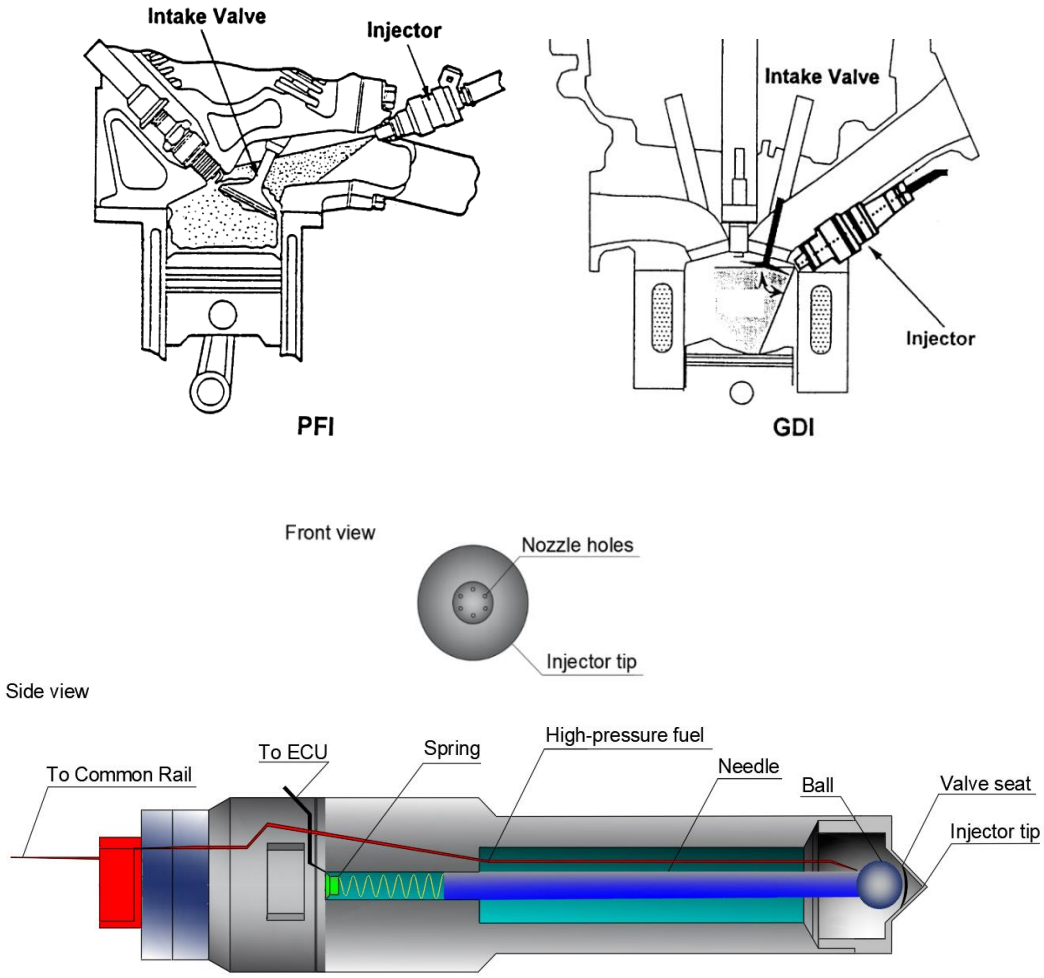


Figure 1.1. (a) *Diagrams comparing port-fuel and direct injection technology in a gasoline engine, adapted from Zhao et al. (1999).*[6] **(b)** *GDI injector schematic with key components labelled. Above, front view of the external parts of the injector. Below, a side view showing some key internal components. The image was drawn by the author using AutoCAD 2020 software. GDI, gasoline direct injection.*

Deployment of GDI into the fleet of light passenger vehicles has seen a drop in emissions of pollutants.[7–10] Also, an increased power output, engine efficiency and fuel economy.[11–14] This is partly achieved by the increased injection pressure and smaller nozzle hole sizes in the injector tip.[9] However, adverse

effects have been observed in this new type of DI system; including an increase in the frequency and severity of injector deposit formation.

Until recently diesel injectors have been worse affected by deposits than PFI due to the direct injection of fuel relying more heavily on a clean fuel spray than indirect injection and the higher-pressure and temperature of injection.[15–17] This has been highlighted as a key factor in promoting deposit formation.[18–21] Since implementing GDI more cases of deposits have been seen. Furthermore, additives with a function to control deposits in PFI systems have been shown to not be effective when used in GDI based engines.[22] Studies into injector deposits have partly focused on the causes and effects of deposit formation. A brief overview into this work is offered as part of this review. The main focus of this review is on attempts at characterizing GDI and diesel fuel injector deposits and evaluating the applicability of each analytical technique to deposit analysis to aid researchers who are working in this field.

1.3. Effects of deposit formation

There are a number of adverse effects caused by injector fouling; drivability issues such as rough idling, stalling and reduced power output from the engine are commonly observed. When deposits form on the internal parts of injectors the injector needle can jam and the entire component may need replacing.[23] It is agreed that a fouled injector's fuel spray exists as more of a jet instead of a fine spray which will result in poor mixing of air and fuel.[24–26] This is also aided by an increase of mean droplet diameter upon injector fouling.[27–29] Other work has shown a fouled injector spray leads to wall-wetting and subsequent fuel-film

formation on the cylinder, which leads to increased emissions of soot, UBHC's, CO, PM and PN.[30–34] Emissions testing from numerous studies has shown deposit formation of deposits leads to increased emission. A study by Wen *et al.* on a GDI based engine found significant deposit formation and tests showed emissions of NO_x, THC, NMHC and PM had increased by 23.4, 17.1, 24.5 and 374 % respectively.[27] Other studies found similar results and emissions of other pollutants such as CO were found to have increased as well.[35]

The use of new fuels derived from crop sources have also shown to increase levels of deposit formation and a resultant increase in NO_x and CO emissions.[32] Overall, a significant rise in pollutant emission and reduction in engine efficiency and power output is expected upon deposit formation. Leading to more widespread issues such as poorer air quality and accelerated global warming.

1.4. Known causes and mechanisms of deposit formation

There are various possible causes for injector deposit formation. Carbonaceous deposits are formed from the breakdown of organic constituents in the fuel.[33,34,36] Studies have also linked the levels of olefins in gasoline and diesel fuel with an increased likelihood of injector fouling as well as other reactive species. This has been attributed to the unsaturation of these compounds, making them prone to reactivity *via* oxidation.[37–40] The presence of sodium and other alkali metals are commonly blamed for forming inorganic and carboxylate soap type deposits too.[41] A possible source from water bottoms has also been identified, where fuel storage tanks may contain trace amounts of sodium, sulphites or sulphated ions and other sodium carrier ions. All of these have been

detected in these deposit types and have affected both gasoline and diesel fuel streams.[41–44] Studies have also linked the levels of zinc or sodium in the fuel and levels of deposit formation.[45,46] Diaby *et al.* expanded this work to cover the role of metals sourced from engine oil and found that metallic elements present catalyzed the deposit formation during engine testing.[45] Furthermore, the industry standard engine test for deposit formation, 'Direct Injection, Common Rail Diesel Engine Nozzle Coking', uses a reference fuel which is dosed with just 1 ppm zinc to accelerate the deposit formation process, highlighting the significant role it can play in the process.[47]

Another cause of deposits may come from the adverse reactivity of certain fuel additives. Work has linked the use of polyisobutylene succinimide (PIBSI) additives to increased injector fouling. It has been postulated that reaction of this acidic complex with sodium or other alkali metals can form polymeric amide lacquer deposits as well as carboxylate soap type deposits in the presence of fatty acids.[48,49] A recent study by Reid *et al.* highlighted that it was only "non-commercial" low MW PIBSI additives which caused injector fouling, with the recommendation that these should not be adopted as deposit control additives.[50] Other long-chain groups such as C-16/C-18 fatty acids have also been detected in internal diesel injector deposits (IDIDs).[48] These are used as corrosion inhibition additives.

Bio-diesel blends have also been blamed for an increase in deposit formation; partly because they contain unsaturated long-chain molecules with high reactivity to oxygen.[24,51] For example, fatty-acid methyl esters (FAME) or

rapeseed based methyl ester compounds present in biodiesel can lead to increased levels of injector fouling and have been identified as being unstable when stored over a long period of time.[17,52,53] A review by Hoang *et al.* covers the consequences of running bio-diesel in diesel engines, finding an increase in lacquer type deposits in particular which was due partly to the variation in components of bio-diesel fuel blends.[24]

Several mechanisms are plausible in both GDI and diesel injector deposits and work exists which goes into detail about the mechanism of deposit formation in both systems.[24,54] To date the mechanism is still not fully understood; kinetic modelling has recently been applied to GDI to help unravel the complex relationship between deposit formation and the fuels bulk properties.[55] Generally, a fuel with a low thermal stability are prone to the formation of deposits.[34] This explains the link with the use of FAME and injector fouling.[56] The generation of alkyl radicals in the fuel can form hydro-peroxides, these are then likely to adhere to the metal wall of the injector to begin deposit formation.[34,36,57] Breakdown of fuel can occur *via* pyrolysis or through polymerization reactions in which polyaromatic hydrocarbons (PAH) form.[34,58,59] PAH's are large aromatic molecules with multiple ring systems in conjugation with one another. Multiple formation routes open the possibility of various structures and overall chemical composition of deposits. Indeed, analytical studies into their characterisation have found this to be the case.

1.5. Analytical techniques used to characterize deposits

A plethora of analytical techniques have been applied to study the chemical composition, morphology and structure of deposits in both GDI and diesel injectors. This is not a facile task since deposits have been found to be rough, porous and non-homogeneous across the surface and, importantly, are comprised of distinct chemical layers.[60] Structural differences have also been reported in samples with respect to the structural ordering of the carbonaceous deposit material.[61] Various types of deposits have been noted to date and are summarized below in **Table 1.1**.[53] The next section summarizes the work done in this field and groups it by technique. Each section roughly follows the chronology of the study to illustrate the developments in the field over time.

***Table 1.1**: Summary of deposit types found in diesel fuel injectors to date and a short description, adapted from Barker et al. (2017)*[53]

Deposit type	Description
Carbonaceous	Commonly seen and black in color
Amides	Brown in color and polymeric in structure
Inorganic Salts	Off-white e.g., sulphates and sulphites
Carboxylate Salts	White in color, sodium or calcium based
Lacquer based	Thought to be a carbonaceous precursor
Aged fuel deposit	“Sticky deposits”, sourced from biofuel

1.5.1. Scanning electron microscopy

SEM utilizes primary electrons sourced from a filament, these are accelerated and focused into a beam to penetrate the sample surface. Detection of secondary and backscattered electrons generates a micrograph of the surface.[62] SEM has

been used extensively to analyse injector deposits. Aradi and co-workers observed obstructions to the fuel flow in a GDI injector *via* SEM during engine testing.[39] Similar work by Ashida *et al.*,[46] and Smith *et al.*[63] related the severity of deposit formation and loss of fuel flow rates with SEM micrographs taken over time in a diesel engine test. Lacey *et al.* linked SEM micrographs to the degradation of micelles which led to formation of insoluble soap type deposits on a diesel injector.[64] Hoang and co-workers used SEM to visualize fouling over the course of an engine testing cycle showing growth of deposits as lubricating oil degraded over time.[65] Dearn *et al.* recently conducted a study of GDI deposits using various analytical techniques including SEM.[66] They imaged deposits on various parts of the injector including the ball, seat, internal and external parts, SEM micrographs are shown in **Figure 1.2**.

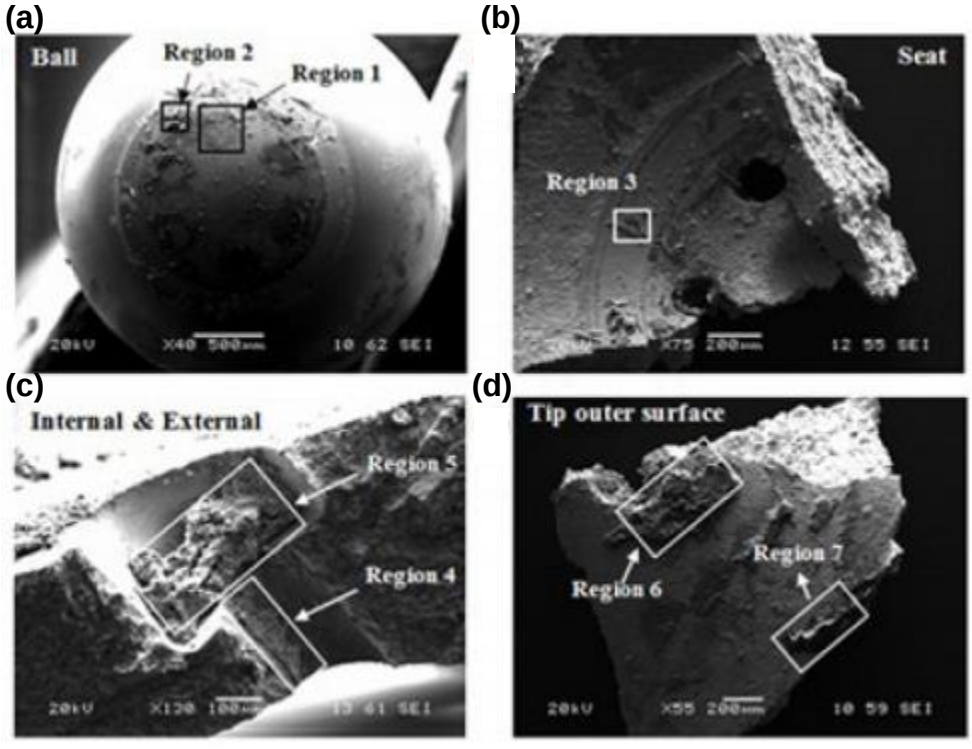


***Figure 1.2**. SEM micrographs of deposits on different parts of a GDI injector needle.*

***a)** ball, **b)** seat, **c)** internal and external nozzle, **d)** outer surface of injector tip.*

Regions highlighted were compared and used for further analysis and illustrated a range of morphologies and chemistries. Adapted from Dearn et al. (2014)[66]

SEM is often combined with other tools to give information on elemental composition. Scanning electron microscopy - energy dispersive spectroscopy (SEM-EDS) is one such hybrid technique which distinguish regions of the deposit by the elements that it contains.[67] SEM-EDS has been used widely for both diesel and GDI deposit analysis. Carlisle *et al.* first showed the presence of elements sourced from lubricating oil in the deposit itself such as calcium and phosphorus. Other elements such as sulfur, sourced from lubricating oil, have also been found in diesel injectors *via* EDS analysis by Von Bacho *et al.*,[68] and later Trobaugh *et al.*[69] Liaquat and co-workers then studied the impact of biodiesel on the deposits overall elemental composition. They found increased carbon levels with the biodiesel blend compared to diesel fuel.[20] Work by Schwab *et al.* highlighted the presence of sodium in a diesel injector deposit. They linked this to the presence of alkenyl succinic acid groups with various potential fuel additive sources.[70] Leedham *et al.*,[71] and D'Ambrosio *et al.*,[72] illustrated the presence of zinc in the resultant deposit after engine testing which has been highlighted as crucial in deposits formation studies. The investigation into GDI with EDS was continued by Dearn *et al.* They showed that deposits closer to the combustion chamber were more fuel derived by monitoring sulfur levels (sourced from lubricant oil).[66] This was backed up recently by Barker and co-workers who used EDS on a GDI injector showing changes in elemental distributions on deposits depending on their proximity to the combustion chamber.[22] Evidently, SEM-EDS is useful technique due to facile sample preparation. Some studies have used EDS and mapping, however for measuring

the surface composition, other techniques are available which are more surface sensitive such as XPS.

1.5.2. X-ray photoelectron spectroscopy

XPS is a surface sensitive technique, its principle relies on the photoelectric effect.[73] That is, when a high-energy X-ray photon is fired at a surface atom causing photoemission of an electron from one of its orbitals.[73] XPS is a quantitative technique has been found to be more accurate than other techniques which offers quantitative elemental information. Carlisle *et al.* first used XPS analysis on GDI injector deposits after running engine tests to promote deposit formation.[74] Elements such as molybdenum, zinc and iron were present. They quantified the amounts present and concluded that deposit formation was more severe closer to the injector tip and that the deposit was entirely fuel derived. Venkataraman *et al.* used XPS for diesel deposit analysis and found predominantly carbon and oxygen to be present. The high-resolution C 1s spectrum contained components corresponding to different carbon environments such as aromatic carbon, alcohol, ether, phenol or furan derived groups and carboxylic acid groups .[58] In this study a PAH type structure was suggested to be present with varying degrees of structural order thought to have formed through hydrogen abstraction from cycloalkanes with hydroperoxide species present at the ideal formation conditions.[75] Dallanegra *et al.* carried out a similar study on a range of diesel injectors. XPS showed a range of carbon bonding modes and indicated the presence of an amide lacquer type deposit characterized by a C-N bond.[43] In these cases, XPS was not conclusive to the type of bonding modes present and often some assumptions need to be made to

justify an assignment. Despite this, XPS can afford more detailed chemical information on injector deposits than other elemental analyses and gives accurate quantification of chemical information. However, due to its sensitivity it only affords information from the surface of the deposit and so chemistry below the top few nm's of the surface may not be identified.[73]

1.5.3. Transmission electron microscopy

Transmission electron microscopy (TEM) relies on similar principles to SEM but utilizes a higher energy beam which is transmitted through the sample itself to a detector plate underneath.[76] One advantage of a higher energy beam is that greater resolutions can be obtained compared with SEM. Thus, TEM can afford detailed information on the structure and morphology of injector deposits. TEM has not been used widely in diesel or GDI deposit analysis to date. Venkataraman *et al.* illustrated high resolution images and visualized an aggregation of particles as well as a single particle in the deposit, with a size in the nm range.[58] Barker and co-workers used TEM to distinguish between ordered and disordered material in injector deposits too (**Figure 1.3**). Finding the presence of ordered and disordered carbonaceous deposit material.

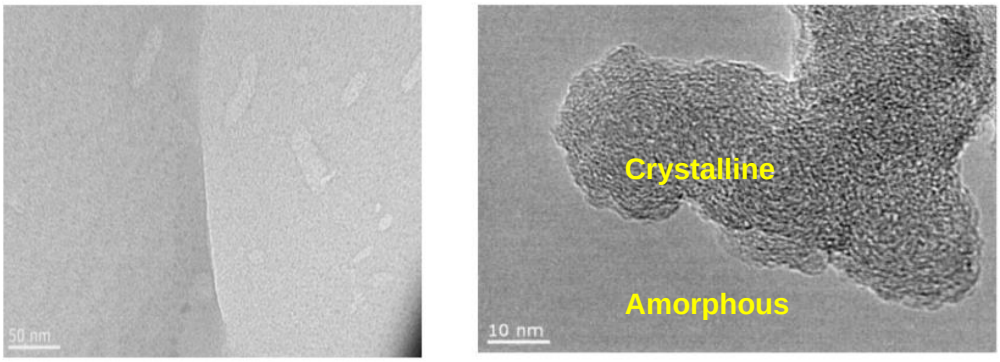


Figure 1.3. TEM micrographs of an IDID*. Left - upper deposit layer, showing 2 layers with similar morphologies. Right, the lower deposit layer showing both amorphous and crystalline carbon deposit. Adapted from Barker et al. (2015)*[61]

TEM is useful for generating high resolution micrographs which distinguishes features in the nm range. However, its drawback lies in difficulty of sample preparation compared to SEM and that no chemical information is afforded.[61]

1.5.4. X-ray diffraction

The potential of detecting both ordered and disordered carbonaceous material is also afforded by X-ray diffraction (XRD). Here, X-rays penetrate the sample and are diffracted by electrons in the crystal lattice.[73] The detected X-rays highlight the atomic spacing between atoms in a sample. Therefore, atoms with different space-groups are distinguished, allowing chemical and structural analysis.[73] Wo *et al.* on a diesel injector nozzle used XRD to study the morphology of the carbonaceous deposit, comparing two different fuel types from engine testing **(Figure 1.4)**.[77] They found the material consisted mainly of amorphous carbon. These findings were in agreement with results from TEM and Raman analysis, showing minimal structural ordering of the deposit sample.

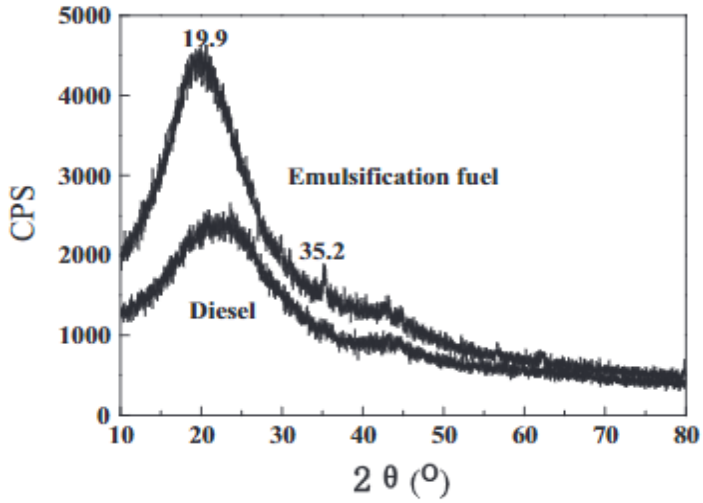


Figure 1.4. *XRD spectra of 2 diesel deposits from engine testing, showing the presence of amorphous carbon. Adapted from Wo et al. (2015).*[77]

1.5.5. Fourier-transformed infra-red spectroscopy

Fourier-transformed infra-red spectroscopy (FTIR) detects the change in the dipole moment of a chemical bond once it has absorbed IR radiation. An FTIR spectrum therefore allows functional group identification. Like EDS, FTIR has been used widely over time for both diesel and GDI deposit analysis and has highlighted the presence of several important organic components to these deposits. Ashida *et al.* first showed the presence of aromatic bonding modes in a GDI injector deposit,[46] Venkataraman and co-workers also highlighted the aromatic type bonding modes present in a diesel injector deposit.[58] Salt type deposits have been commonly identified by FTIR. Schwab *et al*.,[70] and Tanaka *et al*.,[78] showed this by identifying the characteristic C=O stretching mode in the spectrum. Ullman *et al*. found the presence of a peptide bond in a diesel deposit which was attributed to the product of ring opening reaction of a succinimide group.[79] Later, Almena *et al*. identified carboxylic acid backbones through FTIR

analysis.[44] Feld *et al.* also used FTIR in conjunction with time-of-flight secondary ion mass spectrometry (ToF-SIMS), discussed in a later section. The group found evidence of PIBSI type molecules and sulphonate species in a bio-diesel type deposit.[51] Lacey and co-workers used FTIR to distinguish between hard lacquer deposits and soft soap deposits in diesel injection systems.[64] Later, Galante-Fox *et al.* identified and confirm the sources of the amide bond and carboxylate group through engine.[80] Other works use FTIR mapping to overlay with injector parts, the map is made up of many individual spectra at each point which highlights chemistry differences across the surface. Recent examples on a GDI system come from Dearn *et al.*,[66] and Barker *et al*.[22] Overall, the ease of sample preparation and opportunity for *in-situ* analysis makes FTIR a worthwhile technique for bulk deposit analysis. Issues have precipitated in low sensitivity to trace compounds and elements however.[79]

1.5.6. Raman spectroscopy

When a molecule absorbs a photon, several scattering processes can occur: Stokes, Anti-Stokes and Rayleigh. The first two are observable by Raman spectroscopy, which measures the energy difference between an incident and scattered photon once it has been absorbed by a molecule for bond excitation or rotation.[81] A commonly used feature when studying injector deposits with Raman is to distinguish between ordered and disordered carbon structures. In a Raman spectrum there will be a D and G band assigned as peaks. The ratio of G:D, measured by peak area, gives information as to how ordered a region is. Barker *et al*. used Raman in this capacity to analyse an IDID shown in **Figure**

1.5.[61] This highlighted the ordering of material laterally across the deposits surface.

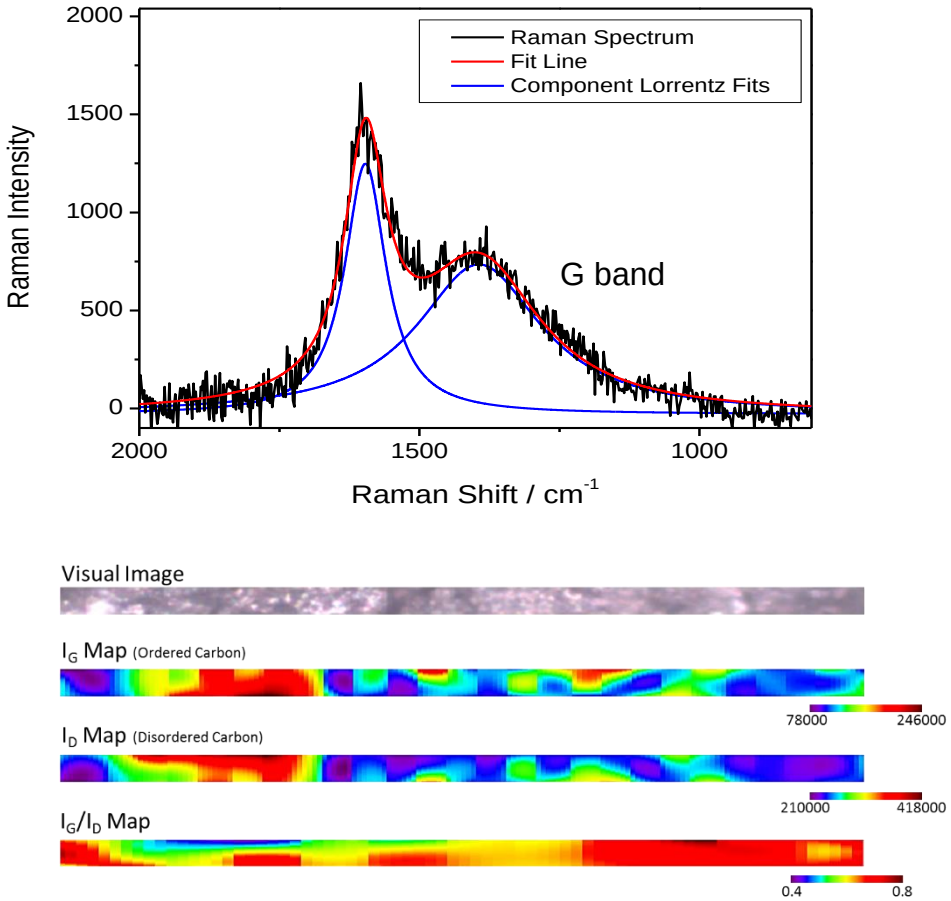


***Figure 1.5**. Raman spectroscopy analysis of a diesel injector deposit. Spectra with deconvoluted peaks for the D and G bands. Adapted from Barker et al. (2015).*[61]

Other work by Wo *et al.* investigated the extent of structural ordering of carbonaceous material in other diesel fuel injectors and diesel soot.[77] The ordering of material in diesel soot has also been investigated by Patel and co-workers more recently.[82] Evidently, Raman spectroscopy is a worthwhile technique for deposit analysis, it offers non-destructive structural group identification similar to FTIR but also gives more information on the relative amounts of ordered carbonaceous material in the deposit which is vital in

distinguishing between different deposit types and understanding their formation mechanism.

1.5.7. Thermal analysis of injector deposits

1.5.7.1 Thermogravimetric analysis

Thermogravimetric analysis (TGA) measures the mass of a sample that is lost at different temperatures during heating.[83] Experiments can distinguish the volatility of material or compare oxidation processes at varying temperatures.[79] Here, material is lost from the sample through evaporation, pyrolysis or oxidation if air is present. TGA has been used in conjunction with other analytical techniques for diesel deposit analysis. Venkataraman *et al.* have used TGA to study oxidation processes in various types of fuel deposits. TGA distinguished between ordered and disordered carbonaceous deposit material *via* a CO_2 evolution profile. Since oxidation of disordered structures begins at lower temperatures in the TGA experiment.[84] They were also able to separate oxygen containing material as well as this oxidized at the lowest temperatures.[58,84] More recently, Barker and co-workers used TGA alongside other thermal analysis techniques, this is discussed in the next section.[85] Whilst TGA has been used in previous studies of deposits, it does have its limitations. First, no information is given about the layering of the deposit since it must be scrapped off the injector for analysis; furthermore, TGA, alongside the other thermal techniques discussed are also destructive to the sample so it cannot be used for further analyses.

1.5.7.2. Temperature programmed oxidation

Temperature programmed oxidation (TPO) is somewhat similar to TGA in that it probes the behavior of a sample once heated. Data from TPO can identify the levels of structural ordering of carbonaceous material in the sample. Since more ordered material is less reactive than amorphous carbon and oxidizes at a higher temperature.[84] Venkataraman *et al.* interrogated diesel deposits with TPO, yielding a spectrum showing oxidation occurring between 150–750 °C. The lower portion was attributed to small, light hydrocarbons.[58] The material oxidizing at approximately 680 °C was assigned as polyaromatic carbonaceous material.[58] Later, Barker *et al*. showed a degree of structural ordering of an IDID using TGA and TPO. **Figure 1.6** shows the TPO results with an internal (needle), external (tip) and clean sample. The fact that the tip showed higher reactivity was explained by a higher content of more reactive amorphous carbon.[85] This was proposed to be due to the different temperatures and pressures that each injector part experiences. Another reason for this difference in chemistry could be due to the role of oxygen. The external parts are exposed to oxygen from the combustion chamber, and so it is likely there was a higher level of oxygenated precursors present in the external deposit.[84]

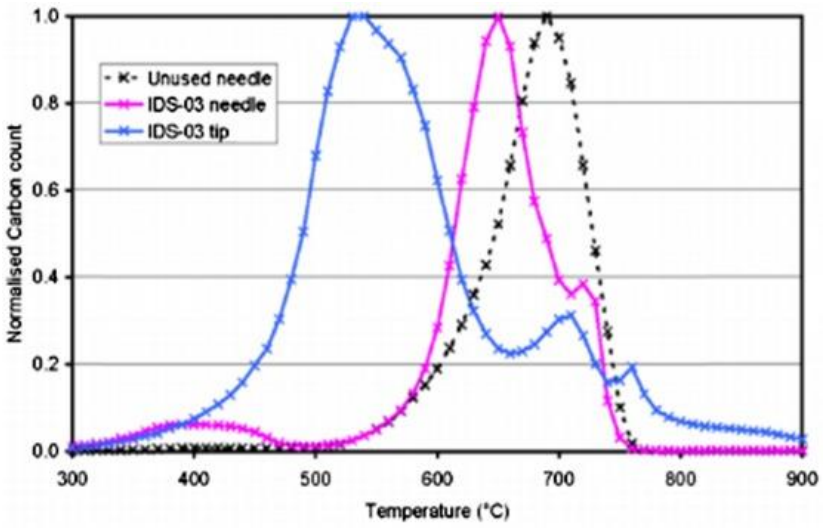


Figure 1.6. *TPO graph from two diesel injector deposits (IDS-03 needle and IDS-03 tip) and a reference sample (unused needle). Showing more ordered material on the needle than the tip. Adapted from Barker et al. (2010).*

Compared with TGA, TPO requires a smaller amount of sample for analysis and opens the possibility for *in-situ* analysis of the deposit on the injector substrate. However, like TGA it is destructive to the sample. A suitable strategy for researchers may be to conduct thermal analysis combined with other non-destructive techniques that could be applied earlier.

1.5.8. Hydrogen pyrolysis

HyPy is performed in the presence of highly pressurized hydrogen (>100 Bar) and high temperatures, causing release of hydrocarbons from the sample without chemical rearrangement. Previous work by Barker *et al.* used HyPy, illustrating different classes of compounds. Some originated from the fuel itself (*n*-hexadecane and *n*-octadecane) as well as alkylbenzenes, methylnaphthalenes and methylphenanthrenes.[86] There was also evidence to suggest the presence of ordered carbonaceous material in the deposit. The group postulated that these may form through hydrogen abstraction of the long chain length fuel to form polyaromatic species.[86] This agrees with other analytical studies using ToF-SIMS,[59] and TEM,[61] showing an archipelago like structure in carbonaceous diesel deposits.

1.5.9. Topographical analysis of deposits

The techniques discussed so far have been used to determine chemical or structural characteristics of deposits. However, techniques are available which

produces profiles of the deposit's surface and may help researchers determine morphology. Dearn *et al.* used 3D profilometry to observe where deposits accumulated most on different GDI injector parts.[66] They concluded that regions closer to the combustion chamber had more deposit accumulation, determined by measuring the minimum and maximum peak deposits heights, than regions which were more shielded from the chamber.[66]

Similar topographical techniques have been applied, such as atomic force microscopy (AFM), which can accurately map the fuel injector surface. Barker *et al.* used AFM to analyse IDID formation. They mapped the surface and were able to highlight regions of 'stickiness' by measuring variables such as adhesion and stiffness at individual points. The adhesion of a deposit surface is an important determinant in the build-up of material on the surface in the presence of aged fuel.[61] In these studies it proved difficult to fully maximize the capabilities of the AFM. This was chiefly owed to the large the fluctuations in the deposit heights and was a limitation of the technique.[61]

1.5.10. Mass spectrometry

The techniques discussed so far have afforded either elemental, structural or topographical information on fuel injector deposits. For full characterisation there is a need to expand this work to afford more detailed molecular information. A suitable technique for this endeavor is MS. Two key examples are discussed below with examples of their characterisation of fuel injector deposits.

1.5.10.1. Gas chromatography mass spectrometry

GCMS is a hybrid technique which separates soluble material in a sample and then labels the peaks according to their molecular mass and has been applied analyzing GDI and diesel deposits. Venkataraman *et al.* illustrated the capability of GCMS for deposit analysis. They identified a range of compound classes such as aldehydes, ketones and alkyl-hydroperoxides. Their presence afforded insight into the oxidative degradation mechanism that occurs during deposit formation.[58] Barker *et al.* used GC-MS alongside HyPy to identify other compound classes such as ordered PAHs and C-16 & C-18 backbones, thought to be derived from carboxylic acids.[87] Similar findings were afforded by Tanaka *et al.* who found these acid derived backbones *via* GCMS which agreed with FTIR data. They argued that at high temperatures these acids would be more likely to precipitate out of the fuel, promoting nucleation of the deposit.[78] Martin *et al.* also utilized pyrolysis-GCMS in multiple studies identified high mass sulfurous compounds. Both were sourced from reactions between common constituents found in gasoline fuel such as aromatics, olefins and benzothiophene.[88,89] Recently, Dearn *et al.* expanded this technique to investigate different GDI parts which were highlighted in **Figure 1.2**. This showed the presence of aliphatic acids such as *n*-hexadecanoic acid, tetra- and penta-decanoic acid in the deposit.[66] Despite its wide applicability to deposit analysis, GCMS does have its drawbacks. Firstly, the sample needs to be dissolved for analysis which assumes that all the material will be soluble. In some cases, testing mixtures needed to be used to confirm solvation of high boiling point material.[66] Furthermore, by using solvents the provenance of the

deposit chemistry is lost. However, employing GCMS after other non-invasive analysis techniques provides useful supplementary data.

1.5.10.2. Time of flight secondary ion mass spectrometry

With SIMS a primary ion beam fires charged particles at the samples surface causing surface molecules to ionize and detach from the surface as secondary ions for identification by a mass analyser.[73] The technique is discussed further in the next section. Two broad types exist: 1) Static SIMS, where the primary ion beam uses a low dose to obtain a spectrum without damaging the sample surface, offering non-destructive analysis of fuel deposits. 2) Dynamic SIMS, where a higher dose is used to sputter a samples surface. This allows depth profiles to be generated and is a useful feature for the analysis of layered injector deposits. SIMS is commonly used in combination with a ToF analyser and affords high spatial resolution and a fast acquisition rate.[90,91] The application of ToF-SIMS is a relatively new development in the field of injector deposits. Barker *et al.* first carried ToF-SIMS on an IDID and have identified elements such as sodium, sulfur, calcium, potassium and nitrogen as well as larger fragments including $Na_2SO_4^+$, $NaOH^+$, C_3N^- and C_6^-.[60] Through dynamic SIMS they found distinct differences between the intensities as sputter times increased. Depth profiling data illustrated that some ions were only present in upper or lower most layers. A schematic was drawn summarizing the data and is shown in **Figure 1.7**.

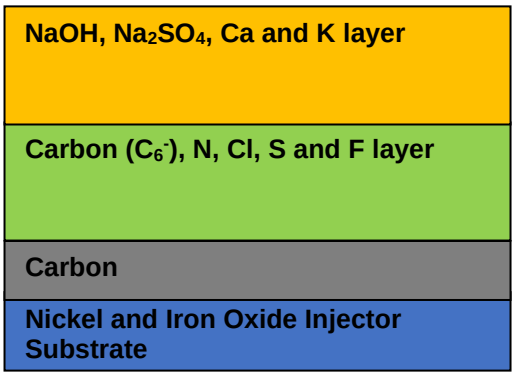


Figure 1.7*. Outline of layering in a US sourced diesel injector deposit, derived from a depth profile provided by time-of-flight SIMS, adapted from Barker et al. (2012).*[60]

Importantly, the C_6^- ion increased in intensity toward the injector surface and evidenced the presence of ordered carbonaceous material in the lower layers of IDID's. Comparative works has identified different layering in IDID's based on the country of origin which was attributed to varying fuel specifications impacting on the chemistry of the deposit.[87] Further work by the group has shown the presence of PAHs with structures greater than six rings. However, this was only achieved by running reference samples to compare to sample spectra.[59]

Dallanegra *et al.* also carried out ToF-SIMS depth profiling which showed 2 distinct layers above the injector surface. They found that the outermost layers were organic in nature and relatively uniform toward the injector surface. The innermost was an interface between the oxide layer on the injector surface.[43] More recently, Oberender *et al.* used ToF-SIMS alongside FTIR. They identified molecules sourced from certain fuel and lubricating oil additives on a diesel injector, such as PIBSI.[51] Variants on ToF-MS do exist such as resonance

enhanced multiphoton ionization (REMPI) ToF-MS. This selectively excites certain classes of compounds in a complex organic matrix to aid researchers in characterizing organic species.[92] Lau *et al*. used REMPI-ToF MS on engine deposits previously, through excitation of the surface they could selectively ionize the PAHs present in engine deposits. This permitted them to identify distribution of aromatic ring sizes at varying temperatures. Finding that as temperature increased by only 20 K the aromatic content of the deposit increased significantly.[93]

Despite its clear applicability to analyzing layered injector deposits, ToF-SIMS does have some drawbacks. First is the relatively low mass resolving power and accuracy that was exhibited when analyzing diesel deposits and resulted in the need for reference samples to be used in some cases.[59,94] Secondly, it is a semi-quantitative technique due to the preferential ionization of certain ions over others.[73] Thus, for quantitative analysis other techniques should be applied in parallel, such as XPS. This again highlights the importance of the use of non-destructive analytical techniques for fuel deposit characterisation.

1.6. Summary of previous capabilities for analyzing deposits

A survey of the literature has shown that there are a number of causes attributable to the formation of fuel injector deposits. They are typically derived from the breakdown of fuel, but other sources of contamination do exist. Furthermore, the mechanism for just how they form is generalized to date. Analytical studies into GDI and diesel deposits have highlighted several key points:

- Both GDI and diesel injector deposits are heterogeneous. Their chemistry varies across the sample surface. Diesel deposits have been found to be layered.
- Elemental analysis from SEM-EDS and XPS has shown a range of elements present, sourced from both the fuel and lubricating oil. Highlighting carbonaceous, lacquer type and metal-based deposits for example.
- Some techniques give information on bonding modes present in deposits such as XPS and FTIR spectroscopy. When combined with elemental analysis these have evidenced molecules such as PAHs in deposits previously.
- TEM and Raman spectroscopy can distinguish between ordered and disordered carbon in the deposit. Raman is also non-destructive to the carbon in the sample.
- Thermal analysis from TPO, TGA and HyPy has characterized specific fuel residues and afforded information on carbonaceous structural ordering. But heating of the sample removes its provenance so the layering of the sample cannot be observed.
- Topographical information from AFM and profilometry has shown that deposit height and adhesion vary significantly.
- MS techniques have been used in accurate characterisation of organic material; some have been applied to diesel injector deposits. However, most techniques cannot analyse the layering of fuel deposits
    - ToF-SIMS is an exception to this rule but has a relatively low mass resolving power and is not fully quantitative to the sample.

Overall, the structural, elemental and topographical data afforded from these techniques are somewhat limited and has given only general information on the chemical species present in deposits. Therefore, the use of a non-destructive MS technique with high resolution and accuracy which can also give spatial information would be well suited to give a comprehensive analysis of GDI and diesel injector deposits.

Part two (unpublished)

1.7. Introduction to SIMS and 3D OrbiSIMS

The methodology for analytical techniques is explained in each separate chapter. However, the fundamentals of SIMS and the 3D OrbiSIMS technique is introduced below as it is a crucial part of the work in this thesis.

1.7.1. The SIMS emission principle

The general principle relies on detecting secondary ions that are liberated from a sample by bombardments from a primary ion source, the specific mechanism is its own area of research.[95–97] An equation can be deduced which describes the basic principle of SIMS (equation 1), which relates the probability of a species being ionized to the sputtering yield (Y_m) of an analyte:

$$I_m = I_p Y_m \alpha \theta_m \eta \qquad \text{(Equation 1)}$$

In SIMS I_m is the number of ionized secondary ions liberated from the sample and is small (typically < 1 %), meaning that most species liberated upon impact are neutral and are not detected.[98] The probability of ionization of a molecule is

dependent on many factors,[73] including its concentration at the surface (θ_m). However, other factors do influence this probability, including the primary ion current (I_p) and the transmission of secondary ions to the analyser (η) which can be affected by charge compensation and surface topography. The ionization probability (α) is partially affected by surface topography, the electronegativity of the molecule, its surrounding chemical environment, and its electronic state. The effect on the ionization probability from uncontrollable factors is referred to as the *matrix effect* in SIMS analysis and results in the ion intensity of species not being fully quantitative (i.e., not just dependent on θ_m). This also affects the ionization probability of different fragments from the same molecule, again adding another layer of complexity to SIMS analysis, particularly for heterogeneous analytes.

A diagram illustrating ion liberation from a sample in positive ion mode is shown in **Figure 1.8**, where a primary ion source causes fragmentation of the analytes surface. Upon impact from a primary ion source, a 'collision cascade' process follows where initial energy is dispersed throughout the material, causing motion of surface particles. If the energy is enough to overcome the surface binding energy, then the specie can leave the surface for detection. More complete ion fragments are liberated further from the impact site of the primary ion source despite the initial vector of the primary ion source.

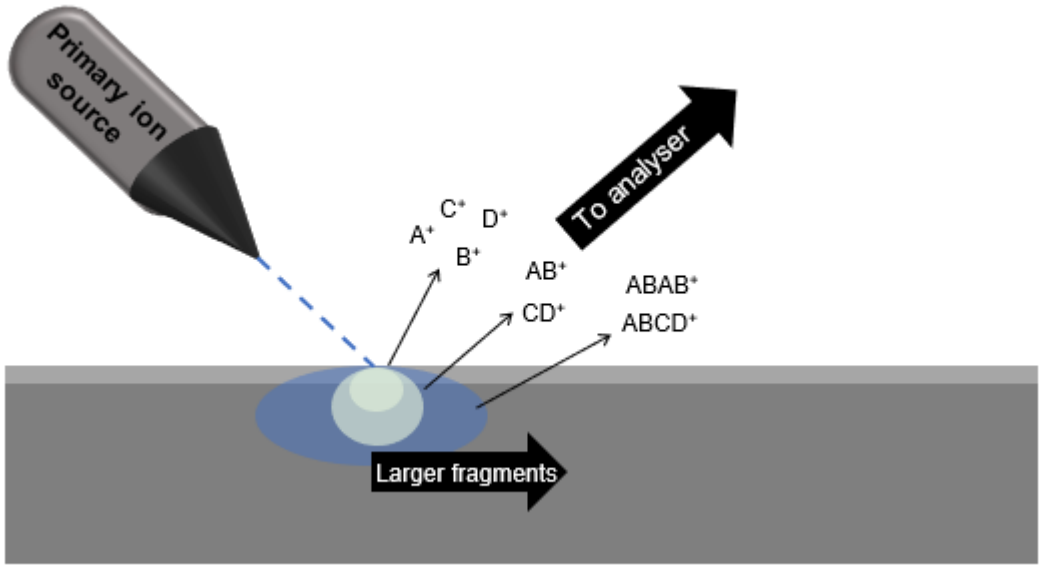


***Figure 1.8**. The principle of SIMS for a heterogeneous analyte made up of molecules 'AB' and 'CD', showing liberation of elemental and molecular ions in positive mode. Larger ions are liberated further from the impact zone.*

Ionization of species can occur in several ways, including[73,98]: 1) impact of the ion source forming a positively charged ion by removing one electron (forming a charged radical); 2) by breaking of chemical bonds to form a positive and negative charged ion; 3) formation of $[M + H]^+$ ions by incorporating neutral species with protons; 4) liberation of neutral molecules that later lose an electron by changing electronic state; 5) liberation of neutral species which collide with secondary electrons. These complex processes mean that several different secondary ion types could be yielded from one ion type. Upon ionization an extraction voltage is applied to the sample to attract charged ions toward the analyser. This voltage is in the opposite polarity to the mode of operation. Bunching of ions to group them together before sending to the analyser is often performed to reduce the spread of kinetic energy which each ion may have upon leaving the analysis area too to improve mass resolving power.[99] This energy

spread can also be overcome by performing delayed extraction, used on both time-of-flight SIMS and matrix-assisted laser desorption ionization (MALDI) ToF MS.[100,101] Here, the extraction potential is applied at a specific time-delay after ionization to further narrow the energy spread of ions with the same *m/z* ratio and is particularly useful in samples with excessive topography.

One issue in SIMS is the accumulation of charged ions at a sample surface which can impede transmission of ions to the analyser, generating charged ions on a conducting surface poses little issue as the charge can be dispersed away from the analysis area. However, for insulating samples, such as organics, this is not the case and so an electron flood gun is employed by SIMS instruments. A low energy relative to the primary ion source is used (usually < 21 eV) to ensure no damage of the surface. Argon flooding can also be used where Ar(g) is passed over the sample and used to regulate main chamber pressure, which also helps to prevent charge accumulation in the analysis area to increase ion transmission.

1.7.2. Primary ion sources

The type of ion source used will heavily influence the types of fragments that are released from the analyte.[73] Traditionally SIMS used monatomic ion sources including O^+, Cs^+ or Ga^+. The high fragmentation of the analyte when using a monatomic Bi LMIG is evident in previous work using ToF-SIMS on fuel deposits (see section 1.5.10). Next there was the development of clustered ion sources such as C_{60}^+, Au_3^+ or Bi_3^+ which are more applicable to organic samples such as polymers.[102] A clustered source with the same overall energy as a monoatomic source will have far less energy per atom as it hits the surface and

breaks up (**Figure 1.9**). This has several benefits including less penetration of the sample, less chemical damage and generation of more intact fragments for analysis.[102,103] One of the most recent developments is the large Argon gas cluster ion beam (GCIB) which can have varying cluster sizes, each size has different benefits depending on the sample and a commonly used size is 3000, although a gaussian distribution of cluster sizes always exists around the selected modal value.[104] Cluster ion sources have also been shown to increase the sputter yield (and ionization) and depth resolution from SIMS measurements.[105,106]

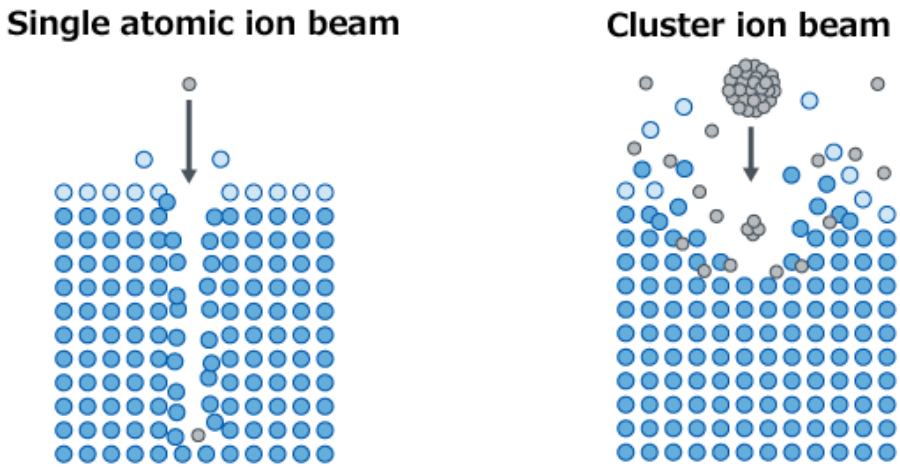


Figure 1.9. *Comparing fragmentation of a samples surface with a cluster ion source and a single atom ion beam. Showing lower fragmentation and more surface information from secondary ions in the cluster source. Adapted from ULVAC-PHI*[107]

1.7.3. Modes of analysis

One of the most attractive features of dual beam SIMS analysis is its ability to perform different types of analysis with a single instrument. Three broad analysis modes exist, spectral analysis, depth profiling and chemical imaging. As mentioned, ionization of sample material physically removes molecules from

the surface, but when a low enough dose of primary ions is used such that each primary ion will hit an area that has not been damaged by a previous pulse, and only the top monolayer is interrogated. This dose is defined roughly as 10^{12} - 10^{13} ions/cm^2 and is termed the *static limit*.[108] When the primary ion dose is increased above this level during beam rastering in a defined area then destructive analysis of the sample proceeds. Dynamic SIMS relies on this process and monitors the intensity of ions measured over the sputtering cycle to generate depth profiles. Increasing the dose to the sample has other benefits such as increased sputtering yield from the sample too. Depth profiling SIMS is particularly applicable to analyzing layered fuel deposits (see **Section 1.5.10.2**).

In chemical imaging, rastering of the primary ion beam over the sample area generates chemical maps by measuring ion intensity at each position, or pixel, to show the spatial distribution of each ion in the raster area. Each pixel contains a full mass spectrum, which are combined into a single mass spectrum to represent the whole analysis area.[73] Imaging introduces another measure to compare instrument performance, spatial resolution. This is dictated by how fine focused the primary ion beam is during analysis and thus the overall pixel size and is dependent on the settings chosen by the analyst and the primary ion sources. There is also a trade-off between the size of primary ion spot-size and imaging current, which is needed to generate well resolved images.

1.7.4. The Orbitrap mass analyser

The Orbitrap™ was developed in the 1990's[109] and is used in various high-resolution mass spectrometry applications including LC/GC-MS, electrospray-

MS, MALDI MS and recently with the HybridSIMS instrument (specifically the Q-Exactive HF Orbitrap).[110] The general concept relies on trapping secondary ions in a C-trap before orthogonally injecting them as a packet into the analyser, which consists of an inner spindle and outer wall.[109,110] Voltages are applied from the outer wall and the inner spindle, causing injected ions to oscillate radially in a stable trajectory held by the electric field. A schematic of the analyser is shown in **Figure 1.10**, taken from the HybridSIMS instrument manual.

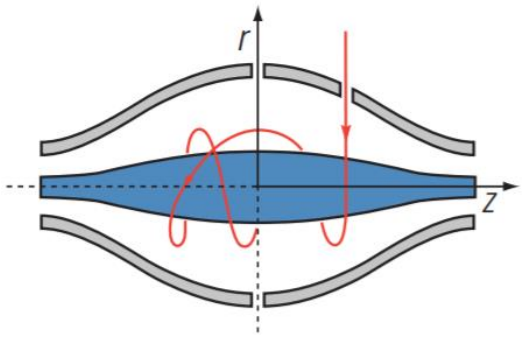


Figure 1.10. *Illustrating the inner cross-section of an Orbitrap analyser with a representative secondary ion after orthogonal injection from the C-trap.*[111]

Each ion with a specific *m/z* ratio will oscillate with both a radial vector and an axial vector (z-direction), the latter is detected as fluctuations to the continuous current on the potential plates, this current change is measured over time and through Fourier transformation is converted to a frequency domain and then into a mass spectrum. The frequency at which an ion will axially oscillate is related to its *m/z* ratio in equation 2 by:[109]

$$\omega = \sqrt{\frac{z}{m} \times k} \qquad \text{Equation 2}$$

The frequency (ω) depends only on the *m/z* ratio and an instrumental constant, k. Ions oscillate radially and axially around the spindle, the latter currents are

used in Fourier transformation since these are not dependent on the initial parameters of injection and so the spread of current detected for ions with the same *m/z* ratio is smaller, translating to sharper spectral peaks.

Orbitrap analyzers in combination with SIMS can yield a mass resolving power of > 240,000 for a peak of *m/z* 200, that is, $m_1/(m_1-m_2)$ for two peaks that partially overlap[112], *i.e.*, it can distinguish between two overlapping peaks at this mass with a difference of 0.0008 u (200/240,000). Fuel deposits are made up of a huge number of different molecules and so being able to differentiate between these accurately is crucial. By comparison, a typical ToF analyser such as that used in previous work in deposit analyses affords a MRP of < 20,000 so could only distinguish, at best, peaks with a mass difference of 0.01 u. Orbitrap analyzers are widely used because of their high mass accuracy (difference between the center of the observed peak and the expected position, which is displayed as a reciprocal in parts per million (ppm)). The Orbitrap routinely achieve accuracies < 2 ppm and can achieve errors in the parts-per-billion range too. ToF analyzers, however, routinely achieve far lower accuracies (> 20 ppm). Another advantage of the Orbitrap over other previous analyzers used in deposit analysis is its MS/MS capabilities. This is used frequently in mass spectrometry, whereby fragmenting a secondary ion into its constituent fragments is used to confirm initial assignments and is often used to give insight into the precise structural orientation of molecules.

1.7.5. The use of high mass resolving power MS in petroleomics

Techniques with high mass resolving power such as Orbitrap and Fourier transformed iso cyclotron (FT-ICR) MS are used extensively in analyzing complex mixtures in the field of 'petroleomics' (analysis of petroleum and related fractions). FT-ICR MS has been used extensively in the analysis of fuels, including diesel and kerosene,[113 114–116] A recent example by Smith *et al.* used a new type of FT-ICR MS on a volcanic asphalt sample, achieving a MRP of 2,700 000 at an *m/z* of 400 with an accuracy of 0.08 ppm. In the spectra some peaks were separated by the mass of an electron (**Figure 1.11**).[117]

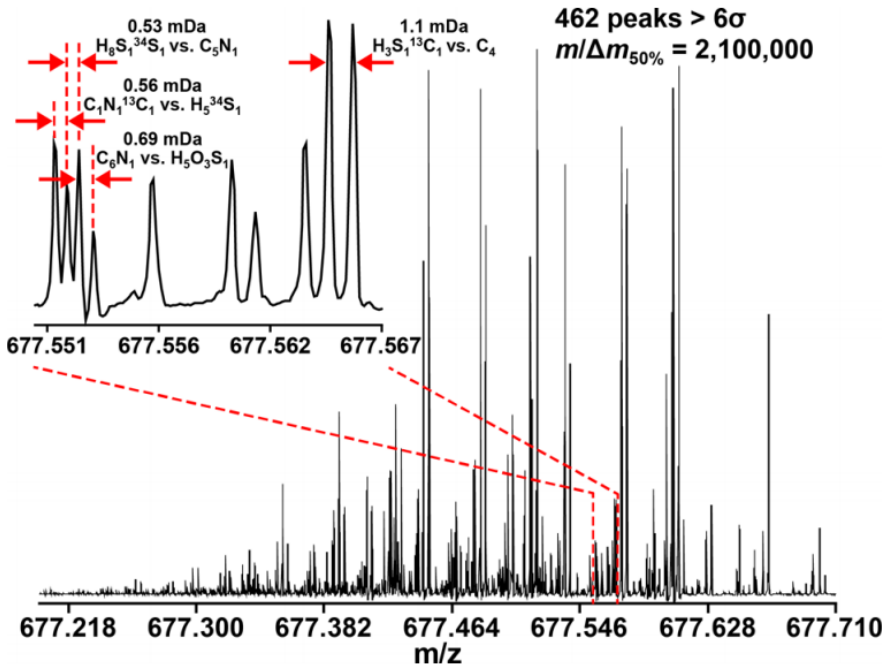


Figure 1.11. *FT-ICR spectra from a volcanic ash sample. Illustrating ultra-high resolution with some peaks separated by just the mass of an electron (0.55 mDa). Adapted from Smith et al. (2018).*

FT-ICR MS has been used to study deposit precursor fuels, Langley *et al.* studied different fuels, some were identified as 'fouling' fuels (those likely to

promote deposit formation) and others as ‘non-fouling’ fuels. They identified species which are attributed for promoting deposit formation.[118]

These types of techniques would be useful for analyzing complex organic material such as engine deposits. However, the lack of a sputtering means they cannot carry out sputtering of the sample to generate depth profiles. These techniques require the use of solvents, making it unsuitable for analyzing insoluble deposits. The high resolving power also has a trade off with long acquisition times. Imaging is only possible when coupled to other spectrometers such as electrospray ionization MS,[119] or MALDI MS.[120] Furthermore, the imaging resolution is lower than in ToF-SIMS (< 100 nm in ToF SIMS and 2 μm in 3D OrbiSIMS).[121]

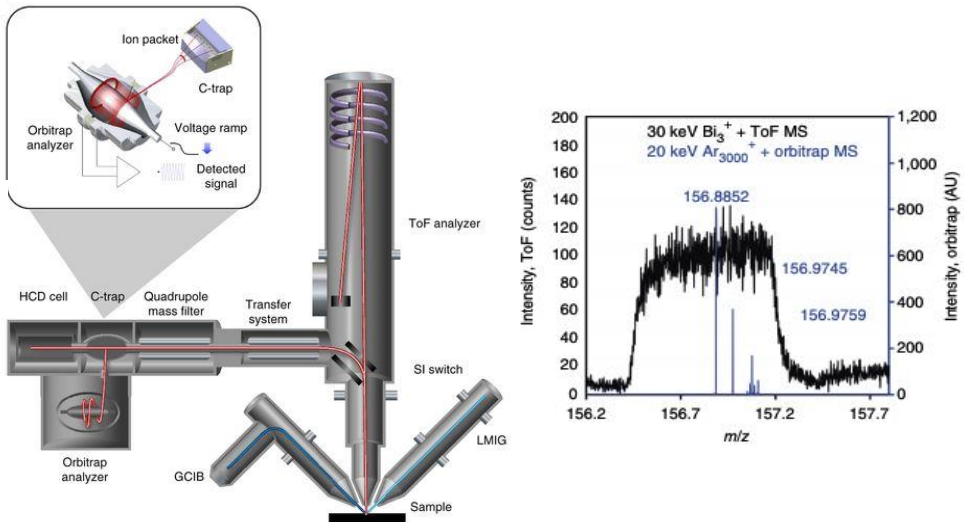
SIMS gives the largest arsenal for analyzing layered injector deposits with both static and dynamic SIMS modes. However, traditional ToF-SIMS suffers with low resolution and accuracy. In answer to this dilemma, a new hybrid technique has been developed which combines ToF-SIMS instrument with a high-resolution Orbitrap mass analyser, termed 3D-OrbiSIMS.

1.7.6. The 3D OrbiSIMS technique

The utility of ToF-SIMS, with its speed of acquisition, high lateral imaging resolution is limited by poor mass resolving power. But this was overcome by combining a ToF-SIMS instrument with an Orbitrap analyser (mass resolving power > 240, 000), the new technique, ‘3D OrbiSIMS’ is performed on a HybridSIMS instrument (IONTOF, GmbH). It combines several primary ion sources, notably a low energy GCIB as well as a Bi LMIG gun for use with the

ToF analyser. A diagram of the 3D OrbiSIMS instrument is given in **Figure 1.12**. The instrument was first demonstrated by Passarelli *et al.*,[121] and they showcase both the improvement of using a GCIB-Orbitrap combination compared to the LMIG-ToF for highly accurate, high-mass resolving power spectral analysis. This is demonstrated by the spectra in **Figure 1.12** which shows the far superior resolving power acquired in this mode (blue) than with LMIG-ToF analysis. The HybridSIMS also includes the benefit of the fast-imaging mode using the LMIG-ToF setup, with a 2 μm chemical image taking just 35 minutes to acquire compared to 10 h with the GCIB-Orbitrap. GCIB-Orbitrap imaging was possible down to resolution of 2 μm and spectral analysis of diagnostic molecular ions > *m/z* 1000 at sub-ppb accuracies.

(a)



(b)

	Method	Beam modality	Mass analyzer	Mode
	Surface spectra (1D)	Single beam (Bi_n or Ar_n)	ToF	1
			Orbitrap analyzer	2
	Depth profiling	Single beam (Ar_n)	ToF	3
		Dual beam (Ar_n and Bi_n)	Orbitrap analyzer	4
			Dual analyzer	5
	Imaging (2D)	Single beam (Bi_n or Ar_n)	ToF	6
			Orbitrap analyzer	7
	3D Imaging	Single beam (Ar_n)	Orbitrap analyzer	8
		Dual beam (Ar_n and Bi_n)	ToF	9
			Dual analyzer	10

Figure 1.12. (a) *Left, schematic of the 3D OrbiSIMS instrument. Right, illustrating the enhanced resolution from the GCIB Orbitrap analysis compared to the LMIG ToF*

setup. ***(b)*** *Modes of analysis from the instrument. Adapted from Passarelli et al. (2017).*[121]

Since the deployment of 3D OrbiSIMS there have been several papers published in various fields of research. Kotowska *et al.* showed how using the soft ionization and high mass resolving power capabilities could yield diagnostic amino acid fragments for protein identification.[122] Starr *et al.* used the technique on skin to advance their field by collecting diagnostic fragment data from layers of the skin *in-situ*.[123] Schaepe *et al.* also compared imaging from 3D OrbiSIMS to ToF-SIMS analysis on the HybridSIMS instrument and MALDI MS for detecting lipids in native human bone sections and found intact lipids with 3D OrbiSIMS whereas ToF-SIMS was able to identify without the need for a matrix spray like with MALDI MS.[124]

In all cases the use of the 3D OrbiSIMS technique gave a step change to the respective field, by providing high mass resolving power of diagnostic molecular fragments. For application to fuel deposits, the *in-situ* analysis capabilities of SIMS by depth profiling demonstrated by Barker et al (see section 1.5.10) was the first step change for the field. But to move forward we need to provide a more comprehensive, molecular characterization at high mass resolving power, and for this the 3D OrbiSIMS technique appears well-suited for the task.

1.8. Aims and objectives of this Thesis

1.8.1. Existing knowledge and challenges for the field

Studies into diesel deposits span several decades and have showed that they derive both from species in fuel and from 'contaminants'. Yet the generic information, either elemental or small molecular fragments from MS analysis, means that we do not know the specific composition nor origin of specific 'bad actors' in fuel compositions or additive packages which may need to be removed or modified to prevent deposit formation. Very little molecular data has been acquired which will be key to provide a comprehensive account of deposit composition and origin of species. Deposits have shown to be layered materials in terms of elemental composition,[60] but without molecular data it is hard to be sure as to why this occurs and where the key deposit components originate from. It is unknown how deposit layering arises *i.e.*, what is the growth pathway for a thin layer of fuel deposited on a surface which causes growth to a carbonaceous deposit?

The key challenge to characterizing these materials is their insolubility and layered nature, which limits the analysis techniques applicable to gain a comprehensive understanding of their chemistry. Therefore, we must use an *in-situ* (solvent free) technique capable of providing diagnostic molecular data at all depths of deposits. Moving forward, as fuel complexity increases with, for example, the inclusion of bio-ethanol into modern fuels then it is imperative that a suitable analysis protocol is established which can pick apart the components of this complex mixture. Overall, there is a lack of knowledge on the

composition, origin and mechanisms of growth of both GDI (gasoline) and diesel deposits.

1.8.2. Thesis aims

To gain molecular information on engine deposits to understand the origin of key constituents and finally to understand the reasons for their existence, i.e., are they deposited or grown on the surface over time.

1.8.3. Thesis objectives

We will embark on a comprehensive analysis of deposits using a series of analytical techniques including, chiefly 3D OrbiSIMS depth profiling. Our objectives are to firstly:

1. Establish a suitable analysis protocol for interrogating deposits from the field (i.e., those which have seen a variety of fuels), we will analyse deposits from different engine types (diesel and gasoline) to compare the effect of temperature on composition.

2. Develop suitable data analysis protocols to allow us to be comprehensive in our analysis, and comparison, of 3D OrbiSIMS data from engine deposits.

3. Use both protocols to apply the method to a suite of samples obtained from controlled engine testing to understand any common growth mechanisms and examine the commonality between samples.

The first results chapter (Chapter 2), comprises of two peer reviewed articles, covers objective 1. The second objective is covered in the second results chapter (Chapter 3) which is from a peer reviewed article. Chapter 4 covers objective 3 and is also from a peer reviewed journal article. Each Chapter is enclosed as a standalone piece of work. Relevant supporting information from each is found in the appendix but can also be found online by following the provided DOI link.

Chapter 2

Comparing the Molecular Compositions of Internal and External Gasoline and Diesel Deposits

The aim of this chapter is to compare spatially resolved compositions of deposits from a range of engine components and types to understand the reasons for compositional differences (i.e., the origin of different deposit contributors). Previous work in this field has analyzed samples from various sources but not provided a detailed comparison on molecular compositions, nor provided any spatially resolved data. Comparison to diesel samples will be a useful benchmark as a lot of analysis on these samples has been done previously and can be used to compare data to other analytical techniques regarding chemical structure and origin elucidation. Far less work has been conducted in gasoline deposit analysis, so this exploratory study will outline the level of information that can be obtained from these samples.

In part 1, we present 3D OrbiSIMS depth profiling and chemical imagine data from a gasoline direct injector, a diesel fuel injector and a diesel engine filter, combined with the first application of MS/MS analysis on these sample types to demonstrate unambiguous identification of molecular species. Subsequently, a comparison of two gasoline deposits formed on different parts of the same

injector is made using the method established to isolate the effect of temperature on deposit composition.

2.1. Chapter 2 objectives

- Establish whether 3D OrbiSIMS depth profiling and chemical imaging can ascribe the identity and origin of whole molecules in deposits.
- Compare the intensity or presence of key species identified across gasoline and diesel deposits.
- To generate supplementary quantified data from XPS to support 3D OrbiSIMS speciation.

2.2. Part one

Spatially Resolved Molecular Compositions of Insoluble Multi-Layer Deposits Responsible for Increased Pollution from Internal Combustion Engines

*Max K. Edney[1], Joseph S. Lamb[1], Matteo Spanu[1], Emily F. Smith[2], Elisabeth Steer[2], Edward Wilmot[4], Jacqueline Reid[4], Jim Barker[4], Morgan R. Alexander[3], Colin E. Snape[1] & David J. Scurr[3]**

[1]University of Nottingham, Department of Chemical and Environmental Engineering, University Park, Nottingham, NG7 2RD, UK.

[2]University of Nottingham, Nanoscale and Microscale Research Centre, University Park, Nottingham, NG7 2RD UK.

[3]University of Nottingham, School of Pharmacy, University Park, Nottingham, NG7 2RD, UK.

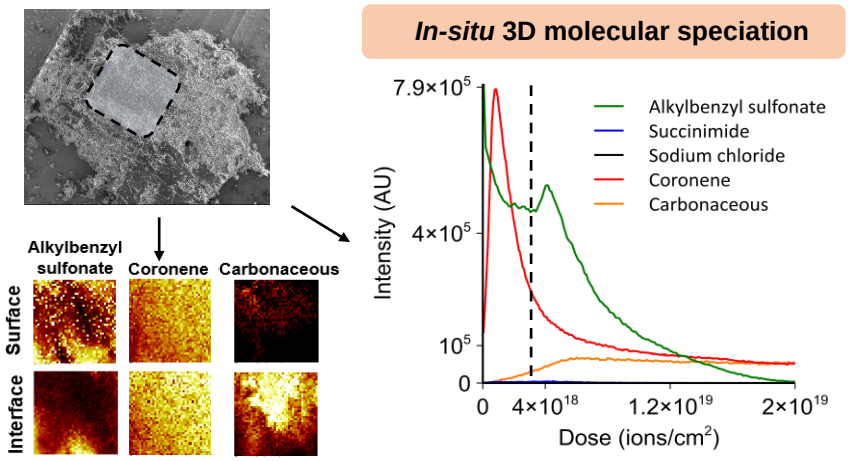
[4]Innospec Ltd., Oil Sites Road, Ellesmere Port, Cheshire CH65 4EY, UK.

Published in *ACS Applied Materials and Interfaces* in 2020 *(DOI: 10.1021/acsami.0c14532).*

Author contributions

M.K.E., J.S.L., D.J.S., and M.S. conducted 3D OrbiSIMS experiments. E.F.S. collected XPS data. M.K.E., J.S.L., M.S., and E.S. collected SEM micrographs. M.K.E., J.B., J.S.L., D.J.S., C.E.S., E.F.S., M.S., E.S. and E.W. interpreted the analytical data. M.K.E. wrote the manuscript. All authors helped in editing the manuscript.

2.2.1. Abstract



Internal combustion engines are used heavily worldwide in diverse applications. Achieving the most efficient operation is key to improving air quality as society moves to a decarbonized energy system. Insoluble deposits form within internal combustion engine components including fuel injectors and filters and negatively impacts CO_2 and pollutant emissions. Understanding the composition, origins and formation mechanisms of these complex materials will be key to their mitigation, however, previous attempts only afforded non-diagnostic chemical assignments and limited knowledge toward this. Here, we uncover the identity and spatial distribution of molecular species from a gasoline direct injector, diesel injector and filter deposit in-situ using a new hyphenation

of secondary ion mass spectrometry and the state-of-the-art Orbitrap^{TM} mass analyzer (3D OrbiSIMS) and elemental analysis. Through a high mass resolving power and tandem MS we unambiguously uncovered the identity, distribution and origin of species including alkylbenzyl sulfonates and provide evidence of deposit formation mechanisms including formation of longer chain sulfonates at the gasoline deposits surface. As well as aromatization to form polycyclic aromatic hydrocarbons up to $C_{66}H_{20}$, which were prevalent in the lower depth of the gasoline deposit. Inorganic salts contributed up to 16 % to the diesel injector deposit throughout its depth, suggesting contamination over multiple fueling cycles. Findings will enable several strategies to mitigate these insoluble materials such as implementing stricter worldwide fuel specifications, modifying additives with adverse reactivity and synthesizing new fuel additives to solubilize deposits in the engine, thereby leading to less polluting vehicles.

2.2.2. Introduction

It is proposed that by 2040, 70 % of light passenger vehicles will still use internal combustion engines.[125,126] These offer benefits such as efficiency, cost, reliability and flexibility of burning new generation fuels, and as such will feature heavily in the future global vehicle mix for road, rail, off-road and marine applications.[127–132] Two processes in internal combustion engines that greatly influence emissions and efficiency are fuel injection, where fuel is injected into the combustion chamber, and fuel filtration, where fuel is repeatedly passed through and cleaned for recirculation back into the fuel injectors. However, insoluble deposits, caused by contaminated or unstable fuel mixtures,[22,37] commonly afflict these components and lead to a decrease in fuel economy and

an increase in pollutant emission from internal combustion engines. [27–29,133] For example, deposit formation can increase particulate emissions by up to five times.[29,134] The World Health Organization estimate that poor air quality leads to 7 million premature deaths each year,[135] therefore mitigating deposits will present benefits from an environmental and healthcare perspective.

A fundamental step in the quest of mitigating deposits is to understand their underlying chemical composition and origins. A review by Edney *et al.* summarizes the key analysis techniques applied to date.[136] Scanning electron microscopy (SEM) offers semi-quantitative elemental analysis and facile sample preparation and has identified contributing elements including sulfur, phosphorus, and calcium. This has implicated possible origins from fuel derived material and lubricating oil.[136] Infra-red spectroscopy allows functional group identification and has inferred the presence of fuel constituents in the past such as C_{16} and C_{18} carboxylic acids and components from additive packages such as "non-commercial" low molecular weight polyisobutylene succinimides.[87] Carboxylic acids have several potential sources such as bio-diesel,[137] or corrosion inhibition additive packages that contain sodium and calcium.[48] XPS has provided quantified elemental surface information from deposits previously.[58,73] SIMS requires no sample preparation for deposit analysis and can probe the provenance of material through ion beam etching. Previous work on internal diesel injector deposits using time-of-flight SIMS with a Bi_3^+ ion beam identified ion fragments such as C_3N^- and C_6^-, but many were non-diagnostic.[51,59,60] This limitation arose due to high fragmentation of analyte and a low mass resolving power of the time-of-flight analyser.

3D OrbiSIMS is a recently developed technique that relies on similar working principles to time-of-flight SIMS.[121] The Orbitrap™ analyser affords greater mass accuracy and a more than 10-fold increase in mass resolving power than the time-of-flight analyser. It also provides the capability for chemical speciation using secondary fragmentation of ions of interest to make unambiguous assignments.[121] The argon gas cluster ion beam can perform simultaneous sample etching and analysis, maintaining diagnostic chemical species for identification.[138] This work is the first application of 3D OrbiSIMS to provide spatially resolved information on key molecular species in insoluble deposits. We present 3D OrbiSIMS data from samples sourced from a gasoline and diesel fuel injector and a diesel filter component, combined with MS/MS analysis to demonstrate unambiguous identification of deposit components and to showcase the suitability of the technique. This study was limited to analyzing one sample type of each component, however analytical repeats were taken on each sample. We focus on molecular species including succinimides that are used in both fuel and engine lubricating oil formulations and alkylbenzyl sulfonates, added directly to lubricating oil additive packages in gasoline and diesel engines,[139] and inorganic salts. We also identify large polycyclic aromatic hydrocarbons (PAHs) extending up to 800 Da, previously only speculated to be present in insoluble deposits. Comparison of the maximum size of PAHs gave insight into how the deposit matrix is formed in the engine components. We performed quantitative elemental surface analysis by XPS to complement the 3D OrbiSIMS data. This is the first comparison of deposits from different engine components across the gasoline and diesel fuel streams. Findings have

significant implications for the upward and downward fuel stream as well as engine, fuel injector and additive manufacturers.

2.2.3. Results and discussion

2.2.3.1 Identification of molecular species

Negative ion data acquired from a 3D OrbiSIMS depth profile of the three deposit samples in the range of *m/z* 75-400 are shown in **Figure 2.1.1**, we provide negative ion data above *m/z* 400 in **Supplementary figure S2.1.1**. Spectra were acquired from external surfaces of a gasoline direct injector component, a diesel injector component and a diesel engine filter component recovered from real-world vehicles previously in operational service. SEM micrographs of the three deposits with the highlighted 3D OrbiSIMS analysis area are shown in **Figure 2.1.1**. Secondary ions were identified and grouped into compound classes, including alkylbenzyl sulfonates, succinimides, inorganic salts, dehydrogenated carbonaceous ion fragments and C_{16} and C_{18} carboxylic acids. Putative structures are displayed, detailing their compound class, mass, and deviation (ppm). An extended list of the ions found in the samples with intensity data are given in **Supplementary table S2.1.1**.

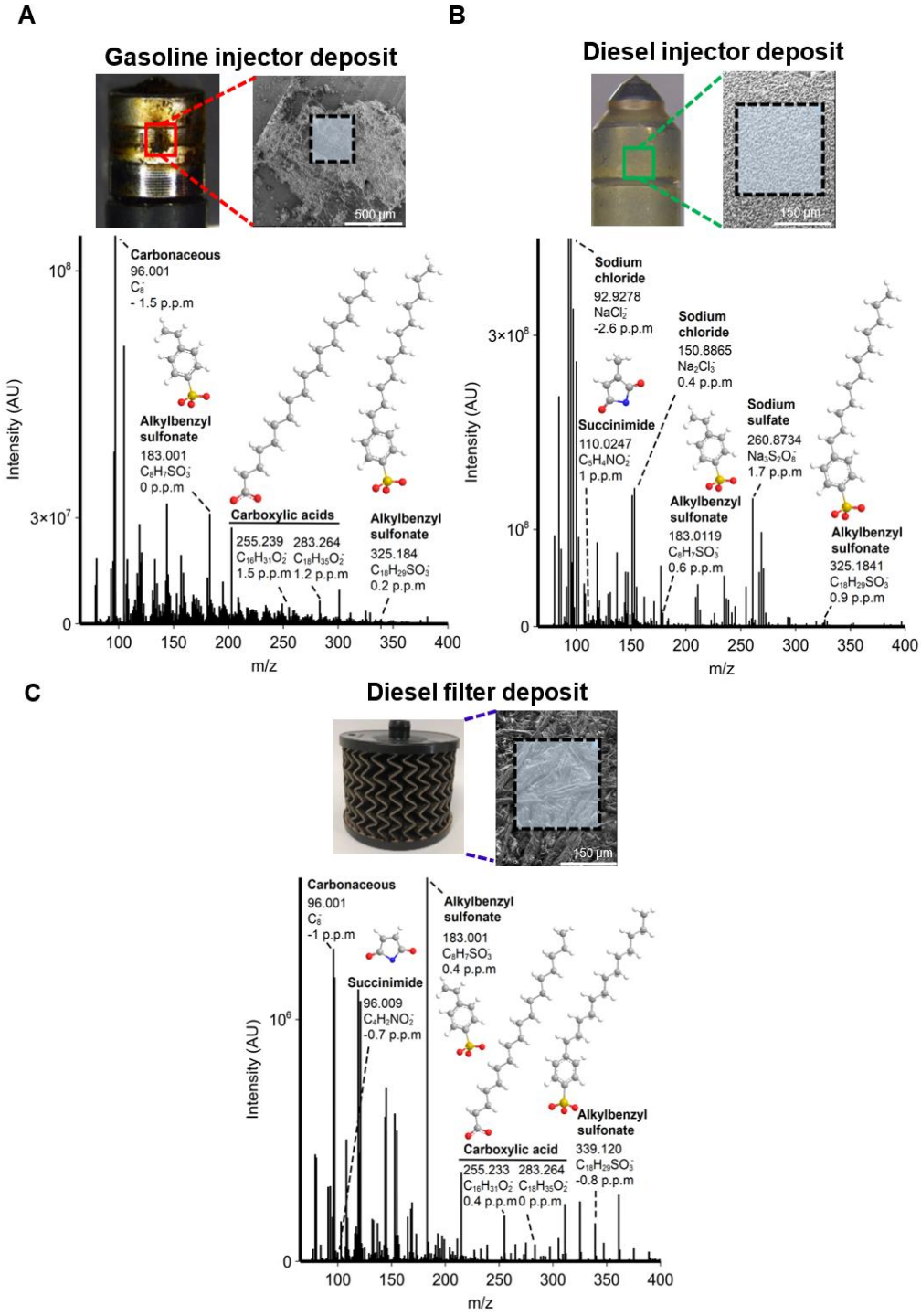


Figure 2.1.1. Identifying key molecular species in insoluble deposits with 3D OrbiSIMS. *Photograph and inset SEM micrograph (above) and 3D OrbiSIMS depth profile accumulation ion data in negative polarity (below) of the* ***(a)*** *gasoline injector,* ***(b)*** *diesel injector and* ***(c)*** *diesel filter deposit samples. Negative ion data for key deposit contributors are displayed with suggested chemical structures.*

Several alkylbenzyl sulfonate ions were present in all engine component deposits and were assigned with the generic formula of $[C_6H_4(SO_3)(C_nH_{2n+1})]^-$, with a saturated hydrocarbon chain extending from the benzyl group (**Figure 2.1.1, a** to **c**). In all deposits the dodecylbenzene sulfonate ion, $C_{18}H_{29}SO_3^-$ ($[C_6H_4(SO_3)(C_{12}H_{25})]^-$), was present and is assumed to be representative of the intact species on the surface because it is cited as the specific molecule added to lubricant oil packages and are known to have a linear saturated hydrocarbon tail.[140,141] This was highest in normalized intensity in the diesel filter and is discussed later. One exception to the generic formula was the $C_8H_7SO_3^-$ (0,0002 ppm) ion, containing a short unsaturated chain (**Figure 2.1.1a**). This is proposed to be a fragment of the parent ion ($C_{18}H_{29}SO_3^-$). Common to the samples were calcium sulphate ions such as $CaSO_4H^-$ (**Supplementary table S2.1.1**), and likely correspond to sulfonates since calcium is the common counter ion used in their additive packages.[139] The presence of sulfonates in fuel-based deposits suggests residual lubricating oil is contaminating the fuel stream and is subsequently embedded in the deposit's matrix since the full parent ion was observed.

We observed several ions in all samples that corresponded to succinimide compounds with a short hydrocarbon chain from the succinimide functional group ($C_4H_2NO_2^-$ (- 0.7 ppm)).[87] Others include $C_5H_4NO_2^-$ (- 1 ppm) (**Figure 2.1.1b**) and they extended up to $C_{12}H_{16}NO_2^-$ (- 1.7 ppm) (**Supplementary table S2.1.1**). Succinimides have several possible origins, low mass species such as those identified here are used in lubricating oil formulations and the presence of lubricant-derived sulfonates points to this as a likely source. Inorganic salts,

present only in the diesel injector and filter deposit had various forms including sodium sulfate ($Na_3SO_4^+$, 1.3 ppm), sodium hydroxide ($Na_3(OH)_2^+$, 0.8 ppm) and sodium chloride ions ($Na_2Cl_3^-$, 1.1 ppm), these correlate to those previously identified in diesel deposits.[41] A likely origin of inorganic salt contamination is from water bottoms present in fuel storage tanks.[41,70] Negative ion data show dehydrogenated carbonaceous ions in all samples with the formula of C_n^-, such as C_8^- (1.5 ppm). These fragment ions are known to originate from highly conjugated dehydrogenated environments in SIMS analysis, such as from graphitic materials.[142]

Two molecular ions, $C_{16}H_{31}O_2^-$ and $C_{18}H_{35}O_2^-$, were assigned as C_{16} and C_{18} saturated linear carboxylic acids and were only present in the gasoline injector and diesel filter component deposit (**Figure 2.1.1**, **a** and **c**). These have been identified in diesel deposits previously but not in gasoline deposits and are cited as being used in corrosion inhibitor fuel additive packages.[137] We identified unsaturated $C_xH_yO^-$ ions and distinguished them from carboxylic acid fragments due to their different depth profiles, these are likely primary ion induced fragments of sulfonates (**Supplementary figure S2.1.2**). Finally, $C_xH_yO_z$ ions were present in both polarity spectra of the diesel filter deposit and originate from the blank filter material (**Supplementary table S2.1.1)**. This was confirmed after 3D OrbiSIMS analysis of the filter control sample (**Supplementary figure S2.1.3**).

2.2.3.2. Relative contributions of key molecular species

To compare relative contributions of key molecular species to the three component deposits, we display normalized 3D OrbiSIMS spectra of representative ions for succinimides, inorganic salts and sulfonates in **Figure 2.1.2**, including MS/MS analysis to support putative assignments.

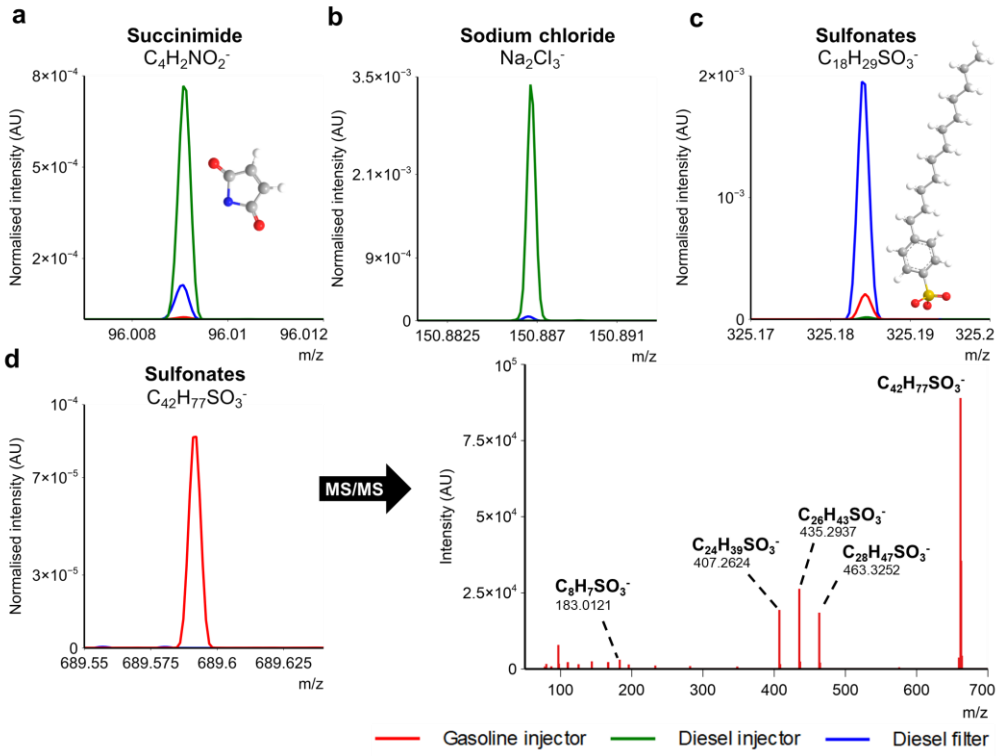


Figure 2.1.2. Normalized spectral comparison and MS/MS analysis of insoluble deposits. *Comparison of ion intensities for representative ions for* ***(a)*** *succinimides* ($C_4H_2NO_2^-$), ***(b)*** *sodium chloride* ($Na_2Cl_3^-$), ***(c)*** *parent sulfonate ion* ($C_{18}H_{29}SO_3^-$). ***(d)*** *Spectra of a higher mass sulfonate ion* ($C_{42}H_{77}SO_3^-$), *unique to the gasoline deposit, and its subsequent fragmentation pattern from a higher energy collisional dissociation MS/MS experiment.*

The succinimide ion ($C_4H_2NO_2^-$) is significant for the diesel injector and filter deposit but of low intensity for the gasoline deposit, so is likely a minor

contributor in this sample (**Figure 2.1.2a**). We evidence high levels of sodium chloride salt contamination in the diesel injector deposit, exemplified by $Na_2Cl_3^-$ (0.8 ppm), this is not evident in the gasoline deposit (**Figure 2.1.2b**). The sulfonate parent ion had highest intensity in the diesel filter and was lowest in the diesel injector deposit (**Figure 2.1.2c**). This shows the filter deposit has the highest levels of sulfonate contamination, whereas the diesel injector deposits chemistry is predominately salt based.

Sulfonates above the mass of the native compound added to lubricating oil packages ($C_{18}H_{29}SO_3^-$) were present in the gasoline deposit including $C_{42}H_{77}SO_3^-$ $[C_6H_4(SO_3)(C_{36}H_{73})]^-$, and $C_{74}H_{141}SO_3^-$ $[C_6H_4(SO_3)(C_{68}H_{137})]^-$ (**Supplementary table S2.1.1**). MS/MS analysis of $C_{42}H_{77}SO_3^-$ showed fragmentation corresponding to loss of the saturated alkyl chain to varying degrees (**Figure 2.1.2.d**). Despite the saturated parent molecule, fragmented ions all show one site of unsaturation on the alkyl bond adjacent to the benzyl group (**Supplementary table S2.1.2**) and are likely stable products in the SIMS fragmentation process, similar to the intense $C_8H_7SO_3^-$ ion (**Figure 2.1**). The presence of higher mass sulfonates suggests the deposited residue is undergoing transformation to form extended structures in the component deposit itself. Combination of the native sulfonate and linear fuel derived hydrocarbon chains e.g., octane, $C_{74}H_{141}SO_3^- = C_{18}H_{29}SO_3^- + (C_8H_{16})_7$ and $C_{42}H_{77}SO_3^- = C_{18}H_{29}SO_3^- + (C_8H_{16})_3$ explains the mass difference between both types of sulfonate ions. This likely proceeds through a free-radical mechanism,[143] and is promoted by the high temperatures of the combustion chamber, which only the gasoline injector component was exposed to. It is possible that these higher mass species

have a branched or linear hydrocarbon chain, but from MS/MS data we can only determine that the long chain is saturated aside from the bond connecting the benzyl group and hydrocarbon chain. These species were not observed in either diesel deposit since they were exposed to a lower temperature. This shows deposit composition is impacted by the addition of native chemical species and from reactivity of such species in the deposit itself.

2.2.3.3. Polycyclic aromatic hydrocarbons

The positive polarity spectrum for the gasoline deposit is shown in **Figure 2.1.3**, for the others samples they are shown in **Supplementary figure S2.1.4**. In all cases the spectra showed more complete fragments of carbonaceous structures than negative ion data, particularly for PAHs. Their presence in diesel and gasoline insoluble deposits has been previously inferred by researchers in this field,[58,59] but here were unequivocally assigned for the first time in insoluble deposits. PAHs, particularly those of high mass, are likely derived from the breakdown products of fuel constituents, the high temperatures and pressures experienced by the engine components facilitates this reactivity through aromatization.[144] Due to fuel recirculation it is likely that the filter may also be exposed to the products of this breakdown.

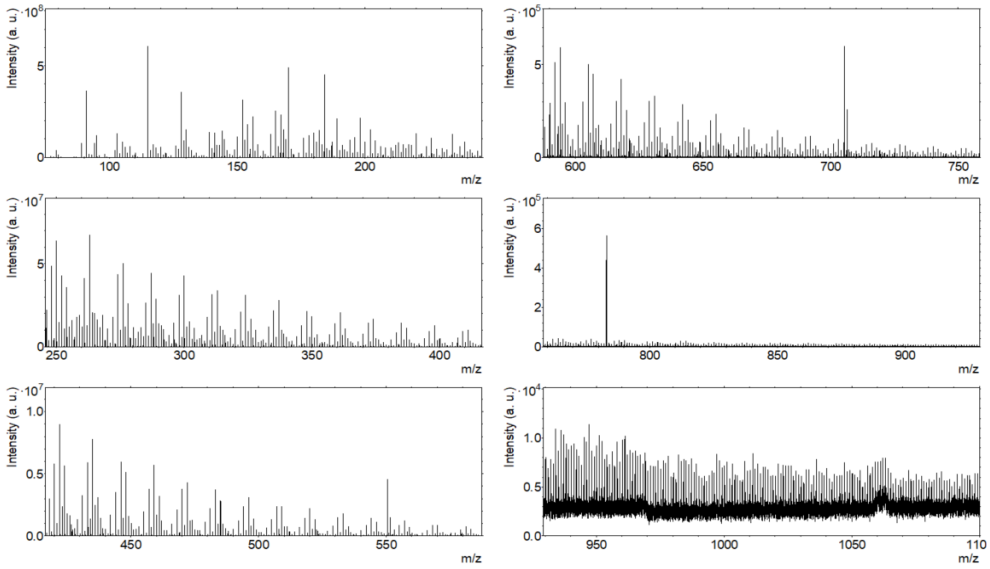


***Figure 2.1.3**. Positive polarity 3D OrbiSIMS spectra from the gasoline injector deposit over 6 mass ranges.*

Looking in more detail, we identified different maximum masses in the three engine component deposits: *m/z* 800 in the gasoline deposit, *m/z* 300 in the diesel injector deposit and *m/z* 550 in the diesel filter deposit (**Figure 2.1.4**). PAHs here exist as radical cations and correspond to known structures previously identified from environmental sources.[145] Coronene ($C_{24}H_{12}^{+}$, 1.0 ppm) was present on all three components but with low intensity on the diesel injector (**Figure 2.1.4a**). Hexabenzocoronene ($C_{42}H_{18}^{+}$, 1.6 ppm) was absent in the diesel injector, we observed a high intensity peak from the gasoline deposit for this ion (**Figure 2.1.4b**). High mass PAHs ($C_{66}H_{20}^{+}$, 0.2 ppm) (**Figure 2.1.4c**) were present only in the gasoline deposit and suggests that considerably larger aromatic structures are being formed in this deposit.

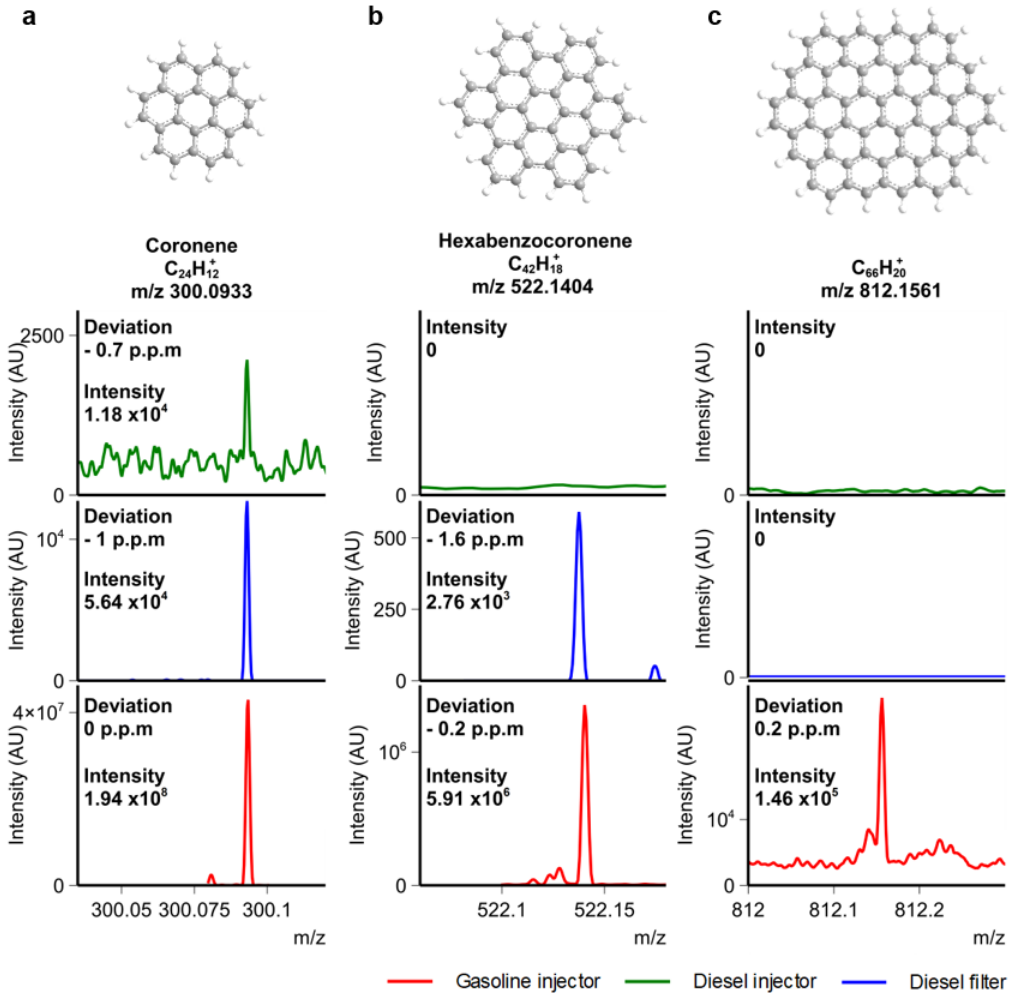


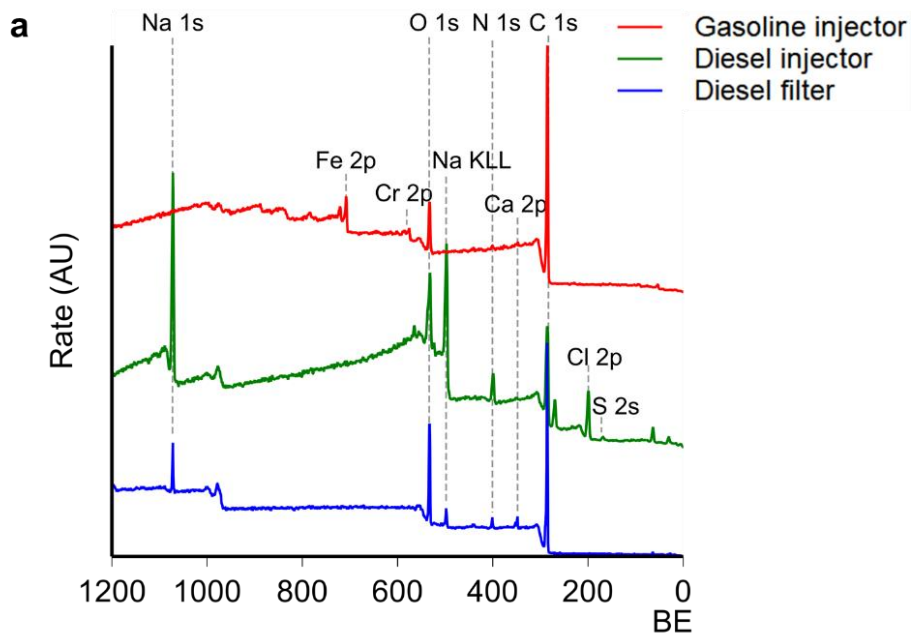
Figure 2.1.4. Molecular PAHs identified in the insoluble deposits. *3D structures for the three PAHs studied (above), and spectra of the PAH in each sample (below).* ***(a)*** *$C_{24}H_{12}^+$ (coronene, m/z 300.093, 1 ppm),* ***(b)*** *$C_{42}H_{18}^+$ (hexabenzocoronene, m/z 522.140, 1.6 ppm).* ***(c)*** *$C_{66}H_{20}^+$ (m/z 812.156, 0.2 ppm).*

This maximum mass ion is comparable to some of the largest PAHs detected in coal tar pitch by other high-resolution MS techniques,[146] and far larger than those inferred by time-of-flight SIMS in previous deposit analyses.[59] The difference between PAH maximum mass was attributed to the location of the component in the engine. The higher temperatures experienced by the gasoline injector component promotes extensive aromatization of fuel derived material

in the resultant deposit to these extended structures. PAH growth from fuel in high temperature environments has been previously postulated to occur,[86] but has not been evidenced to date. It is worth noting we performed three analytical repeats using different areas of each sample and observed the same differences between the samples (data not shown).

2.2.3.4. Quantified elemental surface analysis

SIMS analysis is not inherently quantitative because the different ionization and sputtering of different species is difficult to account for. Thus, we employed XPS to provide estimates of the elemental composition (%) of the three deposits (ca. 10 nm deep). We performed a sub-surface analysis on the gasoline and diesel injector deposits by first sputtering with an argon gas cluster ion beam to remove adventitious carbon and contaminants from the surface, this was not viable for the diesel filter deposit due to the porous nature of the fibrous material. Survey XPS spectra are presented in **Figure 2.1.5** alongside a table quantifying the elemental compositions. We calculated standard deviations using a Monte Carlo simulation and are displayed in (**Supplementary table S2.1.3**), in all cases the largest error was of the C 1s peak and in all cases was < 0.5 %.



Atomic concentration (at. %)						
Peak	Gasoline injector	Std. dev.	Diesel injector	Std. dev.	Diesel filter	Std. dev.
C	85.5	0.5	51.8	0.5	81.5	0.4
O	8.3	0.2	16.2	0.4	13.5	0.2
N	1.2	0.4	8.5	0.4	2.1	0.3
Na	-	-	16.4	0.2	1.5	0.1
Cl	-	-	6.5	0.1	-	-
S	-	-	0.5	0.1	-	-
Ca	0.3	0.1	0.1	0.3	1	0.1
Si	-	-	-	-	0.4	0.2
Fe	3.1	0.2	-	-	-	-
Cr	1.6	0.2	-	-	-	-

Figure 2.1.5. Elemental surface analysis of deposits via XPS after argon gas cluster ion beam cleaning. (***a)*** *Overlaid spectra of the samples.* ***(b)*** *Quantification of the composition of each deposit with errors presented as standard deviation (std. dev.). BE, binding energy.*

The gasoline injector and diesel filter deposit have a significantly higher carbon concentration than the diesel injector deposit, both diesel deposits had high levels of sodium, oxygen, and nitrogen. Salt deposition was highest in the diesel injector deposit, with a sodium concentration of 16.4 % (**Figure 2.1.5**). The

concentration of chlorine in this sample (6.5 %) suggests that approximately 40 % of the inorganic salt present is sodium chloride. Evidently other counter ions are present in this sample and the diesel filter deposit, which correlates with the higher amounts of oxygen and nitrogen. We identified other ions from the SIMS data for both diesel deposits including sulfates, hydroxides, carbonates ($Na_3CO_3^+$), nitrites ($Na(NO_2)_2^-$) and cyanates ($Na_3(CNO)_2^+$) (**Supplementary table S2.1.1**). Sodium cyanate was only present in the diesel injector and had a relatively high normalized intensity, its 1:1 nitrogen-oxygen ratio partly explains the similar offset of these elements between the gasoline and diesel injector deposits elemental composition (**Figure 2.1.5b**). Sulfate salts are attributed as the origin of sulfur in the diesel injector deposit, which correlates with the high sodium levels. It is unlikely to originate from sulfonates due to its low relative intensity for this sample in the 3D OrbiSIMS spectra (**Figure 2.1.2**). The lack of sulfur in the other samples suggests sulfonates exist below the detection limits of XPS analysis, despite their prevalence in the 3D OrbiSIMS spectra. Calcium has several possible sources as it is used as the cation in various detergent additives and can be present in high quantities in lubricating oil formulations.[147] The high amounts in the diesel filter correlates with the normalized 3D OrbiSIMS spectra (**Figure 2.1.2**), suggesting it was exposed to the highest levels of lubricant oil. Silicon was present in the diesel filter and was attributed to silicone surface contamination. Finally, the gasoline deposit showed low concentrations of iron and chromium. This likely relates to areas of exposed clean metal substrate scanned during analysis, topography of the sample is shown in **Figure 2.1.1a**. A list of XPS peaks is in **Supplementary table S2.1.3**.

2.2.3.5. Combined 3D OrbiSIMS depth profiling & chemical imaging

Positive and negative 3D OrbiSIMS data acquired from a combined chemical imaging and depth profiling experiment on the gasoline and diesel injector deposits are detailed in **Figures 2.1.6** and **2.1.7** respectively. We display data for key molecular species including sulfonates ($C_8H_7SO_3^-$), PAHs (coronene, $C_{24}H_{12}^+$), succinimides ($C_4H_2NO_2^-$), a carbonaceous ion (C_8^-) and sodium chloride ($Na_2Cl_3^-$).

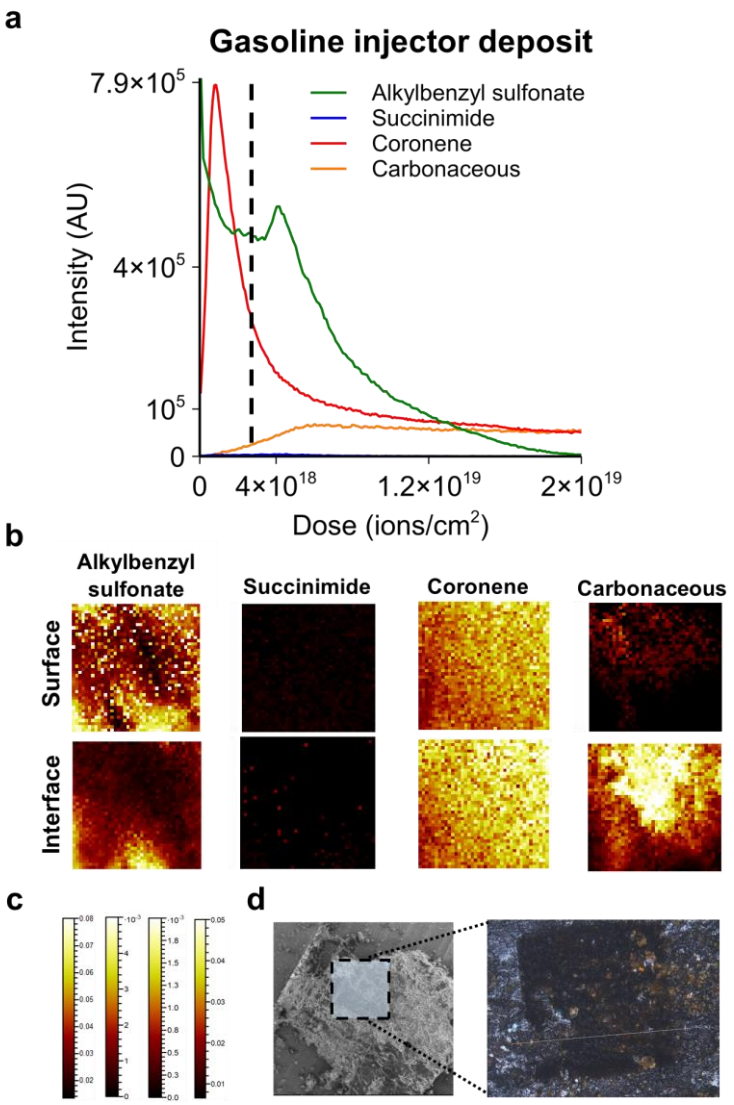


Figure 2.1.6. Combined OrbiSIMS Ar_{3000}^+ depth profiling and chemical imaging of a gasoline fuel injector deposit. ***(a)*** *Depth profiles of key diagnostic ions.* ***(b)*** *Chemical images of these ions, taken at the surface and a lower depth (interface)*

which was reached after observing an increase in the intensity of carbonaceous ions in the deposit. ***c)*** *Scale bars for chemical images for alkylbenzyl sulfonates, succinimide, coronene and a carbonaceous ion (left to right).* ***(d)*** *Optical profilometry image of the resultant crater after sputtering. Chemical images were normalized to the total ion image and cropped to a 200 x 200 μm area.*

The gasoline deposit depth profile shows sulfonates were prevalent at multiple depths but were most intense at the outer surface (**Figure 2.1.6a**). The surface localization of these species suggests a low thermal stability, prompting breakdown shortly after deposition on the engine component. During profiling, the gas cluster ion source could not sputter through the interface exposed after 10^4 s, which correlates with the profile of carbonaceous ions such as C_8^-. This interface is shown from optical profilometry imaging in **Figure 2.1.6d**. The plateauing depth profile of this ion in the gasoline deposit compared with the highest mass PAH identified, $C_{66}H_{20}^+$ (**Supplementary figure S2.1.5**), shows the C_n^- ions originate from a layer lower than these high mass PAHs. We employed chemical imaging to study the lateral distribution of ions at the surface and at a lower deposit depth after argon gas cluster ion beam profiling (**Figure 2.1.6b**). Sulfonates had high intensity at both deposit depths in the gasoline injector deposit and are distributed non-uniformly, this correlates with lubricant-derived sulfonates being a localised trace contaminant, so are not part of the carbonaceous matrix. Conversely, coronene was uniformly distributed at both depths and illustrates its contribution to the organic matrix and correlates with their suggested origin of fuel derived material in the gasoline deposit.

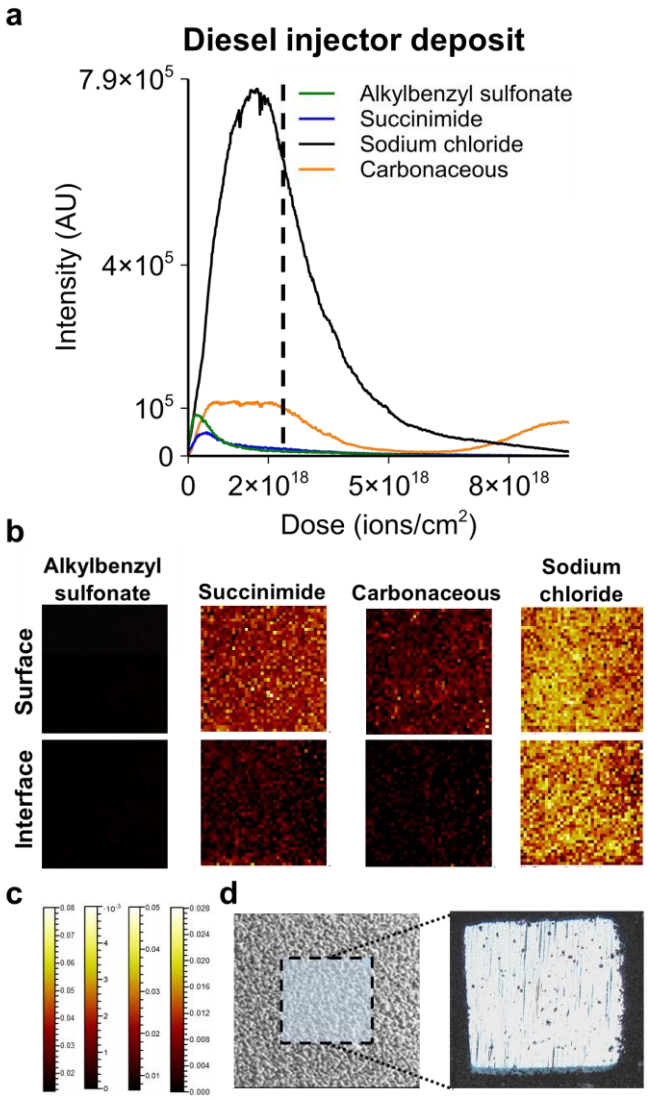


Figure 2.1.7. Combined OrbiSIMS Ar_{3000}^+ depth profiling and chemical imaging of a diesel injector deposit. ***(a)*** *Depth profiles of key diagnostic ions.* ***(b)*** *Chemical images of these ions, taken at the surface and a lower depth (interface).* ***(c)*** *Scale bars for chemical images for alkylbenzyl sulfonates, succinimide, a carbonaceous ion and sodium chloride (left to right).* ***(d)*** *Optical profilometry image of the resultant crater after sputtering. Chemical images were normalized to the total ion image and cropped to a 200 x 200 μm area.*

The offset between sulfonates and succinimide ion intensity is far less in the diesel injector deposit than the gasoline deposit (**Figure 2.1.6a** and **2.1.7a**),

evidencing an increased contribution from sulfonates over the entire deposit depth. The sodium chloride salt ion dominated the chemistry of the diesel injector deposit with a high intensity throughout and suggests sodium salt contamination over multiple fueling cycles (**Figure 2.1.7a**). An important distinction between the samples is the intensity of coronene, with an increasing intensity throughout the gasoline deposit depth and an insignificant intensity in the diesel injector deposit. This correlates with the data presented in **Figure 2.1.4** that shows a lower PAH contribution to the diesel injector. The diesel injector deposit also exhibited a shiny surface after sputtering, marking the substrate (**Figure 2.1.7d**). This layer also correlates with the profile C_8^- in this sample (**Figure 2.1.7a**) and here is thought to originate from a diamond like coating placed above the diesel injector substrate during manufacturing. These are used to try and prevent deposit formation on the substrate.[59,148]

Chemical imaging of the diesel deposit showed delocalized distributions of all targeted ions (**Figure 2.1.7b**). The fact that sodium chloride salt illustrated a homogenous lateral distribution at both deposit depths suggests that this deposit experienced a high contribution from inorganic salts, agreeing with XPS data (**Figure 2.1.5**). Comparison of samples shows different distributions of carbonaceous ions, the gasoline deposit illustrated a localized distribution of carbonaceous material at the lowest deposit depth (**Figure 2.1.6b**), unlike the diesel injector deposit (**Figure 2.1.7b**). In the first case, this layer is indicative of dehydrogenated carbonaceous material and suggests the gasoline deposit is built up from an initial deposition of fuel followed by reactivity to form PAHs of varying mass, then undergoing further condensation to form a

dehydrogenated graphitic like material in the deepest layers. This has been previously postulated in this field,[60,86] but is evidenced here from the insights afforded by diagnostic 3D OrbiSIMS data.

2.2.4. Part one conclusions

In this work we demonstrated the capabilities of 3D OrbiSIMS with its high mass resolving power and MS/MS capabilities to unambiguously uncover the identity and 3D spatial distribution of key molecular components in insoluble deposits formed in internal combustion engine components. Molecular speciation informed us of specific origins of deposit components including lubricant oil residues, combustion products and sodium salts. We evidenced reactions between fuel and specific lubricating oil constituents in the gasoline deposits surface, which highlights the important influence of temperature on overall deposit composition. Depth profiling and chemical imaging gave new evidence into the chemical transformations that contribute to deposit formation such as aromatization to form PAHs and carbonaceous clusters in the lowest depths of the gasoline deposit - previously only speculated to occur in these systems. Quantitative elemental analysis proved valuable to show the prevalence of constituents, such as high levels of sodium salts in the diesel injector deposit. Evidence of a diamond like coating on this component suggests that it does not adequately protect against these salt-type deposits and highlights the importance of a using a fuel stream free of these contaminants.

2.3. Part two

The Effect of Temperature on the Molecular Compositions of External and Internal Gasoline Direct Injection Deposits

*Max K. Edney[1], Emily F. Smith[2], Edward Wilmot[4], Jacqueline Reid[4], Jim Barker[4], Morgan R. Alexander[3], Colin E. Snape[1] & David J. Scurr[3]**

Published in *SAE Journal of Fuels and Lubricants* (DOI: 0.4271/2021-01-1188)

Author contributions

3D OrbiSIMS, optical profilometry and SEM data was collected by M.K.E. E.F.S collected XPS data. All authors aided in interpreting the analytical data. M.K.E wrote the manuscript and all authors aided in its edits and revisions.

2.3.1. Abstract

The increased severity and prevalence of insoluble deposits formed on fuel injectors in gasoline direct injection (GDI) engines precipitates negative environmental, economic and healthcare impacts. A necessary step in mitigating deposits is to unravel the molecular compositions of these complex layered materials. Here, we apply the high mass-resolving power and *in-situ* analysis capabilities of 3D OrbiSIMS to characterize deposits formed on the external tip and internal needle from a GDI injector. This is the first application of the

technique to study internal GDI deposits. PAHs are present up to higher maximum masses in the external deposit. Lubricating oil derived sulfonates are more intense in the internal deposit, however higher mass sulfonates are only present in the external deposit. None of these molecular species have been identified in internal GDI deposits before. 3D OrbiSIMS depth profiles show that the needle deposit has a uniform deposit layer whereas the injector tip has a more complex layered structure. Comparison of 3D OrbiSIMS data suggests that the higher temperature experienced by the external injector tip explains key compositional differences and leads to growth of a thicker, more complex, layered deposit structure.

2.3.2. Introduction

The drive for reduced emissions and more efficient vehicle operation can be partially met by clean-operating GDI based engines which are shown to give higher power output and fuel economy and reduced emissions compared to older gasoline injection strategies.[6] As such, there will be a significant number of GDI based vehicles on the road in developed nations and in developing nations where electric and hybrid vehicle technology will be slower to implement. It is predicted that in 2050, 80 % of global passenger vehicles on the road will use internal combustion engines,[125] highlighting the importance of ensuring clean operation of such engines. Approaches to reduce GDI vehicle emissions are being investigated in the industry, such as the development of gasoline particulate filters,[149] adopting multiple injection strategies per cycle.[150] Or modifying fuel mixtures to improve burn characteristics and reduce emissions, especially of particulates.[151] But the formation of insoluble deposits in both external and internal GDI components threatens to counteract these strategies.

Emissions of particulates are shown to be significantly affected when deposits form,[22,29,152,153] thereby causing negative impacts on the environment and global human health.

A large area of research in the field is in the development of fuel additives to ensure high efficiency and low emissions of vehicles over its lifetime. Recent work represented a paradigm-shift in the use of solubilizing additives to mitigate GDI deposits and reduce emissions, even in vehicles where deposits had previously formed.[22] However, more compositional data on GDI deposits is needed to fully understand their origin and formation mechanisms and will be vital to inform further development of fuel additives to mitigate them. This will become more important as fuel mixtures are changed in the future, such as the increased inclusion of bio-ethanol. However, deposits are complex analytes, and their overall composition comprises several sources including but not limited to 'hydrocarbon' (fuel) material, and other species such as lubricating oil constituents, inorganic salts and impurities from various sources.[152] Various analysis techniques have been applied to study GDI deposits but only revealed limited information on their composition. Dearn *et al.* and Barker *et al.* used elemental analysis to discern the origin of certain species such as from lubricating oil and uncovered trends in the elemental distribution across the injector surface.[22,66] But no molecular information on deposits was gained. The complexity, layered structure and insolubility of these deposits poses a unique analytical challenge. A recent review points out this gap in the realm of analytical instrumentation,[152] and recommends that mass spectrometry techniques are best placed to give a comprehensive molecular characterization.

But that an ideal technique would be able to probe sample provenance *in-situ* without the use of solvents which rules out many mass spectrometry techniques currently.[152]

A recent development in the surface analysis field was the use of the 3D OrbiSIMS technique, which combines a ToF-SIMS instrument with an Orbitrap™ mass analyser (mass resolving power > 240, 000) and a low energy argon gas cluster ion beam (GCIB) which is capable of accurately elucidating larger molecular species from the sample compared to the Bi_3^+ source used in previous ToF-SIMS analysis.[121] The instrument can also perform MS/MS of identified species to confirm assignments and brings this technique in-line with other high-resolution mass spectrometry techniques.[22] A diagram of the technique is shown in **Figure 2.2.1** showing its key features and modes of analysis. We also note the ability of the instrument to accommodate a variety of sample types and sizes, meaning it will be useful for analyzing new fuel injector components which are in continuous development.[154]

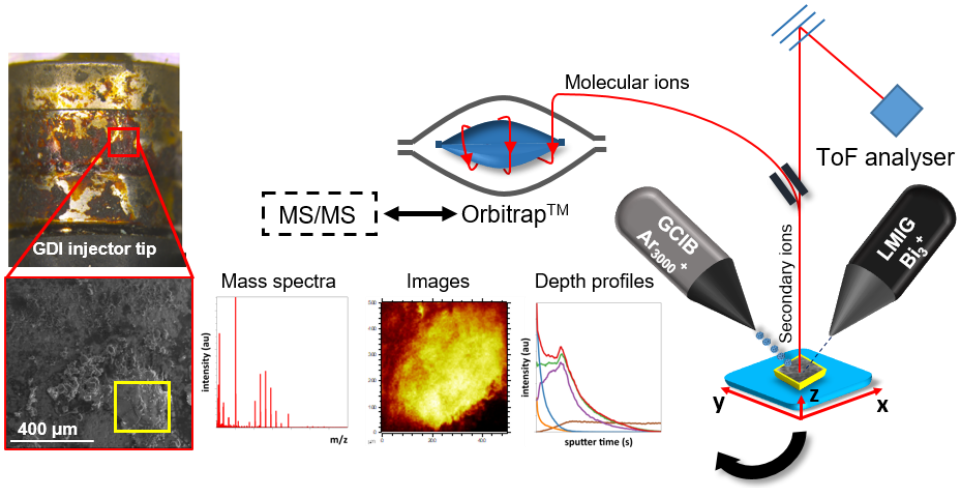


***Figure 2.2.1**. Schematic showing the operation modes, workflow and outputs of 3D OrbiSIMS for in-situ analysis of a gasoline direct injection (GDI) tip.*[155]

In **Section 2.2** we demonstrated this technique for deposit analysis,[155] by performing depth profiles and chemical images with confirmation of assignments using MS/MS for the first time in this field and identified species up to much higher masses than in previous attempts using ToF-SIMS. This allowed us to assign their origin more confidently. While it gave only elemental analysis, XPS provided complementary quantified analysis of samples and showed them to be mainly carbonaceous, highlighting the importance of a mass spectrometry approach. But this work did not focus on samples from internal GDI components and did not compare data from the same fuel stream, which may reveal other reasons behind compositional differences aside from fuel composition.

Here, we analyze and compare datasets from an external and internal GDI injector deposit for the first time using XPS and 3D OrbiSIMS. The injector tip experiences higher temperatures than the injector needle as it is exposed to the combustion flame. We uncover key differences between deposit compositions such as the maximum size of PAH observed, the presence of inorganic salts and intensity of lubricating oil species and partly attribute compositional differences to the effect of temperature. 3D OrbiSIMS revealed species never seen before in internal GDI deposits. Depth profiling and chemical imaging of the external deposit showed similar composition to a sample analyzed by the same method in previous work,[155] despite different sample provenance. While depth profiles of the internal needle deposit exhibited a uniform deposit layer above the substrate.

2.3.3. Results and Discussion

2.3.3.1. Visual and elemental analysis of deposits

To obtain a visual understanding of the injector deposits we performed optical microscopy on the external injector tip and internal needle and performed scanning electron microscopy (SEM) on the injector tip (including the nozzle and the side wall of the tip), data is displayed in **Figure 2.2.2**.

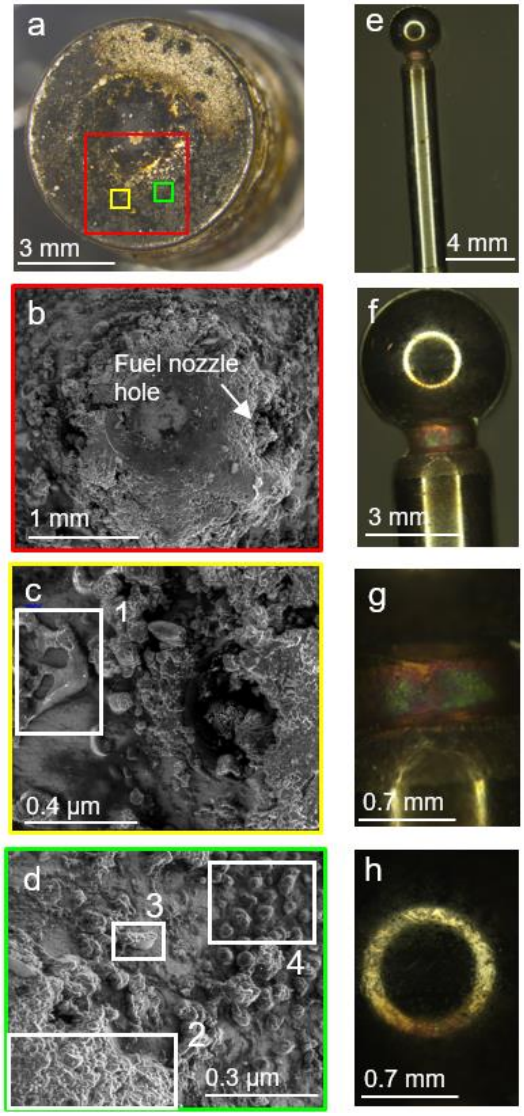


Figure 2.2.2. (a) *Optical micrographs of a GDI external tip deposit.* ***(b-d)*** *scanning electron micrographs (secondary electron mode) of injector deposits on the tip nozzle showing different morphologies highlighted by the numbered white boxes.* ***(e-h)*** *Optical micrographs of an internal injector needle.*

There is clearly a significant build-up of deposit on the external part of the injector including the injector sidewall (**Figure 2.2.1**), including the injector nozzle (**Figure 2.2.2a**), and the fuel nozzle hole itself (**Figure 2.2.2b**), it is apparent that this blockage will severely impact fuel spray and thus emissions. Significant blockage can also lead to injector failure as well. Of note is the range of deposit morphologies present on the injector tip, highlighted by the numbered white boxes in **Figure 2.2.2c-d**. Namely a visibly thin film of deposit (1 in **Figure 2.2.2c**), likely originating from residual droplets of fuel which have leaked from the injector nozzle. Next, small spherical particles of deposits which have been observed by other works using this technique on GDI deposits (4 in **Figure 2.2.2d**).[22] Finally, a visibly thicker deposit type which has been observed before and is attributed to a predominately carbonaceous morphology (2 and 3 in **Figure 2.2.2d**). There was less variation in deposit morphology on the side-wall deposit of the tip, which exhibited a thick carbonaceous deposit structure (**Figure 2.2.1**). It is likely that the absence of fuel droplets on this part of the component results in a more homogenous deposit morphology. Owing to the increased size of these deposits this will be targeted by 3D OrbiSIMS in this work. By contrast, the injector needle showed a marked different morphology, illustrating a thin film structure with more discoloration closer to the injector ball (**Figure 2.2.2e-h**). Interrogation of different areas shows a similar 'deposit film' morphology. There are signs of small 'scratches' on the injector ball (**Figure 2.2.2h**) which may act as nucleation points for carbonaceous deposit formation. Abdallah *et al.* demonstrated that a visibly thin film deposit of this type can still contain a significant level of deposition, however.[156]

Quantified elemental information on the deposits were then obtained using X-ray photoelectron spectroscopy, we analyzed the injector tip deposit after etching for 120 s to remove surface contamination. Only the very top surface of the injector needle was analyzed (0 s etch time) to avoid inclusion of the metal substrate peaks on this thin film deposit, XPS spectra is shown in **Figure 2.2.3** and data is tabulated in **Table 2.2.1**.

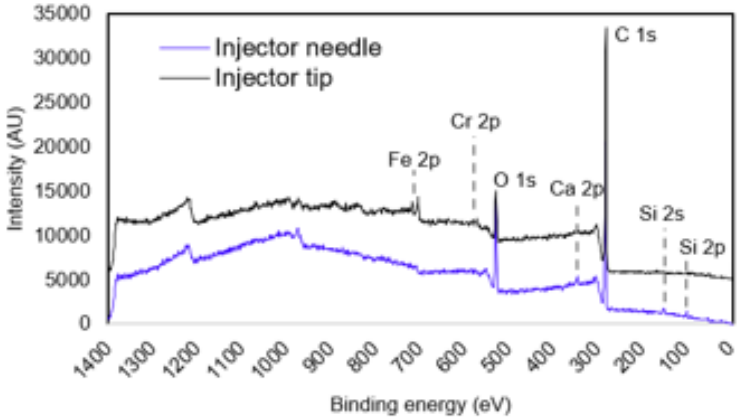


***Figure 2.2.3**. X-ray photoelectron spectroscopy analysis of injector tip and needle deposits. Spectra of both samples with key assignments displayed. Data from the injector tip deposit was taken after cleaning with the Ar_{500}^{+} beam, data from the injector needle is taken from the top surface of the deposit.*

***Table 2.2.1**. Summarized elemental compositions calculated from peak area of XPS analysis shown in **Figure 2.2.3**.*

Atomic concentration (at. %)		
Peak	**External tip deposit**	**Internal needle deposit**
C 1s	87.2	79.1
O 1s	8	17.3
Fe 2p	2.1	0
Cr 2p	1.3	0
Ca 2p	0.6	0.92
S 2s	0.4	-
Si 2p	0.5	2.7

XPS spectra of both samples appeared similar aside from the lack of an intense signal from the substrate (Fe 2p and Cr 2p) in the needle sample (**Figure 2.2.3**). We note a very minor signal for Fe on the blue spectra for the internal needle deposit despite taking this data after etching for 0 s, suggesting a very thin layer of deposit has formed on this component. Interrogation of the wide-scan XPS data highlights that both deposits are predominately carbonaceous (up to 87 % C in the injector tip) with differences being explained by minor contributors (**Table 2.2.1**). There is a slightly increased contribution of Ca in the injector needle which may suggest higher levels of lubricating oil contamination in this component. Si was ubiquitous and is attributed to silicone contamination of the samples. S was only found in the injector tip, but its low contribution (0.4 %) means that it may be present in the needle but below the minimum sensitivity of the instrument and care should be taken reading its exact value. Oxygen was higher in the needle and has several possible origins such as fuel derived species (alcohols or ethers) or from the injector substrate (metal oxides). Fe and Cr were only in the injector tip (up to 2 %) and is attributed to areas of exposed clean metal substrate which were analyzed, the rough 'patchy' topography of the deposit is shown in the micrograph in **Figure 2.2.1**. These peaks were not present in the injector needle deposit as we did not etch this sample, suggesting the needle deposit has smoother topography and a thinner layer than the tip deposit. This will likely affect comparison between other elements, such as oxygen, which is a limitation to comparing XPS data from rough materials with different thicknesses. Overall, both deposits are carbonaceous despite their differing morphology, with trace contributions of lubricating oil constituents.

Other elements such as N have been detected in GDI deposits using XPS, in this work we also found Fe and Cr substrate originating from substrate despite not performing sample etching,[155] and results should be considered as a collective across different works. While elemental analysis is useful as to initially probe deposit chemistry, it is limited in its ability for a comprehensive chemical characterization.

2.3.3.2. Identifying molecular species

Negative ion 3D OrbiSIMS depth profile accumulation spectra for the external injector tip and internal injector needle deposit are displayed in **Figure 2.2.4** in the mass range of *m/z* 75 - 330 with key assignments labelled.

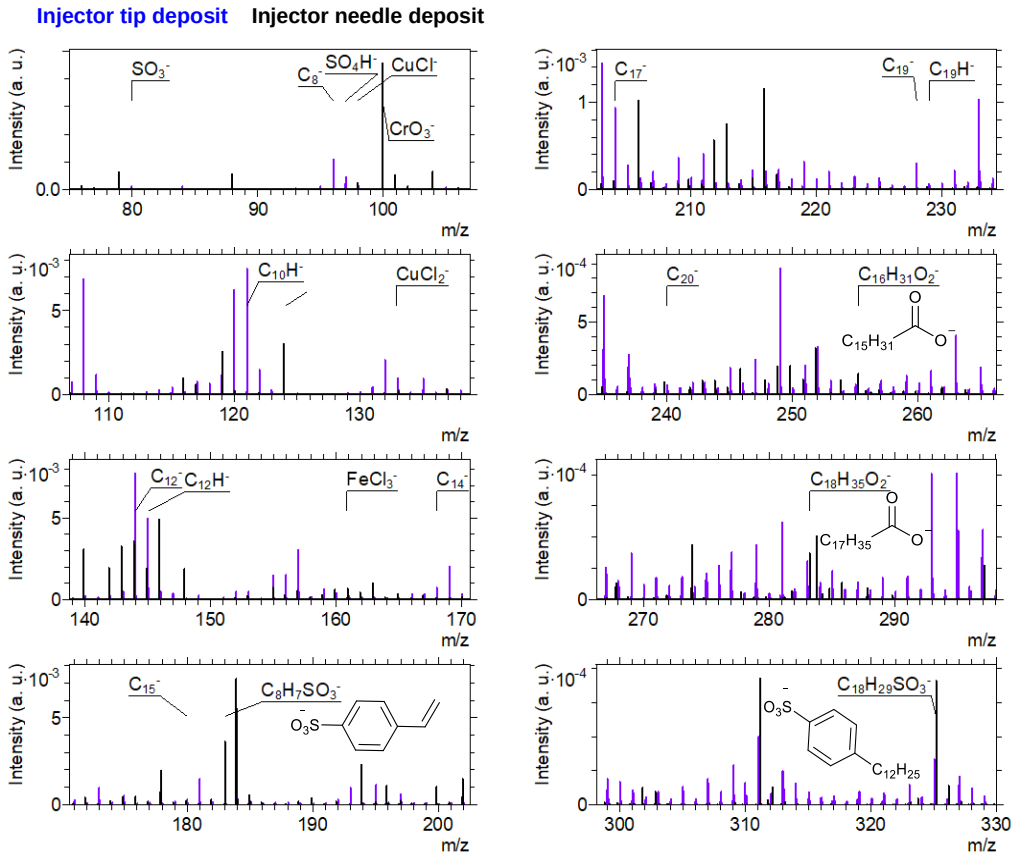


Figure 2.2.4*. Negative ion 3D OrbiSIMS depth profile accumulation spectra, normalized to the total ion count, in the range of m/z 75 – 360. Spectra from the two samples are overlaid, blue = injector tip deposit and black = injector needle deposit.*

Putative chemical structures of some species are displayed. We assign key species on the spectra with < 2 ppm mass deviation. Ion data can be found in the supporting information.

By overlaying normalized ion spectra and comparing intensities of common species (highlighted by the color of each peak in **Figure 2.2.4** showing which component had the highest intensity of each ion), we identified key differences between injector tip and needle deposit chemistries for the first time (ion data for can be found in **Table S2.2.1**). Alkyl benzyl sulfonate ions ($[C_6H_4SO_3(C_nH_{(2n+1)})]^-$, termed sulfonates from here on) were accurately identified in both deposits, including the cited molecule added to additive packages, $C_{18}H_{29}SO_3^-$.[140,141] Sulfonates were more intense in the injector needle, shown by the prominence of the black spectral lines in **Figure 2.2.4** ($C_8H_7SO_3^-$ and $C_{18}H_{29}SO_3^-$). What is of note is that sulfonate ions of higher masses (such as $C_{30}H_{53}SO_3^-$) were present in the injector tip and not in the injector needle. We calculated the mass difference of different sulfonate fragments and propose the high mass species arise from alkyl extension reactions of the deposited sulfonate residue with fuel derived species. For example, $C_{26}H_{45}SO_3^-$ can be explained by addition between sulfonate and different numbers of an octane molecule ($C_{26}H_{45}SO_3^- = C_{18}H_{29}SO_3^- + C_8H_{16}$), once the negative charge and proton abstraction has been accounted for. In our previous work we also found these high mass ions such as $C_{42}H_{77}SO_3^-$ in GDI tip deposits and confirmed their assignment with MS/MS.[155] The fact that these ions are not present in the needle deposit suggests this reactivity does not occur in this component and we attribute this to the reduced temperature this component experiences compared to the external injector tip deposit.

Carboxylic acids such as stearic and palmitic acid were identified in both components and were most intense in the needle deposit (**Figure 2.2.4**). These likely derive from the lubricating oil since the base oils can contain C_8-C_{22} linear monocarboxylic acids,[157] however, they have also been ascribed as being derived from corrosion inhibitor additive packages in the past.[137] The lack of Na in the deposit shown by XPS suggests these are not derived from sodium carboxylate salts. XPS also shows that S was present in very low concentrations (**Figure 2.2.3**), suggesting a trace amount of lubricating oil constituents (sulfonates) despite their high intensity in the 3D OrbiSIMS spectra. This highlights the need for complementary analysis techniques such as XPS to overcome preferential ionization of species in SIMS analysis and to aid in assigning the origin of species.

The injector needle also contained ions corresponding to the metal substrate such as CrO_3^-, this ion was far less intense in the injector tip (**Table S2.2.1**), we propose the rough 'patchy' topography of the injector tip deposit means that some exposed areas of metal were analyzed in this sample, correlating with XPS (**Table 2.2.1**). Inorganic salts such as sodium chloride ($NaCl^-$), copper chloride ($CuCl^-$) and iron chloride ($FeCl_3^-$) were identified and were most intense in the injector needle (**Figure 2.2.4**).

Overall, the negatively ionizing species were mostly common to both sample types, the injector needle appears to have a higher contribution from lubricating oil species and inorganic salts. It is likely that the combustion flame, which only

the injector tip was exposed to, promotes further degradation of lubricating oil species.

2.3.3.4. Carbonaceous species

Unsaturated carbonaceous negative ions (C_n^- and C_nH^-) were identified in both samples and were more intense in the injector tip deposit and present up to higher maximum masses compared with the injector needle sample (**Figure 2.2.4** and **Table S2.2.1**). Their origin is most likely residual fuel, but from spectral analysis alone it is difficult to confirm. SIMS analysis has shown these to be sourced from graphitic like materials,[142] suggesting it marks ordered carbonaceous material in the deposit. Conversely, positive ion data showed intact molecules (positive radicals) corresponding to PAHs in both samples, work has yet to show PAHs in GDI needle deposits. PAHs are noted as being particularly difficult to identify by *in-situ* analysis which showcases the strength of 3D OrbiSIMS for detecting large intact species. Ion data for three example PAHs from both samples, including an analytical repeat dataset from a different area on the injector tip deposit are displayed in **Figure 2.2.5**.

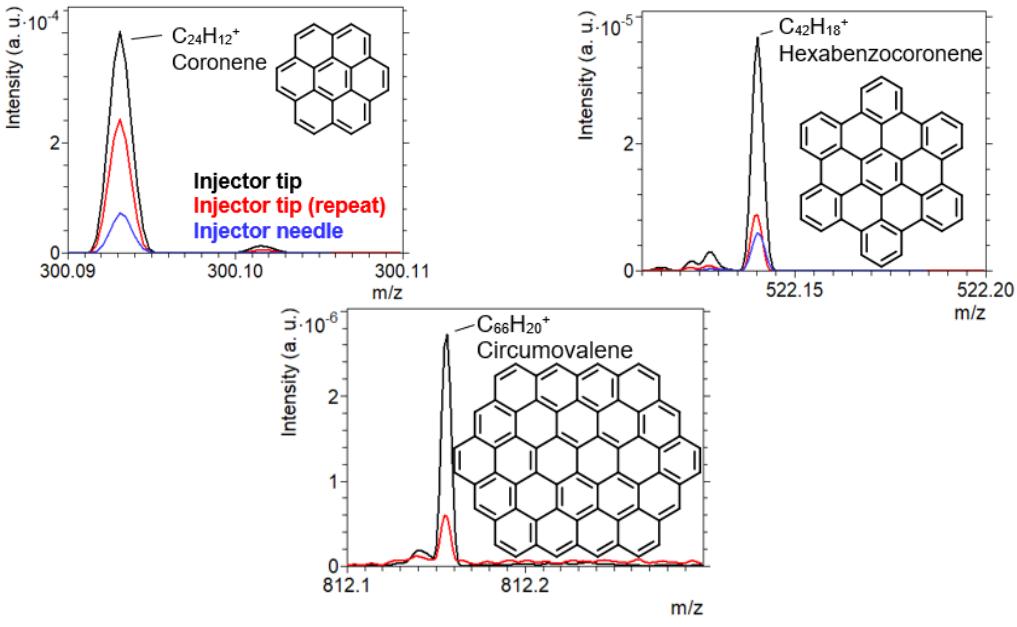


***Figure 2.2.5**. 3D OrbiSIMS positive ion spectra in selected mass regions showing speciation of high mass aromatics for the injector tip deposit (black), a repeat of this sample in a separate area (red) and the injector needle (blue). Putative chemical structures are also displayed, other isomeric structures are possible from the assigned formula.*

PAH intensity and speciation showed insightful differences between sample compositions on both component deposits. Coronene (above), hexabenzocoronene (middle) and circumovalene (below) were accurately assigned with a mass error < 2 ppm in all samples and repeat areas (**Figure 2.2.5**). It should be noted that isomeric structures are possible, for example, with structures containing 5-membered rings and it is unfeasible to distinguish the specific structure from accurate mass alone. We identified PAHs in the needle deposit up to *m/z* 522 (hexabenzocoronene), which was a lower maximum mass compared to the injector tip deposit, shown in the absence of a signal in blue for circumovalene (**Figure 2.2.5**). However, it is still notable that large PAHs were present in an internal GDI deposit, despite its lack of carbonaceous morphologies compared to the injector tip (**Figure 2.2.2**), particularly since the high pressure the needle experiences is expected to suppress carbonaceous deposit formation. We attribute the difference in maximum mass of PAH between components to the lower temperature that the injector needle experiences. The temperature effect also explains the speciation of higher maximum mass negative carbonaceous ions in the injector tip (C_{20}^-) compared with the injector needle (C_{12}^-) (**Table S2.2.1**). It has been hypothesized that PAHs originate from temperature induced aromatization of gasoline in the engine.[155] Evidently the extent of carbonaceous deposit formation and

comparisons between component deposit type can be partially explained by the effect of temperature and highlights how deposit composition is explained by both the deposition of species and their subsequent reactivity.

2.3.3.5. Combined 3D OrbiSIMS depth profiling and chemical imaging on internal deposits

We next performed depth profiles on both the injector needle and tip deposit to understand differences in their layered structure, we also performed chemical imaging of the external injector tip deposit at both the surface and a lower depth after reaching an interface of the deposit. Data from both samples are displayed in **Figure 2.2.6**.

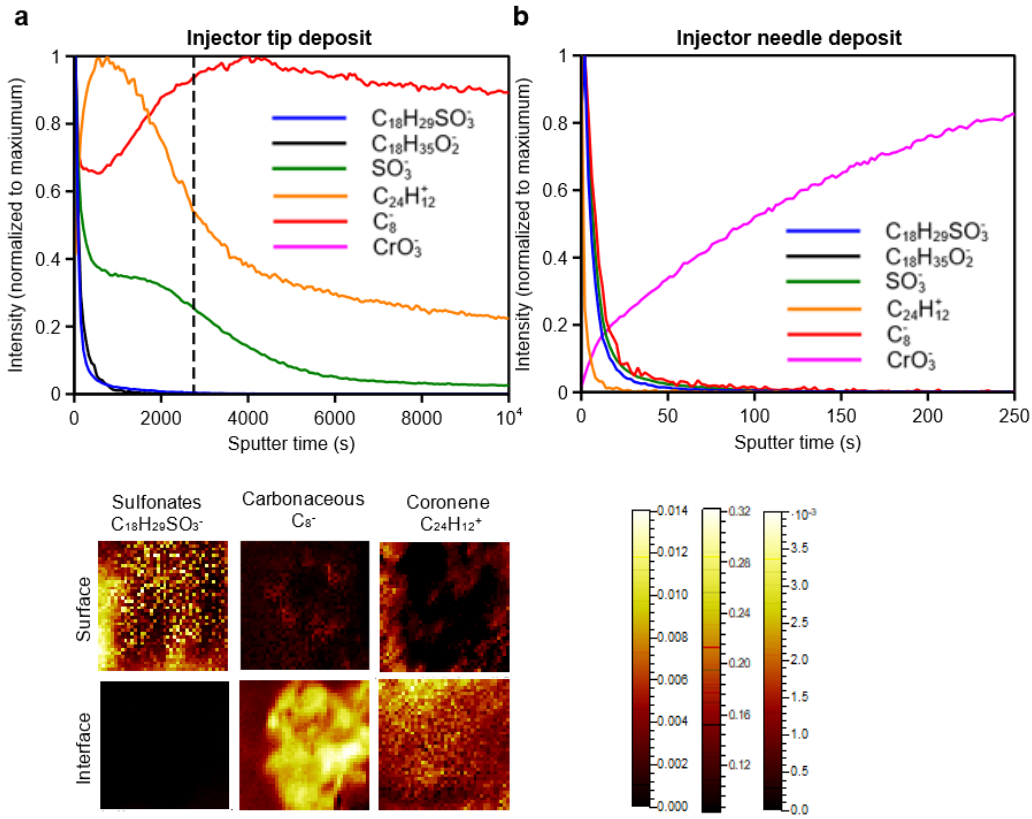


Figure 2.2.6*. Combining 3D OrbiSIMS Ar_{3000}^+ depth profiling and chemical imaging on a GDI tip deposit.* ***(a)*** *left, depth profiles of the injector tip deposit with the lower imaging position marked by the line on the profile. Right, chemical images (200 x 200*

μm) of selected ions at the surface and interface of the injector tip deposit. Image scale bars are shown for each ion and were the same intensity for the surface and interface. ***(b)*** *Depth profiles of the injector needle deposit.*

Evidently the injector tip and needle deposit have a marked different layering structure, in this case the tip deposit (**Figure 2.2.6a**) showed distinct layers, whereas the organic layer of the injector needle deposit (above the CrO_3^- substrate) exhibited a uniform distribution of species above the substrate (**Figure 2.2.6b**). It is likely that the lack of high mass PAHs limits its growth into a layered deposit structure, suggesting they are key constituents of the carbonaceous matrix. The injector tip depth profile shows that the upper layer consists of sulfonates ($C_{18}H_{29}SO_3^-$) and carboxylic acids ($C_{18}H_{35}O_2^-$), (**Figure 2.2.6a**). It is likely that the sulfonates and carboxylic acids break down readily once deposited, partially *via* loss of alkyl chain and so are not embedded in lower deposit layers. Therefore, only smaller organic fragments exist in lower depths for species which are trace contaminants. The profile of the sulfonate head group, SO_3^-, exemplifies this point since it is present not just at the surface. Coronene was present at most layers of the injector tip deposit but was most prevalent in the middle portion (**Figure 2.2.6a**) and the lowest deposit layer of this sample was marked with the carbonaceous ions (C_8^-), which corroborates with data from previous work on another GDI injector tip deposit.[155]

Imaging of the surface and lower deposit depth of the external tip deposit shows informative contrast of species (**Figure 6a**). The sulfonate ion is evidently surface localised and has a relatively non-uniform distribution, which allies with

our hypothesis that these are molecules that are embedded in the deposit matrix from lubricating oil contamination. The previous issue of identifying the origin of carbonaceous ions in this sample is overcome by chemical imaging, since ions had a localised clustering and were more intense at the lower deposit depth, suggesting their origin is from the breakdown of fuel species over time and not lubricating oil contamination. The increased carbonaceous content correlates with previous work where we attributed these species as originating from condensed aromatic clusters.[155] The overall agreement of the combined depth profile and imaging data between this sample and the GDI tip analyzed in our original work is of note, since the samples have different provenance. This points to a universally common composition of the GDI deposits matrix and will be explored in future work.

2.3.4. Part two conclusions

In this work we have used 3D OrbiSIMS and XPS to provide a quantified molecular characterization of deposits formed on external and internal GDI components and compared sample datasets for the first time. 3D OrbiSIMS revealed molecular species not seen in internal GDI deposits before. Comparison of data between both systems highlighted several key points:

- Despite differing morphologies, the external tip and internal needle deposits consisted mainly of carbonaceous species.
- Lubricating oil derived alkyl benzyl sulfonates were common to both samples, but those of higher mass were found only in the external injector tip deposit.

- Carbonaceous ions and PAHs were present in higher intensity and up to higher maximum masses in the external tip deposit.
- Depth profiling showed markedly different deposit layering, with only a thin layer structure in the needle deposit. We attribute this to the differing distribution of high mass aromatics, such as PAHs.
- These key compositional differences can be partially explained by the effect of higher temperature experienced by the external injector tip from the combustion chamber.

Overall, the combination of XPS and 3D OrbiSIMS is a new approach to characterize deposits, and new insight from these techniques into their composition and the influence of temperature across different engine components will provide industry with vital information to mitigate them. This will aid longer term efforts to reduce vehicle emissions and improve global air quality.

2.4. Chapter 2 materials and methods

2.4.1. Materials

The first part compares data from an external gasoline injector tip deposit, an internal needle deposit from a diesel engine and an automotive diesel fuel filter. Part 2 compares a different injector deposit set, here both the external and internal component are compared. Engine components were retrieved from engines recovered from real-world vehicles in operational service. Fuel injector samples were then disassembled, and samples were analyzed *ex-situ*. The filter sample was cut out from the diesel fuel filter and subsequently vacuum oven dried at 140°C and 0.01 mbar for 8 hours to remove diesel volatiles that could

compromise the instrument's vacuum chambers, while retaining the heavier deposit fractions that cause blockage of the filter. Some chemical transformations likely take place below this temperature, however the less volatile material, which is the main focus of this study, is expected to be unaffected at this temperature.

2.3.2. 3D OrbiSIMS

2.4.2.1. Instrumental setup

(Part one and two)

3D OrbiSIMS analysis was conducted using a Hybrid SIMS instrument with the technique outlined by Passarelli *et al*.[121] Secondary ions were collected using the Q Exactive HF Orbitrap mass analyser (affording a mass resolution of 240,000 at *m/z* 200) that was calibrated using clustered silver cluster ions prior to all sample measurements. In all profiling and imaging experiments, a 20 keV Ar_{3000}^{+} gas cluster ion beam was used, defocused to 20 μm with a cycle time of 200 μs, an injection time of 500 ms, a duty cycle of 4.4 % and a target current of 0.23 nA. Charge compensation was achieved with a low energy electron flood gun (2.3 A current and extraction bias of -20 V) and by regulation of the main chamber with argon gas (9×10^{-7} mbar) to delocalize any accumulation of charge surrounding the sample. Deposit sample data was collected over a mass range of *m/z* 75 – 1125 using SurfaceLab software (version 7.1.b (IONTOF GmbH)), with the application programming interface (API) provided by Thermo Fisher for control of the Orbitrap MS portion of the instrument. Data processing was performed using SurfaceLab Version 7.1.c (ION-TOF GmbH).

2.4.2.2. Depth profiles

Single beam depth profiles using Ar_{3000}^{+} ions from the gas cluster source to produce secondary ions which were analyzed by the Orbitrap™ analyzer (Mode 4)[121] were acquired for all deposit samples using one area per polarity.

Part one

The analysis areas were 300 × 300 µm (negative polarity) and 400 × 400 µm (positive polarity) for the gasoline deposit, 200 × 200 µm for the diesel injector deposit and 300 × 300 µm for the diesel filter. In all cases an interlaced border was used to prevent boundary effects. The gasoline deposit profiles were acquired over 128,000 s (negative) and 85,000 s (positive), the diesel injector deposit profiles were acquired over 15,000 s and the filter over 170 s. This afforded a total primary ion dose density of 7.98×10^{16} ions/cm^2 (positive polarity) and 1.27×10^{17} ions/cm^2 (negative polarity) for the gasoline deposit, 2.75×10^{16} ions/cm^2 for the diesel injector deposit, and 1.69×10^{14} ions/cm^2 for the diesel filter deposit. Sawtooth raster mode was used to acquire positive and negative secondary ion data for the gasoline and filter deposit and positive ion data for the diesel injector deposit. Random raster mode was used to acquire negative ion data from the diesel injector deposit.

Part two

All analysis areas were 300 × 300 µm^2 in size (random raster mode) and an interlaced border was used to prevent boundary effects. Profiles were acquired over a total sputter time of 22000 s (negative) and 35000 s (positive) for the

injector tip deposit and 120 s (positive) and 560 s (negative) for the injector needle deposit.

2.4.2.3. Chemical images

For the part one and two of this chapter, chemical images were obtained using Mode 7 of the instrument,[121] where the gas cluster ion beam (Ar_{3000}^{+}) rasters the sample surface with a low current and obtains ion data at different positions. These were all acquired over a total of 2 scans (900 s total acquisition time) with a resultant pixel size of 5 µm and an area of 300 × 300 µm with a non-interlaced border. Images were later cropped to 200 × 200 µm (40 x 40 pixels), normalized to the total ion image and scaled to match the intensity of each depth and for both samples. All imaging and profiles were performed with the same settings outlined prior and with a sputtering area of 200 × 200 µm.

2.4.2.4. MS/MS

MS/MS spectra were acquired over 50 s with an analysis area of 300 × 300 µm in sawtooth raster mode with mass windows of 10 amu and normalized collision energy of 20 eV.

2.4.3. X-ray photoelectron spectroscopy

The samples were subjected to XPS analysis using the Kratos AXIS ULTRA DLD Liquid Phase Photoelectron Spectrometer (LiPPS) with a mono-chromated Al Kα X-ray source (1486.6 eV) with a source power of 120 W for the gasoline and diesel injector deposits and 60 W for the diesel filter deposit. Spectra were acquired with the Kratos VISION II software. A charge neutralizer filament

(2.0 A current, 3.6 V balance, 1.2 V bias) was used to prevent surface charging. Small spot mode was used, measuring a sample area of approximately 200 × 200 μm. The analysis chamber pressure was better than 5×10^{-9} mbar. Gas cluster ion beam etching (20 keV Ar_{500}^{+} cluster beam, etch area of 0.75 mm for all gasoline deposits and 1.2 mm for diesel injector deposit) was performed on the injector parts prior to analysis to remove surface contamination (120 s for the external and internal gasoline deposits and 864 s for the diesel injector deposit. We present the XPS data after cleaning of the gasoline injector tip deposits surface to remove contaminants and adventitious carbon using the beam. Analytical data for the injector needle deposit was taken from the very top surface (0 s etch) etching to avoid inclusion of the metal substrate peaks. This was not performed on the filter deposit due to the porous nature of the filter material, which made etching of the sample surface and interpreting depth profiling data unfeasible with the instrument. Low resolution survey spectra were recorded (binding energy range 1200 eV to -5 eV, the pass energy was 160 eV (gasoline and diesel injector deposits) and 80 eV for diesel filter. The step energy was 1 eV for the gasoline and diesel injector deposits and 0.5 eV for diesel filter. Acquisition times were 3, 10 and 20 minutes for the gasoline deposit, diesel injector and diesel filter deposits, respectively. The spectra were charge corrected to the surface C 1s peak (adventitious carbon) set to 285 eV and used to estimate the total atomic % of the detected elements using CasaXPS (version 2.3.22 PR1.0) software. Peak positions were referenced to the XPS reference pages of XPSFitting,[158] and regions were fitted using a GL30 (30% Gaussian and 70% Lorentzian) lineshape and U2 Tougaard background. Samples were mounted on a standard Kratos sample bar (13 cm × 1.5 cm), using

double sided tape. They were exposed to vacuum in the instrument airlock overnight and placed on the sample stage for analysis. The tape was non-conducting, so the charge neutralizer filament was required to prevent sample surface charging. Peak positions were referenced to the XPS reference pages of XPSFitting.

2.4.4. Profilometry

Images of craters on the gasoline and diesel injector deposits were taken using a Zeta 20 3D Optical Profiler with a 20 × optical lens. Zeta 3D software was used for acquisition and interpretation.

2.4.5. Scanning electron microscopy

SEM micrographs were acquired for all samples using a FEI Quanta^{TM} 650 ESEM instrument equipped with an Everhardt Thornley secondary electron detector. All sample analysis was performed in low vacuum (60 Pa) to prevent sample charging, with an incident energy of 20 kV.

2.4.6. Optical microscopy

Optical microscopy images (20 × lens) of the gasoline and diesel injector deposit samples were taken with a Leica M205 FA Stereo light microscope.

2.4.7. Miscellaneous

Chemical structures were drawn in ChemDraw 14.0.

Graphs for were plotted in Veusz (Version 3.2.1, Jeremy Sanders).

2.5. Comments on Chapter 2

In this chapter we demonstrated the capabilities of 3D OrbiSIMS to unambiguously identify 3D spatial distribution of key molecular components in internal and external gasoline and diesel deposits. The data marks a step change in the level of detailed information that can be obtained from the samples compared to other analyses such as ToF-SIMS and other MS approaches. We focused on a comparison of different engine components from different fuel streams to understand the effect of fuel composition, temperature and pressure on deposit composition. We have compared several components across different fuel streams and found that effects such as temperature and pressure can affect deposit formation and composition. Despite the new insight into deposits in this chapter there are drawbacks. First, the low sample number. Second, we have not fully interpreted the 3D OrbiSIMS data due to the volume and complexity of chemical data afforded from these systems. Before expanding sample population, we will therefore attempt to address the issue of high amounts of 3D OrbiSIMS chemical data by developing and applying new data processing methods which are explored in the next chapter.

Chapter 3

The Application of Molecular Formula Prediction for Chemical Filtering of 3D OrbiSIMS Datasets

Max K. Edney, [1] Anna M. Kotowska,[2] Matteo Spanu, [1] Gustavo F. Trindade[2,4], Edward Wilmot,[3] Jacqueline Reid,[3] Jim Barker, [3] Jonathan W. Aylott,[2] Alexander G. Shard,[4] Morgan R. Alexander,[2] Colin E. Snape[1] & David J. Scurr[2]

[1]*Department of Chemical and Environmental Engineering, University of Nottingham, Nottingham, NG7 2RD, UK*

[2]*School of Pharmacy, University of Nottingham, Nottingham, NG7 2RD, UK*

[3]*Innospec Ltd., Oil Sites Road, Ellesmere Port, Cheshire, CH65 4EY, UK*

[4]*National Physical Laboratory, Hampton Road, Teddington, Middlesex, TW11 0LW, UK*

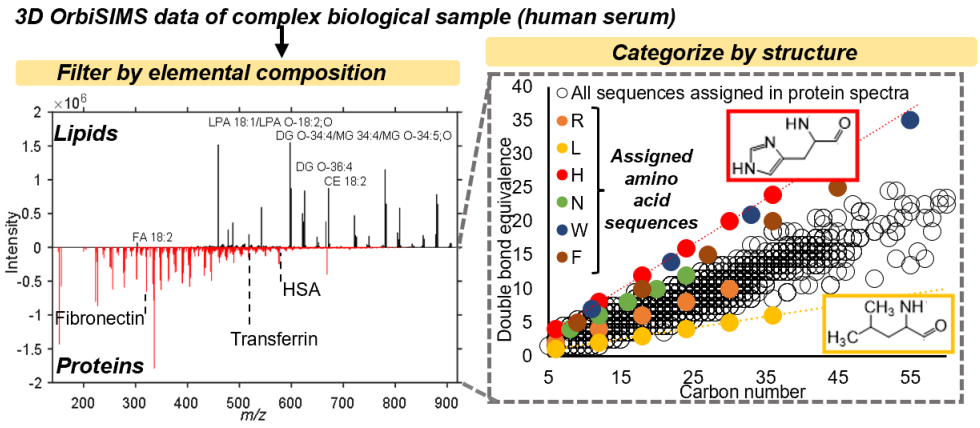
Published in *Analytical Chemistry* in 2022 (DOI: 10.1021/acs.analchem.1c04898)

Author contributions

3D OrbiSIMS experiments were carried out by M.K.E and A.M.K. All authors aided in interpretation of analytical data. Molecular formula prediction software

was developed by M.S., G.F.T. and M.K.E. The manuscript was written by M.K.E and A.M.K and all authors helped in its edits and revisions.

3.1. Abstract



As shown in the previous chapter, 3D OrbiSIMS produces a wealth of spectral data and although this is an advantage in terms of the richness of the information available, the volume and complexity of data can prevent a thorough interpretation to reach useful conclusions. In this chapter we explain the development and application of a novel method for filtering 3D OrbiSIMS data using measures such as molecular formula prediction (MFP) to produce annotated lists of ions that have been filtered by their elemental composition and structural double bond equivalence. These measures have not been applied to SIMS data. We apply this data interpretation approach to 3D OrbiSIMS datasets, testing it for a series of increasingly complex samples. In an organic on inorganic sample, we successfully annotated the organic contaminant overlayer separately from the substrate. In a more challenging purely organic human serum sample, we filtered out both proteins and lipids based on elemental compositions, 226 different lipids were identified and validated using existing databases and we assigned amino acid sequences of abundant serum proteins including albumin,

fibronectin and transferrin. Finally, we tested the approach on depth profile data from layered carbonaceous engine deposits and annotated previously unidentified lubricating oil species. Application of an unsupervised machine learning method on filtered ions after performing MFP from this sample uniquely separated depth profiles of species, which were not observed when performing the method on the entire dataset. Finally, we demonstrate how the approach can rapidly assign complex chemical structures in engine deposits which will be a useful application in assigning polymeric structures such as fuel additives in these sample types.

3.2. Chapter 3 Objectives

- Determine the applicability of chemical filtering using MFP to 3D OrbiSIMS data from various inorganic/organic sample types (both spectra and depth profiling data).
- Use chemical databases to quantify the matches of ions.
- Test the approach by apply multivariate analysis techniques to attempt to discern chemistries on filtered and unfiltered datasets.
- Demonstrate the utility of filtering to rapidly identify complex structures from engine deposit data (see **supplementary note S3.1**).

3.3. Introduction

The use of sophisticated mass spectrometry (MS) techniques with high mass resolving power yields a significant amount of chemical data from a given sample series and often a barrier to fully interpreting these datasets comes from annotating the spectral ions in order to identify the analytes. Calculations for

automated peak assignment based on molecular formula prediction (MFP) are widely used in other areas of MS. Dedicated programs for processing these datasets exist such as MZMine 2,[159,160] which uses MFP from accurate *m/z* values following rules laid out by Kind *et al*.[161] Kew *et al.* recently developed software which uses MFP followed by plotting species in filtered lists by their double bond equivalence (DBE) versus carbon number of each predicted formula. Plotting DBE versus carbon number to categorize chemical species with similar chemistries is a strategy which has been successfully applied in other areas of MS to deconvolute complex datasets, such as in petroleomics using Fourier transformed iso-cyclotron resonance MS, [162–164] and dedicated software for processing these datasets exists such as 'KairosMS'.[165] DBE is a measure used to elucidate chemical structures from predicted molecular formula and determines degrees of unsaturation in a molecule by calculating the ratio of C, H, N, P and halogen atoms in the molecular formula. The DBE of a structure is contributed to by either a double bond and/or a ring system, for example, benzene has a DBE of 4 (3 double bonds and one ring system) and cyclohexane has a DBE of 1. Where category databases exist for species (e.g., Lipidmaps, PubChem and ChemSpider) the putative molecular and structural assignment can then be validated by cross-referencing to these.

SIMS relies on detection of ions which have been liberated from a sample surface by bombardment from a primary ion source.[73] Whilst most MS techniques extract species from a sample using solvent and then coarsely separate them using for example, chromatographic retention time, SIMS collects all ions from the surface. Therefore, these datasets contain molecular ions as

well as fragments, meaning that assigning the parent species in highly complex samples typically requires sophisticated analysis methods. Software developed for other MS techniques regularly use molecular databases (libraries) to assign species, but the high level of fragmentation in SIMS means this is often unfeasible, meaning that 'library-free' interpretations are needed. Green *et al.* showed that even with a mass accuracy of 1 ppm, up to 1000 formulae are possible at *m/z* 385, and concluded that even high accuracy SIMS techniques would need to be combined with filtering techniques for truly library-free interpretation of data from unknown samples, as well as extra steps such as isotopic distribution analysis.[166] SIMS is also uniquely able to perform depth profiling and label-free chemical imaging of samples, but this additional dimensionality adds another layer of complexity to interpreting these datasets. Until recently the low mass resolving power (< 20,000) and mass accuracy and high levels of fragmentation of SIMS techniques was a barrier to performing filtering of data in this way due to the vast number of possible formulae within acceptable errors for each ion.

The introduction of the 3D OrbiSIMS technique,[121] with its superior mass resolving power (240,000 at *m/z* 200), sub parts-per-million mass accuracy and reduced fragmentation using an argon gas cluster ion beam, now permits the use of chemical filtering approaches using MFP and DBE measures as applied in other fields of high mass resolving power MS techniques. The issue of fragmentation, while reduced, is still present and the high amount of data is a barrier to full interpretation which carries the risk that key chemical insights or trends may be missed without this approach. Often, the complexity of SIMS data

demands the use of sophisticated data analysis methods including unsupervised machine learning methods such as multivariate analysis (MVA), which has proven to be of great effectiveness for 3D structured SIMS data.[167,168] However, most MVA methods suffer from bias toward high intensity ions, especially in very high dynamic range datasets typical of the 3D OrbiSIMS. Other tools include *de novo* sequencing of peptides and proteins which was recently shown to be applicable to 3D OrbiSIMS data,[122] but again suffers from the high level of data acquired from the technique and so a pre-processing workflow using chemical filtering would be highly valuable for these applications. To our knowledge, measures of MFP and DBE have not been applied to SIMS data. Therefore, a chemical filtering workflow using MFP to filter all secondary ions by predicted elemental compositions followed by categorizing these ions by plotting their DBE versus carbon number would be useful to not only deconvolute and filter 3D OrbiSIMS data but could be applied to various data analysis tools as a pre-filter, such as MVA.

Here, we demonstrate the utility of chemical filtering using MFP and DBE measures on increasingly complex 3D OrbiSIMS depth profiling datasets from aluminium foil, a human serum sample containing chemically similar proteins and lipids and finally heterogeneous gasoline engine deposits. We applied MVA on filtered datasets from the deposit to showcase the advantage over performing MVA on raw 3D OrbiSIMS datasets.

3.4. Results and discussion

3.4.1. Differentiation of contaminant overlayer and aluminium foil substrate

Here we apply chemical filtering to data from aluminium foil, which is regularly used in surface and materials analysis, and is considered a very clean material but may present trace organic contaminants which would be useful to assign and ascribe to an origin. MFP using elemental and mass error constraints were set, specifically a maximum deviation threshold of 2 ppm for ions > *m/z* 95 and 3 ppm for ions < *m/z* 95, which are typical acceptable errors when interpreting Orbitrap datasets.[110] After automatically annotating aluminium peaks (including oxides and hydroxides) using MFP we performed another search for organic species on the 'unassigned' dataset (**Figure 3.1**). This is a useful test sample as the species we are distinguishing are chemically distinct and are expected to have characteristic depth profiling behavior which can validate our findings. This approach can be used to help uncover the identity and source of contamination or identify miss-assignments to either the substrate or contaminant category.

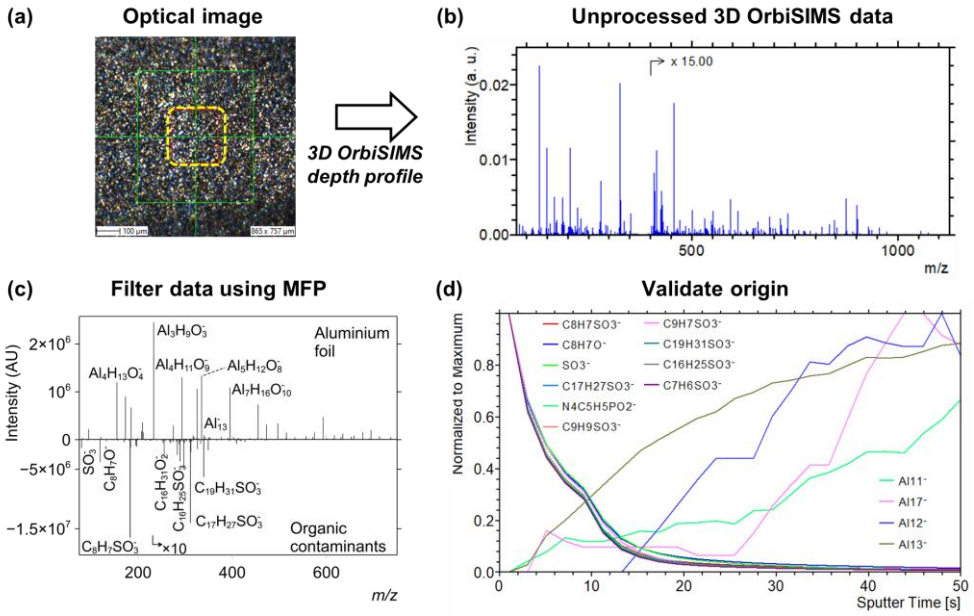


Figure 3.1. Separating organic and inorganic species on aluminum foil 3D OrbiSIMS depth profiling datasets using MFP. (a) *Optical image of the analysis area before* Ar_{3000}^+ *depth profiling.* ***(b)*** *Raw depth profile accumulation spectra in negative ion mode.* ***(c)*** *Positive scale, plots of the inorganic species containing Al, O and H identified using MFP. Negative scale, contaminants identified after performing a repeated mass separation of the initial dataset followed by another formula filtering iteration analysis to identify species with C, H, O, N, S and P (intensity × - 1).* ***(d)*** *Depth profiles of some species in each sub-group. MFP, molecular formula prediction.*

The 3D OrbiSIMS depth profile of aluminium foil (**Figure 3.1a**) yielded a raw spectrum with dominant signals for inorganic ions (**Figure 3.1b**). The first search using MFP was for species containing Al, O and H (any values of each element were considered). Out of a peak list containing 1252 ions, MFP identified 408 corresponding to Al, O and H species (**Supplementary table 1**[169]) which are plotted in the 'Aluminium foil' spectra in **Figure 3.1c**. We then performed MFP again on the discarded dataset (of which no ions could be assigned to the foil), with elemental constrains of C_n, H_n, O_{20}, $N_{0\text{-}10}$, S_1 and $P_{0\text{-}2}$. Filtered spectra of these ions in the contaminant search are shown in the lower plot in **Figure 3.1c** (intensity × -1), in total there were 920 possible formulae for ions which can be found in the data repository. The most intense ions all corresponded to sulfonated compounds (containing an SO_3^- group) and we identified 53 such ions with various double bond equivalencies, suggesting degrees of unsaturation or aromatization. Organic sulfonates such as these have been ascribed to lubricating oil in previous SIMS analysis,[170] we attribute these ions as originating from the manufacturing of the foil where lubricants are used

in the machinery which comes into contact with the foil.[171] We applied the filter to a dataset taken from the 'shiny' side of the foil which showed only 31 sulfonated species and all with lower normalized intensity (**Supplementary table 1**[169]), which is expected as the 'shiny' side of the foil comes into less contact with machinery in the manufacturing process. We also applied MATLAB code which matched the formulas generated by MFP to ions found in the LIPID MAPS database.[172] Out of the list we identified 14 ions on the dull side of the foil, 10 of which were fatty acids and 4 were assigned as sterols, both of which may derive from trace contamination from skincare products.[173] Aside from these we also identified hydrocarbon fragments and a summary of all species in the mentioned compound classes can be found in (**Supplementary table 1**[169]).

Application of chemical filtering to data from solvent-based MS techniques is limited to only distinguishing ions by their formula, but the use of depth profiling in 3D OrbiSIMS uniquely allows further categorization of data by their depth behavior and can help confirm their origin. Ions with increasing intensity as a function of sputtering dose may be ascribed to the substrate and vice versa for organic contaminants (**Supplementary figure S3.4**). Depth profiles of the most intense aluminium species showed two trends, where ions containing only Al increased in intensity in the experiment (example ions are shown in the profile in **Figure 3.1d**), the aluminium oxide/hydroxide ions decreased in intensity, suggesting the presence of an oxide layer. The purely organic species decreased in intensity slightly faster than the metal oxides (**Supplementary figure S3.4**).

Chemical filtering on this sample dataset was useful as an initial test using a system containing elementally distinct species, i.e., organic and inorganic materials. Furthermore, the anticipated depth profiling behavior of each system enabled a validation for the species that MFP had categorized. We note that an alternative approach could be to search for organic species first, however the simpler approach was determined to identify aluminium species initially as there are fewer possible combinations of molecular ions. This approach also shows the flexibility to filter data by first searching for known species and separating them and repeating the process to elucidate unknown chemistries in a sample.

3.4.2. Distinguishing proteins and lipids in a human serum[a]

In the previous example, we distinguished species with very different elemental compositions. In order to further challenge the chemical filtering approach and to introduce the concept of filtering them by their DBE value, we apply the method to a human serum sample, containing proteins and lipids. Interpretation of 3D OrbiSIMS spectra of proteins is challenging, as the fragmentation process produces multiple amino acid sequences, each occurring as different types of ions (a, b, c, y and z ions).[122] The limits applied to the elemental formula were based on manually assigned protein fragments from 16 protein samples reported by Kotowska *et al.*: $C_{4\text{-}100}$, $H_{8\text{-}200}$, $N_{0\text{-}20}$, $O_{0\text{-}20}$, $S_{0\text{-}1}$, $Na_{0\text{-}1}$. MFP returned 58,135 possible assignments based only on the elemental composition in a collated peak list of all manually assigned protein peaks (**Figure 3.2a**, black). Among all assignments suggested by MFP, we highlighted the known structures (**Figure**

[a] Data analysis and writing for Section 3.4.2 was performed by A.M.K with support from myself.

3.2a, red). Due to proteins being composed of different combinations of 20 amino acids, single DBE values or DBE/C_n are not suitable for further filtering of the data. Depending on the amino acid composition of detected protein fragments, the DBE/C_n is placed between the amino acid of the highest (**Figure 3.2b**, histidine, H, red) and lowest DBE/C_n (**Figure 3.2b**, leucine, L, yellow). The peak list exported from the spectrum contains 5,805 peaks and providing a full interpretation of unprocessed data is not feasible. This is especially the case when targeting fragments of macromolecules such as proteins, which are typically of relatively weak intensity and are easily overlooked (**Figure 3.2c**). The spectrum of serum is dominated by readily ionized lipids. Therefore, the first step of the processing was to filter the lipid-related peaks from the data using MFP. We used the LIPID MAPS® database of "bulk" lipid species,[172] and wrote code which automatically matches formula in the list from MFP to lipids in the database (available upon request). The database groups major classes of lipids based on the molecular formula and indicates general classification of a lipid, but not specific chain positions or double bond regiochemistry and geometry. The formulae suggested by SIMS-MFP were matched with the database to automatically assign the lipid peaks in the human serum spectrum. As a result of this matching, possible assignments for 226 lipid peaks were generated (**Figure 3.2d**, black, and **Supplementary Table 2**.[169] Peaks assigned as lipids were removed from the dataset using the 'separate' function in the software which can generate a list of ions that were not assigned in the original formula prediction search. MFP was run again on the 'unassigned' peaks to aid assignment of protein peaks. The search found 69,602 possible formulas based on the allowed elemental composition. A database of up to 6-membered peptides

was calculated using known formulas of each amino acid. A total of 3,328 assignments were found to match with elemental composition of sodiated or protonated protein fragments gathered in this database (**Figure 3.2d**, red). Example protein assignments and possible amino acid assignments are listed in **Supplementary Table 3**.[169] Molecular formulae of protein fragments obtained using MFP, together with *de novo* sequence search, described in previous work,[12] enabled automatic assignment of sequences of abundant serum proteins such as serum albumin, transferrin and fibronectin on filtered datasets (**Supplementary Table 4**.[169] Additionally, phosphate salts were assigned in the serum spectrum by searching compounds of composition: C_0, H_{1-10}, N_{0-0}, O_{0-10}, S_{0-1}, $P_{0-5,}$ $Na_{0-5,}$ $Ca_{0-5,}$ and Cl_{0-5} in the list of peaks unassigned as either lipids or proteins (**Supplementary Table 5**).[169] Overall, filtering using MFP and grouping of species by DBE significantly reduced the complexity of the 3D OrbiSIMS human serum spectrum by separating and assigning secondary ions associated with lipids from fragments of large biological molecules such as proteins.

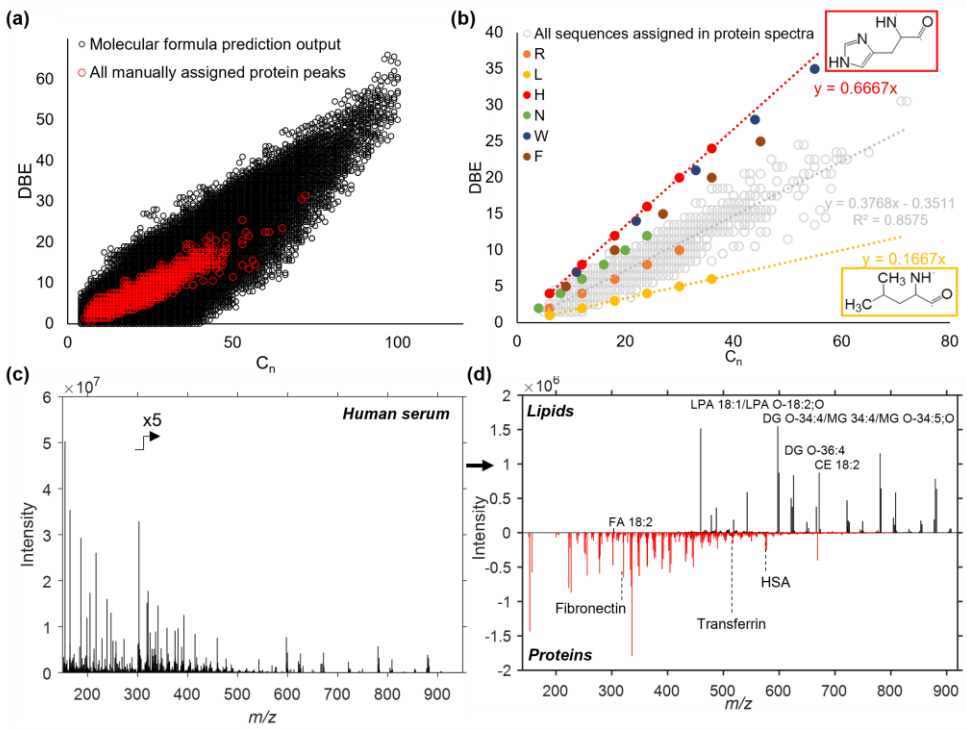


Figure 3.2. ***(a)*** *Comparison of all assignments proposed by MFP in a collated peak list of all manually assigned protein peaks in 16 different protein samples (black) and only correct protein assignments (red).* ***(b)*** *All protein peaks assigned in 16 protein samples are widely spread around the trend line of DBE/C_n (grey). The variability of DBE/C_n of protein assignments is caused by different amino acid DBE/C_n (orange – asparagine, R; yellow – leucine, L; red – histidine, H, green – asparagine, N; brown – phenylalanine, F).* ***(c)*** *Human serum sample is too complex to manually assign fragments of biological molecules.* ***(d)*** *MFP combined with the LIPID MAPS® database automatically assigns lipid groups (black). Additional MFP on the rest of the spectrum enables assignment of proteins in serum (red). Peaks assigned as fragments of fibronectin ($C_{15}H_{22}N_4O_3Na^+$, m/z 329.1585), transferrin ($C_{24}H_{44}N_6O_5Na^+$, m/z 519.3258) and human serum albumin ($C_{24}H_{40}N_8O_7Na^+$, m/z 575.2918). Chemical filtering was carried out on SIMS-MFP software.*

3.4.3. Using chemical filtering as a pre-filtering tool to MVA techniques on 3D OrbiSIMS data from carbonaceous engine deposits

The final application of the chemical filtering approach is to gasoline engine deposits, which are the most challenging samples to interpret in this work owing to the similarity of chemical species it contains. In addition they are heterogeneous samples and previous work found that most species had different depth profiling behavior.[170] We employed MFP and DBE filtering to depth profiling data from several samples, followed by performing MVA on the filtered data. The first type is sulfated species, which can be indicative of contamination of lubricating oil in engines.[170] Filtered spectra and DBE plots from the engine deposit samples after searching for species with compositions of $C_nH_nS_1O_3^-$ are shown in **Figure 3.3**.

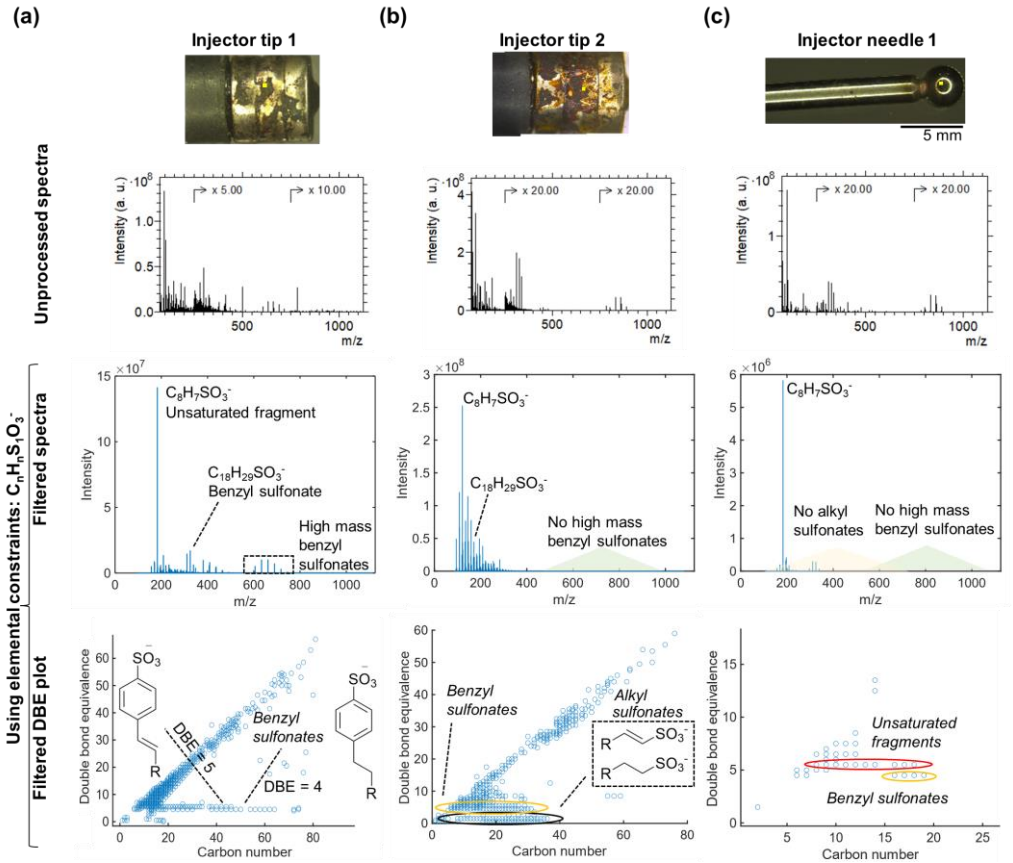


Figure 3.3. Using MFP to search for sulfated species in gasoline engine deposits. *In each case the raw 3D OrbiSIMS depth profile accumulation spectrum is shown above*

the spectrum of sulfated ions and the lowest is the filtered DBE plot of these species. ***(a)*** *Deposit on injector tip 1, showing benzyl sulfonates present up to high masses (*C_{75}*).* ***(b)*** *Injector tip deposit 2, showing benzyl sulfonates <* C_{40} *and a unique distribution of alkyl sulfonates with a DBE value < 2.* ***(c)*** *Results from the injector needle, showing only benzyl sulfonates but to a lower maximum mass than other samples.*

Filtered DBE plots allowed us to make distinctions between sample chemistry that would have remained lost in the high amount of chemical data in the raw spectra without the use of MFP. In all samples we easily identified beznyl sulfonates (DBE = 4), depicted in **Figure 3.3a**, including the cited parent ion ($C_{18}H_{29}SO_3^-$).[140,141] An intense SIMS induced fragment ion ($C_8H_7SO_3^-$, DBE = 5) was also in all filtered spectra and DBE plots (**Figure 3.3a**, **b** and **c**) which has been confirmed previously using 3D OrbiSIMS and MS/MS.[170] Benzyl sulfonates with masses higher than the cited parent ion were present in both injector tip deposits, termed 'high mass benzyl sulfonates' (**Figure 3.3a** and **b**) which extended up to much higher masses in injector tip 1 (C_{78}) but were not present in the injector needle deposit (**Figure 3.3c**). High mass sulfonates have been identified and confirmed with MS/MS in previous work and are attributed to the product of reactivity of the deposited residue in the engine itself. Understanding the extent of this reactivity by visualizing maximum mass of ions is important in unraveling key deposit formation mechanisms.[170] The filtered DBE plot also highlighted a unique series in injector tip 2 with a DBE of 1 and 2 which we putatively assign as alkyl sulfonates which have not been identified in these systems before. Their low intensity compared to benzyl sulfonates meant that without the visualization approach they were unidentified in the

previous analysis of these sample types.[170] In total 410, 353 and 35 sulfated ions were detected in injector tip 1, injector tip 2 and injector needle 1, respectively. The comprehensive nature of this categorization of species is evidently a useful feature and is shown in the tabulated output of ions found in all samples in **Supplementary table 8**.[169] Depth profiles of the 10 most intense ions all showed consistent behavior which further validates grouping of these assignments into this compound class (**Supplementary figure S3.3**).

The next two key compound classes discussed are oxygenated species containing possible carboxylate functional groups ($C_nH_nO_2^-$) and carbonaceous ions (C_n and C_nH^-) and using MFP we identified possible ions. To interogate the depth profile behavior and further categorize these species we next performed MVA on the filtered list of ions, outputs from these steps are shown in **Figure 3.4** with data taken from injector tip 1.

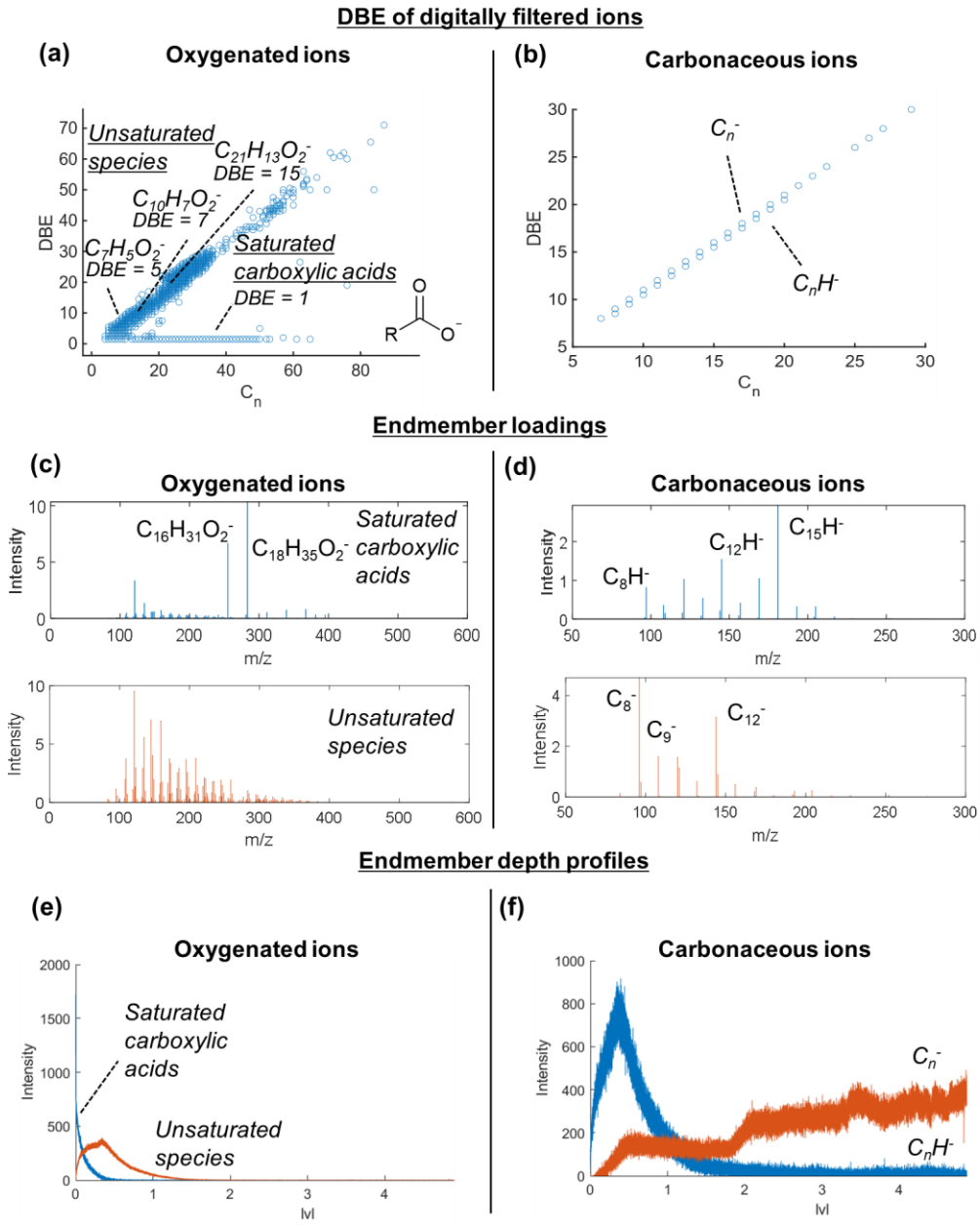


Figure 3.4. Demonstrating MVA on datasets after performing MFP on 3D OrbiSIMS depth profiling data from injector tip 1 deposit. ***(a)*** *DBE versus carbon number plots of all oxygenated ions ($C_nH_nO_2^-$) identified using MFP.* ***(b)*** *DBE versus carbon number plots of all carbonaceous ions ($C_nH_{<1}^-$) identified using MFP.* ***(c)*** *Loadings of oxygenated ions after performing NMF on the filtered list of oxygenated ions identified using MFP.* ***(d)*** *The first two loadings of carbonaceous ions identified using MFP.* ***(e)*** *Depth profiles of the first two endmembers of the oxygenated ions.* ***(f)*** *Depth profiles of the first two endmembers of the carbonaceous ions.*

In total 522 discrete oxygenated ions were automatically identified which fit the criteria (with no other option within the deviation threshold) (**Supplementary figure S3.4**). DBE plots showed different trends of unsaturation of ions, and we easily identified saturated carboxylic acids by their DBE value of 1.5 (which corresponds to a DBE of 1 for the neutral ion if we assume $[M - H]^-$ ions were generated) (**Figure 3.4a**). The depth profiles of the top 10 most intense ions in this filtered list showed separation into two distinct behaviors, one for species with a higher DBE (> 5) and one for saturated species (**Supplementary figure S3.4**), which we attribute to carboxylic acids. We repeated MFP of oxygenated ions for the two other deposits; injector tip 2 also contained saturated carboxylic acids and the thin film deposit on the injector needle did not contain any long chain carboxylic acids (**Supplementary table 7**).[169]

We annotated 34, 52 and 19 carbonaceous ions in injector tip 1, injector tip 2 and injector needle 1, respectively (**Figure 3.4b** and **Supplementary table 6**).[169] Depth profiles of the most intense ions revealed subtle differences in depth behaviour where where purely carbonaceous (C_n^-) ions had higher intensity at the lowest deposit depth compared to hydrogenated ions (C_nH^-) (**Supplementary figure S3.5**). This aligns with the hypothesis from previous work of the origin of these ions being condensed carbonaceous clusters which increase in C:H ratio in lower deposit depths.

MVA on depth profiling data in theory negates the need to interogate each ion in a dataset, however applying MVA on complex SIMS data often leads to issues such as overfitting of data in output loadings, replicating intense ions in multiple

loadings and generally under-performing in discerning ions with subtle differences in their spatial distributions. To demonstrate the utlility of MVA on chemically filtered data we performed NMF analysis of the depth profiles of oxygenated and carbonaceous ions annotated using MFP. This is of particular importance when considering the oxygenated ions which still contained > 500 ions in its filtered dataset so interogating each one would be unfeasible. NMF (described in the methods) analysis on the dataset was performed with two factors on the list of oxygenated ions after MFP was performed. This clearly separated into two depth profile behaviors (**Figure 3.4c**), one corresponded to saturated carboxylic acids, and one corresponded to unsaturated ions. Of note is that this is comparable to the trends identified by levels of unsaturation in the DBE plots (**Figure 3.4e**).

NMF output using two factors on the dataset of carbonaceous ions after MFP also showed distinction into the two depth profiling trends identified by manual peak picking (**Figure 3.4f**). This is despite these ions only having a sublte difference in depth profile behavior and only one proton difference in composition (**Figure 3.4d**). NMF on the filtered dataset from the injector needle did show a similar trend shown by higher scores of purely carbonaceous ions for the component profile which increased at lower depths (**Supplementary figure S3.6**). This is despite the analysis time being significantly shorter (561 s on the needle and 22094 s on the tip), suggesting the depth profiles reflects real chemical differences and is not an effect of long sputter times. This will be explored further in future work but does highlight the importance of depth profiling in assigning the origin of species in MS data.

To illustrate the advantage of filtering the data prior to MVA, we performed NMF on the unfiltered 3D OrbiSIMS dataset to attempt to recreate the MVA outputs from the three classes discussed so far (sulfated, oxygenated and carbonaceous ions). Results from using 4 endmembers to constrain the output data is shown in **Figure 3.5**.

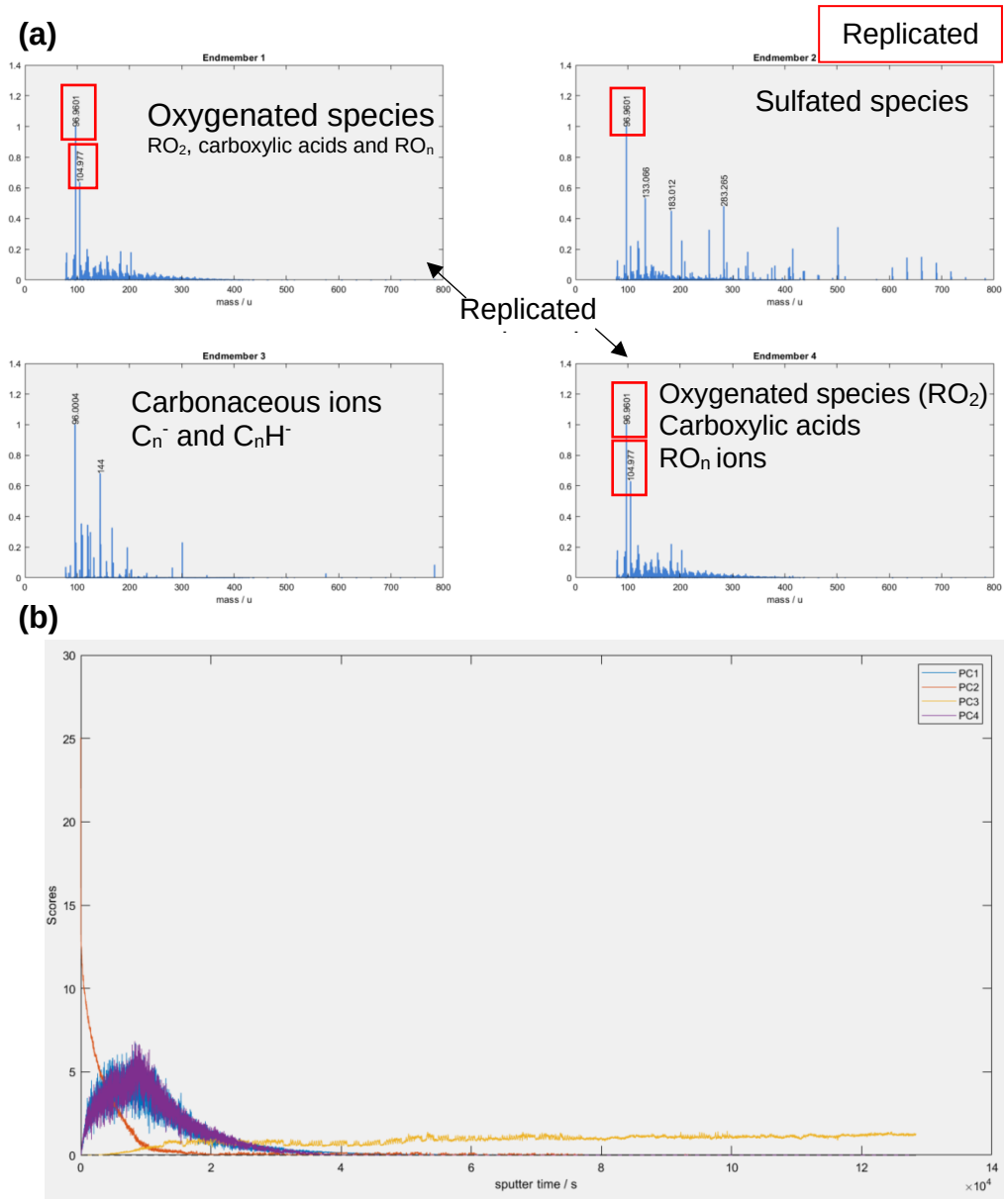


Figure 3.5*. NMF analysis on the raw 3D OrbiSIMS spectra with 4 endmembers.* ***(a)*** *Loadings of each endmember, showing overfitting and replication of peaks.* ***(b)*** *Score*

plots corresponding to depth profile trends, these were replicated and did not separate into the known behaviors of each class of known chemistries in the sample.

Loadings of the first 4 endmembers generally separated chemistries by their elemental composition, but many ion peaks were present in multiple loadings and one loading dataset was entirely replicated (**Figure 3.5a**). Moreover it failed to distinguish subtle differences in the profiles of sulfated, oxygenated or carbonaceous ions (**Figure 3.5b**), for example, it did not separate C_n^- and C_nH^- ions, which was achievable when using NMF after perfoming an initial filtering using MFP (**Figure 3.4f**). We increased the number of endmembers to four to try and discern more subtle differences, but again we observed overfitting of loadings and an entire loading dataset was replicated without revealing the subtle differences in profile trends. Overall this shows the utility of performing MFP followed by MVA on filtered datasets to unveil subtle chemical trends in complex heterogeneous samples.

The full chemical filtering method described in this work was carried out by a piece of software, SIMS-MFP, which was developed using MATLAB and has a dedicated graphical user interface described in **Supplementary note S3.1.** The software is freely available as part of this work (https://github.com/medney96/SIMSMFP) and we believe it will be of great use to many users in the SIMS community whether performing MFP, or in addition to other data analysis tools such as MVA or *de novo* sequencing. Finally, we propose chemical filtering can be applied to other SIMS techniques including time-of-flight SIMS, including MS/MS data, to further refine possible

annotations per peak, making this approach applicable in some format to all SIMS datasets. Yet, the poor resolving power on this instrument will result in a considerable number of possibilities of formula for peaks – so it should be used in conjunction with other annotation tools such as MS/MS.

3.5. Relevant work not included in the publication

3.5.1. Application of chemical filtering to identify complex additive species in deposits

While chemical filtering was used to search for chemistries in deposits that were observed in previous work, an obvious advantage is to make putative assignments on chemical structures that are unkown in deposits. There is a great importance in this field as, in the past, evidence of polymeric additives in deposits can be indicative of them breaking down and therefore they may need modifying. We targetted functional groups from a commonly used additive, poly-isobutylene succinic acid (PIBSI). This additive is used in a variety of fuel and lubricating oil additive packages and in diesel deposits has been inferred by the presence of an $–NO_2$ functionality by FT-IR spectroscopy.[50] The generic structure is shown in **Figure 3.6a** and from this we used chemical filtering to identify ions containing a formula of $C_nH_nN_2O_2^+$, as its generic formula is $[(C_4H_9)(C_4H_8)_nC_{14}H_{24}N_2O_2]^+$ with a DBE of 4. We applied this to data from injector tip 1 and 2 and found no such ions with a DBE of 4. In Chapter 4 we describe the data analysis from a suite of other fuel injector samples (namely injectors 3-8), the origin of the samples is discussed in more detail but for the purposes of this chapter we applied the filtering process on these samples,

finding a match for possible PIBSI ions from injector tip 7 and 8 only. Filtering results from a search for PIBSI ions in injector 7 are in **figure S3.1b**.

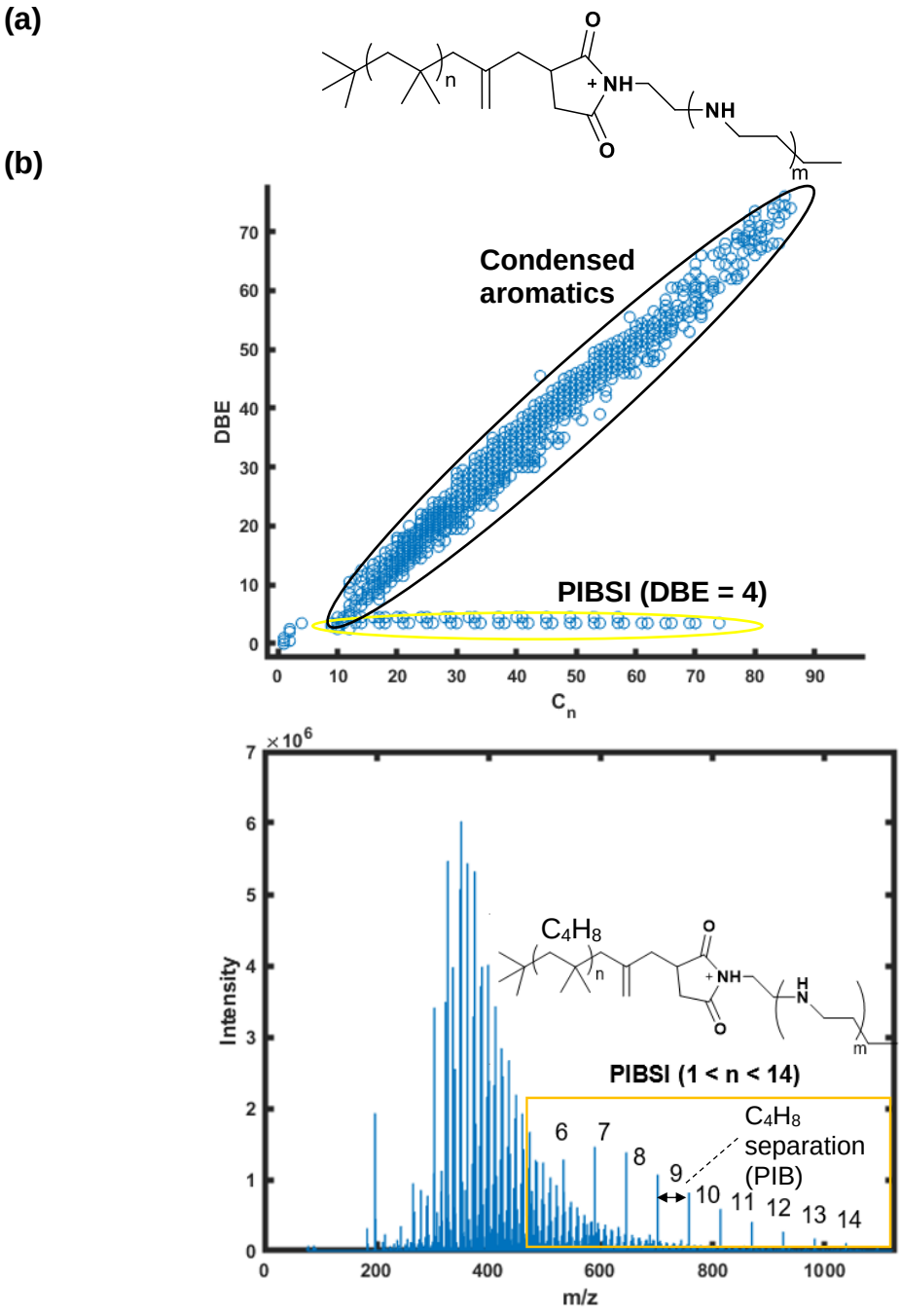


Figure 3.6. Identification of polyisobutylene succinimide species in deposits via chemical filtering using MFP and DBE categorization. ***(a)*** *Chemical structure of PIBSI where n and m can be any value.* ***(b)*** *DBE plots, showing two distributions.* ***(c)*** *filtered spectra of species with matching formula.*

The DBE plot from injector 7 (**Figure 3.6b**) showed two clear distributions, one which likely corresponds to condensed aromatics containing oxygen and nitrogen (blue circle) which could be attributed to various functional groups on the PAH framework (**Figure 3.6b**). The second distribution (yellow circle) had a DBE value of 4 (assuming $[M + H]^+$ ions) which matches that of the PIBSI structure. The filtered spectra from injector tip deposit 7 showed a repeating unit with mass separation corresponding to C_4H_8 which is consistent with loss of the PIB group (n in **Figure 3.6a**). Formulas were assigned to those of PIBSI with different repeating values of n, these extended up to a mass of 1094.1290 with an assigned formula of $C_{74}H_{145}N_2O_2^+$ ($[(C_4H_9)(C_4H_8)_{14}C_{14}H_{24}N_2O_2]^+$) (**Figure 3.6c**). The error is < 2 ppm as this was a constraint when running filtering software. We expanded the search criteria to find structures where m may be > 1, but no matching distributions were found, suggesting the chemical identified has m = 1 and n < 14. We note that 3D OrbiSIMS settings selected only allow measurement up to *m/z* 1125 and so it is possible that higher mass species are present but the trend of reducing intensity toward *m/z* 1125 suggests we were at the highest/higher end of the MS peak distribution.

PIB mannich amines are a key gasoline fuel additive which are dispersed in fuel mixtures to clean internal engine components and are designed for use in older port-fuel injection systems.[137] The general structure is shown in **Figure S3.2a** and has the general formula of $[C_{20}H_{39}(C_4H_8)_nN_5O]^+$ with a DBE of 4. The application of MFP filtering on tip deposit 7 showed a distribution of ions with this formula (**Figure 3.7b**).

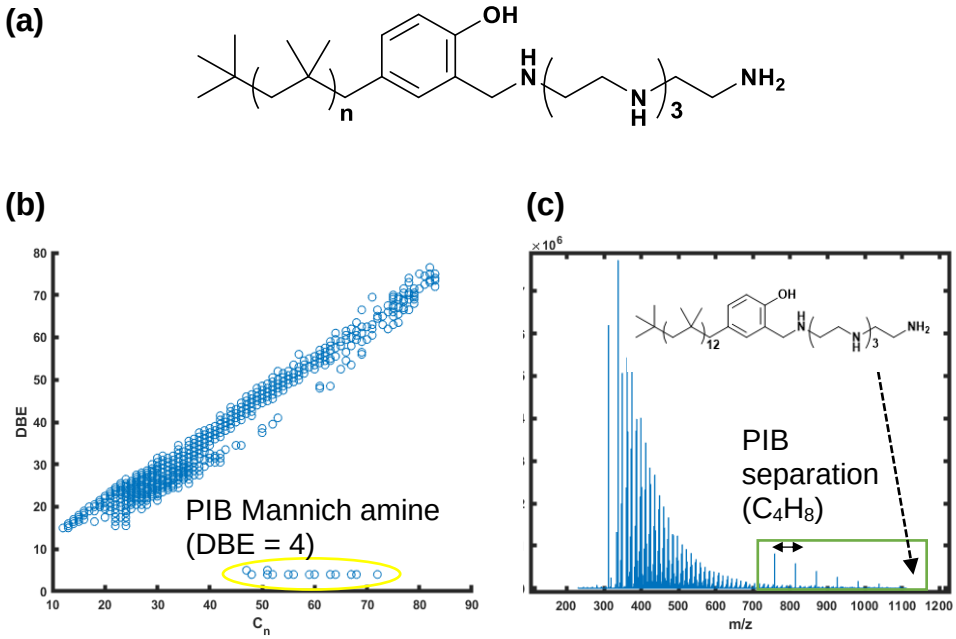


Figure 3.7. Identification of PIB Mannich Amine additives in deposits via filtering using MFP and DBE categorization. ***(a)*** *Chemical structure of PIBSI where n and m can be any value.* ***(b)*** *DBE plots, showing two distributions.* ***(c)*** *filtered spectra of species with matching formula.*

We performed filtering for the PIBSI and Mannich amine additive structures on all external and internal samples analyzed in this project (including analytical repeats). A summary of samples which contained an intense signal (above the noise threshold and within a 2 ppm accuracy) is shown in **Table 3.1**. It is worth noting that these are putative assignments and chemical filtering still does not negate the importance of confirming assignments using MS/MS.

Table 3.1. *Samples containing ions putatively assigned as PIBSI or PIB Mannich amines, ion data for the maximum mass ion is displayed. N refers to the suggested number of polyisobutylene units on the polymer backbone.*

Tip deposit	**PIBSI** $[C_4H_9(C_4H_8)_nC_{14}H_{24}N_2O_2]^+$	**PIB Mannich Amine** $[C_{20}H_{39}(C_4H_8)_nN_5O]^+$
Tip 1		
Tip 1 repeat		
Tip 2		
Tip 2 repeat		
Tip 3		
Tip 3 repeat		
Tip 4		
Tip 4 repeat		
Tip 5		
Tip 5 repeat		
Tip 7	$C_{74}H_{145}N_2O_2^+$ (n = 14) *m/z* 1094.1293, - 0.70 ppm	$C_{72}H_{143}N_5O^+$ (n = 13) (*m/z* 1094.1293, 0. 53 ppm)
Tip 7 repeat	$C_{74}H_{145}N_2O_2^+$ (n = 14) *m/z* 1094.1284, - 1.53 ppm	$C_{72}H_{143}N_5O^+$ (n = 13) (*m/z* 1094.1284, 0. 53 ppm)
Tip 8	$C_{54}H_{105}N_2O_2^+$ (n = 9) *m/z* 813.8169, - 0.16 ppm	
Tip 8 repeat	$C_{54}H_{105}N_2O_2^+$ (n = 9) *m/z* 813.8162, - 1.06 ppm	
Needle deposit	**PIBSI**	**PIB Mannich Amine**
Needle 1		
Needle 2		
Needle 3		
Needle 4		
Needle 5		
Needle 7	$C_{74}H_{145}N_2O_2^+$ (n = 14) (*m/z* 1094.1295, 0.62 ppm)	$C_{72}H_{143}N_5O^+$ (n = 13) (*m/z* 1094.1295, 0. 72 ppm)
Needle 8	$C_{70}H_{137}N_2O_2^+$ (n = 13) (*m/z* 1038.0861, 0.62 ppm)	

The fact that both additives were only observed in samples using a specific fuel suggests it originates from a batch-to-batch use of the additive since PIBSI may only be present in certain fuel/lubricating oil batches. Notably the internal samples also contained high mass species of additive structures and of higher masses than in the high temperature tip component, perhaps the heat is causing more extensive degradation of the polymer in the tip component (**Table 3.1**).

This demonstrates how chemical filtering can be applied to find species of interest. For the automotive industry, it can be used to find reactive species which have been implicated in deposit formation initiation (such as low molecular weight PIBSI polymers[87,174]) with ease which could be responsible for vehicle failure. A topical example was in 2007 when polymeric Si contamination in a supermarket fuel caused the failure of 10,000 vehicles and so a technique which can interpret data from more complex structures is of importance to this area of research going forward.

3.6. Chapter 3 conclusions

In this chapter we have developed a new approach for interpreting 3D OrbiSIMS datasets by chemical filtering of possible assignments by elemental compositions and DBE measures. This addresses a major problem in the field and will no doubt help other researchers in the pursuit of comprehensively interpreting these rich datasets. We demonstrated the use of the approach on a range of samples and coupled with database searches can improve the reliability of the method. Species from adventitious organic contamination upon aluminium foil were readily filtered and separated from the substrate peaks. In human serum we automatically matched putatively assigned molecular and fragment lipid ions with the LIPIDMAPS database. Further filtering of serum data by applying a protein fragment database aided amino acid sequence assignment by reducing the number of non-protein related peaks. In carbonaceous deposits formed on metal in engines, we elucidated species not observed previously, allowing easier discernment of sample chemistry differences than when comparing unfiltered data. We showed how performing

unsupervised machine learning on filtered datasets gave superior distinction of sample chemistries in layered systems compared to applying the techniques on the unfiltered dataset. In **Section 3.5** (not included in the publication), we also demonstrated how filtering can target complex chemical additive structures in deposits in the field to identify 'bad-actors' in fuels which can be responsible for engine component failure.

3.7. Comments on Chapter 3

The application of chemical filtering by elemental composition and structural measures (DBE and carbon number) has many useful applications in other fields of research in assigning components in complex mixtures; such as the adsorbed biomolecular layer of implanted biomaterials and the influence of the biointerface on biofilm formation with importance in infection. We have demonstrated here that the chemical filtering approach allowed us to make assignments which we could not have made without this tool, yet we note that we have not completely mitigated challenges inherent with 3D OrbiSIMS of these complex samples, such as that within a 2-ppm window there are often many possible assignments for high mass species. This was evident in the human serum where even after removing lipid peaks and then filtering the resultant dataset by elemental composition there were still > 3000 possible protein assignments to those peaks classified as likely peptides. A 3D OrbiSIMS database of protein fragments could help identify the proteins by limiting number of peaks for amino acid sequence search. But even for peaks that are automatically matched in databases there will need to be structural assignments made using MS/MS which is currently time consuming. Alternatively, it is

alluring to envisage digitally predicting which peptides will be seen in 3D OrbiSIMS, in an analogous way as the proteomics community has developed for liquid chromatography MS. That being said, without the filtering method it would have been unfeasible to generate the > 3000 possible protein assignments and this method will no doubt reduce data analysis time and help unveil new chemical insights from even the most complex 3D OrbiSIMS datasets. In the next chapter we will re-focus our efforts on comprehensively characterizing engine deposits using 3D OrbiSIMS and chemical filtering from a suite of samples obtained from engine testing methods.

3.8. Chapter 3 Materials and Methods

3.8.1. Materials

3.8.1.1. Aluminium foil

Standard aluminium (as available from any supermarket) was purchased and analyzed using 3D OrbiSIMS on both the shiny and dull side of the foil.

3.8.1.2. Engine deposits

In this work we analysed deposits *in-situ* on different gasoline direct injection fuel injector components from different vehicles, sourced from the USA. Two samples were fuel injector tips which had a thick carbonaceous deposit and one was a needle of the injector which exhibited a thin-film coating of deposit. Samples are termed injector tip 1, injector tip 2 and injector needle 1.

3.8.1.3. Model protein samples and human serum

Proteins: lysozyme from chicken egg white, α-chymotrypsin from bovine pancreas, insulin solution human, recombinant bovine serum albumin, horse

skeletal muscle myoglobin, L-lactate dehydrogenase from rabbit muscle, human holo-transferrin, concanavalin A from Jack Bean, bovine plasma fibronectin, alcohol dehydrogenase from Saccharomyces cerevisiae, porcine lipase, bovine liver catalase, human serum albumin and cytochrome c from equine heart were purchased from Sigma Aldrich. Porcine pepsin and porcine trypsin were purchased from Promega. Serum from human male AB plasma, USA origin, sterile-filtered was purchased from Sigma Aldrich. Proteins and the human serum were spotted and dried onto separate gold slides 3 times to obtain protein films.

3.8.2. Methods

3.8.2.1. 3D OrbiSIMS

Instrument setup was the same as outlined in chapter 2 (2.3.2). Sample data was collected over a mass range of *m/z* 75 – 1125 for all samples except the human serum sample which was measured in the mass range of *m/z* 150 – 2250.

Engine deposit samples were analyzed in negative polarity mode, the analysis area was 200 x 200 μm with an interlaced border (random raster mode). Measurement times for the samples were as follows: injector tip 1, 22094; injector tip 2, 128000; injector needle 1, 561 s. Primary ion currents were as follows: injector tip 1, 238 pA; injector tip 2, 260 pA; injector needle 1, 230 pA. The human serum sample was analyzed in positive polarity mode over a 200 x 200 μm area (random raster mode) using 3D OrbiSIMS single beam depth profiles as described in the data acquisition section. The measurement lasted 30 scans and the primary ion current was 218 pA. Aluminium foil was analyzed

using 3D OrbiSIMS single beam depth profiles as described in the data acquisition section. Data was collected in negative polarity in an analysis area of 150 μm^2 (random raster mode) and the measurement time was 134 s.

3.8.2.2. DBE calculations

DBE relates the number of double bonds or rings in a molecule and is calculated using the following formula which relates to elemental formula as:

$$DBE = 1 + N_C + (\frac{N_N}{2} + \frac{N_P}{2}) - (\frac{N_H}{2} + \frac{N_X}{2})$$

Where N_C = the number of carbon atoms, N_H = the number of hydrogen atoms, N_X = the number of halogen atoms (Br, Cl, I and F), N_N = the number of nitrogen atoms and N_P = the number of phosphorus atoms. Isotopes for C, Br and Cl are considered. It is important to note that non-integer DBE values are generated which arises from the inclusion of [M+/- H] ions. Therefore, the inclusion of these non-integer DBE values is necessary, and the true value of DBE needs to be considered by the user, particularly when considering positive ions which can exist as $[M + H]^+$ and $[M]^{\cdot +}$ ions.

3.8.2.3. Data interpretation

The chemical filtering method for interpreting 3D OrbiSIMS data laid out in this work was performed using SIMS-MFP software which was developed in MATLAB and is available for use in this work, a description of the softwares functions is given in **Supplementary note S3.1** and the graphical user interface is shown in **Supplementary Figure S3.1**. Briefly, the software requires input of

a depth profiling dataset as a .txt file format or as a matrix in MATLAB. To do this we first performed a peak search on raw data, a minimum intensity threshold was manually determined by discerning the minimum count of a peak that distinguished it from a noise peak (this value varied between samples). For the engine deposit samples the peak search generated a file containing ion peak data for 13437 ions for injector tip 1, 12707 ions for injector tip 2 and 1600 ions for injector needle 1. The aluminium foil file contained 1252 ion peaks and the serum sample had 5805 ion peaks. MFP is then performed to produce spectra of filtered ions based on elemental compositions in the 'search constraints', namely the maximum error of each ion and the minimum and maximum value of each element in the molecular formula. The DBE value of predicted formula of each ion is calculated and plotted against its carbon number to allow observation of different trends in the data by the level of unsaturation in different molecules. More information on the method can be found in **Supplementary note S3.1**. To advance this methodology we propose performing MVA on the filtered datasets (depth profiles or spectra), to further elucidate differences in the trend of each sub-group. We apply all these features to a range of different samples which were analyzed by 3D OrbiSIMS in subsequent sections. Multivariate analysis – specifically non-negative matrix factorization (NMF) was performed using SIMS-MFP software which is linked to SIMS-MVA algorithms.[167] In each case the optimal number of factors was determined by performing NMF using different numbers of factors until excessive repetition of endmember loadings was observed. In each case the number of iterations was 200.

Chapter 4

Time Resolved Growth of (N)-Polycyclic Aromatic Hydrocarbons in Engine Deposits Uncovered with OrbiSIMS Depth Profiling

Max K. Edney[1], Wenshi He,[2] Emily F. Smith,[3] Edward Wilmot[4], Jacqueline Reid[4], Jim Barker[4], Rian L. Griffiths[2], Morgan R. Alexander[2], Colin E. Snape[1] and David J. Scurr[2]*

[1]Department of Chemical and Environmental Engineering, Faculty of Engineering, University of Nottingham, University Park, Nottingham, NG7 7RD, UK.

[2]School of Pharmacy, University of Nottingham, University Park, Nottingham, NG7 2RD, UK.

[3]Department of Chemistry, University of Nottingham, University Park, Nottingham, NG7 2RD

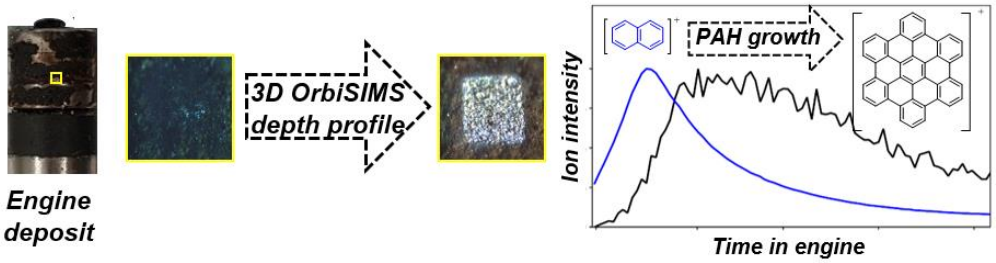
[4]Innospec Ltd., Oil Sites Road, Ellesmere Port, Cheshire, CH65 4EY, UK.

Published in *Analyst* in 2022 (DOI: 10.1039/d2an00798c)

Author contributions

D.J.S, J.B, C.E.S and M.K.E planned and coordinated the work. M.K.E conducted 3D OrbiSIMS experiments. M.K.E, W.H. and R.LG. conducted AP-MALDI experiments. E.F.S conducted XPS experiments. All authors aided in interpreting the analytical data. M.K.E wrote the manuscript and all authors helped in its edits.

4.1. Abstract



Carbonaceous deposits are ubiquitous, being formed on surfaces in engines, fuel systems and on catalysts operating at high temperatures for hydrocarbon transformations. In internal combustion engines, their formation negatively affects worldwide vehicle emissions and fuel economy, leading to premature deaths and environmental damage. Deposit composition and formation pathways are poorly understood due to their insolubility and the intrinsic complexity of their layered carbonaceous matrix. Here, we apply the *in-situ* high mass resolving power capabilities of 3D OrbiSIMS argon cluster depth profiling on 16 lab grown deposits and evidence common molecular distributions in deposit depth and in positions relative to the combustion chamber. We observe the products of the growth of both planar and curved polycyclic aromatic hydrocarbons to form small fullerenes over time in the engine and propose possible formation pathways which explain the molecular distributions

observed. These include alkyl scission, cyclisation of aliphatic side chains and hydrogen abstraction C_2H_2 addition to form larger aromatic structures. We apply this pathway to previously unidentified nitrogen containing structures in deposits including quinolines and carbazoles. For the first time, 3D OrbiSIMS results were compared and validated with data from atmospheric pressure matrix assisted laser desorption ionization MS. The comprehensive characterization provided will help the development of a new generation of chemical additives to reduce deposits, and thus improve vehicle emissions and global air quality.

4.2. Chapter 4 Objectives

- Apply the chemical filtering method to 3D OrbiSIMS depth profile data from an expanded population size of deposits of different origins to compare the compositions in detail, particularly of the carbonaceous matrix.
- Interrogate the depth profiles of carbonaceous ions and hypothesize reasons for differing chemical distributions to compare the effect, if any, on the use of different fuels on the layered structure of injector tip deposits.
- Measure differences in speciation and ion intensity of key molecules along the injector needle deposits to gain more insight into the effect of temperature on composition.

4.3. Introduction

Gasoline direct injection equipment is implemented in most light passenger vehicles today.[6,54] It is proposed that vehicles with internal combustion engines will be the most common type of passenger vehicle used in 2040.[125] Ensuring high efficiency and low emissions of these engines for their lifetime is therefore vital. However, the breakdown and reactivity of complex fuel mixtures leads to deposit formation and their complexity partially results from the fact that they contain species derived directly from fuel and from the reactivity of these species. Deposits can lead to a catastrophic increase in emissions of gaseous pollutants, particulates and a reduced efficiency from internal combustion engines and so threaten the strive for cleaner operating vehicles.[16,21,54,134,175,176] Therefore, mitigating deposits will reduce the cost of fueling vehicles, reduce pollution and improve air quality. Current work aims to mitigate deposits by developing deposit solubilizing fuel additives or by suppressing adverse reactions which cause deposit formation and growth. Both strategies rely on understanding the composition, origin and formation pathways of deposits.[38,41,152,177] However, the complexity of the organic matrix and its layered nature means that probing its formation is difficult and there is limited understanding into how a thin film layer transforms into a carbonaceous deposit. Due chiefly to analytical limitations since most techniques offer only generic chemical information and cannot probe material provenance.[152] Work has been carried out into understanding how fuel mixtures undergo the initial stages of deposit formation by leakage in the injector, oxidation and adhesion to the engine component wall, leading to some initiation mechanisms being proposed.[55,178,179] This, however, has not been aligned with analytical data from

real-world samples and has yet to explain how the reactions precipitate into a layered carbonaceous deposit. To do this we should turn to high resolution mass spectrometry (MS) techniques, such as atmospheric pressure matrix-assisted laser desorption/ionization MS (AP-MALDI-MS). This technique has been used to analyze insoluble carbonaceous materials and has revealed possible pathways of formation of PAHs by looking at neutral losses of ions in 1 dimensional spectra.[146,180] But this does not give spatial information with either depth nor lateral position on a given sample type. Ordered carbonaceous material has been identified in deposits using Raman spectroscopy and transmission electron microscopy,[61] which opens the possibility of formation of flat graphitic type PAHs.[58] Flat and curved PAHs can form from smaller PAHs and can go onward to form soot particles and their mechanisms of formation have been well studied.[181–183]

To advance this work we propose the use of the 3D OrbiSIMS depth profiling function to analyse deposits *in-situ* on fuel injector component surfaces to establish the fate of molecules once deposited on a surface. This technique combines a low energy gas cluster ion beam to generate relatively large diagnostic secondary ions *in-situ* for accurate identification and confirmation using the high mass resolving power (> 240, 000) and MS/MS (fragmentation/structural characterization) capability of the Orbitrap™.[121] Not only can this approach tackle insoluble samples but it can yield *in situ* depth information, and has been successfully used by our group to elucidate the origin of key species such as alkylbenzyl sulfonates, succinimides and PAHs in such samples.[170] We will focus on probing the full chemical nature of the deposits as

a function of depth which is correlated with time (i.e. age) of the deposit, as older deposit regions are accessed with longer sputtering times. We compare data from 16 different engine components with different origins and elucidate common molecular profiles which were comparable regardless of sample provenance. The universal nature of our data has important implications to mitigating deposits across the entire fleet of gasoline powered vehicles and will therefore bring global environmental benefit by reducing emissions and improving air quality.

4.4. Results and Discussion

4.4.1. Time resolved growth of flat and curved PAHs

Engine deposits were 'grown' in a controlled engine testing rig (**Figure 4.1a**) using conventional gasolines of differing compositions (GC-MS analysis of the fuel is summarized in **Supplementary figure S4.1**), which varied by the types of olefins or indene compounds they contained as well as quantified compositions of each class. Work has been done using 3D OrbiSIMS to define the optimum analytical conditions for biological samples,[121,184] however, little has been done on petroleomics type samples. As a result, we first performed 3D OrbiSIMS experiments on one of the grown deposits by varying experimental parameters inlcluding Ar cluster size and energy, pressure of nitrogen feed to the Orbitrap analysers collision cell, and Ar pressure for charge compensation. We assesed performance by looking at the ion intensity of molecular ions of known species explored in previous work.[170] A description of the optimization experiments is in **Supplementary note 4.1** & **Supplementary figure S4.3**. Subsequently we performed 3D OrbiSIMS depth profiling on all 16 deposits

using these determined settings. Positive secondary ion data from deposits on injector tip 1 is shown in **Figure 4.1** and was representative of data from all other injector tip samples.

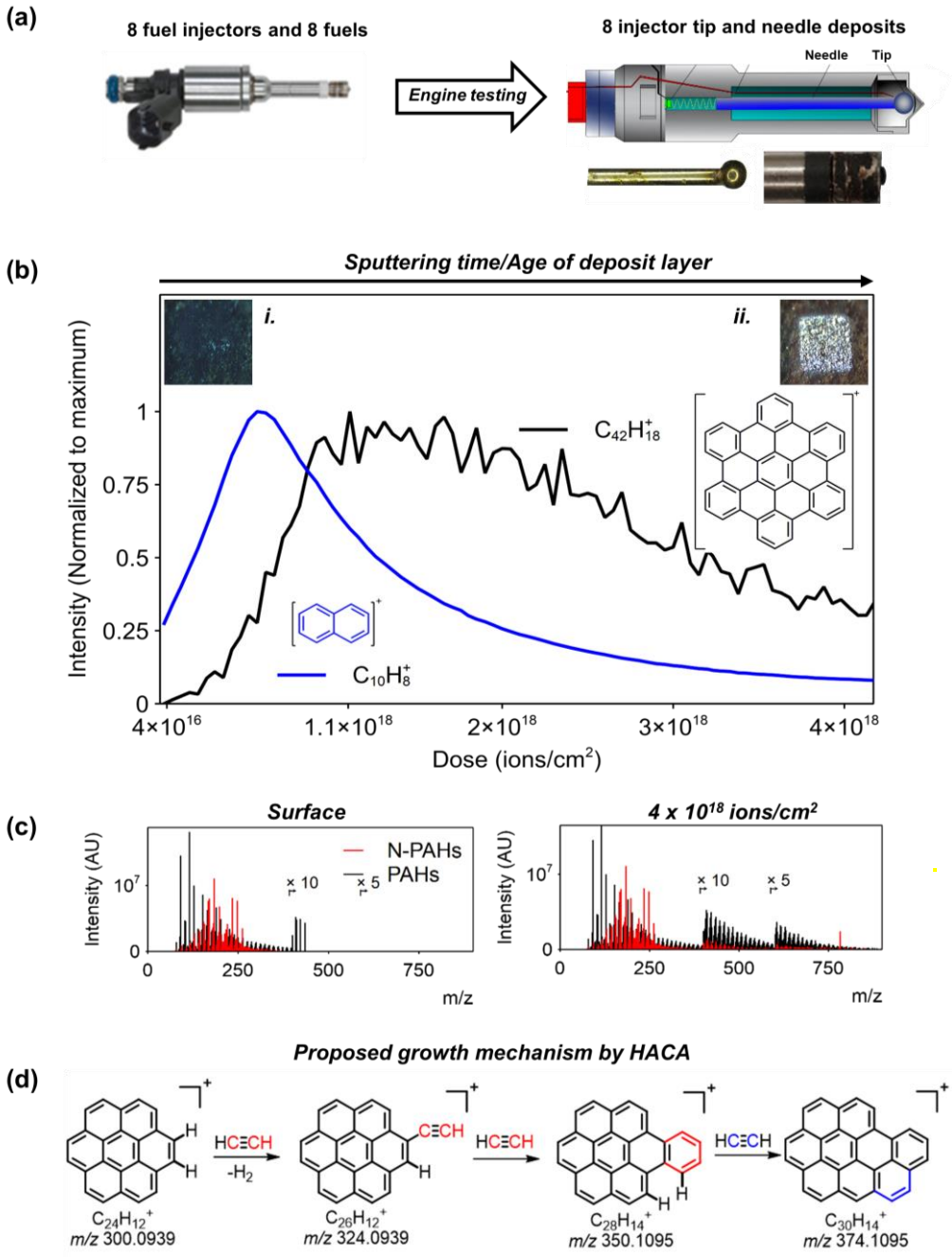


Figure 4.1. (a) *Schematic of the fuel injector and key components studied in this work.* ***(b)*** *3D OrbiSIMS depth profiles from injector tip 2 showing the profiles of*

hexabenzocoronene ($C_{42}H_{18}^+$) and naphthalene ($C_{10}H_8^+$). Optical images taken from i. before and ii. after sputtering are displayed. ***(c)*** *Depth profile accumulation spectra (normalized to maximum) from two portions of the depth profile displayed in the region of m/z 75-1125. Species were annotated putatively using a chemical filtering technique (molecular formula prediction), in black are ions annotated with a formula of $C_nH_n^+$ and in red we annotate those ions with a formula of $C_nH_nN^+$.* ***(d)*** *A proposed growth pathway of the build-up of PAHs via hydrogen abstraction acetylene addition (HACA), illustrated as an example from coronene using peaks identified in the 3D OrbiSIMS spectra. AU, arbitrary units.*

3D OrbiSIMS depth profiling data was assessed using a chemical filtering approach (described in previous work by this group[185]) to comprehensively account for the composition of the gasoline deposits. We propose formation pathways of deposit buildup by profiling into older deposit zones and elucidating the reasons for differences in observed chemistries between older and newer areas of the deposit (**Figure 4.1b**). From the total number of CH species, uncovered by chemical filtering, we accurately assigned radical cations ($[M]^{+\bullet}$) of PAHs up to masses > *m/z* 1000 using accurate mass which corresponded to known structures.[145] Injector tip 2, 5 and 8 had the highest mass PAHs (**Supplementary figure S4.6**). Of note is the assignment of molecular ions for 5-membered PAHs in all tip deposits including (in order of size) fluorene ($C_{13}H_{10}^+$, *m/z* 166.0776), cyclopentapyrene ($C_{18}H_{10}^+$, *m/z* 226.0777), benzofluoranthene ($C_{20}H_{12}^+$, *m/z* 252.0933) and corannulene ($C_{20}H_{10}^+$, *m/z* 250.0776) (**Supplementary table S4.5**). We next confirmed the identity of several key PAHs not seen in deposits previously using MS/MS experiments, including secondary ions at *m/z* 202.07755 (pyrene), *m/z* 178.0776 (anthracene),

corannulene, *m/z* 300.0932 (coronene) and *m/z* 394.0778 (ovalene) by assigning neutral losses of functional groups including C_n and C_nH (**Supplementary figure S4.7**). These were also observed in MS/MS experiments using other MS techniques on the same ions.[186,187] Here, MS/MS spectra of coronene and coranulene included several CHNO containing species, which was attributed to the inclusion of intense CHNO containing species in the isolation window due to low parent ion intensity requiring a wider isolation window (**Supplementary figure S4.7**).

3D OrbiSIMS depth profiles of the deposits on a substrate showed lower mass PAHs are more prevalent nearer the deposit surface (newly deposited region) compared with higher mass PAHs. Shown by the stark difference between depth prevalence of naphthalene ($C_{10}H_8^+$) and hexabenzocoronene ($C_{42}H_{18}^+$) in **Figure 4.1b**. We attribute this to the formation of larger PAHs over time once fuel is deposited on the injector substrate. Depth profiles of injector tip 1 and all others showed this growth of PAHs throughout the deposit depth, despite the samples being derived from different fuels (**Supplementary figure S4.8**). The trend also held for 5-membered PAHs with larger structures being prevalent in the lower depth (**Supplementary figure S4.9**). Comparison of mass spectra at the surface and a lower depth after sputtering indicated much higher masses of CH species in lower layers (black in **Figure 4.1c**). Using chemical filtering we also identified N containing aromatics (including N-PAHs) and noted an increase in their intensity after sputtering (red in **Figure 4.1c**), their importance is discussed in the next section. It has long-been hypothesized that PAH growth occurs during deposit formation but has never been shown. The presence of alkylated

benzene in high concentrations in the initial seeding fuel opens the possibility of cyclisation of alkyl chains to form larger aromatic structures (**Supplementary figure S4.1**).[143,146,188] Depth profiles of species with both an aliphatic and aromatic content fits with the hypothesis too as they were only present at the deposits surface (**Supplementary figure S4.10** and **Supplementary table S4.11**).

Using depth profiling trends, we can then move forward and link possible formation pathways from previous studies to explain deposit buildup. In all mass spectra we identified a repeating mass difference between PAHs corresponding to an alternating C_2 and C_2H_2. We illustrated this for the growth of coronene from accurate masses of ions in injector tip 2 in **Figure 4.1d** and show this was present for other samples in **Supplementary figure S4.12**. This is consistent with a hydrogen abstraction acetylene addition (HACA) growth mechanism (**Figure 4.1d**),[29] a widely studied mechanism in the buildup of PAHs[183] which has been proposed in the buildup of coal-tar pitch and other carbonaceous materials previously.[180,189,190] 5-membered rings such as those found here have been shown to form from the direct involvement of acetylene in the HACA reaction from mechanistic studies.[191] The presence of indene is a likely precursor to 5-membered PAH formation (**Supplementary figure S4.1**). Acetylene is likely sourced from the pyrolysis of hydrocarbons in the engine.[192,193] It is important to state that we are not observing radical intermediates and many formation mechanisms are possible, such as addition of phenyl and subsequent alkyl cyclization, [194] or direct addition of vinylacetylene (C_4H_2).[183]

The presence of 5-membered PAHs also opens the possibility of formation of fullerenes since the strained 5-membered ring causes curvature in the PAH structure.[181,182] We found low intensity peaks corresponding to molecular ions for the smallest fullerenes, C_{24}^+ and C_{28}^+, in injector tip 2, 5 and 8 (**Figure 4.2**).

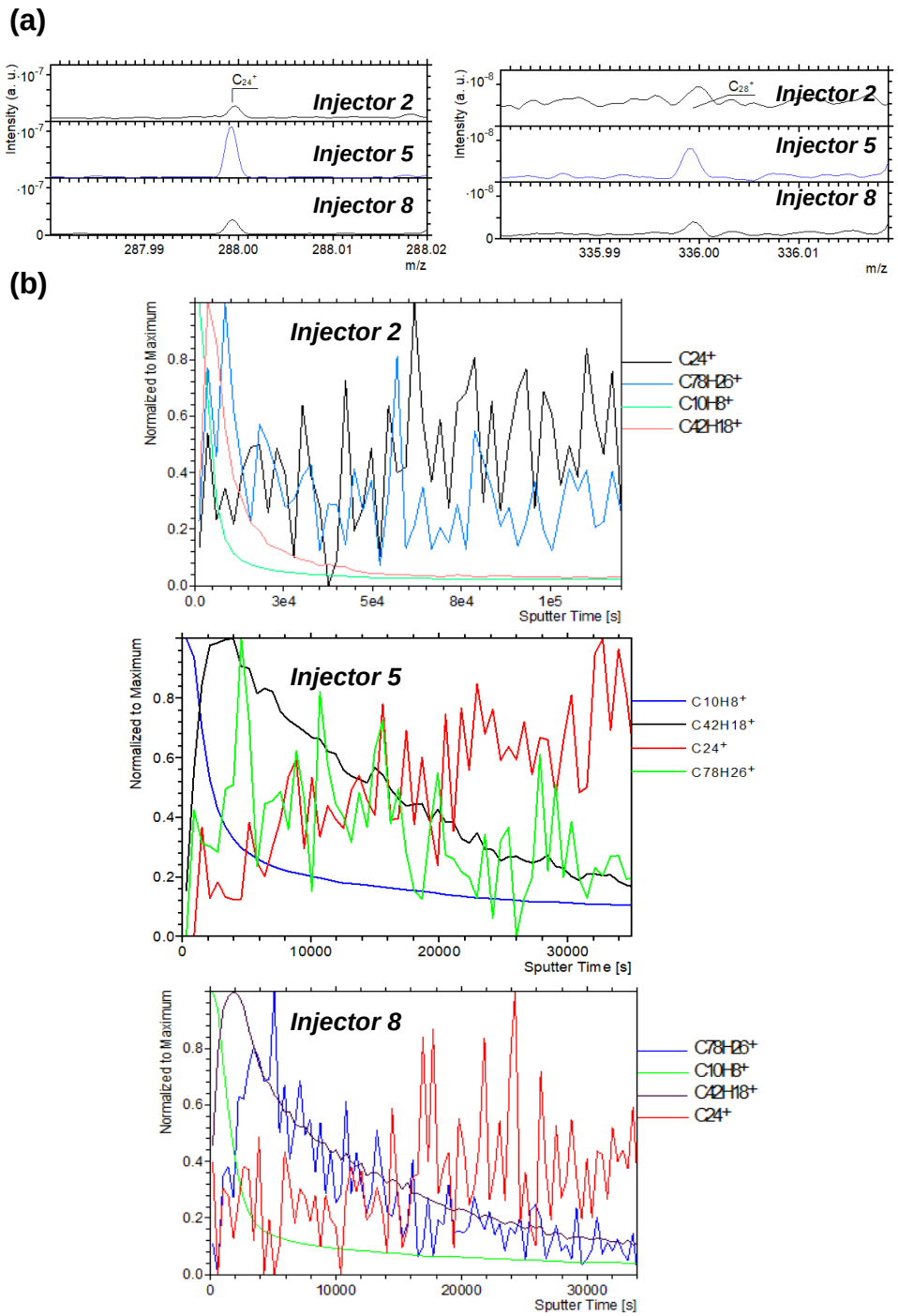


Figure 4.2. Fullerenes in deposits. (a) *3D OrbiSIMS spectra showing molecular ion peaks for C_{24} and C_{28} peaks.* ***(b)*** *Depth profiles showing the behavior of the C_{24}*

fullerene compared to naphthalene, hexabenzocoronene and a large PAH, $C_{78}H_{26}^{+}$, in injector 2, injector 5 and injector tip 8.

Notably these samples had the highest accurately assignable maximum mass of PAHs as shown by the summary of CH species plots in **Supplementary figure S4.6**. Further, depth profiles from these samples showed prevalence of fullerenes in the lowest portion of the deposit, even after large PAHs such as $C_{78}H_{26}^{+}$ (**Figure 4.2**). We postulate that one destination of PAH growth in engine deposits is fullerenes and overall show the growth of carbonaceous deposits involves formation of PAHs into large flat PAHs, curved PAHs and fullerenes over time.

The ballistic effect of SIMS may mean that we are observing smaller fragments of the 'true' maximum assignable mass of key ions such as PAHs. To compare data to a more established technique with different ionization mechanisms we ran AP-MALDI analysis using a TCNQ matrix on the deposit after scraping it off the injector substrate. This is the first comparison between these techniques. Spectra from the deposit from injector tip 5 (chosen as this had the most amount of visible deposit to scrape off for analysis) showed many PAHs observed in 3D OrbiSIMS, shown by plotting the carbon number versus double bond equivalence value of possible CH containing ions using molecular formula prediction (**Supplementary figure S4.13**).

In comparing this data to the AP-MALDI analysis we note several differences. Firstly, the maximum mass of accurately assignable PAH identified, $C_{90}H_{26}^{+}$ and

$C_{114}H_{38}^{+}$ for 3D OrbiSIMS (within a 2 ppm error) and AP-MALDI (within a 5 ppm error) respectively, spectra and putative structures are shown in **Figure 4.3**. Importantly, the similar maximum mass of assigned PAH in these systems validates our analytical approach using 3D OrbiSIMS for assigning PAH structures, but also in the wider context of SIMS analysis as 3D OrbiSIMS appears to be generating a comparable dataset to an established AP-MALDI approach. Secondly, we observed fewer ions via AP-MALDI than in 3D OrbiSIMS, which is expected as it is a softer ionization method, producing more intact ions and fewer fragments. Finally, it is observed that ionized species in AP-MALDI have a higher carbon number to double bond equivalence ratio (**Supplementary figure S4.13**) as compared with 3D OrbiSIMS, which are indicative of archipelago/island type PAH structures which contain alkyl chains between clusters of condensed PAHs. It is likely that SIMS is fragmenting these species to isolate only purely condensed PAHs or those with only short alkyl chains (detailed in **Supplementary figure S4.11**).

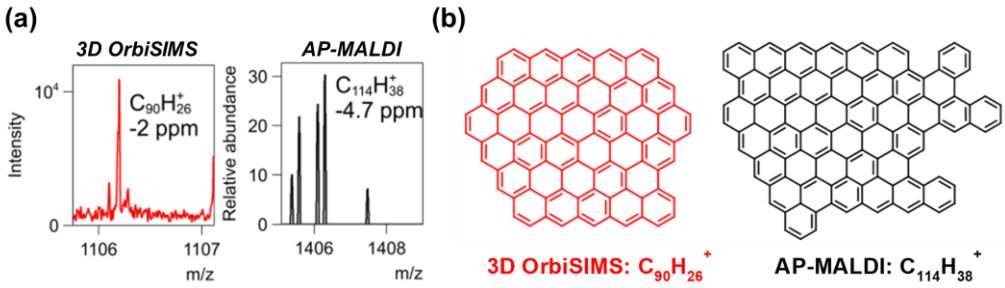


Figure 4.3. *Comparison of the accurately assigned maximum mass of polycyclic aromatic hydrocarbon by 3D OrbiSIMS and AP-MALDI techniques from tip deposit 5.* ***(a)*** *Spectra of the maximum assigned peak with accuracy data shown.* ***(b)*** *Putatively assigned structures of the highest mass polycyclic aromatic hydrocarbon assigned from each technique.*

The 3D OrbiSIMS depth profiles acquired on samples were all relatively long (some > 24 h) and therefore a possibility with exposure to a sputtering beam for this time is that some of the observed chemical changes in the profiles are resulting from this sputtering instead of representing real chemical differences. To explore this, we prized an intact piece of the deposit off the injector substrate which could be interrogated on either side with short analysis times. We then performed relatively short (30 scans) 3D OrbiSIMS analyses on the upper and underside of the extracted sample (with three analytical analyses). Application of chemical filtering (molecular formula prediction and plotting double bond equivalence versus carbon number) showed higher maximum masses of PAHs on the underside of the deposit (**Figure 4.4**).

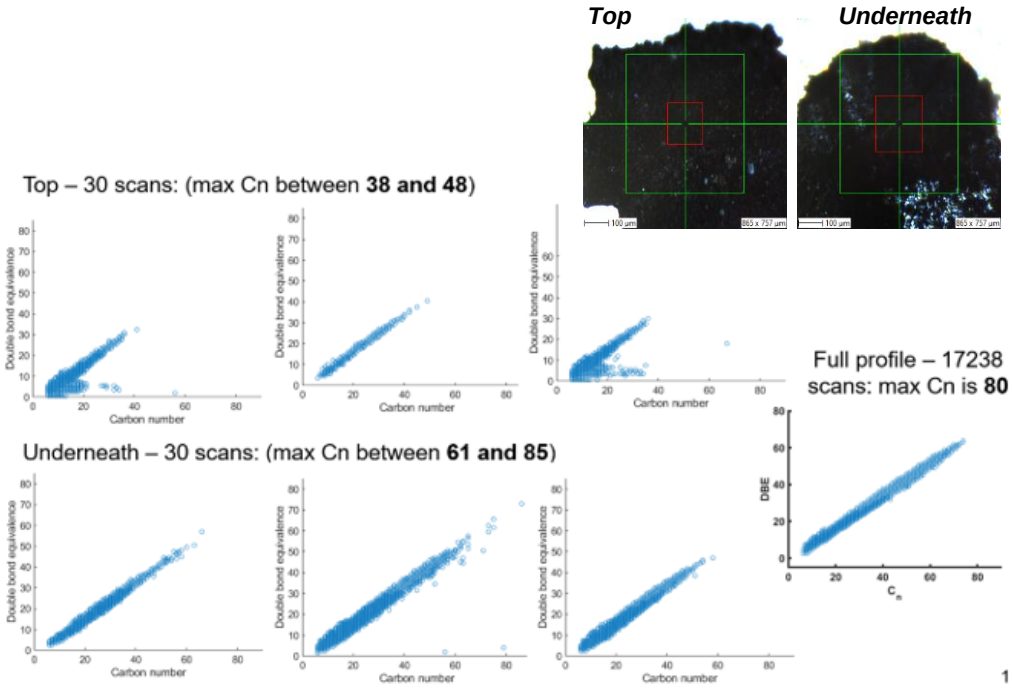


Figure 4.4. *Summary of all species with a formula of $C_nH_n^+$ under 2 ppm error from three analysis areas on the topside and underside of a scraping of deposit from injector tip 2.*

Small PAHs were present on both sides with comparable intensity, medium mass PAHs (up to $C_{42}H_{18}^{+}$) were present on both sides but were less intense on the upper side (spectral data is shown in **Supplementary figure S4.14**). PAHs above $C_{42}H_{18}^{+}$ were only present on the underside. Hence, we are confident that observed chemistries are genuine and not due to the Ar_{3000}^{+} sputtering induced chemical changes to the sample. This agrees with other SIMS studies of organic materials.[195,196] Chemical imaging of injector tip 1, 2 and 3 at the surface and a lower deposit depth after sputtering showed a different lateral distribution of high and low mass PAHs, suggesting they are representative of unique species and not fragments of one another (**Supplementary figure S4.15**). Overall, this demonstrates that molecular differences shown in the depth profile represent true sample chemistry differences and indeed that 3D OrbiSIMS can probe the time resolved growth of insoluble materials formed on a surface.

4.4.2. Formation of aromatic nitrogen species in deposits

In all cases the most intensely ionizing species in 3D OrbiSIMS spectra were those containing 1 N-atom. Despite crude oil containing quinolines and carbazoles naturally,[197,198] the level of N in gasoline is restricted to the ppm scale due to poor storage capabilities, adverse reactivities and effects on NOx emissions.[199,200] To accurately assess the quantified depth distribution of N we used XPS with an Ar sputtering beam on deposit 1 and 2 (**Supplementary figure S4.16**). In both cases the level of nitrogen increased in lower layers with a maximum contribution of 4 % in injector deposit 1 (**Figure 4.5a**), with no nitrogen at the surface of the deposit. This suggests it is introduced after initial

deposition of fuel on the injector substrate, hence they are of particular interest in this work.

Intense secondary ions in 3D OrbiSIMS spectra were identified and assigned to nitrogen containing moieties which are summarized in **Figure 4.5b**. Chemical images were used to distinguish them by their spatial distribution (ion data for other samples are in **Supplementary table S4.17**). We first determined that these general moieties explained the significant molecular distributions in deposits using chemical filtering to annotate all species containing CHN_x (where x = 1), finding that deposit 5 had the most secondary ions attributable to this formula (**Supplementary figure S4.18**). In all samples we assigned a range of N-substituted PAHs (N-PAHs) as $[M + H]^+$ ions including benzoquinolines up to $C_{35}H_{18}N^+$ (-0.6 ppm) (**Figure 4.5b**), suggesting addition of up to 10 benzyl units on the heterocyclic core. We performed MS/MS on key ions, results from quinoline ($C_9H_8N^+$) and benzoquinoline ($C_{13}H_{10}N^+$) confirmed the assignment with a loss of $[M - CHN]^+$, characteristic of N-aromatics.[201] Alkylated quinolines secondary ions were identified in all samples up to $C_{43}H_{76}N^+$ (- 0.5 ppm). MS/MS of $C_{11}H_{12}N^+$ and $C_{10}H_{10}N^+$ both showed alkyl and CHN losses (MS/MS data for all N-PAHs are shown in **Supplementary figure S4.19**). Carbazoles were again common and identified up to $C_{28}H_{18}N^+$ (-0.8 ppm) (**Figure 4.5b**), MS/MS of $C_{12}H_{10}N^+$ and $C_{16}H_{12}N^+$ both showed losses of pyridine $[M – CHN]^+$ and ethylene $[M – C_2H_2]^+$ as observed on reference samples.[202] The most intensely ionizing N-containing species in all samples were those with a generic proposed formula of $[C_5H_5N(C_6H_5)(C_nH_{(2n+1)})]^+$ with an alkyl chain length up to $C_{25}H_{51}$ (**Figure 4.5b**). MS/MS of $C_{13}H_{14}N^+$ showed losses corresponding to the

alkyl chain ($[M - CH_3]^+$), pyridine group, and a CH aromatic fragment. Together this data suggests an alkylated phenyl pyridine structure (**Figure 4.5b**) which is structurally equivalent to a biphenyl unit, commonly observed in combustion of pure hydrocarbons.[188]

AP-MALDI using a DHB matrix on deposit 5 (total of 3 analytical repeats) showed that for purely aromatic N-species (quinolines etc.) the maximum masses of assigned ions were within a few carbon numbers. For species with aliphatic components (alkyl phenyl pyridine and alkyl quinolines) there were differences between analytical repeats on different deposit areas (**Supplementary figure S4.20a**). We repeated the experiments using TCNQ matrix and found higher maximum masses for purely aromatic groups compared to DHB. However, for species with an aliphatic component, there was a lower maximum mass (**Supplementary figure S4.20a**). This variation of maximum mass is evidently based on the technique and highlights the importance of matrix selection for different chemical classes (as is typical of this approach). However, in each case the maximum mass of aromatic N species, which is the focus of this work, was within approximately 1 - 3 aromatic rings **Supplementary figure S4.20b**.

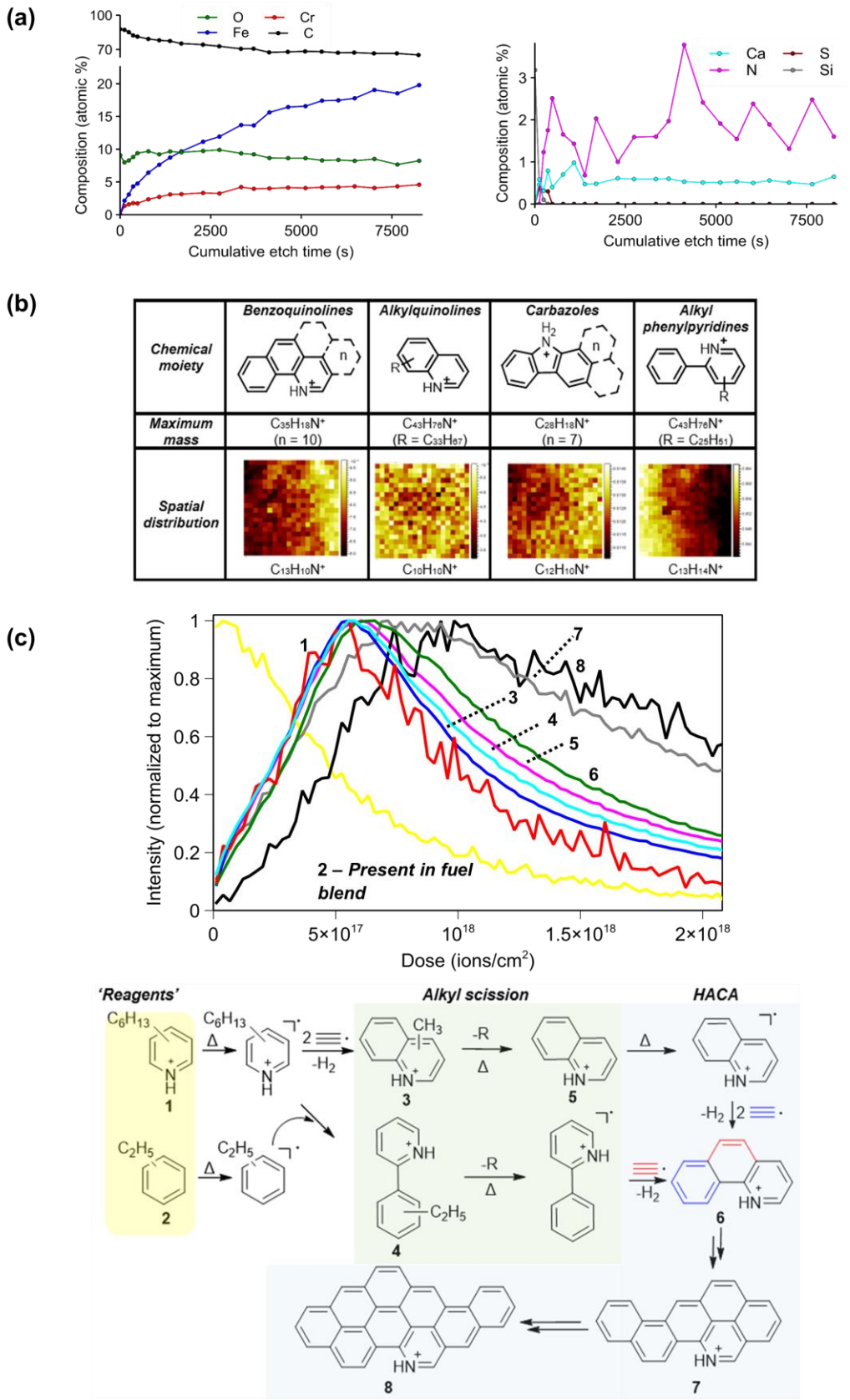


Figure 4.5. Speciation of N-containing species and uncovering possible formation pathways using 3D OrbiSIMS depth profiles of key ions. (a) *X-ray photoelectron*

spectroscopy Ar_{500}^+ depth profiling results from injector tip 2. ***(b)*** *Table detailing general identified compound classes with maximum mass ions error data shown (n denotes the number of fused 6 membered rings on the heterocyclic core, R = saturated alkyl chain). Chemical images (200 x 200 μm) from the surface of the deposit from injector tip 2 of an exemplar ion belonging to each molecular series is displayed with the ion formula shown.* ***(c)*** *Above, 3D OrbiSIMS Ar_{3000}^+ depth profiles (normalized to maximum) of nitrogen containing species, below, a suggested formation pathway that links the species based on their prevalence in the deposit depth. Numbered products are observed and correspond to those in the depth profiles.*

Next, to investigate the origin of N-species we present 3D OrbiSIMS depth profiles of compound classes from deposit tip 2 in **Figure 4.5b**. The spatial distribution of ions captured by chemical imaging enabled us to separate ions into different classes (**Figure 4.5b**). The formation of small N-PAHs species such as quinoline can occur by gas phase reaction of acetylene (C_2H_2·) and pyridyl (C_5H_4N·) radicals in high temperature conditions (700 K).[203,204] Depth profiles and a suggested scheme of these ions correlate with expected prevalence as the 'reactant' alkylated benzyl secondary ion ($C_9H_{13}^+$, **2** in **Figure 4.5c**). These alkylated benzene compounds were present in the initial fuel composition (**Supplementary figure S4.1**). This class of ions in deposits with enough intensity for an informative depth profile (all except injector tips 3 and 4) were present at the uppermost deposit layers. Again, it is important to state we are observing numbered products in the scheme (positive ions) and proposing radical intermediates to form the observed secondary ions. An example alkylated pyridyl ion ($C_{11}H_{18}N^+$, **1** in **Figure 4.5c)** increased in intensity during sputtering, suggesting it is formed after initial deposit initiation and is consistent

with the hypothesis that the origin of N-containing species is from reaction with air after deposit formation initiation and not from the fuel. The reaction of these two can then form the alkyl phenyl pyridine species observed in SIMS data (example shown as **4** in **Figure 4.5c**) and is analogous to the formation of biphenyl species by free radical pyrolysis of 2 benzyl units (which has been well documented[188]). The electron withdrawing nature of the nitrogen can promote reaction at the ortho position on the ring, hence our suggested structure in the scheme ($C_{13}H_{14}N^+$, **4** in **Figure 4.5c**).

Separately, the initial pyridyl ion (**1** in **Figure 4.5c**) can undergo HACA to form alkylated quinolines ($C_{10}H_{10}N^+$, **3** in **Figure 4.5c**); both the alkyl phenyl pyridines and alkyl quinolines were more prevalent in deposit layers lower than the suggested 'reagents'. Quinoline ($C_9H_8N^+$, **5** in **Figure 4.5c**) was prevalent after alkyl quinolines, suggesting that scission of the alkyl chains occurs next. The specific free-radical mechanism of the alkyl scission (- R in **Figure 4.5c**) is complex but generally follows subsequent reduction of carbon chain length to form a radical and an unsaturated species.[143,205,206] The formation of the positive secondary ion observed in the SIMS data likely arises from addition of a proton to the radical on the terminal carbon on the chain. Next, the formation of benzoquinoline, $C_{13}H_{10}N^+$ (**6** in **Figure 4.5c**) can be accessed by HACA from both the quinoline and the alkyl phenyl pyridine ion and had expected depth behavior. Finally, the buildup of larger N-PAHs, exemplified by the ions $C_{23}H_{14}N^+$ and $C_{31}H_{16}N^+$ (**7** and **8**, respectively in **Figure 4.5c**), suggested through HACA, is shown with higher mass aromatics to have prevalence at lower layers which is analogous to PAH growth. This trend was common for all

other injector tip deposits despite different sample provenance (**Supplementary figure S4.21**).

4.4.3. Analysis of thin-film deposits to probe early stages of deposit formation

Thin-film injector needle deposits were retrieved from engine testing and allow us to explore the effect of temperature across the components surface since one end of the needle is closer to the combustion chamber (marked by 'High T' and 'Low T' in **Figure 4.7c**). It has long been thought that these are precursors to the carbonaceous deposits seen in injector tips. We applied chemical filtering to 3D OrbiSIMS depth profile accumulation spectra from the ball (orange box in **Figure 4.7**) on all 8 needle samples, and identified many PAHs, but they were accurately assigned up to a lower maximum mass than the tip deposits for all samples (**Figure 4.6** shows data for injector 2).

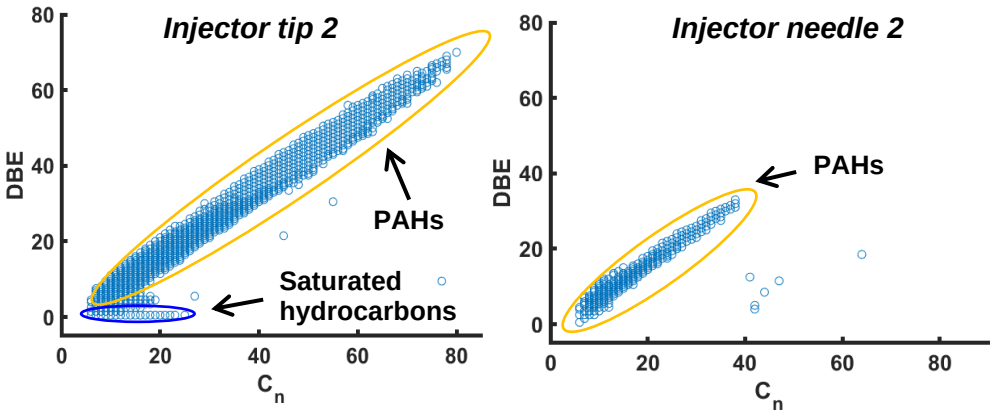


Figure 4.6. *Double bond equivalence plots output from chemical filtering of 3D OrbiSIMS data of injector tip 2 and injector needle 2. In this case searching for all ions with a formula of* $C_nH_n^+$.

The difference in maximum mass between sample types is due to the reduced temperature experienced by this component, showing how the key signpost in assessing deposit severity is the PAH size distribution. To further probe the temperature effect, we performed relatively short (< 200 s) 3D OrbiSIMS analyses on 3 positions along the needle (at different distances to the combustion chamber) on 3 of the samples. The variation in the presence of three example PAHs of varying size are plotted in **Figure 4.7a**.

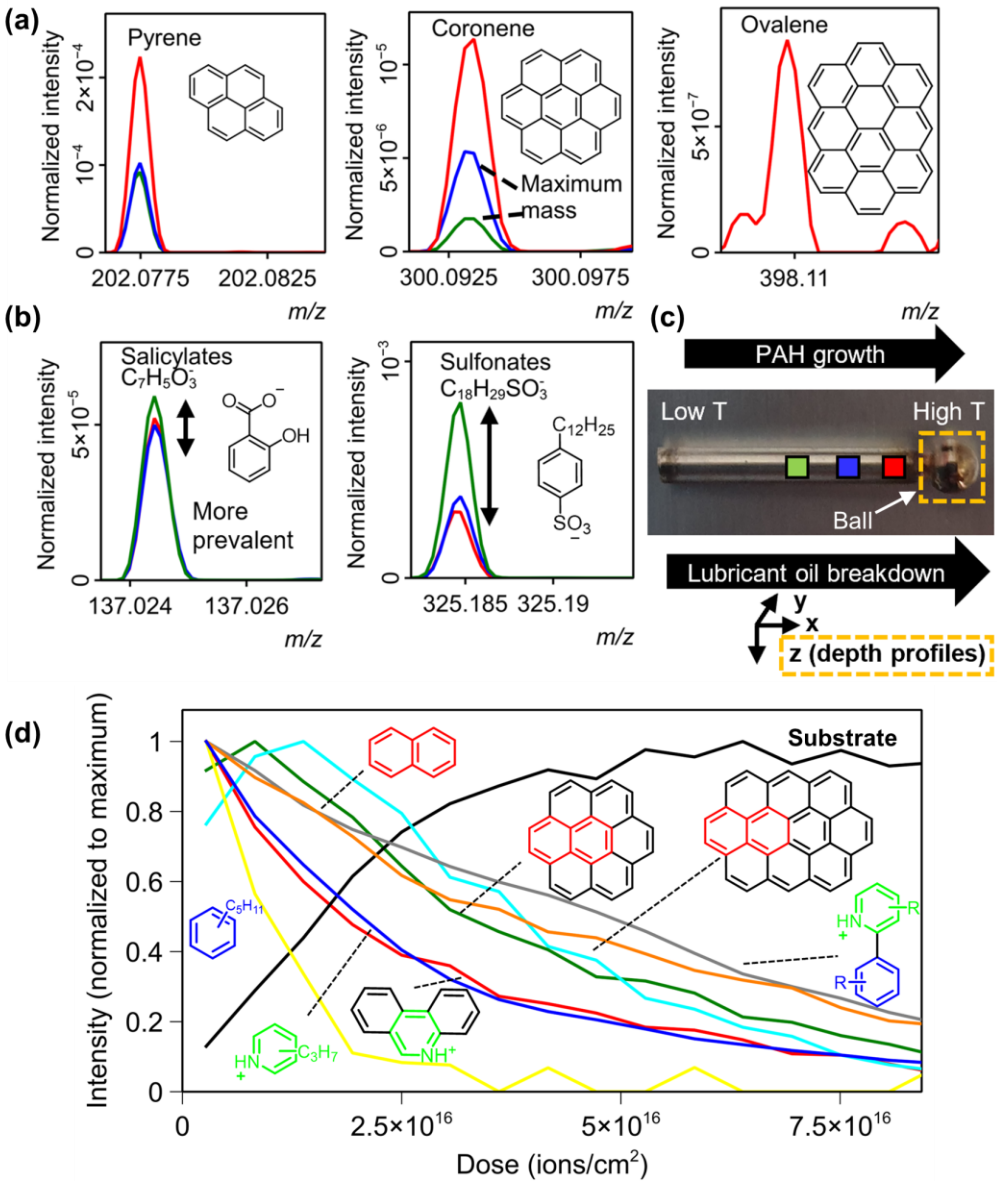


Figure 4.7. Tracking molecular transformations in-situ on a fuel injector needle.

(a) *3D OrbiSIMS depth profile accumulation spectra from different positions along*

injector needle 3 of PAHs, pyrene ($C_{16}H_{10}^{+}$), coronene ($C_{24}H_{12}^{+}$) and ovalene ($C_{32}H_{14}^{+}$) (left to right) intensity and maximum mass at each position. ***(b)*** *Intensities of salicylates ($C_7H_5O_3^{-}$) and sulfonates ($C_{18}H_{29}SO_3^{-}$).* ***(c)*** *Photograph of injector needle 3 with color-coded boxes representing each analysis area (not to scale).* ***(d)*** *Depth profiles from the ball of the injector needle (orange box in* ***c****).*

The intensity of PAHs increased closer to the combustion chamber, as did their maximum mass, for example we observed coronene in each position, whereas ovalene was only identified in position 1 (**Figure 4.7a** and **Supplementary figure S4.24b** for other samples), showing how the effect of temperature can lead to enhanced growth of PAHs across a surface. Depth profiles from the injector ball (orange box in **Figure 4.7c**) of injector needle 3 correlate with those of the injector tip deposits (**Supplementary figure S4.8** for PAHs and **Supplementary figure S4.21** for N-PAHs), where larger PAHs and N-PAHs were more prevalent at lower depths (**Figure 4.7d**). In all cases the maximum mass of N-PAHs were relatively uniform across the surface (**Supplementary figure S4.22**), suggesting their formation is not just tied to temperature and breakdown of fuel. It is plausible that with air being a likely origin of N in the system that access to it is another rate determining step, and in the high-fuel pressure injector needle the scarcity of air makes it the limiting step, conversely to the external deposits with access to 'excess' air.

We accurately identified lubricant oil derived alkyl benzyl sulfonates which were found in previous work,[170] and alkyl salicylates ($[C_7H_5O_3C_nH_{(2n+1)}]^-$). which were confirmed using MS/MS in these systems (**Supplementary figure S4.23**) by observing characteristic neutral losses of -CO, -CO_2 and -OH

functionalities (negative ion details can be found in **Supplementary table S4.4**). Conversely to PAH formation their intensity decreased in positions closer to the combustion chamber (**Figure 4.7b** and **Supplementary figure S4.24a**). Overall, this work has shown how we can map the time resolved growth of aromatic structures and breakdown of other species with an *in-situ* analysis technique and infer possible formation mechanisms. Our repeated identification of the same chemical structures for fuel deposits, regardless of the input fuel in the engine test has significant implications for worldwide efforts to understand deposit formation and mitigate them.

4.5. Chapter 4 conclusions

In this study we comprehensively characterized a range of lab-grown gasoline deposits *in-situ* on engine components which were derived from different fuels using 3D OrbiSIMS accurate mass assignments, MS/MS, AP-MALDI and XPS. This enabled identification of a plethora of species previously unseen in these materials including structurally diverse PAHs and nitrogen containing species such as alkylated quinolines, carbazoles and biphenyl derivatives. We used depth profiling behavior of key species to explain their formation over time by possible formation pathways, following a trend of initial alkyl scission and HACA which explains the growth of large aromatic structures, most notably the growth of flat and curved PAHs to small fullerenes in the engine. We also provide a first-time comparison of 3D OrbiSIMS to AP-MALDI data, demonstrating the presence of similar maximum mass species. Importantly, pathways of deposit formation are shown to be common regardless of the fuel used. Our new insights will contribute to several mitigation strategies, for

example, synthesizing next-generation additives to solubilize deposits, which is particularly viable now we have a far-greater understanding of deposit matrix composition.

4.6. Comments on Chapter 4

The application of a chemical filtering approach (Chapter 3) to 3D OrbiSIMS data was demonstrated here for sample datasets from carbonaceous deposits. However, this is a targeted approach when searching for ions of certain formulae, so care must be taken to consider other possible assignments, particularly for these samples of unknown composition. Nevertheless, the common composition of the carbonaceous matrix, regardless of fueling provenance is a new finding for this field and opens the possibility of a more universal approach to targeting the carbon matrix of deposits by solubilizing additives. The approach of using depth profiles to assess the deposits layer-by-layer to reveal formation pathways is new and is certainly a significant advance for this field. However, we must consider that there are many specific formation pathways possible for these materials and this approach is by no means a measurement of specific intermediates. Nevertheless, the presence or absence of key species may be used to rule in or rule out other mechanisms and will contribute to the picture of how layered deposits are formed. A more detailed study into the formation of deposits could be carried out and is discussed in the final chapter of conclusions and possible future work.

4.7. Chapter 4 materials and methods

4.7.1. Engine testing bed

All gasoline direct injectors were retrieved from a vehicle with a 2.0 Liter turbocharged four-cylinder EcoTech LHU engine produced by General Motors after deliberately causing deposit formation using a dynometer test bed. The engine test was run for 100 h at steady state at 1500 rpm. At the end of the test the injector was removed and replaced, and the test was repeated using a different gasoline fuel and injector set. Images of the test rig are in **Supplementary figure S4.1**.

4.7.2. Fuels

All gasoline fuels were sourced from the USA from retail sources. A summary of the fuel composition from gas chromatography electron ionization mass spectrometry analysis performed on the gasoline fuel prior to the test is given in **Supplementary figure S4.1**. This summarizes the types of compounds present. We also quantified compositional data (wt. %) of each compound class for all samples aside from injector 7 and 8 (see data repository). Injector 7 was run on E10 EEE Lube certification gasoline and injector 8 was run on US 'toptier' E10 retail gasoline. After retrieval, all fuel injectors were disassembled into their constituent parts for analysis, we analyzed deposits *in-situ* on the injector tip and injector needle of each injector set (photographed in **Supplementary figure S4.1**), a total of 16 samples were analyzed from 8 injector sets. Deposits on two types of fuel injector components were interrogated in this work. First, the injector tip, which points into the combustion chamber and experiences high

temperatures. Second, the injector needle, which is housed inside the injector casing, experiencing lower temperatures.

4.7.3. 3D OrbiSIMS

3D OrbiSIMS analysis was conducted using a Hybrid SIMS instrument (IONTOF, GmbH) with the technique outlined by Passarelli *et al*.[121] Secondary ions were collected using the Q Exactive HF Orbitrap mass analyzer (with a mass resolving power of 240,000 at *m/z* 200) that was calibrated using Bi_3^+ clusters to produce secondary ions from a silver strip prior to all sample measurements. In each case a 20 keV Ar_{3000}^+ gas cluster ion analysis beam was used, which was defocused to 20 μm with a cycle time of 200 μs, duty cycle of 4.4 % using a target current between 0.2 and 0.3 nA, depending on the sample. Charge compensation was achieved with a low energy electron flood gun (21 V) and by regulation of the main chamber with argon gas (9×10^{-7} mbar) to delocalize any accumulation of charge surrounding the sample. A flow of pressurized nitrogen was fed to the Orbitrap™ at 12 bar. Sample data was collected over a mass range of *m/z* 75 – 1125 using SurfaceLab software (version 7.1.c (IONTOF GmbH)), with the application programming interface provided by Thermo Fisher for control of the Orbitrap MS portion of the instrument. Data processing was performed using SurfaceLab Version 7.1.c (IONTOF GmbH). On all samples, profiles were taken from different areas for each polarity. We chose areas as close to each other as possible without overlapping craters. Sample specific parameters such as analysis areas and times, total ion doses and raster mode for depth profiling and imaging experiments on all samples are tabulated in **Supplementary table S4.2**.

Instrumental parameters used in single beam depth profiles which afforded the highest overall normalized secondary ion intensity of positively ionizing species were first determined after repeated depth profiles on injector tip 3. Here, depth profiles were performed in the same area, using short analysis times (< 10 s) to allow comparison of sequential datasets without analyzing significantly different chemistries of the deposit. A summary of this work can be found in **Supplementary figure S4.3**. Settings which afforded both the highest normalized ion intensity (to the total ion count) and speciation of molecular peaks were using the Ar_{3000}^{+} primary ion beam at an incident energy of 20 keV with argon flooding of the main chamber to give a pressure of 9×10^{-7} mbar, a nitrogen flow pressure to the Orbitrap^{TM} analyser of 12 bar and a flood gun energy of 21 eV. Analysis on injector tip samples were performed in areas with high levels of carbonaceous deposit formation which yielded the highest level of secondary ion counts (determined in instrument set-up). Injector needles deposits on the 'ball' were analyzed on all internal samples, this part is closest to the combustion chamber (**Supplementary figure S4.1**). Three extra positions were analyzed on injector needle 1, 2 and 3 in positions subsequently further away from the combustion chamber. In all cases the apex of the injector component was analyzed and was accessed by rotating the sample holder to reveal a 'new' apex for positive and negative polarity analysis.

Combined chemical imaging and depth profiling experiments were carried out on injector tips 1, 2 & 3 using the same settings as single beam depth profiles. Chemical imaging was performed using an Ar_{3000}^{+} analysis beam in random

raster over a 300 μm^2 area with a non-interlaced border. Acquisition times and resolution are detailed in **Supplementary table S4.2.** Secondary ion images were then cropped to 200 x 200 μm, normalized to the total ion image, and scaled to match the intensity at both depths. MS/MS spectra were all acquired over an analysis time between 10 s and 50 s in an area of 300 μm^2 using sawtooth raster mode. Mass windows were between 1 u and 10 u and normalized collision energies were between 10 eV and 100 eV depending on the isolated ion.

4.7.4. Chemical filtering

SIMS-MFP version 1.1 (molecular formula prediction) software (MATLAB 2021A) was used to assign species based on elemental compositions – this is an in-house software package described in previous work by this group.[185] The software takes an inputted data file (either a spectra output after a peak search or a depth profile dataset) and the user simply inserts the elemental constraints (type and number of each element) they wish to apply to the search. SIMS-MFP then assigns species which fit under the pre-defined deviation (2 ppm here) and plots the carbon number versus the double bond equivalence value of each possible assignment. Here spectra outputs were used after applying a peak search using SurfaceLab software (IONTOF, GmbH). Elemental constraints used in the search are detailed in the manuscript.

4.7.5. AP-MALDI

10 mg of the deposits were weighed after scraping it off the injector tip substrate using a scalpel. This was suspended in 1 ml of tetrahydrofuran (THF) and diluted further to create a 1 mg/ml concentration. A 0.5 μL drop was spotted onto an

ABI Opti-TOF 192-well target plate and on top of this spot (once dried for 10 minutes) a 1 μL of 2,5-dihydroxybenzoic acid (DHB) or tetracyanoquinodimethane (TCNQ) (depending on the experiment) matrix was added, at a concentration of 5 mg/ml in THF. A Q Exactive Plus hybrid quadrupole-Orbitrap mass spectrometer (Thermo Scientific, San Jose, USA) was coupled to an AP-MALDI source (MassTech Inc., Columbia, MD). Target-ng software (MassTech) was used to control the XY stage motion and operation of the laser. The source utilized a diode-pumped solid-state Nd:YAG laser (λ = 355 nm) operating at a 0.1−10 kHz repetition rate. Maximum laser pulse energy was 3 μJ at a 1 kHz repetition rate. A beam attenuator was used to adjust laser energy. The voltage applied between the MALDI plate and inlet capillary of mass spectrometer was 4 kV. The distance between the plate and the capillary was 3 mm. The inlet capillary was set to 400 °C.[207] Each dried-droplet spot was scanned with a 50 μm wide laser spot. Mass spectra were acquired in a positive-ion mode with mass resolving power up to 180,000 at *m/z* 200 and a mass range of *m/z* 150−1500. Tandem MS parameters were the following: mass resolving power: 15000; max injection time: 200 ms; AGC target was switched on: isolation width: 1 Da; HCD: 20 (normalized collision energy, NCE). Data was acquired and analyzed using Tune and Xcalibur software (Thermo Fisher Scientific, Waltham, MA). Specie identification was carried out in Xcalibur 3.1 software with a 6-ppm mass accuracy threshold. In all cases 3 analytical repeats were taken on different areas of the sample spot.

4.7.6. XPS

We present data from X-ray photoelectron spectroscopy (XPS) in conjunction with an argon gas cluster ion beam etching of deposit 1 and 2. Samples were mounted on a standard Kratos sample bar (13 cm × 1.5 cm) using double-sided adhesive non-conducting tape. Samples were then subjected to XPS analysis using the Kratos AXIS ULTRA DLD liquid phase photoelectron spectrometer with a monochromated Al Kα X-ray source (1486.6 eV) with a source power of 120 W. Gas cluster ion beam etching (20 keV, Ar_{500}^{+} cluster beam) over etch area of 0.75 mm^2 on the injector tip deposit was performed prior to analysis for a cumulative etch time of 2787 s for Injector tip 1 and 8253 s for Injector tip 2. Spectra were acquired with the Kratos VISION II software. Low-resolution survey spectra of both samples were recorded between a binding energy range of 1200 to −5 eV, a charge neutralizer filament was used to prevent surface charging; the pass energy was 160 eV, both with a step energy of 1 eV. The spectra were charge corrected to the surface C 1s peak (adventitious carbon) set to 285 eV and used to estimate the total atomic % of the detected elements using CasaXPS (version 2.3.22 PR1.0) software. Peak positions were referenced to the XPS reference pages of XPSFitting.

4.7.7. Miscellaneous

Chemical structures were drawn in ChemDraw 14.0. Graphs were plotted in Veusz (Version 3.2.1, Jeremy Sanders) or were exported from SurfaceLab (version 7.1).

Chapter 5

Concluding Remarks and Future Perspectives

5.1. Concluding remarks

The aim of this research project has been to further understand the nature of engine deposits through providing a comprehensive characterisation using high resolution mass spectrometry techniques. Previous work, summarized as a literature review in Chapter 1, has been limited at providing a generic picture of deposit composition, only showing either elemental or basic functional group information. Thus, it has been difficult for researchers to understand the origin of contributing species, particularly of the deposit's carbonaceous matrix. To make more confirmed assignments of deposit contributors, molecular information needed to be obtained.

In Chapter 2, 3D OrbiSIMS argon GCIB depth profiling and chemical imaging was applied for the first time to gasoline and diesel samples from 'real-world' vehicles, which could ascribe the origin of whole molecules in deposits at all depths and separate them into molecular classes by using chemical imaging. Species never seen previously were identified and their specific origin was ascribed, including lubricating oil derived alkyl sulfonates and fuel derived PAHs, along with the first application of MS/MS on these ions. Quantified elemental data from XPS showed us that PAHs were a significant contributor in gasoline deposits, but diesel deposits had more an inorganic contribution. The

presence of N above levels expected in fuel mixtures was a surprising result, which was probed later. We also showed that PAH maximum size was linked to components with higher temperatures.

Furthermore, a novel workflow for filtering 3D OrbiSIMS datasets using molecular formula prediction and structural double bond equivalence measures was developed and described in Chapter 3. Application to a series of sample types from key areas of SIMS research showed its value by reducing the volume of data, which allowed new insight into sample chemistry and yielded improved results from MVA with respect to separation of datasets from the deposits. This workflow is currently being applied to datasets across multiple fields.

Lastly, in Chapter 4, we applied 3D OrbiSIMS and XPS depth profiling and chemical filtering to deposits which had been grown in a controlled engine testing rig to further probe the relationship between fuel type and composition. Both approaches enabled a comprehensive characterisation of the bulk carbonaceous matrix. Importantly we used depth profiles to track molecular changes as a function of deposit depth (*i.e.*, time in the engine). This unveiled common molecular trends in all samples, namely the growth of PAHs and their N-substituted derivatives. This important finding was validated by analyzing the top and underside of a 'chip' of deposit and for the first time showed how PAHs can grow to larger ring sizes in engine deposits. Chapter 4 also showcased several key new validation experiments too. Key 3D OrbiSIMS parameters were altered when analyzing a deposit and, finding that the 20 keV Ar_{3000}^{+} settings used throughout the work were optimal for liberating intact molecules of

interest. We confirmed that the large PAHs seen in deposits were genuine and not the effect of GCIB etching on the deposit, a result which will be of significance for researchers using large gas cluster ion beams in other areas of research. Thirdly, we showed that 3D OrbiSIMS yielded ions comparable in maximum mass to that from other MS techniques including AP-MALDI.

Overall, it has been possible to develop and apply a methodology to unveil the composition of deposits at a molecular level, discern the origin of contributing species and gain new insight into how carbonaceous deposits grow in engines regardless of the fuel used to generate it. Thus, meeting the aim and objectives of the project (**Chapter 1, Section 1.7**). Combined efforts to understand deposit composition, origin and mechanisms from our work and others will help global efforts to reduce their impacts by developing targeted additives capable of dissolving their carbonaceous matrix, or by disrupting their formation, or by altering fuel specifications to remove/reduce the content of deposit formation 'initiators' once their formation is better understood. This will help reduce global vehicle emissions, improve air and environmental quality and have positive effects for human health.

5.2. Future perspectives

The fuel and additive industries are constantly evolving with legislation, leading to changes to fuel blends, such as the recent increased inclusion of ethanol to UK sold gasoline. This change will lead to changing deposit composition and deposit formation processes. To keep updated with any possible compositional changes, a suitable screening process will need to be used. This could involve

the 3D OrbiSIMS methods developed in this work, but others are possible. Linking of ToF-SIMS data to 3D OrbiSIMS data by comparing observed peaks could be achieved if we analyzed the same set of deposits and identified common markers. In addition, recent work by the group developed a rotating stage for bullets where ToF-SIMS imaging creates a map of the cylindrical surface,[208] which could be used to create a large map of the deposits surface to relate topography to 3D OrbiSIMS spectral data on regions of interest. This has merit as a ToF-SIMS method is a more 'accessible' technique to researchers than 3D OrbiSIMS.

Further development of the chemical filtering process developed could be seen if we are able to integrate it to principal component analysis, allowing an unsupervised comparison of filtered lists of ions across multiple samples. This is being investigated at the University of Nottingham currently. The significant amount of data from biological samples, even with the filtering steps, is still challenging to make large protein assignments too. Future work may see the integration of existing chemical databases outside those explored here to further validate assignments.

Our insight into a possible common formation pathway of deposits could be further explored by several experiments. Firstly, the use of an experimental rig to generate deposits with fuel doped with ^{13}C labelled compounds, such as toluene, which would enable tracking of the fate of species more accurately as deposit formation occurs. A detailed ^{13}C nuclear magnetic resonance spectroscopy study (either in solvent phase or in the solid-state) may give insight

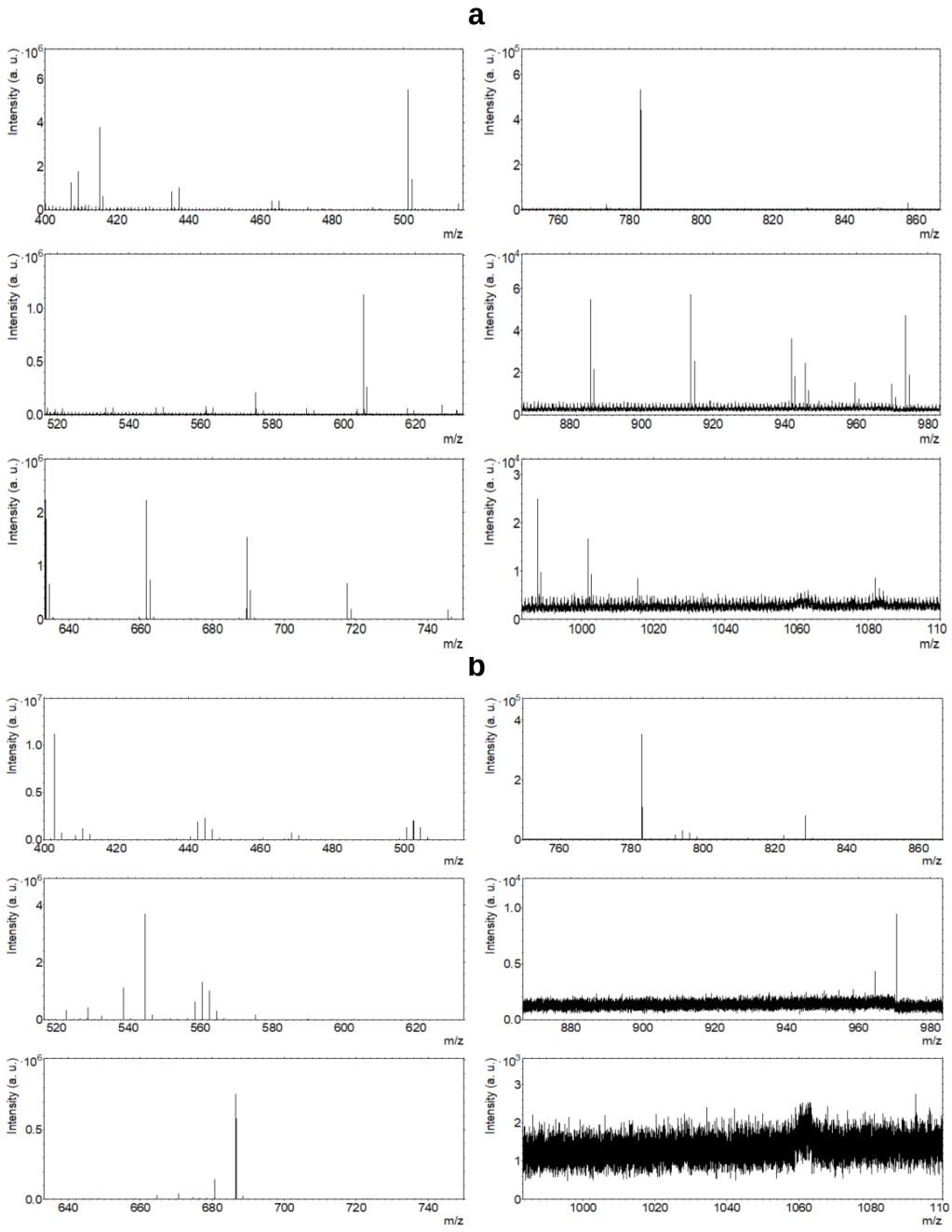
into the specific mechanism of deposit formation. A similar approach could be to reflux a mixture of gasoline and aluminium pieces, followed by analysis of the residual gasoline and aluminium surface at specific time points, which may yield more detailed mechanistic information at specific temperatures.

Chapter 6

Supporting Information for Results Chapters

6.1. Chapter 2 supporting information

6.1.1. Supporting information for part one



c

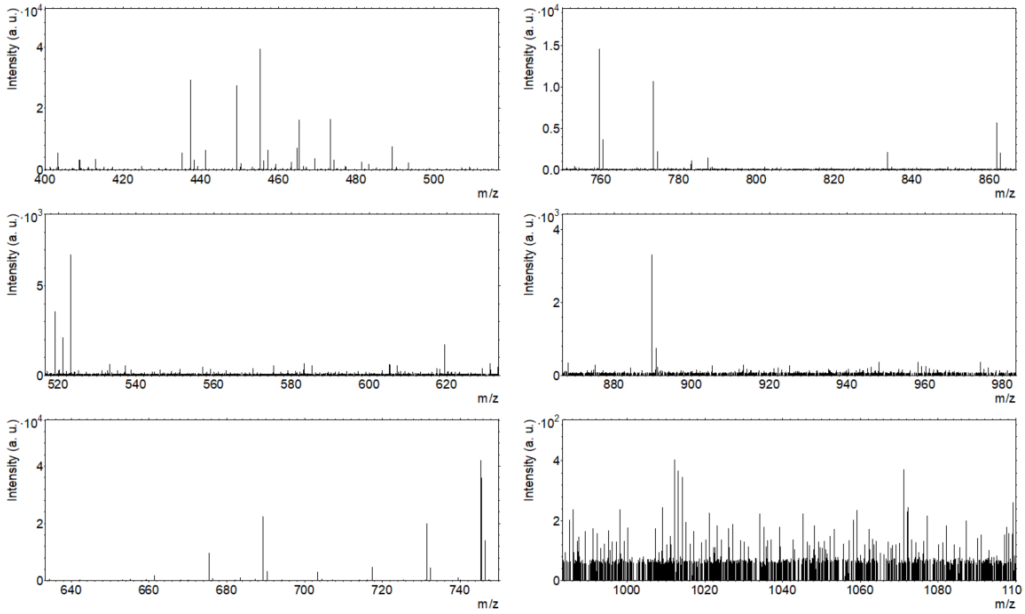
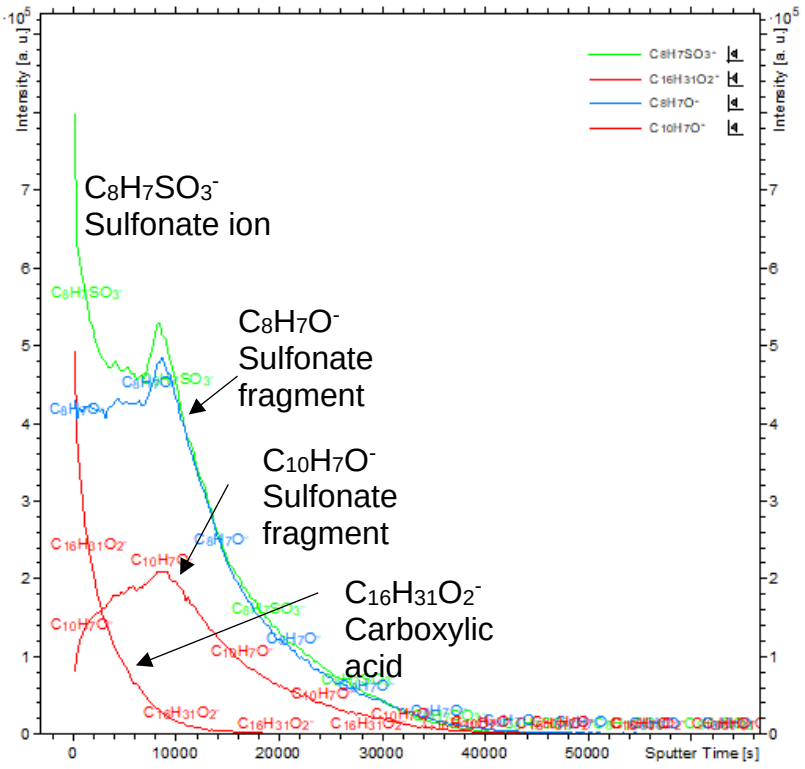


Figure S2.1.1. 3D OrbiSIMS negative ion spectra over six mass ranges for each sample in the range of m/z 400-1100 for each sample. ***a)*** *gasoline injector deposit,* ***b)*** *diesel injector deposit,* ***c)*** *diesel filter deposit. Acquired from SL7 software. AU, arbitrary units.*

a



b

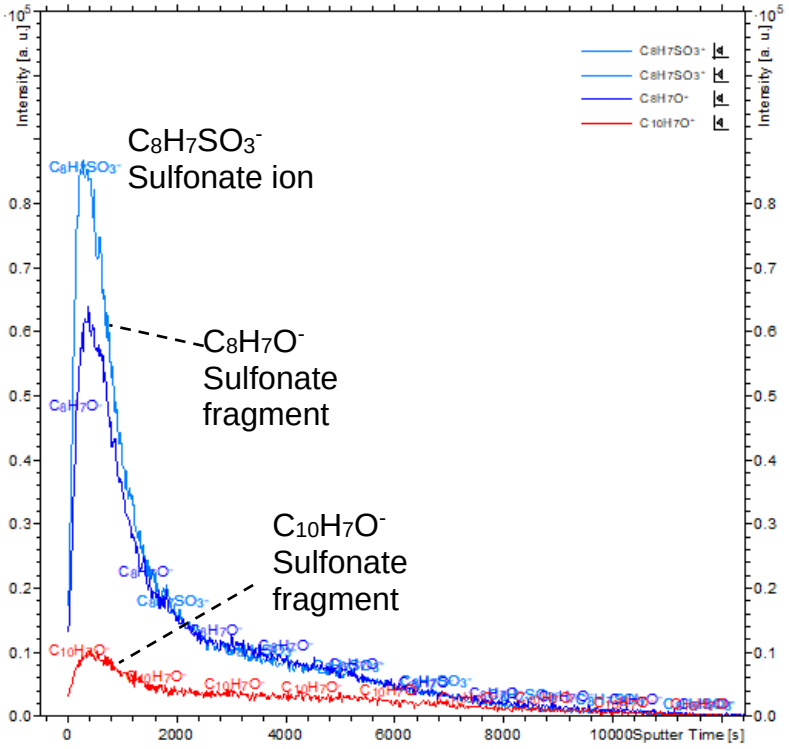


Figure S2.1.2. 3D OrbiSIMS depth profiles comparing depth behavior of carboxylic acids, sulfonates, and related secondary ion fragments*. **a)** gasoline injector deposit, **b)** diesel injector deposit. AU, arbitrary units.*

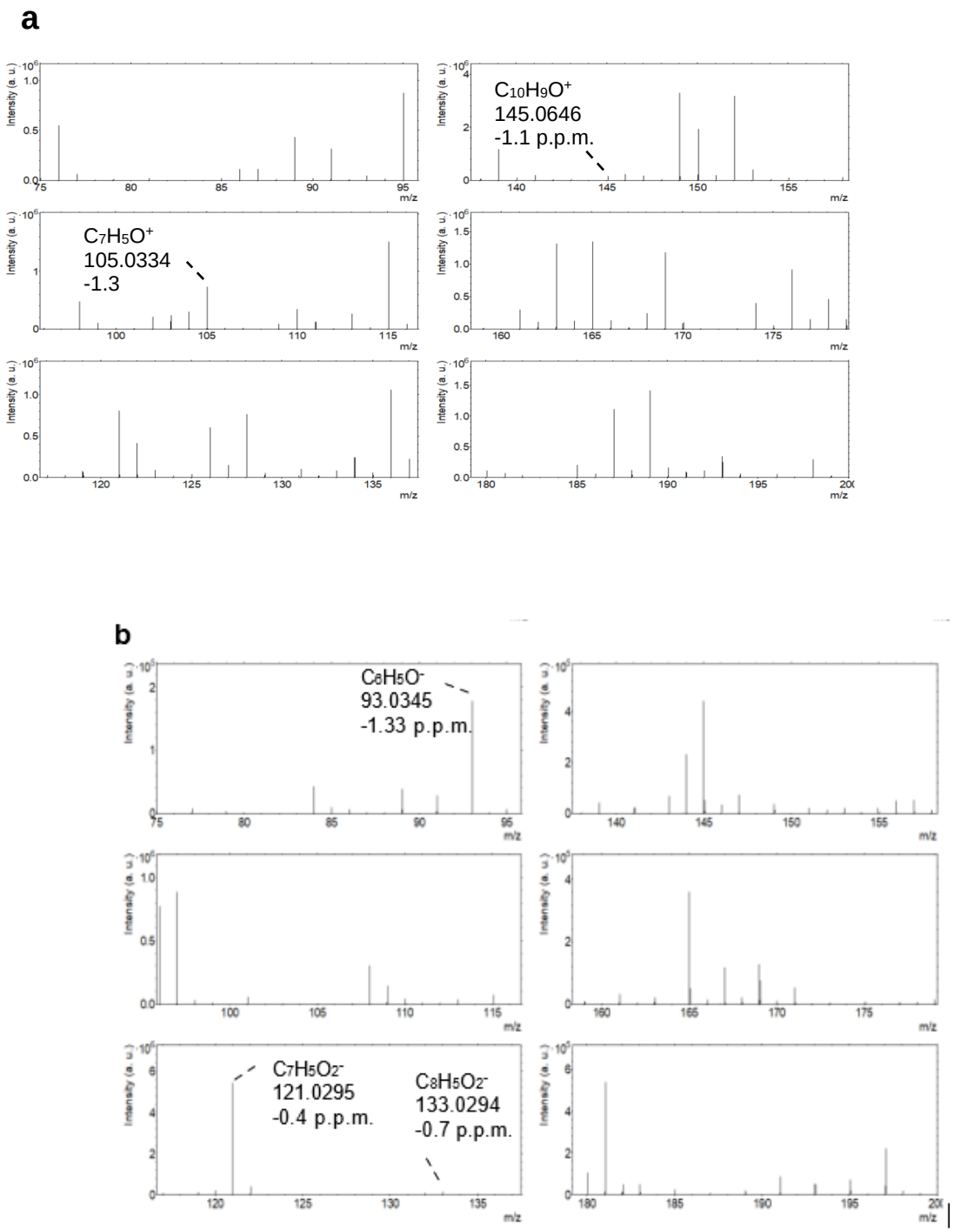
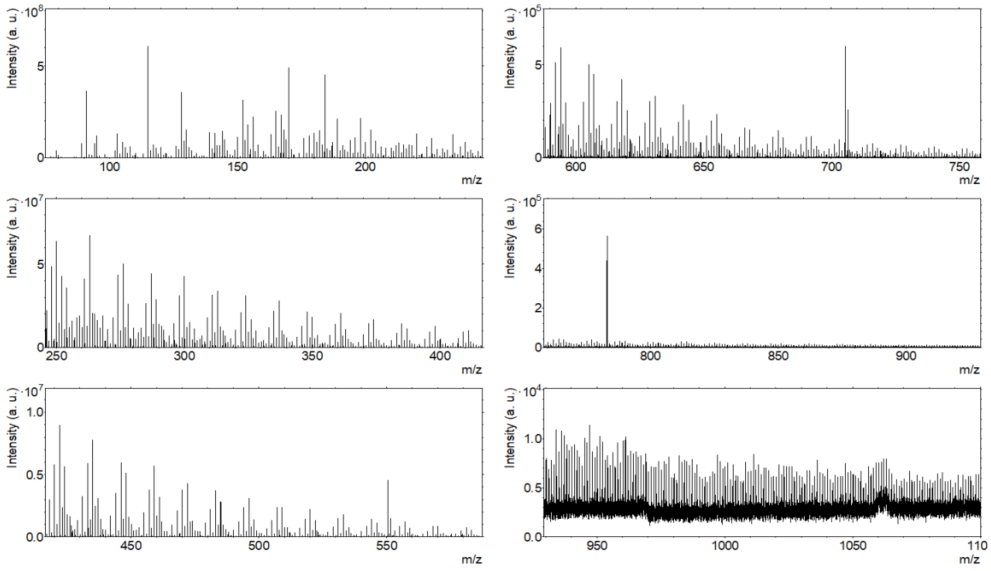
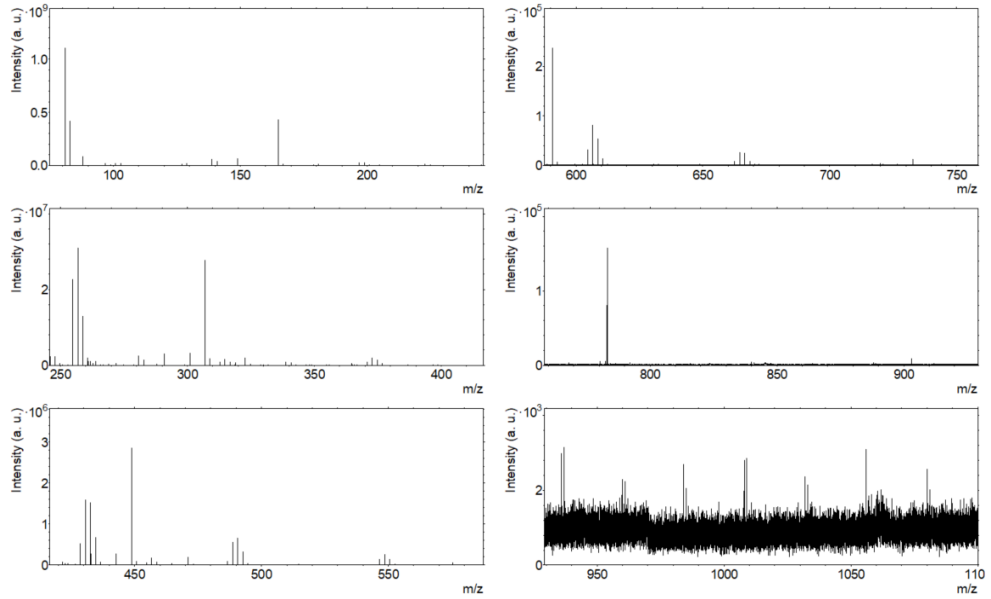


Figure S2.1.3. 3D OrbiSIMS negative ion spectra obtained from a blank diesel fuel filter medium and assignments for oxygenated ions that were also found in the deposit*. **a)** positive ions, **b)** negative ions. AU, arbitrary units.*

a



b



c

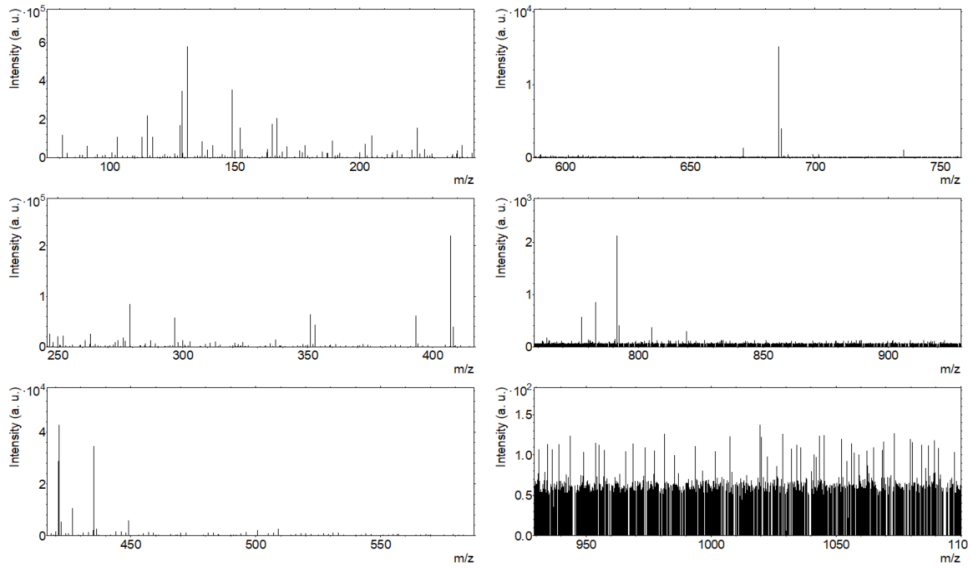


Figure S2.1.4. 3D OrbiSIMS positive ion spectra over six mass ranges between m/z 75 and 1100 for each sample. a) *gasoline injector deposit,* ***b)*** *diesel injector deposit,* ***c)*** *diesel filter deposit. Acquired from SL7 software. AU, arbitrary units.*

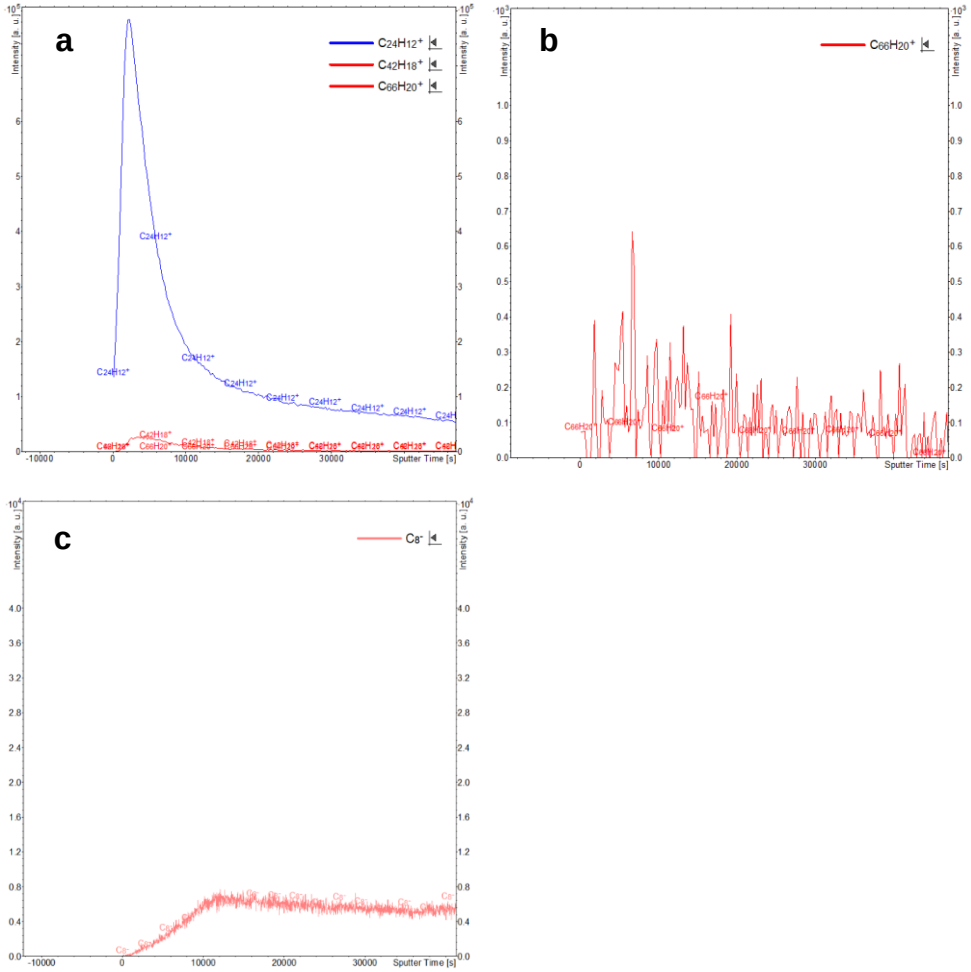


Figure S2.1.5. 3D OrbiSIMS depth profiles of PAHs and a carbonaceous ion. *a) Behavior of $C_{24}H_{12}^{+}$, $C_{42}H_{18}^{+}$, b) Zoomed in view of the $C_{66}H_{20}^{+}$, profile. All PAHs showed a decrease in intensity by 10,000s, c) Behavior of the C_8^{-} ion, showing maximum intensity at 11,000 s. AU, arbitrary units.*

Table S2.1.1. 3D OrbiSIMS ion table for ions identified in deposit samples*. Detailing peak assignment, observed mass, mass error, (deviation from expected mass) (p.p.m.) and peak area normalized to the total ion count (AU). Above, negative ions. Below, positive ions.*

	Gasoline injector deposit			Diesel injector deposit			Diesel filter deposit		
Molecular formula	**Centre Mass (u)**	**Mass Error (ppm)**	**Normalized Area (Intensity)**	**Centre Mass (u)**	**Mass Error (ppm)**	**Normalized Area (Intensity)**	**Centre Mass (u)**	**Mass Error (ppm)**	**Normalized Area (Intensity)**
Sulfonate									
SO_3^-	79.9571	-3.3661	5.61E-03	79.9570	-4.3219	9.39E-03	79.9571	-3.5102	1.53E-02
$CaSO_4H^-$	136.9227	-0.1462	1.24E-05	136.9925	-1.6121	1.69E-04	325.1841	-0.5207	8.87E-03
$C_8H_7O^-$	119.0502	0.0540	6.97E-03	119.0501	-1.3345	5.29E-04	119.0502	-0.2088	3.94E-02
$C_8H_7SO_3^-$	183.0121	0.0259	7.99E-03	183.0119	-1.2054	6.1E-04	183.0121	-0.2243	5.16E-02
$C_{16}H_{25}SO_3^-$	297.1532	0.5748	9.83E-05	297.1528	-0.4896	1.17E-05	297.1529	-0.4055	2.28E-03
$C_{17}H_{27}SO_3^-$	311.1689	0.9427	8.20E-04	311.1686	-0.0669	3.68E-05	311.1686	-0.0272	8.39E-03
$C_{18}H_{29}SO_3^-$	325.1844	0.2259	9.59E-04	325.1841	-0.6406	2.43E-05	325.1841	-0.5207	8.87E-03
$C_{22}H_{37}SO_3^-$	381.2470	0.1638	5.06E-04	-	-	-	-	-	-
$C_{38}H_{69}SO_3^-$	605.4977	0.7499	2.88E-04	-	-	-	-	-	-
$C_{42}H_{77}SO_3^-$	661.5604	0.7274	5.68E-04	-	-	-	-	-	-
$C_{44}H_{81}SO_3^-$	689.5915	1.2757	3.96E-04	-	-	-	-	-	-
$C_{50}H_{93}SO_3^-$	773.8650	-0.0968	7.01E-06	-	-	-	-	-	-
$C_{60}H_{113}SO_3^-$	913.8418	0.8013	1.44E-05	-	-	-	-	-	-
$C_{66}H_{125}SO_3^-$	997.9360	04829	1.83E-06	-	-	-	-	-	-
$C_{74}H_{141}SO_3^-$	1110.062	0.2444	6.05E-06	-	-	-	-	-	-
Carboxylic acid									
$C_{16}H_{31}O_2^-$	255.2333	1.4979	1.23E-03	-	-	-	255.2331	0.4641	1.22E-03
$C_{18}H_{35}O_2^-$	283.2646	1.1721	1.63E-03	-	-	-	283.2643	0.0819	2.46E-03
Carbonaceous									
C_8^-	96.0004	-1.5064	1.24E-02	96.0003	-2.2993	6.18E-03	96.0004	-1.5064	4.24E-02
C_9^-	108.0005	-0.3280	4.75E-03	108.0004	-1.0548	3.43E-03	108.0005	-0.3280	1.70E-02
C_{12}^-	144.0004	-0.8713	8.61E-03	144.0003	-1.5423	2.55E-03	144.0004	-0.8713	2.00E-02
C_{14}^-	168.0005	-0.4846	5.73E-04	168.0004	-1.1527	1.92E-04	168.0005	-0.4846	2.15E-03
Succinimide									
$C_4H_2NO_2^-$	96.0091	-0.4019	2.12E-05	96.0089	-2.4077	1.04E-03	96.0090	-0.6892	3.11E-04
$C_5H_4NO_2^-$	110.0248	0.6161	3.03E-04	110.0247	-0.9008	3.83E-04	110.0248	0.3593	2.44E-04
$C_6H_6NO_2^-$	124.0404	-0.0421	1.52E-04	124.0402	-1.4917	1.56E-04	124.0403	-0.4358	3.50E-05
$C_{12}H_{10}NO_2^-$	200.0718	0.5052	3.51E-04	200.0716	-0.7149	1.13E-05	200.0717	-0.0514	4.43E-05
$C_{12}H_{16}NO_2^-$	206.1187	0.1174	1.94E-06	206.1185	-0.6607	5.98E-07	206.1186	-0.4935	1.05E-05
Inorganic salts									
$NaCl_2^-$	-	-	-	92.9278	-2.5524	2.81E-01	150.8866	-0.5693	2.83E-04
$Na(NO_2)_2^-$	-	-	-	114.9760	-0.8519	4.10E-05	-	-	-
$NaSO_4^-$	-	-	-	118.9419	-1.2279	8.19E-03	92.9279	-1.4328	1.13E-02
$Na_2Cl_3^-$	-	-	-	150.8865	-1.1247	1.34E-02	118.9420	-0.2258	2.82E-04
$Na_3Cl_4^-$	-	-	-	208.8451	-0.6333	3.10E-03	208.8453	-0.0184	4.61E-05
$Na_3S_2O_8^-$	-	-	-	260.8734	0.4695	1.25E-02	260.8734	0.3674	1.23E-03

Blank filter medium									
$C_6H_5O^-$	-	-	-	-	-	-	93.0345	-1.3340	2.38E-03
$C_7H_5O_2^-$	-	-	-	-	-	-	121.0295	-0.2594	1.64E-02
$C_8H_5O_2^-$	-	-	-	-	-	-	133.0294	-0.5764	3.44E-04

	Gasoline injector deposit			**Diesel injector deposit**			**Diesel filter deposit**		
Molecular formula	**Centre Mass (u)**	**Mass Error (ppm)**	**Normalized Area (Intensity)**	**Centre Mass (u)**	**Mass Error (ppm)**	**Normalized Area (Intensity)**	**Centre Mass (u)**	**Mass Error (ppm)**	**Normalized Area (Intensity)**
Polycyclic aromatic hydrocarbon									
$C_{24}H_{12}^+$	300.0933	-0.0132	2.22E-03	300.0933	-0.3329	2.25E-06	300.0930	-1.0109	1.43E-03
$C_{42}H_{18}^+$	522.1404	0.2396	6.72E-05	-	-	-	522.1395	-1.6303	6.95E-05
$C_{66}H_{20}^+$	812.1561	0.1713	1.67E-06	-	-	-	-	-	-
Inorganic salt									
Na_2CNO^+	-	-	-	87.9772	2.1036	2.53E-02	-	-	-
$Na_3H_2O_2^+$	-	-	-	102.9743	0.2168	7.12E-03	102.9742	-0.7502	1.27E-02
$Na_4O_3H_3^+$	-	-	-	142.9666	-1.2771	4.75E-04	142.9666	-0.9468	3.92E-04
$Na_3SO_3^+$	-	-	-	148.9254	-1.0591	1.96E-02	148.9254	-0.9459	3.34E-03
$Na_3CO_3^+$	-	-	-	128.9534	-0.7951	6.35E-03	128.9533	-1.3990	3.74E-02
$Na_3(CNO)_2^+$	-	-	-	152.9645	-1.6015	8.45E-06	-	-	-
Blank filter medium									
$C_7H_5O^+$	-	-	-	-	-	-	105.0334	-0.7123	1.19E-05
$C_{10}H_9O^+$	-	-	-	-	-	-	145.0646	-1.1054	5.91E-05

Table S2.1.2. MS/MS ion table of the high mass sulfonate ion at m/z 661.5957. *Detailing peak assignment, observed mass, mass deviation from expected mass (p.p.m.) and peak area (intensity).*

Molecular formula	**Centre mass (u)**	**Mass error (ppm)**	**Area (Intensity)**
SO_3^-	79.9570	-4.1391	9.83E+03
SO_4H^-	96.9600	-1.0320	3.98E+04
$C_8H_7SO_3^-$	183.0121	-0.4485	1.29E+04
$C_{24}H_{39}SO_3^-$	407.2624	-0.3044	8.52E+04
$C_{26}H_{43}SO_3^-$	435.2937	-0.3834	1.17E+05
$C_{28}H_{47}SO_3^-$	463.3252	0.1412	7.85E+04

Table S2.1.3. Subsurface XPS results. *Detailing at. % (2 d.p.) and errors (st.dev.) for elements found in the deposit samples. Errors calculated using a Monte Carlo simulation with CasaXPS software.*

	Gasoline injector deposit		Diesel injector deposit		Diesel filter deposit	
Peak	**at. %**	**st.dev.**	**at. %**	**st.dev.**	**at. %**	**st.dev.**
C 1s	85.48	0.45	51.82	0.49	81.48	0.37
O 1s	8.31	0.22	16.16	0.41	13.47	0.23
N 1s	1.24	0.36	8.50	0.41	2.08	0.29
Na 1s	0	0	16.39	0.23	1.52	0.06
Cl 2p	0	0	6.47	0.13	0	0
S 2p	0	0	0.53	0.08	0	0
Ca 2p	0.31	0.12	0.13	0.07	0.99	0.14
Si 2p	0	0	0	0	0.47	0.15
Fe 2p	3.08	0.19	0	0	0	0
Cr 2p	1.58	0.16	0	0	0	0

6.1.2. Chapter 2 Part 2 supporting information

Table S2.2.1. *3D OrbiSIMS spectral data from injector tip deposit 2 and the injector needle deposit*

Injector tip deposit			
Center Mass (*m/z*)	**Assignment**	**Mass deviation (ppm)**	**Peak area (AU)**
79.957067	SO_3-	-3.70744	294407274.5
92.927895	$NaCl_2$-	-1.385249	66728.22
96.000394	C_8-	-1.612967	2476056959
96.959992	SO_4H-	-1.145556	483097791.8
N/A	CuCl-	NOT PRESENT	
99.925747	CrO_3-	-0.576939	2089209.86
121.008291	$C_{10}H$-	-0.685133	843439669.5
144.000407	C_{12}-	-0.982304	885052473
145.008256	$C_{12}H$-	-0.808359	577501322.2
160.841935	$FeCl_3$-	-0.707965	10637.47
168.000412	C_{14}-	-0.812636	94337288.81
180.000455	C_{15}-	-0.518602	39054629.71
183.012084	$C_8H_7SO_3$-	-0.298697	71499254.56
204.000385	C_{17}-	-0.802696	110276467.3
228.000498	C_{19}-	-0.223328	36870452.13
229.00838	$C_{19}H$-	0.028317	8179214.59
240.000532	C_{20}-	-0.068567	7692389.01
255.233092	$C_{16}H_{31}O_2$-	0.539951	1829649.95
283.264347	$C_{18}H_{35}O_2$-	0.32756	1886796.86
325.184309	$C_{18}H_{29}SO_3$-	0.062801	10578874.62

339.199883	$C_{19}H_{31}SO_3$-	-0.166396	5372771.93
437.309584	$C_{26}H_{45}SO_3$-	0.21577	249441.27
465.340824	$C_{28}H_{49}SO_3$-	0.074424	101220.68
479.356579	$C_{29}H_{51}SO_3$-	0.291454	169514.26
493.372288	$C_{30}H_{53}SO_3$-	0.402009	16345.87

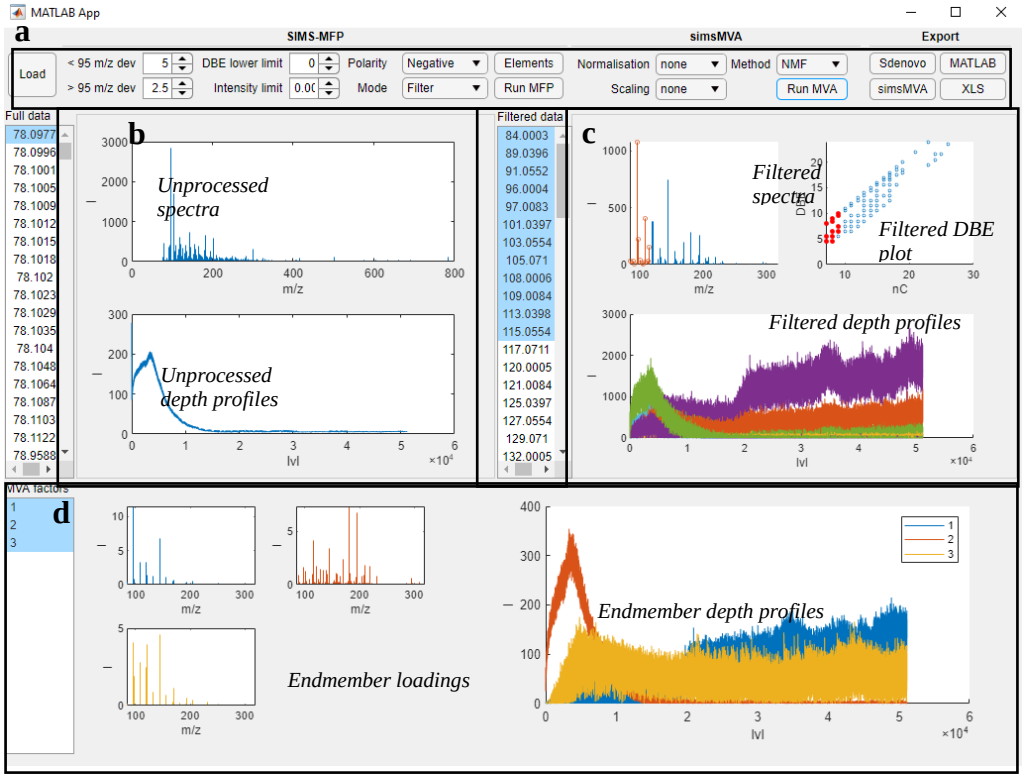
Injector needle deposit			
Center Mass (*m/z*)	**Assignment**	**Mass deviation (ppm)**	**Peak area (AU)**
79.957104	SO_3-	-3.246292	31361141.32
92.927893	$NaCl_2$-	-1.406125	140498.31
96.000477	C_8-	-0.740976	1162911.56
96.960053	SO_4H-	-0.513407	3766461.23
97.899022	CuCl-	0.199886	25343.33
99.925665	CrO_3-	-1.39163	2374376623
121.008293	$C_{10}H$-	-0.668607	412165.41
132.867787	$CuCl_2$-	-0.510081	260866.57
144.000476	C_{12}-	-0.503583	58429.13
145.008337	$C_{12}H$-	-0.254088	95968.46
160.842315	$FeCl_3$-	1.655659	2077.16
N/A	C_{14}-	NOT PRESENT	
N/A	C_{15}-	NOT PRESENT	
183.012119	$C_8H_7SO_3$-	-0.106631	93708441.86
N/A	C_{19}-	NOT PRESENT	
N/A	$C_{19}H$-	NOT PRESENT	
N/A	C_{20}-	NOT PRESENT	
255.233253	$C_{16}H_{31}O_2$-	1.170473	3880297.95
283.264506	$C_{18}H_35O_2$-	0.889484	3987266.41
325.184524	$C_{18}H_{29}SO_3$-	0.721666	10024047.42
339.200094	$C_{19}H_{31}SO_3$-	0.455633	6884376.54
N/A	$C_{26}H_{45}SO_3$-	NOT PRESENT	
N/A	$C_{28}H_{49}SO_3$-	NOT PRESENT	
N/A	$C_{29}H_{51}SO_3$-	NOT PRESENT	
N/A	$C_{30}H_{53}SO_3$-	NOT PRESENT	

6.2. Chapter 3 supporting information

N.B. Supplementary tables for this chapter are not included but can be found in at https://pubs.acs.org/doi/10.1021/acs.analchem.1c04898.

Supplementary note S3.1 - SIMS-MFP software graphical user interface

The need to simplify high-resolution 3D OrbiSIMS datasets is ever-growing in the field, SIMS-MFP software combines tools for MFP, categorization of species by double bond equivalence (DBE) and integrates existing MVA tools which can be linked to existing SIMS-MVA software.[167] A unique feature of this program is its incorporation to SIMS depth profiling data and the graphical user interface (GUI) (**Supplementary Figure S3.1**) is to display the profiles in both the pre and post filtered list and throughout this work we show its use for validating the grouping of secondary ions.



Supplementary Figure S3.1. Interface of the SIMS-MFP software showing key steps for the workflow on an example 3D OrbiSIMS dataset. *A. Display of the pre-filtered data including raw*

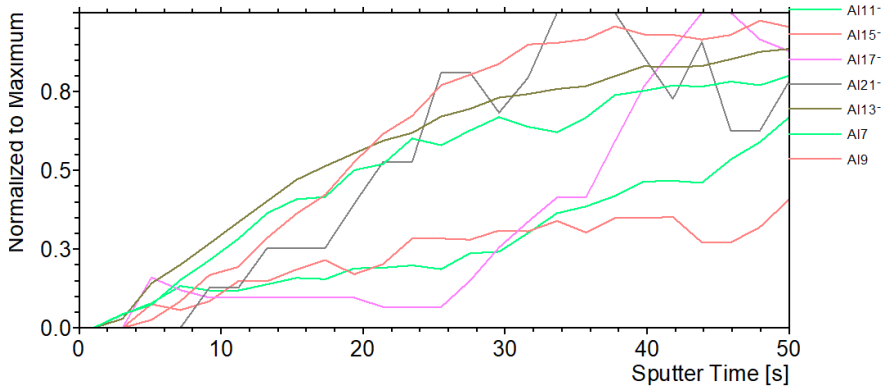
spectra and profiles of selected species. B. Inputting search criteria, error thresholds, DBE and intensity lower limits, polarity and the elemental compositions ('elements' button must be selected). C, After selecting 'Run MFP' the output data is shown. The filtered spectra of ions identified (left) and DBE versus carbon number of ions found in the search are displayed. Depth profiles for species can be selected also. D. The result of 'Run MVA' on the filtered depth profiling data. Data output is shown after performing MVA on the filtered list.

Upon loading a selected depth profile matrix by selecting the 'Load' button, the software displays the peak list and profiles for each ion in the list (**Supplementary Figure S3.3a**). Next, the user enters pre-set criteria for the filter, namely elemental compositions by clicking the 'elements' button (**Supplementary Figure 3.3b**), which brings up a table where maximum and minimum values are chosen, an untargeted approach can be used by selecting '-1' in the maximum value. Other constraints can be determined such as minimum DBE value, maximum error threshold (we recommend < 2 ppm for ions > *m/z* 95) and minimum peak intensity which are selected using the buttons in **Supplementary Figure S3.3b**. After selecting the 'Run MFP' button the program will run and cycle through each *m/z* value in the list and attempt to calculate its formula based on the preset criteria and will calculate DBE on proposed molecular formula. The program generates several plots (**Supplementary Figure S3.3c**). Firstly, a mass spectrum containing only ions with formula meeting the preset criteria (termed 'filtered spectra'). Second, a plot of the DBE versus carbon number of all possible assignments in the filtered data ('filtered DBE plot'). The list of ions with possible matching formula are displayed and their profiles can be displayed as well. A file is also produced which is exported to MATLAB and contains the formula predictions of each ion, and DBE value of each candidate for further interrogation by the user. If more than one formula can be assigned to a peak this is also shown. We include code which can match assigned ions to those in the LIPIDMAPS. Another feature in the SIMS-MFP toolkit is a 'mass separator' button which is accessed in the 'mode' drop-

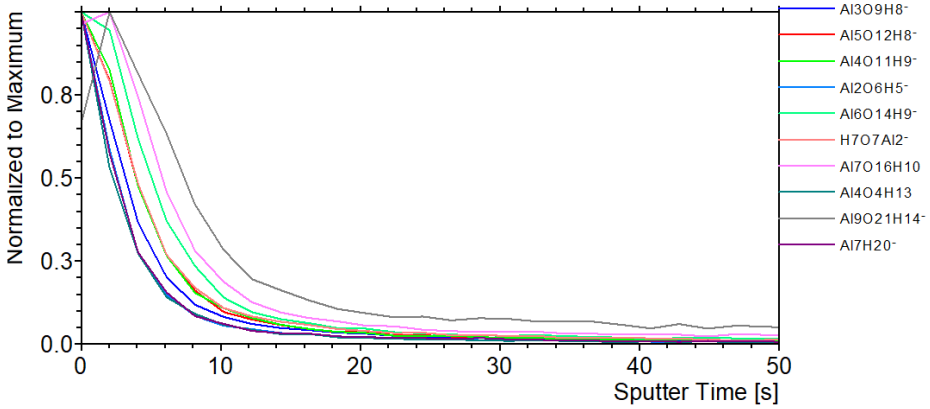
down menu (**Supplementary Figure S3.3a**). This generates a separated spectrum containing all peaks that could not be matched to the preset criteria. A list of non-included ions is generated which can be put back into the formula finder if the user wishes to further interrogate separated species which may be of use when analyzing sample and substrate peaks, for example. The user can perform MVA on filtered datasets by accessing the MVA tab in the GUI (**Supplementary Figure S3.3b**). We show an example after running non-negative matrix factorization (NMF) on the filtered depth profile data. The number of iterations and endmembers can be chosen and are displayed in the lower portion of the GUI which shows loadings and profiles of each endmember (**Supplementary Figure S3.3d**). In each case the plots can be exported as png. or svg. files. SIMS-MFP can incorporate datasets from multiple samples, allowing other MVA techniques to be performed such as principal component analysis or K-means clustering. Filtered data can be exported to simsMVA[209] for further interrogation by MVA techniques.

Chapter 3 Supplementary Figures

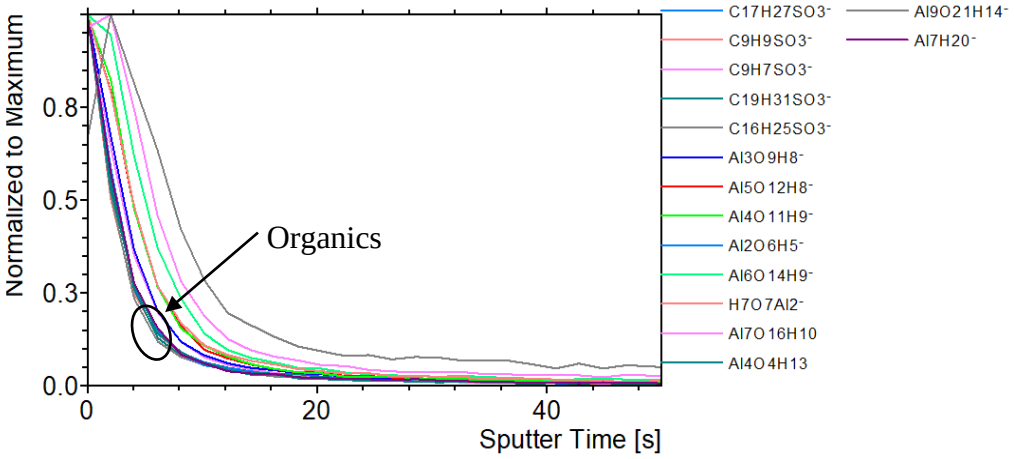
(a) Al clusters



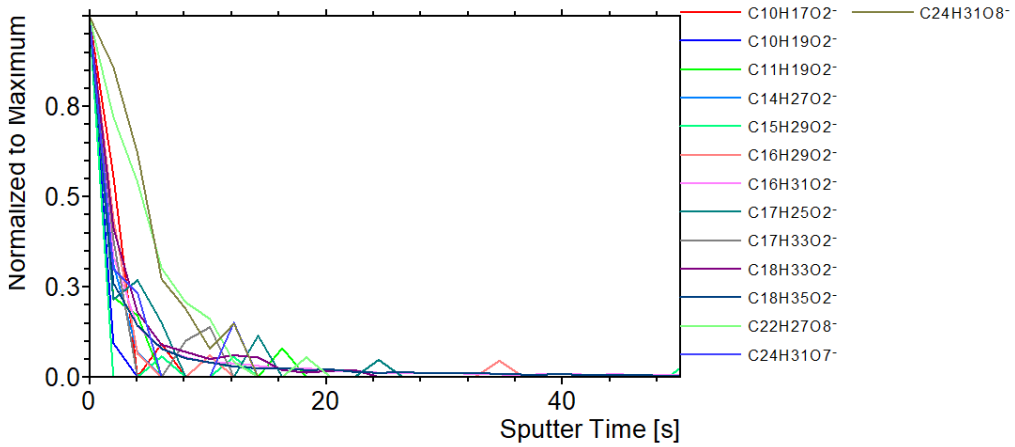
(b) Al oxides and hydroxides



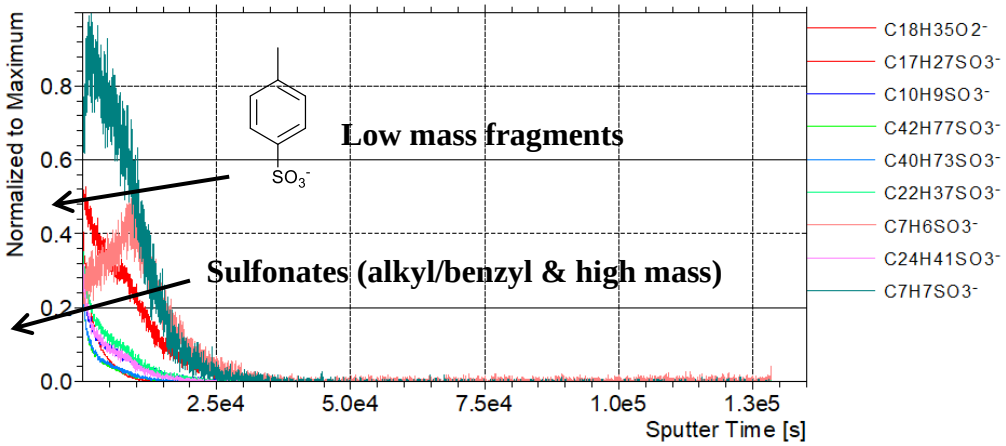
(c) Al oxides and hydroxides and intense organics ions



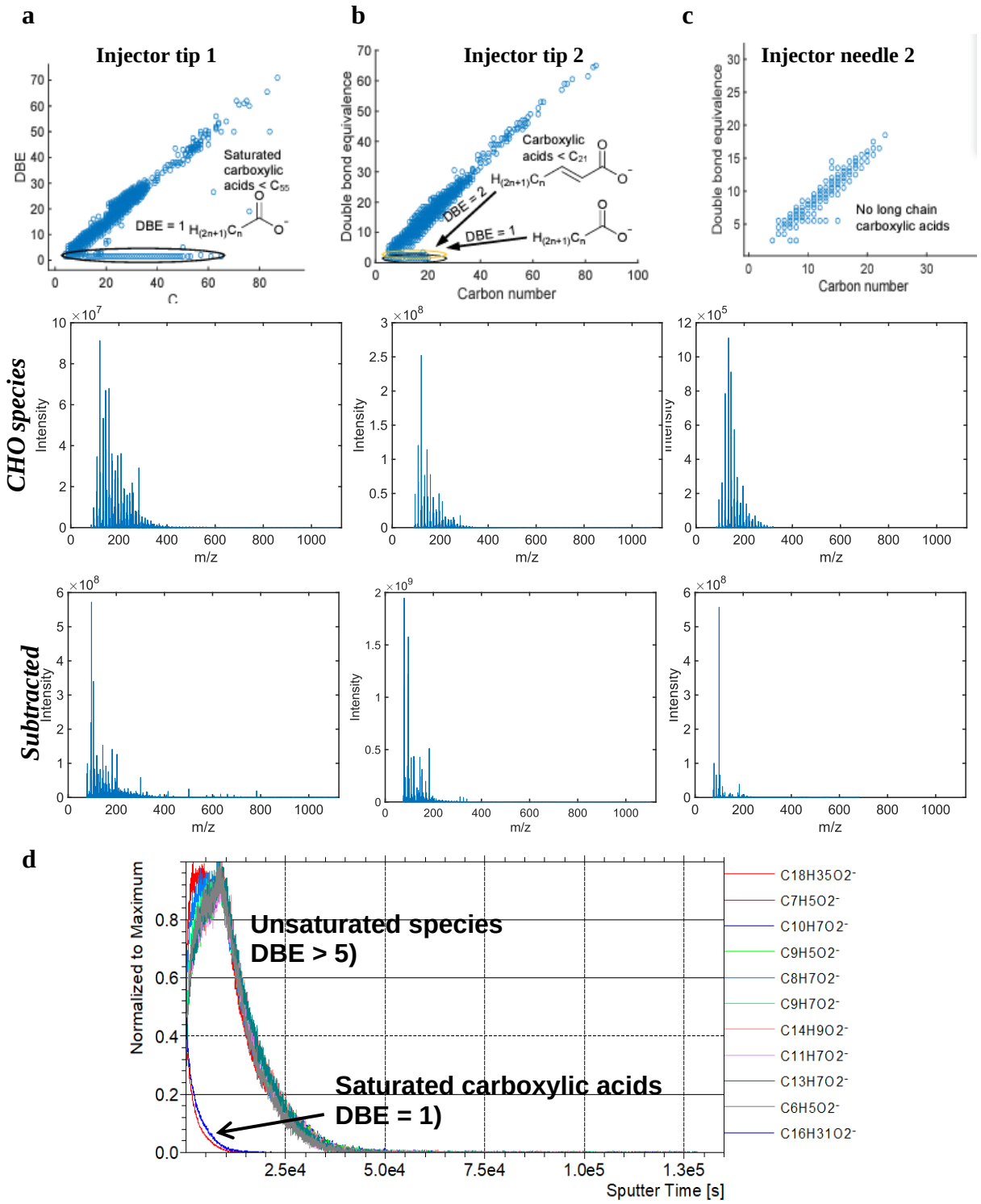
(d) Species in LIPIDMAPS



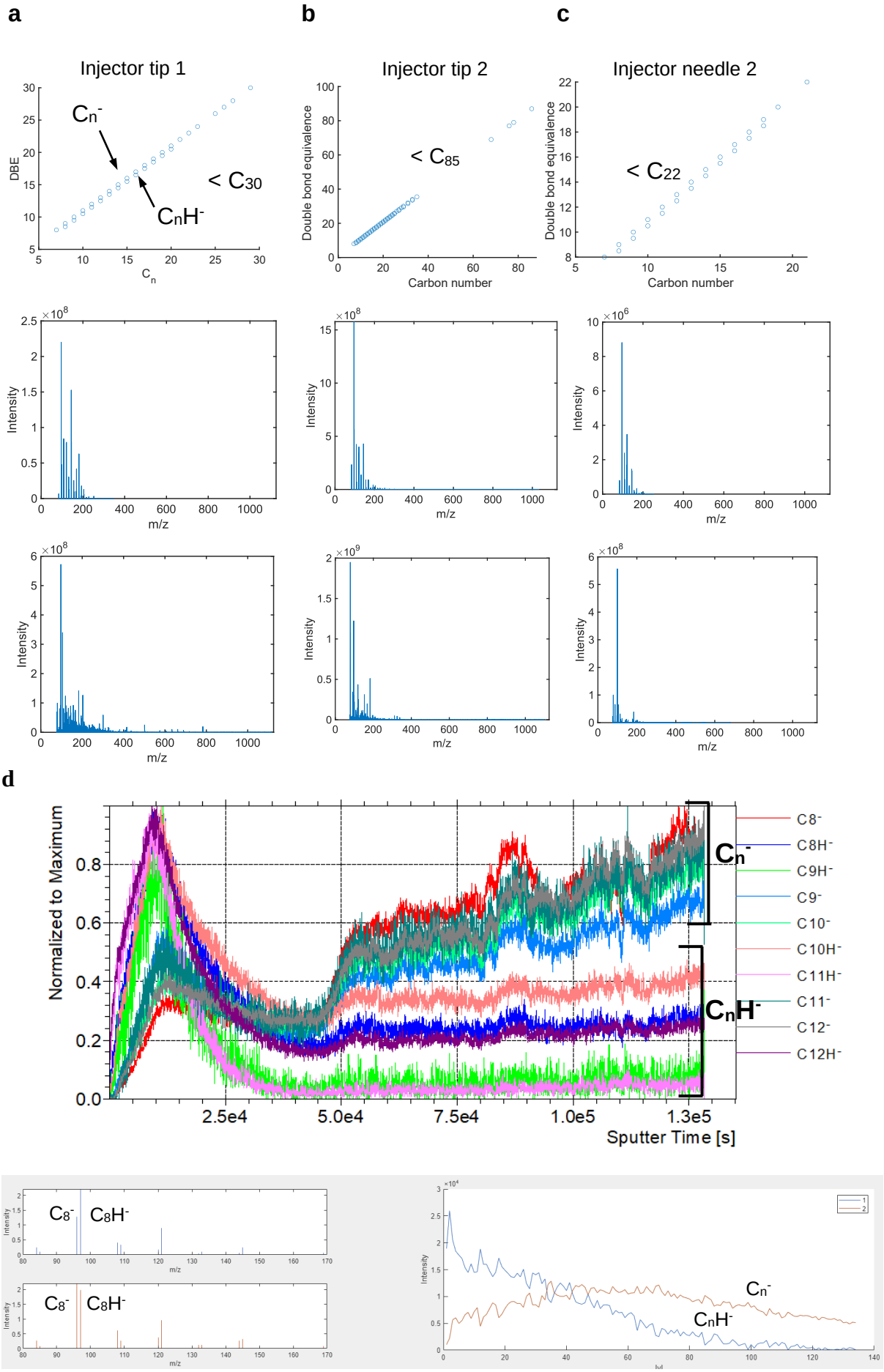
Supplementary Figure S3.2. *3D OrbiSIMS depth profiles of the organic and inorganic species on the dull side of the aluminum foil.*



Supplementary Figure S3.3*. Application of MFP to identify sulfated species (C & H = any, O = 3, S = 1) in engine deposits. Depth profiles of the 10 most intense species found in the search are shown.*



Supplementary figure S3.4*. Application of MFP to identify oxygenated species (C, H = any, O = 2) in engine deposits. a) injector tip 1, b) injector tip deposit 2 and c) injector needle 1. In each case the double bond equivalence (DBE) versus carbon number of each ion identified is displayed above, the middle plot shows the spectra of species identified and below are the subtracted spectra of species not found in the search. (d) Depth profiles of intense ions found in filtered lists.*

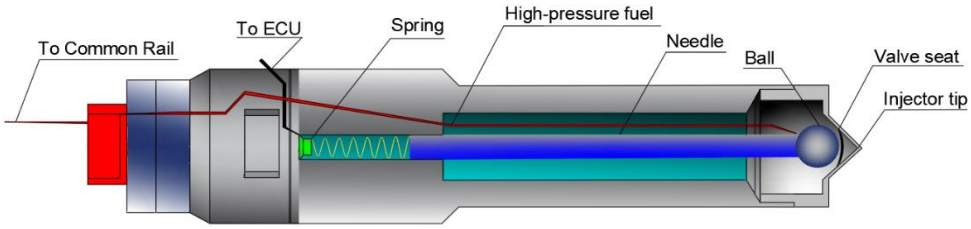

a
b
c
Injector tip 1
Injector tip 2
Injector needle 2
DBE
Cn-
< C30
CnH-
Cn
Double bond equivalence
< C85
Carbon number
< C22
Intensity
m/z
d
Normalized to Maximum
Sputter Time [s]
C8-
C8H-
C9H-
C9-
C10-
C10H-
C11H-
C11-
C12-
C12H-
Cn-
CnH-

***Supplementary figure S3.5**. Application of the SIMS-MFP software to identify carbonaceous ions (C = any, H ≤ 1) in engine deposits. a) injector tip 1, b) injector tip deposit 2 and c) injector needle 1. In each case the double bond equivalence (DBE) versus carbon number of each ion identified is displayed above, the middle plot shows the spectra of species identified and below are the subtracted spectra of species not found in the search. d) Depth profiles of intense ions in the filtered data set. e) NMF outputs on carbonaceous ions from injector needle 1.*

6.3. Chapter 4 Supporting Information

S4.1

(a)





(b)





(c)

Fuel injector set	origin	Gasoline type/tier	alcohols: ethanol	alcohols: larger alcohols	paraffins: linear	paraffins: branched	paraffins: cyclic	olefins: linear	olefins: branched	olefins: cyclic	benzene rings: toluene	benzene rings: with paraffinic chains	benzene rings: with olefinic chains	napht-halenes	indene: indene	indene: with paraffinic chains	indene: with olefinic chains
Injector 1*	Corpus Christi, TX, USA	Standard retail E10	present	present	present	present	present	present	present	not present	present	present	present	present	not present	not present	not present
Injector 2	USA	Standard retail E10	present	present	present	present	present	not present	present	present	present	present	present	present	not present	present	not present
Injector 3*	Martinez, CA, USA	Standard retail E10	present	present	present	present	present	present	present	present	present	present	present	present	not present	not present	not present
Injector 4*	Baton Rouge, LA, USA	Standard retail E10	present	present	present	present	present	present	present	present	present	present	present	present	not present	present	not present
Injector 5	USA	Standard retail E10	present	present	present	present	present	present	present	not present	present	present	present	present	not present	not present	not present
Injector 6*	Richmond, CA, USA	Standard retail E10	present	present	present	present	present	present	present	not present	present	present	present	not present	not present	not present	not present
Injector 7	USA	EEE Lube certification	Unknown														
Injector 8	USA	US 'top tier' retail E10															

present

not present

* Quantified data available in data repository for article

Supplementary figure S4.1. (a) *Schematic of a gasoline direct injection unit (above), photographs of injector tip and needle 1 as an example of the components studied in this work (below).* ***(b)*** *Photographs of the engine testing rig used to generate the deposits used in this work. Images provided courtesy of Intertek USA.* ***(c)*** *Summary of the composition of fuel used in the deposit formation engine test acquired from GC-EI-MS analysis. The quantified information is unknown but adhered to USA fuel specification.*[210] *Injectors 1-6 were retrieved from engine testing using one fuel. E10, 10 % ethanol containing.*

Supplementary table S4.2. *Experimental 3D OrbiSIMS parameters that varied on all samples. Common parameters are detailed in the methods.* ***(a)*** *Injector tip samples, including full depth profiles and 'depth profile & imaging' experiments.* ***(b)*** *Injector needle samples.*

(a)

	Parameter	Tip 1		Tip 2		Tip 3		Tip 4		Tip 5		Tip 6		Tip 7		Tip 8	
		+	-	+	-	+	-	+	-	+	-	+	-	+	-	+	-
Depth profile	Sputter time (s)	8000	34300	85000	128000	49430	122420	35315	10151	17379	8222	4543	30666	11992	6015	34131	22094
	Total dose (ions)	5.5×10^{12}	2.5×10^{13}	1.9×10^{14}	1.8×10^{14}	3.51×10^{13}	2.54×10^{13}	5.5×10^{13}	1.58×10^{13}	2.49×10^{13}	1.18×10^{13}	3.23×10^{12}	4.71×10^{13}	2.1×10^{13}	1.05×10^{13}	5.54×10^{13}	3.58×10^{13}
	Analysis area μm^2	200	200	400	300	200	50	200		200		200		200		200	
	Target current (pA)	219	230	238	238	233	230	250		230		248		280		260	
	Raster mode	sawtooth		sawtooth		random		random		random		random		random		random	
Combined imaging & depth profile	Sputter polarity	-		+		+											
	Analysis area (μm^2)	200		150		150											
	Total sputter time (s)	510		2650		1860											
	Total dose (ions)	5.25×10^{11}		1.52×10^{12}		1.11×10^{12}											
	Image scans	2		3		3											
	Pixels	60 × 60		30 × 30		30 × 30											
	Image area (μm^2)	300															
	Raster mode	random															

(b)

	Parameter	Needle 1		Needle 2		Needle 3		Needle 4		Needle 5		Needle 6		Needle 7		Needle 8	
		+	-	+	-	+	-	+	-	+	-	+	-	+	-	+	-
Depth profile	Sputter time (s)	911	2786	1069	978	1622	3762	122	370	245	745	511	887	204	239	120	561
	Total dose (ions)	6.2×10^{11}	?	7.27×10^{11}	6.80×10^{11}	1.15×10^{12}	2.56×10^{12}	3.60×10^{11}	1.09×10^{12}	3.53×10^{11}	1.07×10^{12}	7.31×10^{11}	1.27×10^{12}	2.93×10^{11}	3.42×10^{11}	1.73×10^{11}	8.05×10^{11}
	Analysis area (μm^2)	200		200		200		200		200		200		200		200	
	Primary ion current (pA)	220		220		220		235		230		230		230		230	
	Raster mode	random		random		random		random		random		random		random		random	

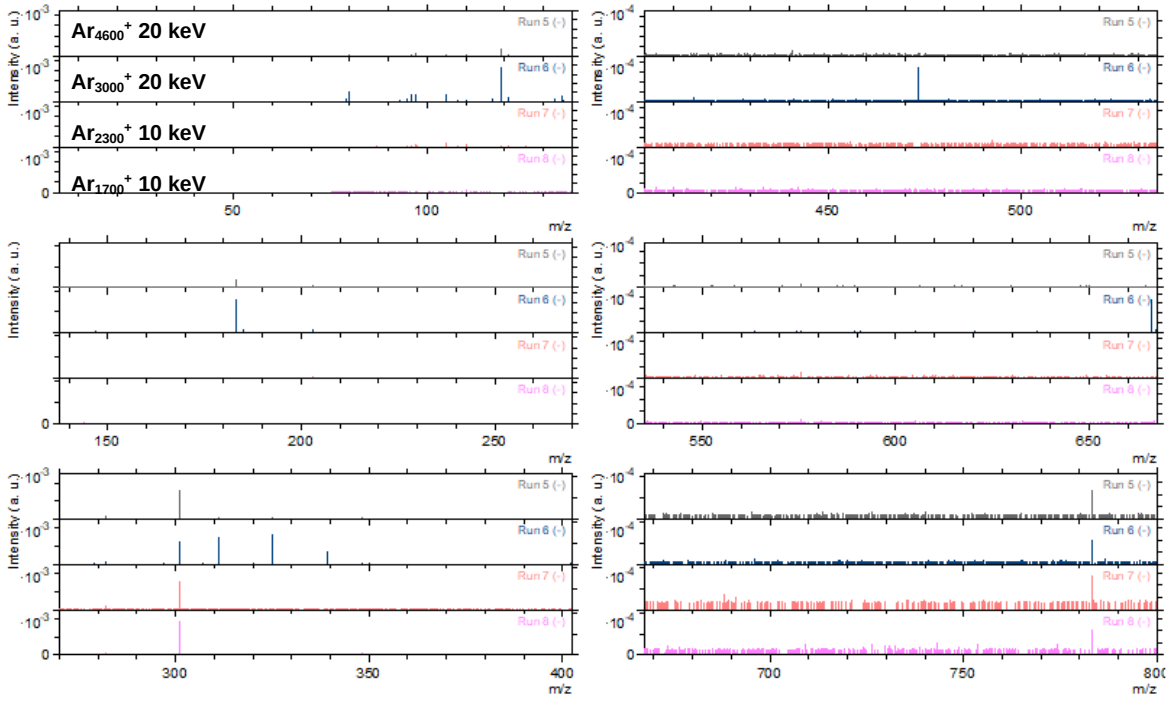
S4.3 – Optimization experiments

Before conducting extensive analysis with 3D OrbiSIMS we investigated the effect on ion intensity and chemical speciation (particularly of positively ionizing carbonaceous species) by altering key analysis settings. The aim of this work is to achieve maximum secondary ion intensity without affecting speciation of known species in deposits. We performed analytical repeats of depth profiles on injector tip 3 by carrying out short depth profiles (10 s) in one analysis area using different instrumental settings. We altered ion source cluster size and energy, pressure of nitrogen flow and argon flow for charge compensation, and flood gun energy. In each case the best setting was compared to the last and carried forward into the next experiment (**Supplementary table S4.3a**). We kept analysis times short to prevent sputtering into layers with different deposit chemistry, datasets were only compared with the next in sequence, so we were observing comparable chemistries with < 20 s difference in sputtering (accounting for both polarities). Previous work (Chapter 2) found that it took up to two days of sputtering to reach the lowest deposit layer. We found that Ar_{3000}^+ gave the best overall ion intensity in both polarities compared to larger and smaller cluster sizes/energies (**Supplementary figure S4.3bi**). Negative polarity mode also showed a far lower peak intensity when cluster size was altered from Ar_{3000}^+ (**Supplementary figure S4.3bii**). This agrees with previous work which explored the ideal cluster size for homogeneous organic reference materials.[138,211] An Ar flooding pressure of 1 x 10^{-6} mbar (the setting used so far in this work), which is used to delocalize charge surrounding the analysis area,[121] was ideal for identifying PAHs of high mass (> *m/z* 500) (**Supplementary figure S4.3bi**). Intensity of negative ions varied when the flood pressure was increased, for example the parent ion of alkyl benzyl sulfonates, identified in previous work ($C_{18}H_{29}SO_3^-$, *m/z* 325.18), had higher intensity with less Ar flooding, and its fragments (SO_3^-, *m/z* 80.01 & $C_8H_7SO_3^-$, *m/z* 183.01) had lower intensity (**Supplementary figure S4.3cii**). Other settings (**Supplementary figure S4.3a**) yielded insignificant changes to the ion intensity or chemical speciation (data not shown). Importantly there was little difference in the speciation of carbonaceous material including PAHs. This further ratifies the method and instrument parameters used in this and previous work in this thesis.

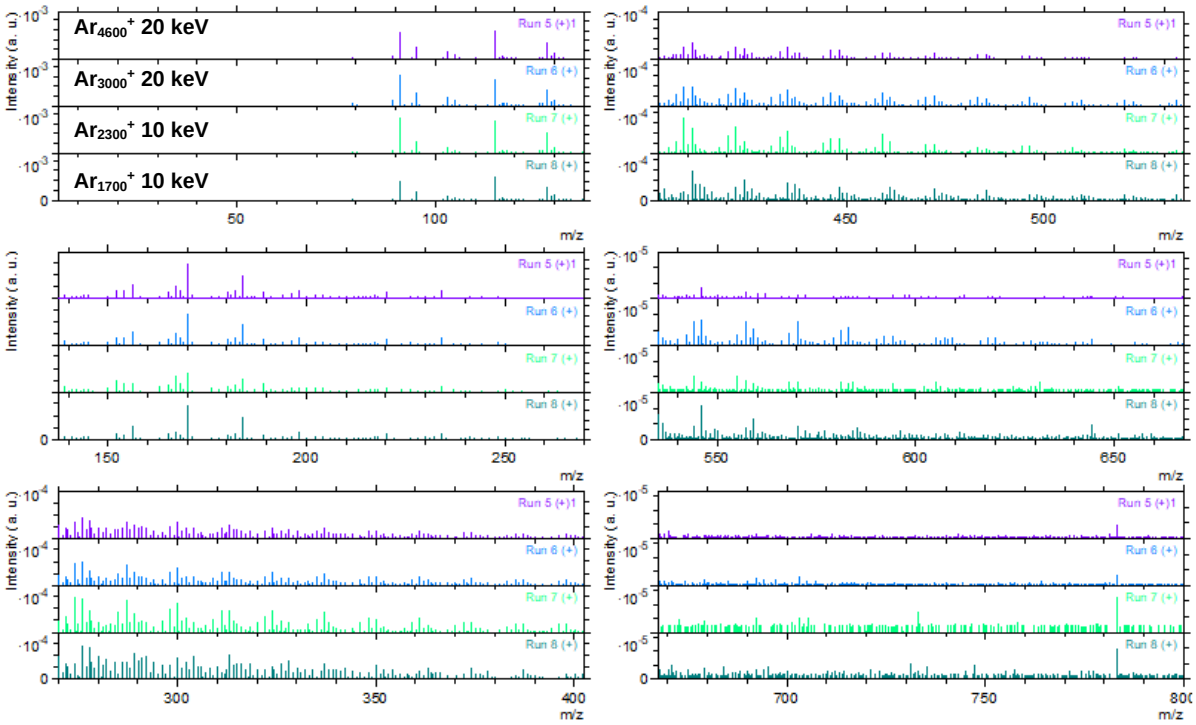
(a)

		Experiment number & parameter Investigated										
		1	2	3	4	5	6	7	8	9	10	11
Ion beam energy and cluster size	20 kV, Ar_{3000}^{+}	x	x	x			x			x	x	x
	20 kV, Ar_{2300}^{+}							x				
	10 kV, Ar_{1700}^{+}								x			
	20 kV, Ar_{4600}^{+}				x	x						
N pressure (bar)	12					x	x	x	x	x	x	x
	10	x	x	x	x							
Flood gun energy	21 V	x										
	10 V		x		x	x	x	x	x	x	x	x
	10 V low anode			x								
Ar pressure (mbar)	1.00×10^{-6}	x	x	x	x	x	x	x	x			
	1.00×10^{-5}									x		
	1.00×10^{-7}										x	
	OFF											x

(b)
i.

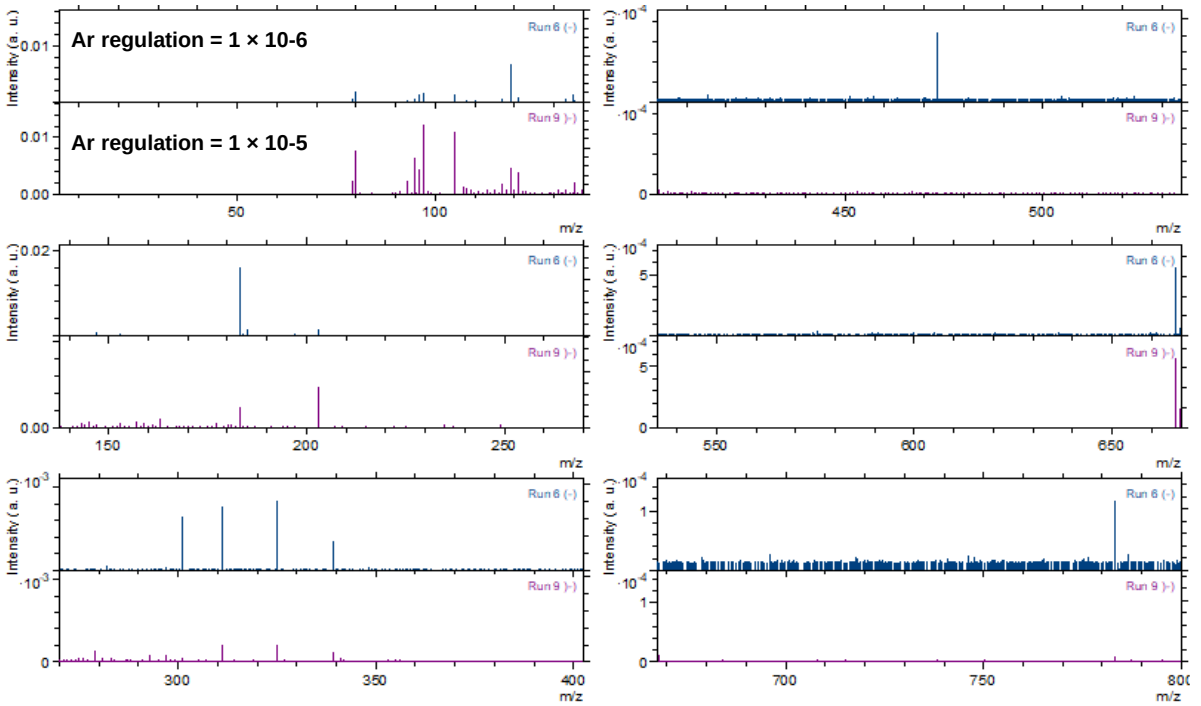


ii.

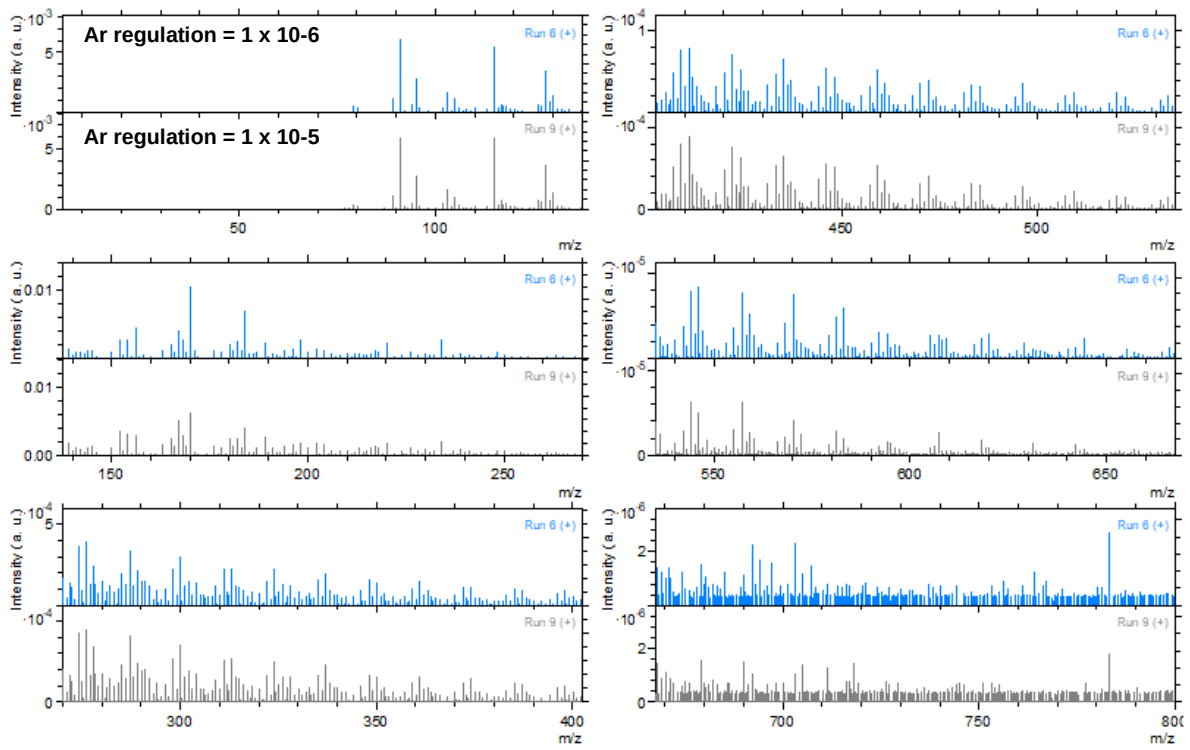

Ar4600+ 20 keV
Ar3000+ 20 keV
Ar2300+ 10 keV
Ar1700+ 10 keV
Run 5 (+)1
Run 6 (+)
Run 7 (+)
Run 8 (+)
Intensity (a. u.)
m/z

(c)

i.


Ar regulation = 1 × 10-6
Ar regulation = 1 × 10-5
Run 6 (-)
Run 9)-)
Intensity (a. u.)
m/z

ii.



***Supplementary figure S4.3**: **(a)** Table of experiments summarizing the interchangeable settings used, carried out on the deposit on injector tip 3. In each case a 10 s depth profile was carried out in both polarities. Green boxes represent the most ideal settings determined. **(b)** Comparing the effects of cluster size on the ion intensity and speciation for **i.** positive ions and **ii.** negative ions. Cluster sizes are displayed in the first mass window and are consistent for others. **(c)** Comparing the effects of Ar flood pressure (lower pressure = upper spectra, higher pressure = lower spectra) on the ion intensity and speciation for **i.** positive ions and **ii.** negative ions.*

Supplementary table S4.4. *3D OrbiSIMS accurate mass ion table for negative ions identified in* ***(a)*** *injector tip deposits,* ***(b)*** *injector needle deposits All ion peak tables were exported from Surface Lab software (IONTOF GmbH, version 7.1.b). Deviation (ppm) refers to the difference between the observed and expected ion mass. The observed mass is measured as the center mass of the ion peak.*

(a)

	Injector tip 1			Injector tip 2			Injector tip 3			Injector tip 4		
Formula	Centre Mass (u)	Deviation (ppm)	Area	Centre Mass (u)	Deviation (ppm)	Area	Centre Mass (u)	Deviation (ppm)	Area	Centre Mass (u)	Deviation (ppm)	Area
Linear carboxylic acids												
C_16H_31O_2-	255.233584	2.468516	50086698	255.233336	1.498798	21786870	255.233479	2.058172	78645	255.233119	0.648538	9023913.7
C_18H_35O_2-	283.264906	2.301217	84017259	283.264585	1.168911	29131807	283.264475	0.779082	99461	283.264379	0.442219	9945651.6
alkyl benzyl sulfonate												
C_8H_7SO_3-	183.01236	1.213189	399902141	183.012143	0.025332	141536538	183.012234	0.523136	4834713	183.012097	-0.226048	395473361
C_17H_27SO_3-	311.169216	1.855658	70336741	311.16893	0.935851	14549883	311.168948	0.993089	552765	311.168824	0.594391	68874475
C_18H_29SO_3-	325.184685	1.217576	79811853	325.184363	0.227101	16971174	325.184507	0.670856	517889	325.184333	0.135293	66890572
Alkyl salicylate												
C_7H_5O_3-	137.024529	0.80966	16644925	137.024397	-0.150398	25384207	137.024403	-0.103103	1770285	137.024329	-0.645321	39319868
C_8H_7O_3-	151.040165	0.647327	10203394	151.040047	-0.136584	14535173	151.040055	-0.082127	852242	151.039962	-0.6973	16274609
C_9H_9O_3-	165.055796	0.474686	4214774	165.055694	-0.14192	4849130	165.0557	-0.105381	173366	165.055587	-0.789488	3685157.3
C_10H_11O_3-	179.071531	0.909078	1577751	179.071424	0.313803	1039881	179.071419	0.286865	26959	179.071316	-0.291531	752593.23
C_11H_13O_3-	193.087151	0.688197	510866	193.087056	0.197871	242533	193.087083	0.338146	6513	193.086937	-0.419875	117912.63
Fused salicylate												
C_11H_7O_3-	187.040223	0.831044	14221637	187.040116	0.260133	22303999	187.040113	0.240227	876828	187.039971	-0.517678	33280509
C_15H_9O_3-	237.056051	1.406505	5006857	237.055964	1.040837	16911459	237.055889	0.72434	381577	237.055707	-0.046611	11481717
C_19H_11O_3-	287.071957	2.052184	2759323	287.07176	1.366587	8058797	287.071631	0.916464	75028	287.071466	0.343286	4171746.5
Inorganic salts												
NaCl_2-	**x**	**x**	**x**	**x**	**x**	**x**	**x**	**x**	**x**	92.927915	-1.165	241238.22
CuCl-	97.899094	0.940184	26367	**x**	**x**	**x**	**x**	**x**	**x**	132.867826	-0.220729	2509513.6
FeCl_3-	**x**	**x**	**x**	**x**	**x**	**x**	**x**	**x**	**x**	160.84198	-0.426674	78836.73

	Injector tip 5			Injector tip 6			Injector tip 7			Injector tip 8		
Formula	Centre Mass (u)	Deviation (ppm)	Area	Centre Mass (u)	Deviation (ppm)	Area	Centre Mass (u)	Deviation (ppm)	Area	Centre Mass (u)	Deviation (ppm)	Area
Carboxylic acids												
C_16H_31O_2-	255.233262	1.20686	54308142.03	255.23304	0.337925	299352.31	255.233279	1.275937	14963596.2	255.233091	0.537181	1828903.87
C_18H_35O_2-	283.264516	0.926456	41285465.36	283.264288	0.121534	140512.28	283.264583	1.163223	17473572.77	283.264347	0.329323	1884037.29
alkyl benzyl sulfonate												
C_8H_7SO_3-	183.012169	0.169717	2486345453	183.012009	-0.70949	433640679	183.012229	0.497405	511434944.5	183.012084	-0.298616	71510485.24
C_17H_27SO_3-	311.168869	0.737874	229965508.9	311.168635	-0.013401	31251568.36	311.169047	1.310638	48850826.95	311.168803	0.52569	12471095.46
C_18H_29SO_3-	325.184382	0.284433	222058756.5	325.184171	-0.362732	30829940.28	325.18457	0.864633	43767912.32	325.18431	0.063479	10581554.48
Alkyl salicylate												
C_7H_5O_3-	137.024365	-0.387448	65032584.16	137.024285	-0.970042	95400107.47	137.024396	-0.160016	72399052.36	137.024308	-0.802657	32887063.29
C_8H_7O_3-	151.040013	-0.358782	32846961.37	151.039923	-0.9587	37560269.68	151.039998	-0.458912	14488279.81	151.039946	-0.807477	17425619.18
C_9H_9O_3-	165.055654	-0.383689	10458385.36	165.055562	-0.94458	7172130.37	165.055578	-0.844564	2202901.85	165.055579	-0.840663	4564124.62
C_10H_11O_3-	179.071382	0.082049	2374353.47	179.071284	-0.469488	860390.62	179.071321	-0.263784	225325.56	179.0713	-0.377747	837939.91
C_11H_13O_3-	193.087011	-0.037827	630588.52	193.086916	-0.528209	147144.48	193.086922	-0.497044	32373.17	193.086909	-0.565063	111938.79
Fused salicylate												
C_11H_7O_3-	187.040053	-0.079896	54001188.44	187.039948	-0.639915	82027502.44	187.039996	-0.384023	25939567.87	187.039959	-0.579344	17617872.44
C_15H_9O_3-	237.055841	0.521741	30061528.6	237.055666	-0.218618	66906255	237.055698	-0.084594	18292292.83	237.055705	-0.053135	13418415.05
C_19H_11O_3-	287.071588	0.768552	16661977.05	287.071355	-0.044337	31409105.04	287.071458	0.31443	7574136.72	287.071462	0.329639	6904281.1
Inorganic salts												
NaCl_2-	92.927944	-0.86086	1832671.34	92.927887	-1.469435	536664.72	92.927859	-1.770034	30824829.07	92.927902	-1.312747	65464.48
CuCl-	132.867868	0.099266	974714.12	132.867778	-0.581307	407694.97	132.867883	0.210764	15893844.16	132.867815	-0.30521	110199.04
FeCl_3-	160.842022	-0.1673	19007.93	160.841949	-0.618379	654837.59	160.841937	-0.696757	1375610.61	160.84204	-0.054896	11855.11

(b)

	Injector needle 1			Injector needle 2			Injector needle 3			Injector needle 4		
Formula	Centre Mass (u)	Deviation (ppm)	Area (Intensity)	Centre Mass (u)	Deviation (ppm)	Area (Intensity)	Centre Mass (u)	Deviation (ppm)	Area (Intensity)	Centre Mass (u)	Deviation (ppm)	Area (Intensity)
Linear carboxylic acids												
C_16H_31O_2-	255.233534	2.274657	32392	119.050203	1.447582	1427	255.233142	0.738967	26283.07	255.23324	1.120394	1688051.07
C_18H_35O_2-	283.264786	1.877228	26343	79.957079	0.55141	2210	283.264451	0.694995	32452.69	283.264486	0.817631	1569883
alkyl benzyl sulfonate												
C_8H_7SO_3-	183.012386	1.353485	22192537	183.012139	0.00209	5819556	183.012136	-0.011823	1430864.97	183.012231	0.503664	44010176.65
C_17H_27SO_3-	311.169307	2.147868	1583050	311.16883	0.614004	295070	311.168877	0.764692	95440.35	311.168926	0.923153	2597729.87
C_18H_29SO_3-	325.18481	1.603105	1684842	325.18431	0.06375	275893	325.184338	0.150447	94921.67	325.184439	0.461729	2493037.29
Alkyl salicylate												
C_7H_5O_3-	137.024452	0.253141	66999	137.024361	-0.416457	49711	137.024348	-0.5071	23777.63	137.024397	-0.149005	262706.6
C_8H_7O_3-	151.040154	0.573618	30294	151.040014	-0.356927	13662	151.039979	-0.586557	5957.47	151.040083	0.101392	119569.78
C_9H_9O_3-	165.055861	0.865653	5359	**x**	**x**	**x**	**x**	**x**	**x**	165.055687	-0.185419	21534.68
C_10H_11O_3-	**x**	**x**	**x**	**x**	**x**	**x**	**x**	**x**	**x**	179.071536	0.940997	5449.47
C_11H_13O_3-	**x**	**x**	**x**	**x**	**x**	**x**	**x**	**x**	**x**	**x**	**x**	**x**
Fused salicylate												
C_11H_7O_3-	187.040136	0.363198	147936.98	187.04006	-0.040527	115834	187.040091	0.12669	72968.62	187.040078	0.053729	1022747.02
C_15H_9O_3-	237.056015	1.253406	28430.83	237.055871	0.646441	31860	237.055988	1.138332	5266	237.055876	0.667145	203301.73
C_19H_11O_3-	287.072042	2.350046	24136.44	287.071727	1.251244	12624	287.071536	0.586644	5490.39	287.071666	1.039181	212776.18
Inorganic salts												
NaCl_2-	**x**	**x**	**x**	92.927933	-0.979267	12669	**x**	**x**	**x**	92.927915	-1.171798	1667331.01
CuCl_2-	132.867997	1.067715	2204821	132.867809	-0.348502	327848	132.867835	-0.154615	339527.04	132.867898	0.319417	20307913.51
FeCl_3-	160.842106	0.357264	286684	160.841993	-0.347658	657101	160.842019	-0.182576	427201.64	160.842082	0.206867	8520590.69

	Injector needle 5			Injector needle 6			Injector needle 7			Injector needle 8		
Formula	Centre Mass (u)	Deviation (ppm)	Area (Intensity)	Centre Mass (u)	Deviation (ppm)	Area (Intensity)	Centre Mass (u)	Deviation (ppm)	Area (Intensity)	Centre Mass (u)	Deviation (ppm)	Area (Intensity)
Linear carboxylic acids												
C_16H_31O_2-	119.050203	1.447582	1427	255.233208	0.994485	21970.59	255.233422	1.833339	2835332.13	255.233252	1.170195	3879830.75
C_18H_35O_2-	79.957079	0.55141	2210	283.264482	0.80433	12433.23	283.264685	1.520272	2873077.9	283.264505	0.886701	3987783.12
alkyl benzyl sulfonate												
C_8H_7SO_3-	183.012139	0.00209	5819556	183.012142	0.02027	4578121.59	183.012252	0.618415	85145793.81	183.012119	-0.106631	93708486.39
C_17H_27SO_3-	311.16883	0.614004	295070	311.168798	0.50959	259537.35	311.169219	1.865243	8927499.02	311.168997	1.149114	10068750.28
C_18H_29SO_3-	325.18431	0.06375	275893	325.184274	-0.045777	241332.47	325.184756	1.435994	8625199.93	325.184524	0.721693	10023950.19
Alkyl salicylate												
C_7H_5O_3-	137.024361	-0.416457	49711	137.024354	-0.467618	26262.31	137.024393	-0.178848	85505.23	137.024341	-0.559588	8463.23
C_8H_7O_3-	151.040014	-0.356927	13662	151.040027	-0.266522	9760.36	151.040141	0.488705	5252.86	**x**	**x**	**x**
C_9H_9O_3-	165.055727	0.056165	2044	**x**	**x**	**x**	**x**	**x**	**x**	**x**	**x**	**x**
C_10H_11O_3-	**x**	**x**	**x**	**x**	**x**	**x**	**x**	**x**	**x**	**x**	**x**	**x**
C_11H_13O_3-	**x**	**x**	**x**	**x**	**x**	**x**	**x**	**x**	**x**	**x**	**x**	**x**
Fused salicylate												
C_11H_7O_3-	187.04006	-0.040527	115834	187.040039	-0.152058	72097.98	187.03986	-1.1127	9859.57	187.03992	-0.787472	3877.94
C_15H_9O_3-	237.055871	0.646441	31860	237.055825	0.4508	12700.64	237.05586	0.600935	8653.92	237.055703	-0.060512	3247.7
C_19H_11O_3-	287.071727	1.251244	12624	**x**	**x**	**x**	287.074033	9.2849	10854.44	287.074189	9.827158	17419.53
Inorganic salts												
NaCl_2-	92.927933	-0.979267	12669	92.927862	-1.742616	3816520.31	92.927906	-1.264266	697180.81	92.927893	-1.410817	140822.78
CuCl_2-	132.867809	-0.348502	327848	132.867827	-0.214709	1837499.93	132.867953	0.739501	2901434.06	132.867787	-0.513206	260626.41
FeCl_3-	160.841993	-0.347658	657101	160.84202	-0.179157	5641960.92	160.842011	-0.237538	103094.27	**x**	**x**	**x**

Supplementary table S4.5*: 3D OrbiSIMS accurate mass ion table for a selection of PAHs manually identified in* ***(a)*** *injector tip deposits* ***i.*** *injector tips 1-4,* ***ii.*** *Injector tips 5-8.* ***(b)*** *Deposits from injector needles* ***i.*** *injector tips 1-4,* ***ii.*** *Injector tips 5-8. All ion peak tables were exported from Surface Lab software (IONTOF GmbH, version 7.1.b). Deviation (ppm) refers to the difference between the observed and expected ion mass. The observed mass is measured as the center mass of the ion peak.*

(a) i.

	Injector tip 1			Injector tip 2			Injector tip 3			Injector tip 4		
Formula	**Center Mass (u)**	**Deviation (ppm)**	**Area (intensity)**	**Center Mass (u)**	**Deviation (ppm)**	**Area (intensity)**	**Center Mass (u)**	**Deviation (ppm)**	**Area (intensity)**	**Center Mass (u)**	**Deviation (ppm)**	**Area (intensity)**
C_7H_7+	91.054391	1.803584	220248460.8	91.054417	2.092466	1688466270	91.054481	2.79573	680990858.6	91.054452	2.473783	2060640240
C_9H_7+	115.054227	0.000425	264994336.1	115.054235	0.076433	2671248376	115.054302	0.65455	481265460.1	115.054227	0.003842	2911749255
C_10H_8+	128.062054	0.017629	191543903.4	128.062012	-0.308323	1587896933	128.062041	-0.085723	353653717.6	128.061963	-0.69352	1535026175
C_11H_7+	139.054282	0.396924	55000463.42	139.05419	-0.260142	623939207.4	139.054194	-0.232484	124562511.6	139.05409	-0.983115	513424322.9
C_11H_9+	141.069913	0.253898	65774547.74	141.069816	-0.432129	586445049.9	141.069808	-0.485367	112755911.6	141.069717	-1.13554	527778865.7
C_12H_6+	150.046465	0.422541	31340871	150.046372	-0.196337	505157693.4	150.046384	-0.116456	104486745.9	150.04626	-0.946871	399261801.7
C_12H_8+	152.062114	0.408928	113574249.7	152.062013	-0.255315	1384768718	152.062026	-0.170764	249410086.8	152.061906	-0.960141	1096427815
C_13H_10+	166.077746	0.268938	4017204.32	166.07761	-0.551346	42290992.91	166.07759	-0.672667	7792591.18	166.077533	-1.015587	32486735.42
C_14H_8+	176.06212	0.389718	28107938.92	176.062031	-0.117553	478926799.9	176.062041	-0.058784	90913536.11	176.061897	-0.877556	338591407.8
C_14H_10+	178.077762	0.340157	32863797.52	178.077669	-0.186154	517217800.8	178.077664	-0.210667	91531335.35	178.077536	-0.932558	383419333.1
C_15H_10+	190.077764	0.327878	5163717.52	190.077615	-0.454913	85913043.55	190.077541	-0.847861	13133460.62	190.077523	-0.940806	70446656.07
C_16H_10+	202.077805	0.509798	39654177.03	202.077699	-0.015732	662653320.5	202.07769	-0.057531	121381964.2	202.077547	-0.767199	520942328.9
C_17H_9+	213.069885	0.040996	20938074.46	213.069875	-0.007109	368564736	213.069942	0.307054	71759257.86	213.069791	-0.40305	282481375.4
C_17H_12+	216.09327	-0.376328	1057136.32	216.093314	-0.175679	14844662.97	216.093396	0.206441	2828815.04	216.093385	0.154943	14480617.56
C_18H_10+	226.077611	-0.399706	25830389.84	226.077696	-0.026091	469273992.9	226.077855	0.677506	82336582.99	226.077678	-0.102933	345454275.1
C_18H_12+	228.093254	-0.427101	5405813.56	228.093287	-0.283097	77185699.57	228.093343	-0.038075	12765687.31	228.093334	-0.076095	75772286.45
C_19H_11+	239.085412	-0.48178	21659776.36	239.085501	-0.106089	379258842.4	239.08562	0.388567	59134767.88	239.085483	-0.182817	276958371.1
C_20H_10+	250.077588	-0.456598	15698956.32	250.077671	-0.12362	295830313.1	250.07779	0.351657	50162800.61	250.077649	-0.212215	210718873.1
C_20H_12+	252.09323	-0.483495	11625833.55	252.093299	-0.211116	193311549.7	252.093365	0.050868	28880456.22	252.093295	-0.2238	149439774.3
C_21H_11+	263.085425	-0.388063	16217857.96	263.085516	-0.042452	299889979.4	263.08563	0.390543	45629264.92	263.085499	-0.104591	205369941.8
C_21H_13+	265.101094	-0.311131	4427366.56	265.101129	-0.180566	75335344.4	265.101203	0.097048	10753232.52	265.101165	-0.044997	53652078.18
C_22H_12+	276.09327	-0.297847	12279667.64	276.093351	-0.004242	224419161.1	276.093448	0.347041	32871673.44	276.093347	-0.018182	155035369.6
C_22H_13+	277.101106	-0.254852	1504207.16	277.101147	-0.10745	28805716.72	277.101266	0.322414	4368354.62	277.101186	0.033475	15500463.82

C_22H_14+	278.108925	-0.275	509231.14	278.108961	-0.146095	9860535.29	278.109101	0.355281	2062768.54	278.109017	0.056135	4902314.65
C_23H_13+	289.101074	-0.356261	7243789.37	289.101136	-0.139728	131472811.3	289.101225	0.167471	18263229.42	287.085481	-0.159803	136092035.3
C_24H_12+	300.093263	-0.296302	10108302.67	300.093348	-0.013013	194826587.9	300.09345	0.32765	29293136.06	300.093325	-0.09056	132710367
C_25H_13+	313.101063	-0.365151	8015296.98	313.101132	-0.144102	151806745.9	313.101236	0.188085	21760579.55	313.101097	-0.256354	102942215.1
C_28H_14+	350.10891	-0.26334	4259903.17	350.108986	-0.046172	84904202.31	350.109172	0.484767	13780740.34	350.108944	-0.16661	58778231.64
C_30H_14+	374.108887	-0.306656	3597497.03	374.108985	-0.043883	74873512.38	374.109205	0.543553	13399136.28	374.108938	-0.170996	51386140.88
C_31H_15+	387.116719	-0.279998	2477593.21	387.116805	-0.056591	51458629.42	387.11703	0.525071	9785221.46	387.116749	-0.200088	34944255.36
C_32H_14+	398.108878	-0.312269	2641992.08	398.109004	0.006091	57438287.82	398.109249	0.619819	11626574.96	398.108949	-0.133665	39473599.56
C_34H_16+	424.12454	-0.264376	1087448.21	424.12465	-0.005062	25009825.52	424.124925	0.644423	6367120.12	424.124574	-0.1847	15994521.82
C_36H_18+	450.14026	-0.094399	128990.8	450.140373	0.15853	4165924.76	450.14078	1.061213	1794847.12	450.140244	-0.128952	1867108.07
C_40H_10+	490.07773	0.057351	46938.28	490.077789	0.178336	2422968.76	490.07828	1.179391	1729546.04	490.077654	-0.097153	754829.58
C_40H_16+	496.124577	-0.151049	492886.13	496.12473	0.158034	13918251.76	496.125206	1.116745	5034944.31	496.124598	-0.109689	7523590.3
C_40H_18+	498.140288	-0.028221	195151.52	498.140401	0.198034	6121946.57	498.140868	1.136672	2743033.86	498.140249	-0.106578	2984368.84
C_42H_16+	520.124591	-0.116461	281452.24	520.124774	0.23409	9660272.38	520.125305	1.254704	4249984.64	520.124632	-0.037548	4997282.98
C_42H_18+	522.140263	-0.074126	184985.21	522.140427	0.239649	5905570.22	522.140987	1.31266	2876498.39	522.140286	-0.030681	2876519.89
C_46H_20+	572.155742	-0.366705	35810.07	572.155992	0.069164	1417866.96	572.156644	1.209089	1164152.94	572.155835	-0.205423	655321.62
C_49H_21+	609.163533	-0.40033	27343.82	609.163785	0.013407	803178.97	609.164505	1.194545	753367.24	609.163656	-0.199075	386861.06
C_52H_22+	646.1718	0.306888	11905.84	646.171516	-0.132575	384985.01	646.172336	1.135587	389211.44	646.171392	-0.324515	222833.16
C_54H_22+	670.171874	0.40496	8172.84	670.171657	0.082133	337742.43	670.172363	1.135747	406085.88	670.171535	-0.099958	196045.3
C_60H_22+	742.171626	0.031837	8933.26	742.171709	0.144038	216199.94	742.172483	1.186508	303925.62	742.171551	-0.068581	131816.75
C_62H_22+	766.168875	-3.559309	13624.09	766.170327	-1.664216	286349.07	766.171881	0.363601	286907.57	766.170472	-1.474839	167655.43
C_66H_20+	812.155857	-0.117511	6648.86	812.155296	-0.807252	174863.42	812.156783	1.022671	169566.58	812.155073	-1.082687	110667.08
C_80H_22+	x	x	x	x	x	x	982.169805	-1.830246	21981.16	982.168633	-3.023176	59581.5

ii.

	Injector tip 5			Injector tip 6			Injector tip 7			Injector tip 8		
Formula	Center Mass (u)	Deviation (ppm)	Area (intensity)	Center Mass (u)	Deviation (ppm)	Area (intensity)	Center Mass (u)	Deviation (ppm)	Area (intensity)	Center Mass (u)	Deviation (ppm)	Area (intensity)
C_7H_7+	91.054378	1.665768	2519091033	91.055613	1.325198	195146624.4	91.054401	1.919228	262648770.9	91.054392	1.816091	3605472890
C_9H_7+	115.054158	-0.592953	2698071741	115.055754	-0.780821	198111469.6	115.054179	-0.415317	546745763.7	115.054172	-0.476754	3883322076
C_10H_8+	128.061878	-1.357532	1632267769	128.063613	-1.733088	136164450.4	128.061913	-1.085077	279432184.7	128.061894	-1.231983	2205441645
C_11H_7+	139.053993	-1.680742	577418249.4	139.0559	-2.11091	52664446.13	139.054037	-1.365939	102500279.2	139.054028	-1.428099	752710393.8
C_11H_9+	141.069609	-1.894562	468225857.7	141.071508	-2.329546	47505843.47	141.069662	-1.522097	98588972.18	141.069643	-1.653963	810299129.8
C_12H_6+	150.046156	-1.634965	503766064.8	150.048901	-2.090925	28374388.67	150.046201	-1.333922	97923238.8	150.046198	-1.360288	690098208.6
C_12H_8+	152.061799	-1.661396	1052351121	152.064616	-1.898514	87514535.17	152.061848	-1.339913	327177251.3	152.06184	-1.391724	1844808883
C_13H_10+	166.077384	-1.912228	29620142.45	166.078812	-2.100303	3379524.91	166.077399	-1.825465	10999315.53	166.077387	-1.895508	76262623.35
C_14H_8+	176.06176	-1.655941	338745009.8	176.065384	-2.127207	30453188.52	176.061847	-1.16213	120029979.3	176.061833	-1.239935	676163344.7
C_14H_10+	178.077394	-1.729909	313627250.3	178.079262	-2.049098	38552000.24	178.077482	-1.234279	126187417.7	178.077467	-1.316605	826412272.2
C_15H_10+	190.077343	-1.88665	52274227.13	190.079136	-2.894279	5606906.5	190.077377	-1.70758	25680972.4	190.077344	-1.882091	159876313.7
C_16H_10+	202.077382	-1.583697	472579165.8	202.07941	-2.019224	44580838.61	202.077486	-1.067523	211692051.1	202.077468	-1.156988	1159567296
C_17H_9+	213.069605	-1.274248	300352330.3	213.072671	-1.854997	18403650.94	213.069722	-0.725332	106404447.1	213.06971	-0.781283	603873904.6
C_17H_12+	216.093164	-0.870285	12571129.96	216.096182	-1.984568	1618091.22	216.093208	-0.667104	8545442.71	216.093159	-0.890938	47475048.02
C_18H_10+	226.077492	-0.926711	316371030.1	226.081059	-1.236709	18615642.91	226.07762	-0.362435	156540611.6	226.077608	-0.416354	768057334.1
C_18H_12+	228.093111	-1.054395	63287409.17	228.095193	-1.631755	4201532.44	228.093162	-0.833435	30537896.56	228.093118	-1.024119	177680303.6
C_19H_11+	239.085273	-1.059842	246985918.6	239.088059	-1.840824	14275628.2	239.085408	-0.498633	128608038.2	239.085372	-0.645398	581878015
C_20H_10+	250.077435	-1.065285	209353472.7	250.079933	-1.871107	8262272.3	250.077545	-0.628144	82695760.44	250.077509	-0.77139	432225470
C_20H_12+	252.09307	-1.116495	127426798.1	252.095452	-2.048458	6732121.75	252.093163	-0.747584	59504988	252.093107	-0.970073	286924041.8
C_21H_11+	263.085273	-0.963699	193152191.7	263.08784	-1.823974	7836917.02	263.085393	-0.507428	88828276.58	263.085349	-0.675983	416673527.4
C_21H_13+	265.100932	-0.922587	45710343.61	265.103653	-1.700594	2289855.48	265.100967	-0.79106	25475542.66	265.100926	-0.946606	116333686.6
C_22H_12+	276.093117	-0.85194	139350785.2	276.095753	-1.602453	5555215.76	276.093214	-0.500631	64565967.96	276.093167	-0.670542	304815203.9
C_22H_13+	277.100954	-0.803947	14010164.71	277.103592	-1.423508	687781.82	277.100958	-0.791229	9651024.54	277.100975	-0.727809	44452820.51
C_22H_14+	278.10878	-0.796409	5643422.32	278.111661	-1.594163	480500.04	278.108817	-0.664088	4817813.38	278.108779	-0.80171	22001916.78
C_23H_13+	287.085245	-0.982947	143008777	287.088053	-1.730315	4208630.12	287.085321	-0.715267	48977377.39	287.085292	-0.81755	277851740.3
C_24H_12+	300.093089	-0.874758	128231848.2	300.096251	-1.561978	3727457.1	300.093154	-0.660241	51367469.03	300.093125	-0.754712	264826232.1
C_25H_13+	313.100862	-1.004977	96715352.09	313.103786	-1.467476	2655324.47	313.100911	-0.848388	42440546.42	313.100891	-0.913288	204888569.2

C_28H_14+	350.108704	-0.849385	59928190.96	350.112271	-0.852717	1286982.26	350.108735	-0.761425	23446746.22	350.108757	-0.699919	126069259.4
C_30H_14+	374.108676	-0.870206	58887821.76	374.112857	-0.864883	964401.44	374.108722	-0.749105	19705056.87	374.108756	-0.657828	119155502.2
C_31H_15+	387.116504	-0.833766	41035088.04	387.120765	-0.56942	636111.17	387.116525	-0.779168	15712273.01	387.116577	-0.646708	88383692.77
C_32H_14+	398.108668	-0.837702	52580334.03	398.11324	-0.534482	623134.23	398.108728	-0.686875	14907027.19	398.108773	-0.57541	102930938.3
C_34H_16+	424.124296	-0.84034	24404654.95	424.131182	-0.320692	254578.88	424.124346	-0.72048	8881133.02	424.124399	-0.595631	56168308.05
C_36H_18+	450.139999	-0.673295	3592425.98	450.146314	-0.045063	47227.05	450.140097	-0.45513	2493675.89	450.140166	-0.303017	13884671.76
C_40H_10+	490.077342	-0.733679	9757347.9	490.083052	0.064426	11005.33	490.077434	-0.545971	445438.69	490.077536	-0.338533	17151515
C_40H_16+	496.124303	-0.702819	20385786.25	496.130392	0.374045	89438.04	496.1244	-0.508638	4678790.73	496.124499	-0.30924	44434175.7
C_40H_18+	498.139983	-0.641168	7359834.48	498.146156	0.474814	64622.8	498.140078	-0.449847	3042856.36	498.140188	-0.228189	22609913.97
C_42H_16+	520.124318	-0.64183	17238631.12	520.130313	0.121766	51327.11	520.12442	-0.446627	3349713.41	520.124554	-0.188727	37587701.47
C_42H_18+	522.139991	-0.595122	8278585.93	522.145884	0.289244	49886.09	522.140114	-0.360761	2793213.88	522.140233	-0.131288	23914717.28
C_46H_20+	572.155575	-0.658543	1968437.88	572.162095	-1.068799	17812.21	572.155714	-0.416932	984313.77	572.155867	-0.149394	8052819.67
C_49H_21+	609.163322	-0.747002	1201892.65	609.170948	1.48598	10525.98	609.163501	-0.452838	655401.91	609.163665	-0.183319	5384772.86
C_52H_22+	646.171073	-0.819222	602624.36	646.178463	-0.897059	9687.84	646.171166	-0.675656	308519.61	646.171406	-0.304107	2723504.91
C_54H_22+	670.17111	-0.734879	646615.87	670.179833	-0.559566	4955.31	670.171195	-0.607273	344240.8	670.171443	-0.237347	2946489.58
C_60H_22+	742.171004	-0.806497	597373.24	742.17951	1.2439	454.79	742.171219	-0.516149	190333.66	742.171441	-0.217442	2581448.82
C_62H_22+	766.170283	-1.721811	659534.12	766.187631	-0.469373	1184.41	766.170699	-1.178938	175158.88	766.170925	-0.883742	2496503.02
C_66H_20+	812.154988	-1.18707	557076.32	**x**	**x**	**x**	812.155316	-0.783691	69317.29	812.155543	-0.503374	1752231.43
C_80H_22+	982.1703	-1.3402	88021	**x**	**x**	**x**	982.170143	-1.486115	22370.9	982.16904	-2.608936	287088.25

(b) i.

	Injector needle 1			Injector needle 2			Injector needle 3			Injector needle 4		
Formula	**Center Mass (u)**	**Deviation (ppm)**	**Area (intensity)**	**Center Mass (u)**	**Deviation (ppm)**	**Area (intensity)**	**Center Mass (u)**	**Deviation (ppm)**	**Area (intensity)**	**Center Mass (u)**	**Deviation (ppm)**	**Area (intensity)**
C_7H_7+	91.054442	2.36962	10795.52	91.05446	2.567513	2487062.32	91.054474	2.720858	8900815.18	91.054426	2.187108	2753536.42
C_9H_7+	115.054233	0.051761	81638.75	115.054267	0.35057	4070307.73	115.054272	0.394698	23371405.35	115.05422	-0.057023	5256106.67
C_10H_8+	128.061973	-0.616866	42735.47	128.062002	-0.390263	2369330.81	128.062007	-0.345617	12022456.55	128.061944	-0.842741	3201968.46
C_11H_7+	139.054078	-1.071567	12319.76	139.054124	-0.741279	893598.47	139.054133	-0.675542	2648937.8	139.054062	-1.183246	1114582.08
C_11H_9+				141.069744	-0.942825	735626.36	141.06976	-0.825352	3686255.77	141.069684	-1.364855	958071.86
C_12H_6+				150.046292	-0.733505	746654.73	150.046311	-0.602751	2034093.29	150.046232	-1.133459	611952.75
C_12H_8+				152.061929	-0.805109	1964987.66	152.061959	-0.608235	8152101.92	152.061868	-1.208676	1925381.66
C_13H_10+				166.077492	-1.260469	53684.9	166.077536	-0.995255	388911.21	166.077453	-1.497085	38107.99
C_14H_8+				176.061919	-0.750987	559120.07	176.061969	-0.468863	2555733.46	176.061858	-1.099376	514380.51
C_14H_10+				178.077559	-0.79943	644913.34	178.077613	-0.500801	3241625.46	178.077495	-1.159113	656872.07
C_15H_10+				190.077521	-0.949856	99159.82	190.077537	-0.86471	688258.16	190.07744	-1.377907	89528.9
C_16H_10+				202.07755	-0.750198	714654.85	202.077635	-0.331052	5349477.51	202.077496	-1.019208	826564.73
C_17H_9+				213.069817	-0.281822	375038.06	213.069878	0.005138	2221680.22	213.069756	-0.564598	430336.61
C_17H_12+				216.093419	0.309181	11269.27	216.093403	0.235761	281288.34	216.093264	-0.404041	14140.2
C_18H_10+				226.077693	-0.038272	392783.06	226.077783	0.360531	3404985.41	226.07764	-0.275038	463741.6
C_18H_12+				228.093369	0.0749	73860.44	228.093348	-0.016496	755955.5	228.093271	-0.356224	102264.68
C_19H_11+				239.085494	-0.1387	296869.73	239.08558	0.220704	2997585.06	239.085438	-0.370387	386630.79
C_20H_10+				250.077677	-0.098953	206749.3	250.077729	0.10843	1607670.27	250.077629	-0.289352	242896.01
C_20H_12+				252.093302	-0.196721	138313.11	252.093365	0.054202	1422720.13	252.093284	-0.27085	179907.56
C_21H_11+				263.085549	0.083363	185859.92	263.085594	0.254341	1890089.44	263.085466	-0.231246	235375.2
C_21H_13+				265.101212	0.132138	46951.48	265.101207	0.112235	637186.68	265.101109	-0.256957	60209.56
C_22H_12+				276.093395	0.157916	121893.5	276.093428	0.274921	1404540.75	276.093341	-0.038612	160799.08
C_22H_13+				277.101252	0.273044	10305.16	277.101228	0.186392	273390.96	277.101044	-0.480459	9235.13
C_22H_14+				278.108996	-0.022743	4136.82	278.109087	0.307702	123027.71	278.108859	-0.514162	6699.09
C_23H_13+				289.101174	0.042435	66577.76	287.085556	0.101604	958929.48	287.085484	-0.147571	131662.16
C_24H_12+				300.093349	-0.008866	87711.33	300.093412	0.201669	1068440.5	300.093329	-0.076425	102718.69
C_25H_13+				313.10117	-0.020713	59954.72	313.101193	0.051772	944141	313.101078	-0.315146	78540.63
C_28H_14+				350.10901	0.024645	22395.56	350.109048	0.132216	499448.63	350.108944	-0.164713	26967.89

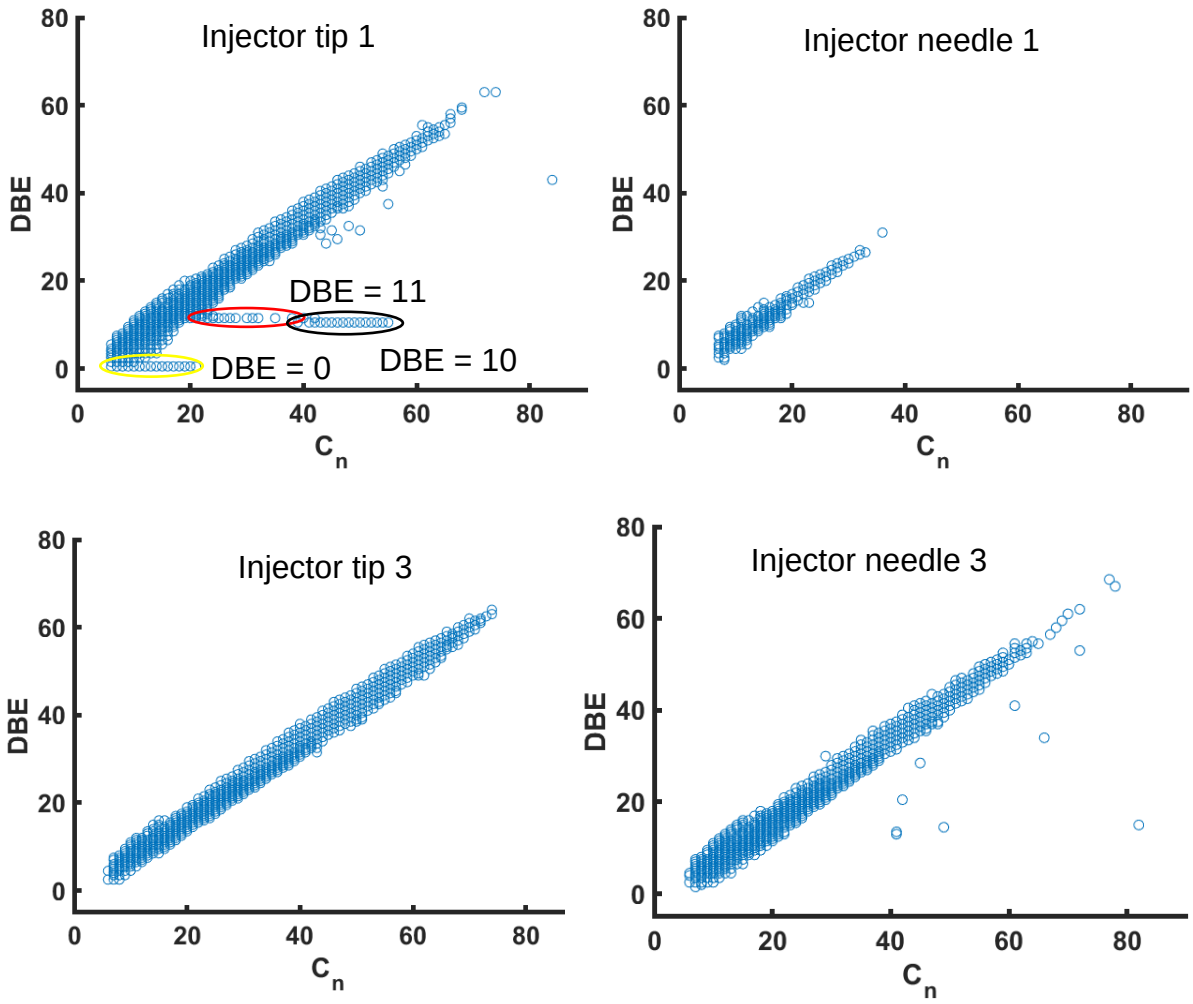
C_30H_14+		374.109015	0.034357	21020.63	374.109037	0.093319	377793.25	374.108933	-0.184251	12541.58
C_31H_15+		387.117001	0.450215	11137.93	387.116841	0.035719	320463.9	387.116795	-0.081329	7701.38
C_32H_14+		398.10912	0.296831	12184.16	398.109077	0.189256	260855.39	398.108906	-0.240462	11622.62
C_34H_16+					424.124709	0.133657	165581.84	424.124685	0.078784	4369.54
C_36H_18+					450.140444	0.314601	38668.45			
C_40H_10+					490.077995	0.597615	547.14			
C_40H_16+					496.124726	0.149499	51100.27			
C_40H_18+					498.140596	0.591081	32116.4			
C_42H_16+					520.124716	0.12295	24890.5			
C_42H_18+					522.140347	0.086731	34349.63			
C_46H_20+					572.156197	0.428248	6460.84			

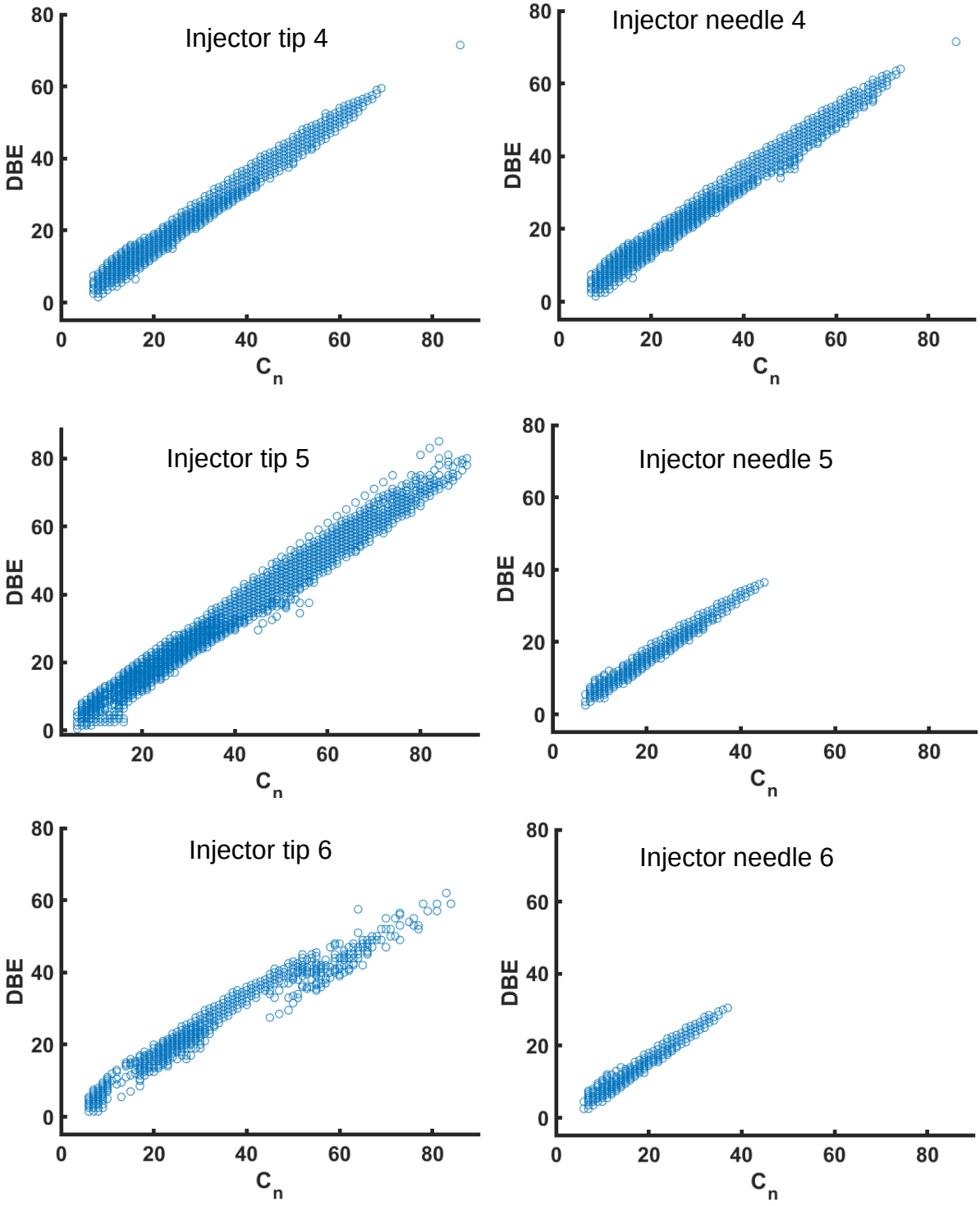
ii.

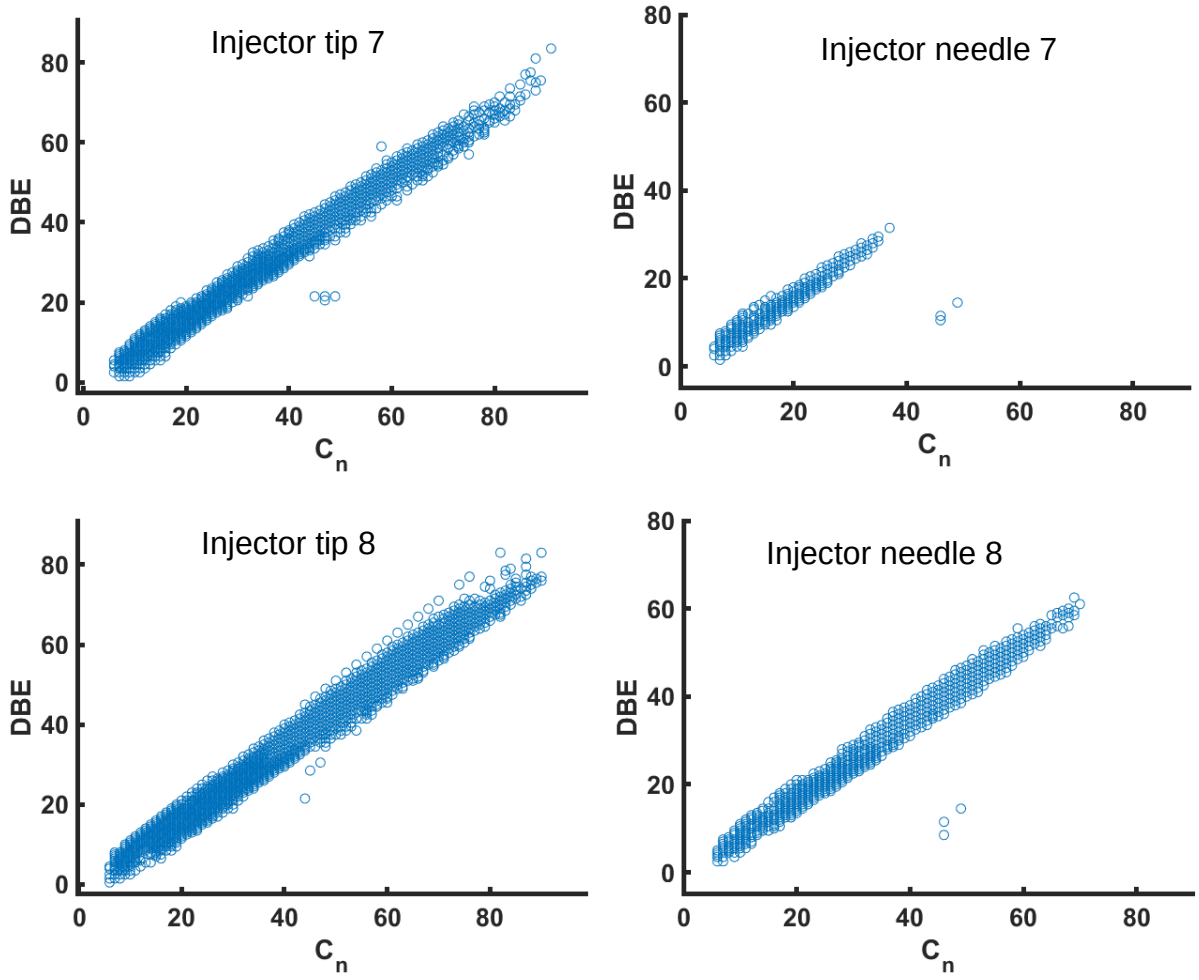
Formula	Injector needle 5			Injector needle 6			Injector needle 7			Injector needle 8		
C_7H_7+	**Center Mass (u)**	**Deviation (ppm)**	**Area (intensity)**	**Center Mass (u)**	**Deviation (ppm)**	**Area (intensity)**	**Center Mass (u)**	**Deviation (ppm)**	**Area (intensity)**	**Center Mass (u)**	**Deviation (ppm)**	**Area (intensity)**
C_9H_7+	91.054429	2.217383	48917767.81	91.053336	2.173303	2385472.48	91.053336	2.173303	2385472.48	91.054414	2.058531	2073659.82
C_10H_8+	115.054223	-0.027953	72336337.31	115.052851	-0.065253	5607633.77	115.052851	-0.065253	5607633.77	115.054202	-0.212122	3727549.35
C_11H_7+	128.061953	-0.771347	44650777.51	128.060691	-0.817399	3402542.25	128.060691	-0.817399	3402542.25	128.061941	-0.866345	2165602.59
C_11H_9+	139.054065	-1.16508	9248577.96	139.052374	-1.179581	1153835.83	139.052374	-1.179581	1153835.83	139.054042	-1.327213	882600.66
C_12H_6+	141.069693	-1.30117	12980909.03	141.068355	-1.35092	1091975.2	141.068355	-1.35092	1091975.2	141.069653	-1.586892	750449.41
C_12H_8+	150.046232	-1.13022	5705294.61	150.044949	-1.127418	979656.23	150.044949	-1.127418	979656.23	150.046151	-1.667082	489216.28
C_13H_10+	152.061869	-1.200424	17242455.6	152.059701	-1.204068	2776259.93	152.059701	-1.204068	2776259.93	152.061833	-1.438311	1810167.74
C_14H_8+	166.077475	-1.365104	589765.99	166.076799	-1.44059	71826.7	166.076799	-1.44059	71826.7	166.07745	-1.51397	38606.42
C_14H_10+	176.061848	-1.159092	4984750.52	176.059575	-1.100357	817814.19	176.059575	-1.100357	817814.19	176.061828	-1.27102	450314.9

C_15H_10+	178.077485	-1.218599	6482070.29	178.076866	-1.176204	974862.57	178.076866	-1.176204	974862.57	178.077493	-1.172197	704143.21
C_16H_10+	190.077457	-1.285667	1243810.68	190.076671	-1.372013	154164.3	190.076671	-1.372013	154164.3	190.077345	-1.875594	131513.85
C_17H_9+	202.077492	-1.036787	9541383.74	202.076707	-1.045905	1260511.87	202.076707	-1.045905	1260511.87	202.077496	-1.016327	877613.9
C_17H_12+	213.069742	-0.633433	4828923.66	213.067445	-0.610196	612504.02	213.067445	-0.610196	612504.02	213.069673	-0.955733	329605.95
C_18H_10+	216.093334	-0.08201	407474.73	216.092126	-0.165106	23779.12	216.092126	-0.165106	23779.12	216.093079	-1.26306	16727.51
C_18H_12+	226.077643	-0.262022	5547389.76	226.075119	-0.270591	755109.62	226.075119	-0.270591	755109.62	226.077555	-0.650352	414271.76
C_19H_11+	228.09327	-0.358528	1858708.87	228.091952	-0.388635	153725.21	228.091952	-0.388635	153725.21	228.093113	-1.045301	117032.88
C_20H_10+	239.085445	-0.343003	5127481.53	239.083338	-0.384497	586824.51	239.083338	-0.384497	586824.51	239.085354	-0.721052	372164.24
C_20H_12+	250.07762	-0.327695	3093150.35	250.076212	-0.308384	399317.06	250.076212	-0.308384	399317.06	250.077473	-0.913018	175493.83
C_21H_11+	252.093264	-0.349654	2791235.51	252.091686	-0.363972	299323.68	252.091686	-0.363972	299323.68	252.093094	-1.022886	186883.68
C_21H_13+	263.085481	-0.173578	3255689.85	263.083825	-0.243278	379020.56	263.083825	-0.243278	379020.56	263.085307	-0.836001	185885.06
C_22H_12+	265.101119	-0.218555	1060565.12	265.099592	-0.33116	100341.95	265.099592	-0.33116	100341.95	265.100946	-0.87025	66358.81
C_22H_13+	276.093328	-0.086218	2392278.47	276.091745	-0.137451	268370.67	276.091745	-0.137451	268370.67	276.093176	-0.637183	144058.46
C_22H_14+	277.101154	-0.082059	262567.7	277.099562	-0.123638	36466.24	277.099562	-0.123638	36466.24	277.10094	-0.853409	20614.15
C_23H_13+	278.108962	-0.144602	141728.16	278.107298	-0.11711	14994.65	278.107298	-0.11711	14994.65	278.108798	-0.732798	13882.81
C_24H_12+	289.101109	-0.22639	1485867.56	287.083804	-0.24428	213953.71	287.083804	-0.24428	213953.71	287.085326	-0.699453	93245.45
C_25H_13+	300.093317	-0.116511	1898227.42	300.09136	-0.108394	195568.68	300.09136	-0.108394	195568.68	300.093132	-0.734122	79115.36
C_28H_14+	313.101078	-0.315022	1577861.26	313.099318	-0.277459	148029.88	313.099318	-0.277459	148029.88	313.100922	-0.815098	70341.11
C_30H_14+	350.108925	-0.220355	804612.73	350.106988	-0.303351	61979.29	350.106988	-0.303351	61979.29	350.108832	-0.486147	25399.31
C_31H_15+	374.108906	-0.256646	654207.59	374.106535	-0.301773	43086.65	374.106535	-0.301773	43086.65	374.108943	-0.156697	13390.15
C_32H_14+	387.11671	-0.30089	466112.13	387.114622	-0.266519	30586.86	387.114622	-0.266519	30586.86	387.116632	-0.504044	10820.12
C_34H_16+	398.1089	-0.256123	476417.3	398.1063	-0.282261	31175.22	398.1063	-0.282261	31175.22	398.108929	-0.183461	9942.12
C_36H_18+	424.124539	-0.266164	205316.63	424.121789	-0.322677	8195.01	424.121789	-0.322677	8195.01	424.124762	0.260276	3871.22
C_40H_10+	450.140132	-0.378626	33250.2	450.13797	1.167836	339.61	450.13797	1.167836	339.61			
C_40H_16+	490.077629	-0.14851	5419.74	490.074303	-0.004446	704.52	490.074303	-0.004446	704.52			
C_40H_18+	496.124511	-0.283477	96324.92	496.120738	-0.783292	2651.11	496.120738	-0.783292	2651.11			
C_42H_16+	498.140132	-0.340657	37093.8	498.137189	0.202674	724.75	498.137189	0.202674	724.75			
C_42H_18+	520.1246	-0.09996	57554.88	520.120747	-0.884376	1313.03	520.120747	-0.884376	1313.03			
C_46H_20+	522.140169	-0.254016	31503.29									

S4.6


Injector tip 1
DBE = 11
DBE = 0
DBE = 10
Injector needle 1
Injector tip 3
Injector needle 3
DBE
C_n
0
20
40
60
80


Injector tip 4
Injector needle 4
Injector tip 5
Injector needle 5
Injector tip 6
Injector needle 6
DBE
C n
0
20
40
60
80

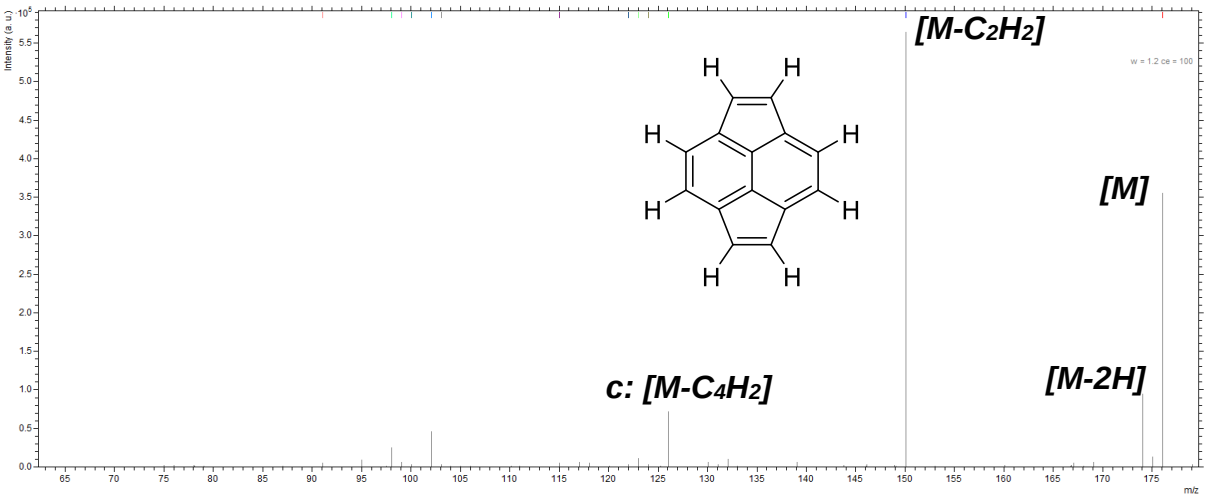


Supplementary figure S4.6. *Double bond equivalence versus C number plot for all CH containing species in deposits.*

S4.7

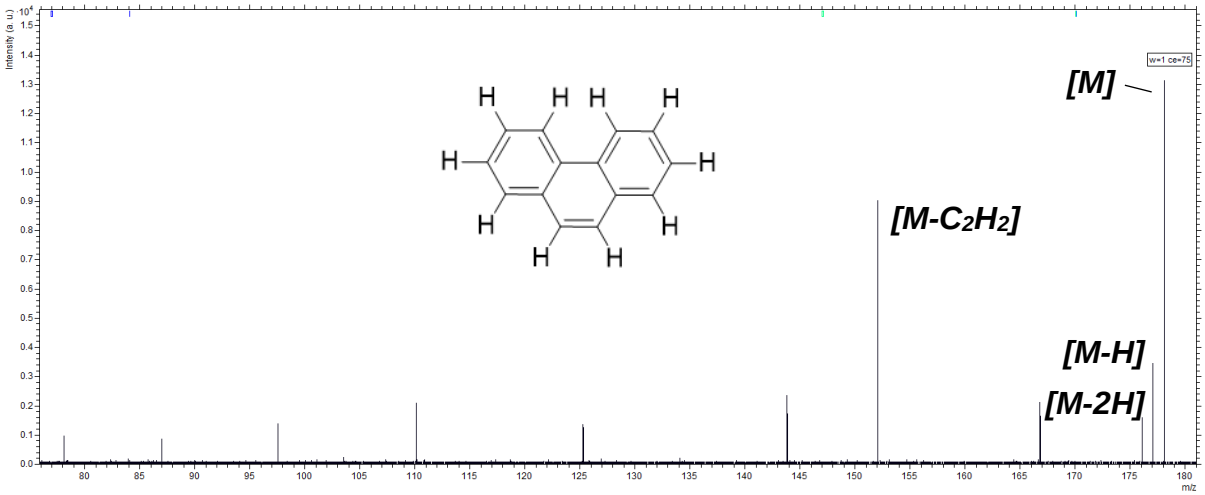
(a)

Parent ion	Secondary fragments				
C_14H_8+	Center Mass (u)	Formula	Mass Deviation (ppm)	Area (intensity)	Neutral loss
	176.061895	C_14H_8+	-0.85552	1456367.92	-
	174.04620	C_14H_6+	-0.9381	415372	[M – 2H]
	150.046251	C_12H_6+	-1.003395	2471493.3	[M – C_2H_2]
	126.046337	C_10H_6+	-0.513255	317449.17	[M – C_4H_2]
	124.030706	C_10H_4+	-0.367688	14827.48	[M – $(C_2H_2)_2$]
	122.015045	C_10H_2+	-0.459973	14826.21	[M – C_4H_6]
	102.046525	C_8H_6+	1.207614	228100.11	[M – $(C_3H)_2$]
	100.030897	C_8H_4+	1.454325	16344.19	[M – $(C_3H_2)_2$]
	98.015273	C_8H_2+	1.747147	123642.9	[M – $(CH)_6$]



(b)

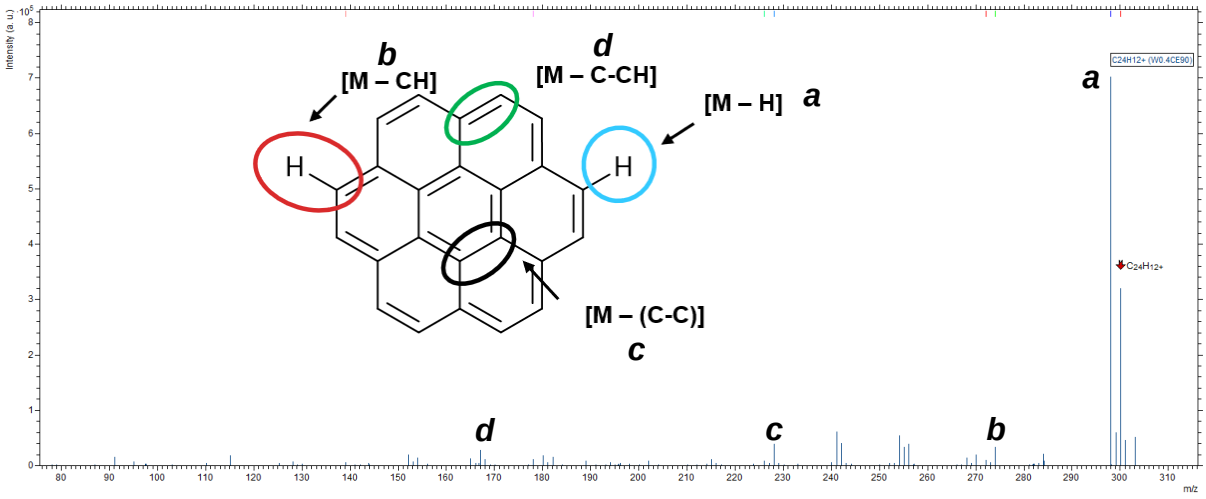
Parent ion	Secondary fragments				
C_14H_10+	Center Mass (u)	Formula	Mass Deviation (ppm)	Area (intensity)	Neutral loss
Phenanthrene	178.0775	C_14H_10+	-0.85552	58443.21	-
	177.0698	C_14H_9+	-0.704189	15289.6	[M – H]
	176.0619	C_14H_8+	-0.986089	7011.52	[M – 2H]
	152.0619	C_12H_8+	-0.999984	40077.07	[M – C_2H_2]



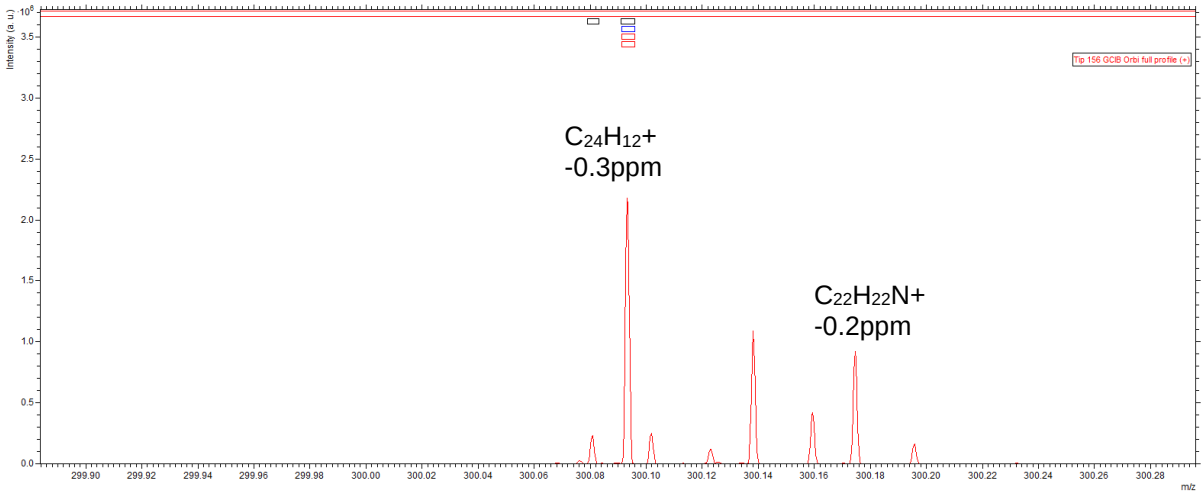
(c)

Parent ion	Secondary fragments				
C_24H_12+ (Coronene)	**Center Mass (u)**	**Formula**	**Mass Deviation (ppm)**	**Area (intensity)**	**Neutral Loss**
	300.093206	C_24H_12+	-0.486209	1364687	-
	298.077598	C_24H_10+	-0.34793	2971778	[M – 2H]
	274.077588	C_22H_10+	-0.413692	137214.9	[M – C_2H_2]
	228.093164	C_18H_12+	-0.824654	3708.26	[M – C_6]
	226.077673	C_18H_10+	-0.128147	36816.25	[M – C_6H_2]
	178.077454	C_14H_10+	-1.390035	49025.84	[M – $C_{10}H_2$]

i. MS/MS

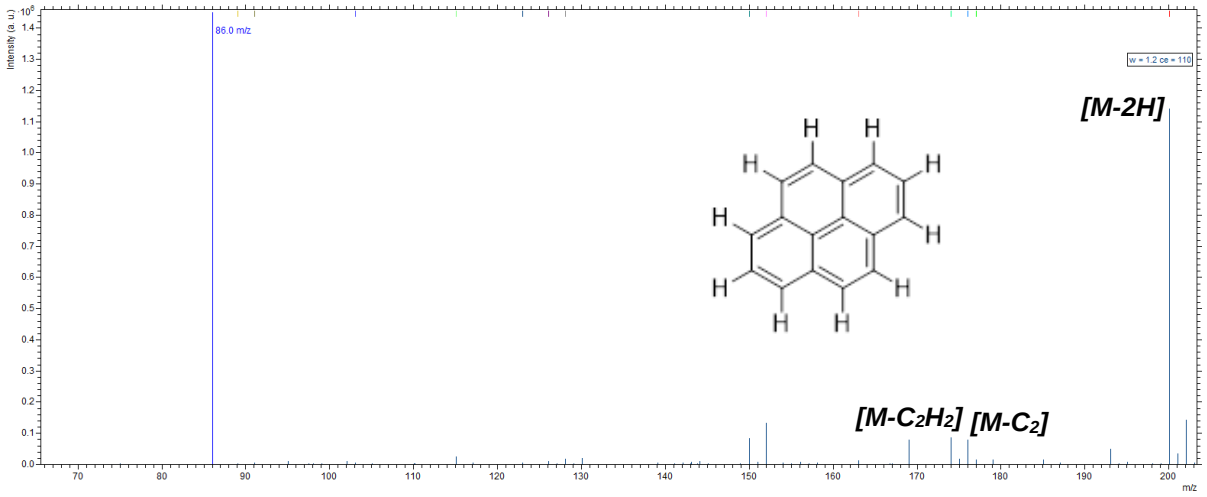


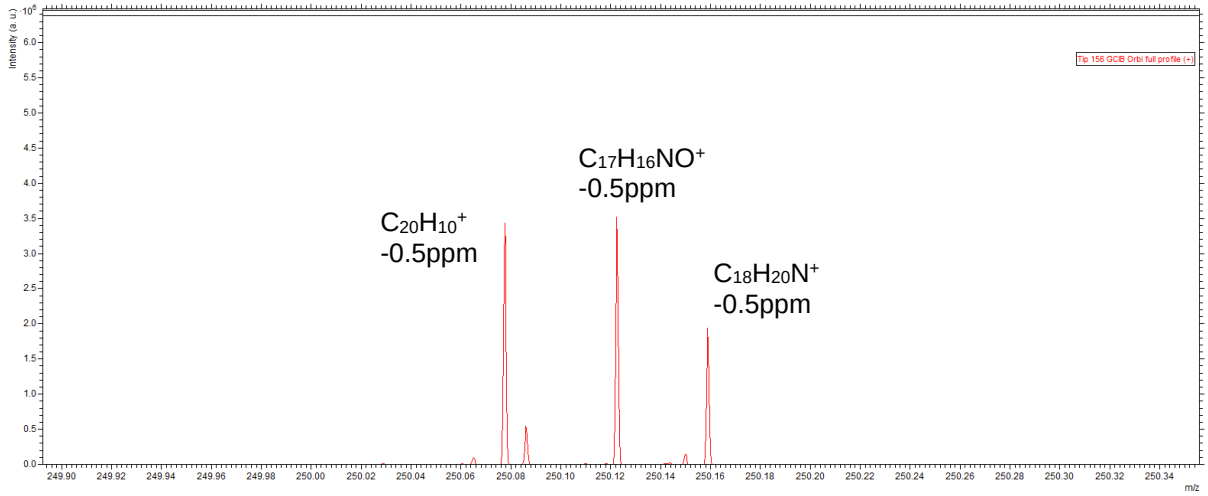
ii. MS1 showing incorporation of $C_{22}H_{22}N^+$ (0.2 ppm) into the analysis window of MS/MS peaks



(d)

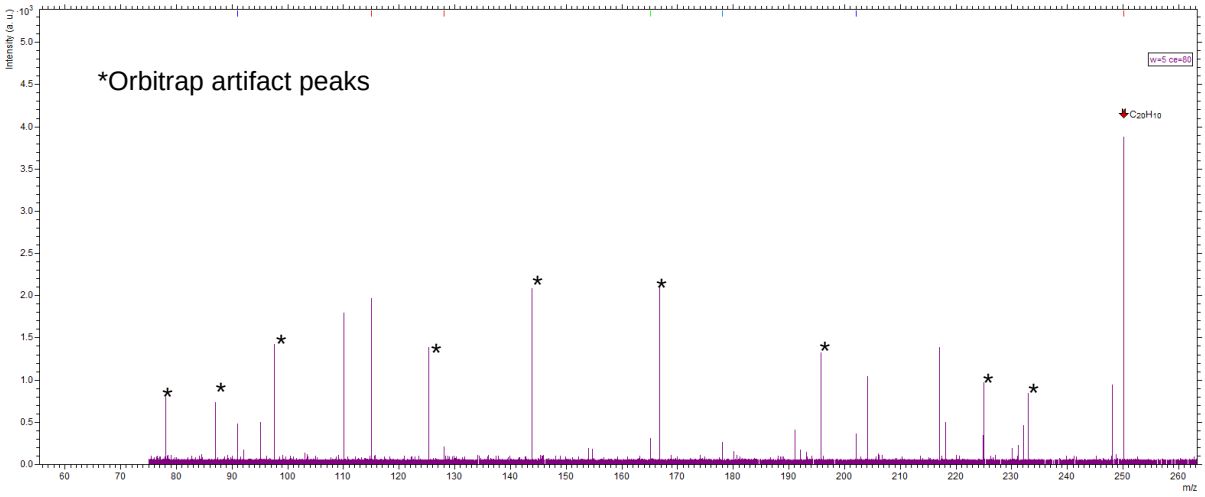
Parent ion	Secondary fragments				
C_16H_10+	**Center Mass (u)**	**Formula**	**Mass Deviation (ppm)**	**Area (intensity)**	**Neutral Loss**
(Pyrene)	200.061899	C_16H_8+	-0.763843	4924050.79	[M – 2H]
	176.061865	C_14H_8+	-1.06155	356336.51	[M – C_2]
	174.046231	C_14H_6+	-0.98235	374845.95	[M – C_2H_2]
	152.06186	C_12H_8+	-1.262254	565560.68	[M – C_4]
	150.046229	C_12H_6+	-1.150128	358354.58	[M – C_4H_2]
	128.061952	C_10H_8+	-0.778506	76947.64	[M – C_6]
	126.046328	C_10H_6+	-0.580416	46241.78	[M – C_6H_2]





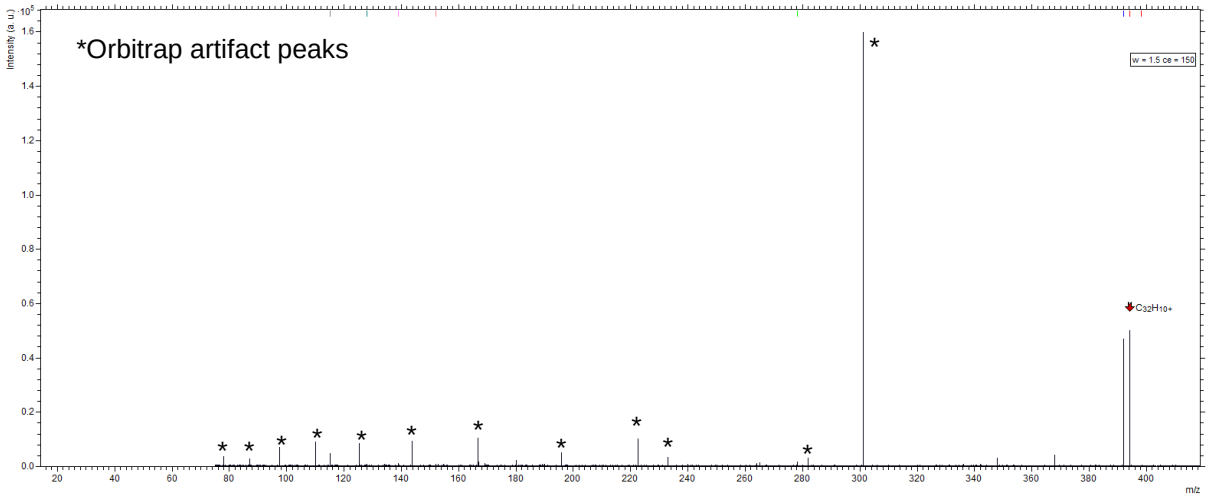
(e)

Parent ion	Secondary fragments				
C_20H_10+	**Center Mass (u)**	**Formula**	**Mass Deviation (ppm)**	**Area (intensity)**	**Neutral Loss**
(corannulene)	250.077625	C_20H_10+	-0.307937	16490.38	-
	248.0620	C_20H_8+	-0.1411	1478	[M – H_2]
	202.077403	C_16H_10+	-1.476591	1585.07	[M – C_4]
	178.077438	C_14H_10+	-1.48358	1081.03	[M – C_6]
	128.061943	C_10H_8+	-0.850891	834.67	[M – $C_{10}H_2$]
	115.054196	C_9H_7+	-0.262497	9798	[M – $C_{11}H_3$]
	91.054415	C_7H_7+	2.070339	2535.49	[M – $C_{13}H_{13}$]



(f)

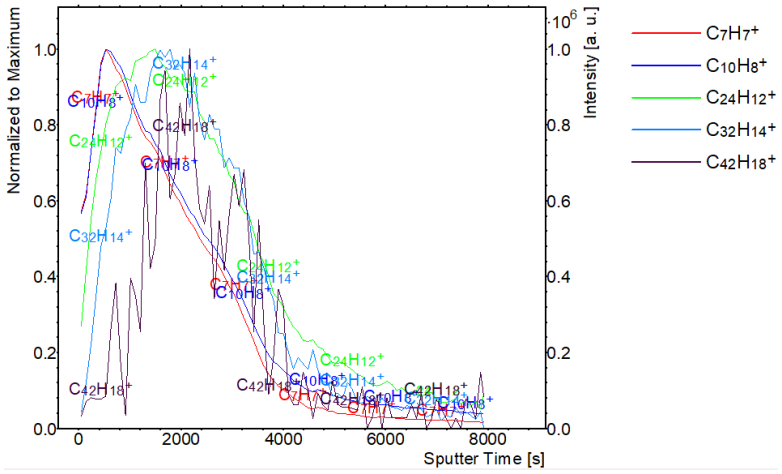
Parent ion	Secondary fragments				
C_32_H14+	**Center Mass (u)**	**Formula**	**Mass Deviation (ppm)**	**Area (intensity)**	**Neutral Loss**
(Ovalene)	394.077868	C_32H_10+	0.421509	215353.63	-
	392.062192	C_32H_8+	0.357463	201406.39	$[M - H_2]$
	152.061736	C_12H_8+	-2.075409	3864.36	$[M - C_{20}H_2]$
	139.054059	C_11H_7+	-1.205653	4964.57	$[M - C_{21}H_3]$
	128.062003	C_10H_8+	-0.377032	4006.6	$[M - C_{22}H_2]$



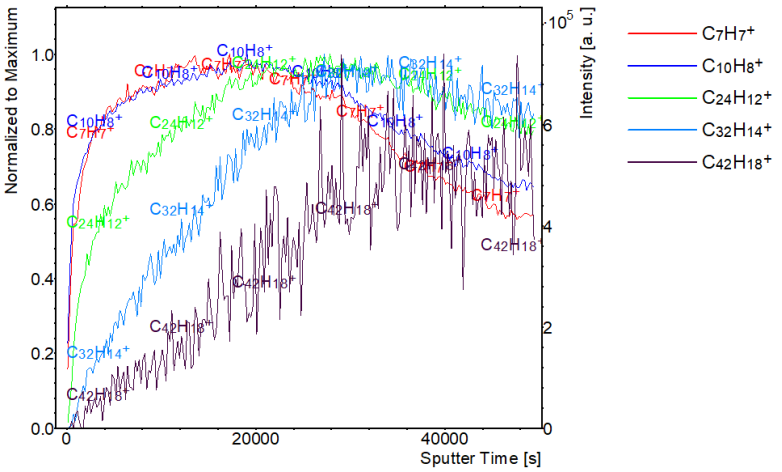
Supplementary figure S4.7*: MS/MS data for key PAHs with relevant spectra.* ***(a)*** *Anthracene ($C_{14}H_8^+$, NCE 100, IW 1.2 u),* ***(b)*** *$C_{14}H_{10}^+$ (NCE, 75 IW 1 u),* ***(c)*** *$C_{16}H_{10}^+$ (NCE 110, IW 1.2 u)* ***(d)*** *Coronene ($C_{24}H_{12}^+$, NCE 90, IW 0.4 u),* ***(e)*** *corannulene ($C_{20}H_{10}^+$, NCE 80, IW 5 u),* ***(f)*** *Ovalene ($C_{32}H_{14}^+$, NCE 150, IW 1.5). NCE, normalized collision energy. IW, isolation width. Where suitable, chemical structures and suggested fragments are assigned.*

S4.8

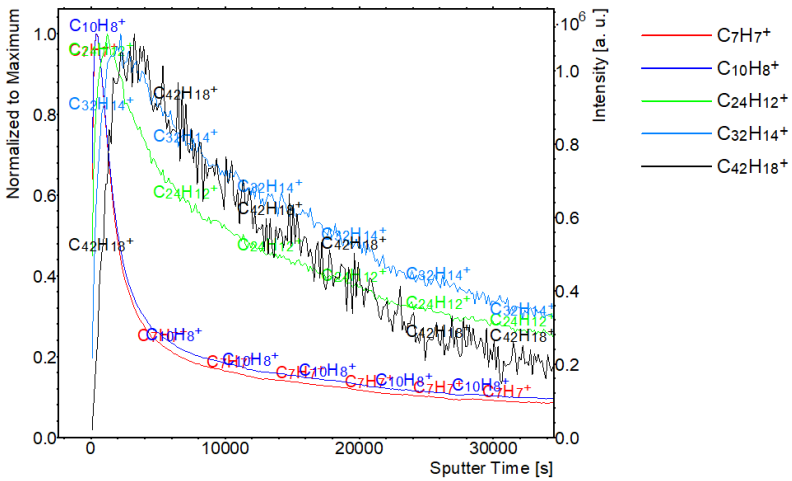
(a)


Normalized to Maximum
Intensity [a. u.]
Sputter Time [s]
C7H7+
C10H8+
C24H12+
C32H14+
C42H18+

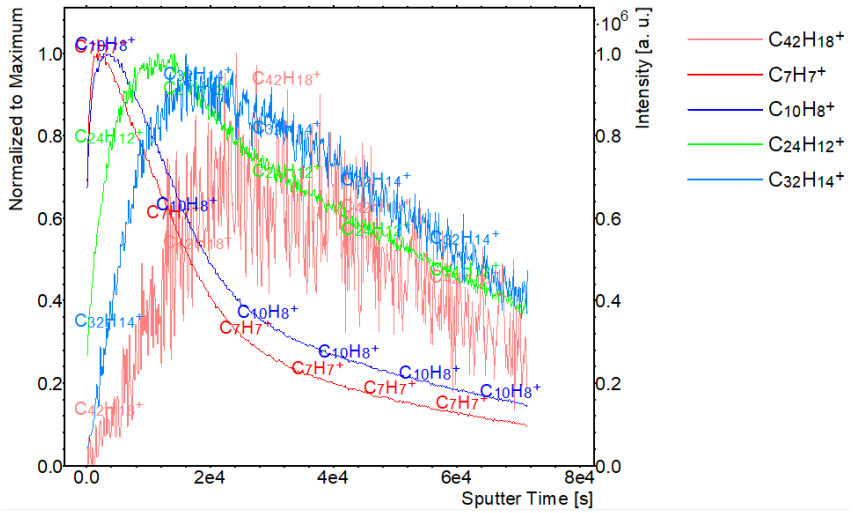
(b)


Normalized to Maximum
Intensity [a. u.]
Sputter Time [s]
C7H7+
C10H8+
C24H12+
C32H14+
C42H18+

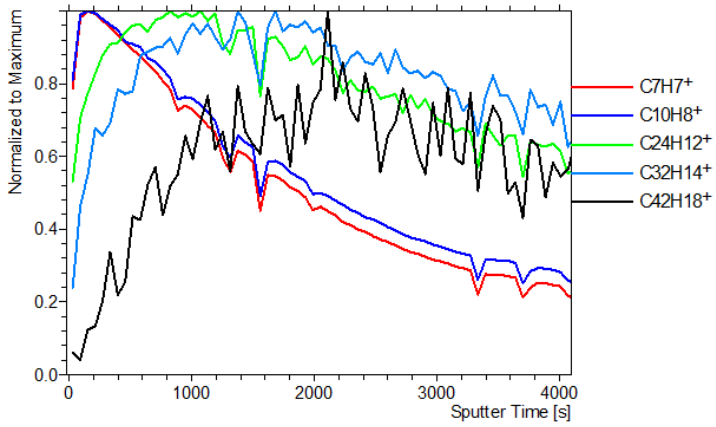
(c)


Normalized to Maximum
Intensity [a. u.]
Sputter Time [s]
C7H7+
C10H8+
C24H12+
C32H14+
C42H18+

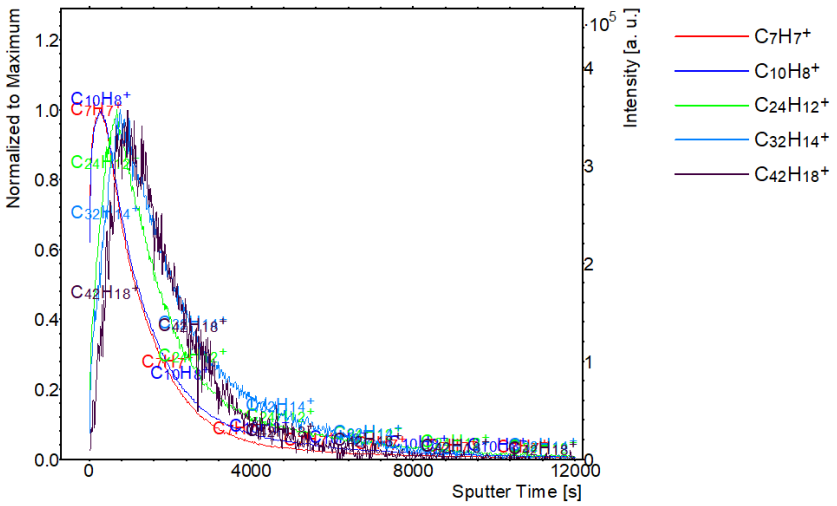
(d)


Normalized to Maximum
Intensity [a. u.]
Sputter Time [s]
C42H18+
C7H7+
C10H8+
C24H12+
C32H14+

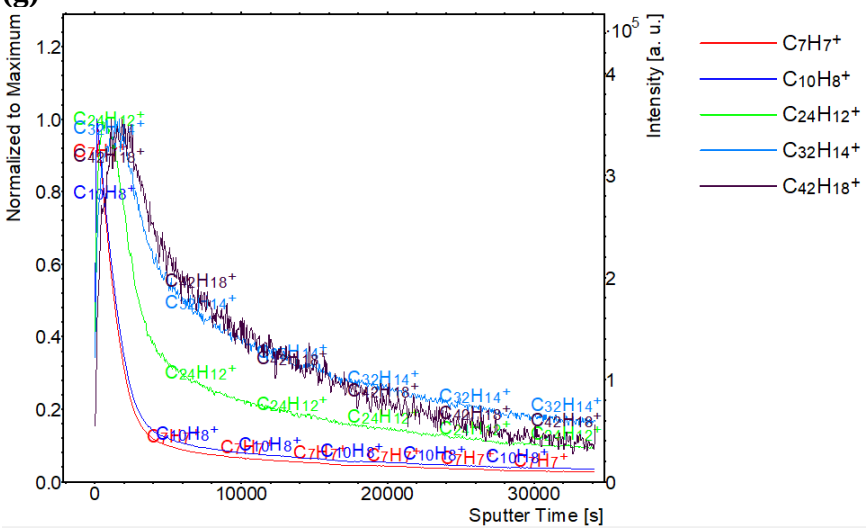
(e)


Normalized to Maximum
Sputter Time [s]
C7H7+
C10H8+
C24H12+
C32H14+
C42H18+

(f)

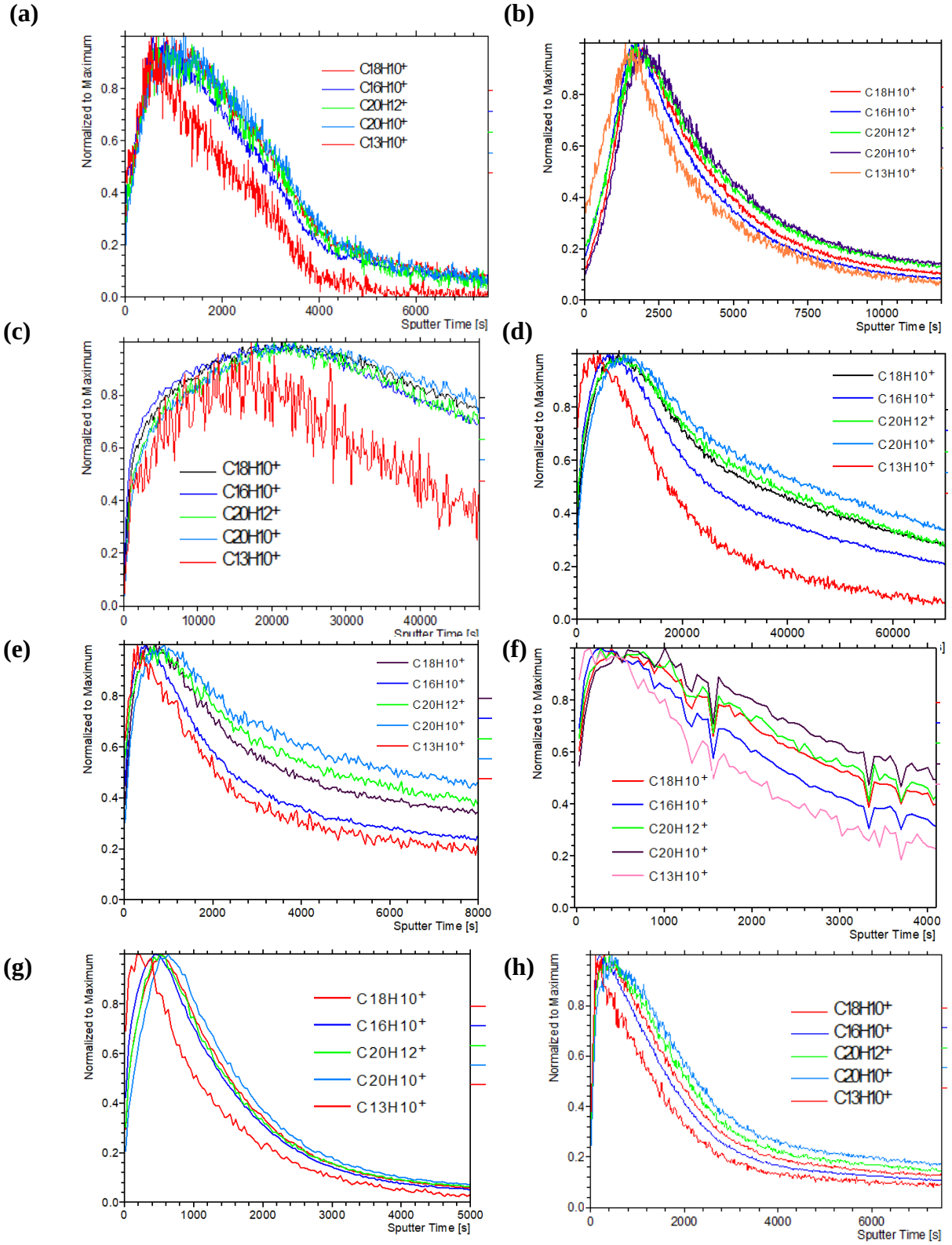

Normalized to Maximum
Intensity [a. u.]
Sputter Time [s]
C7H7+
C10H8+
C24H12+
C32H14+
C42H18+

(g)



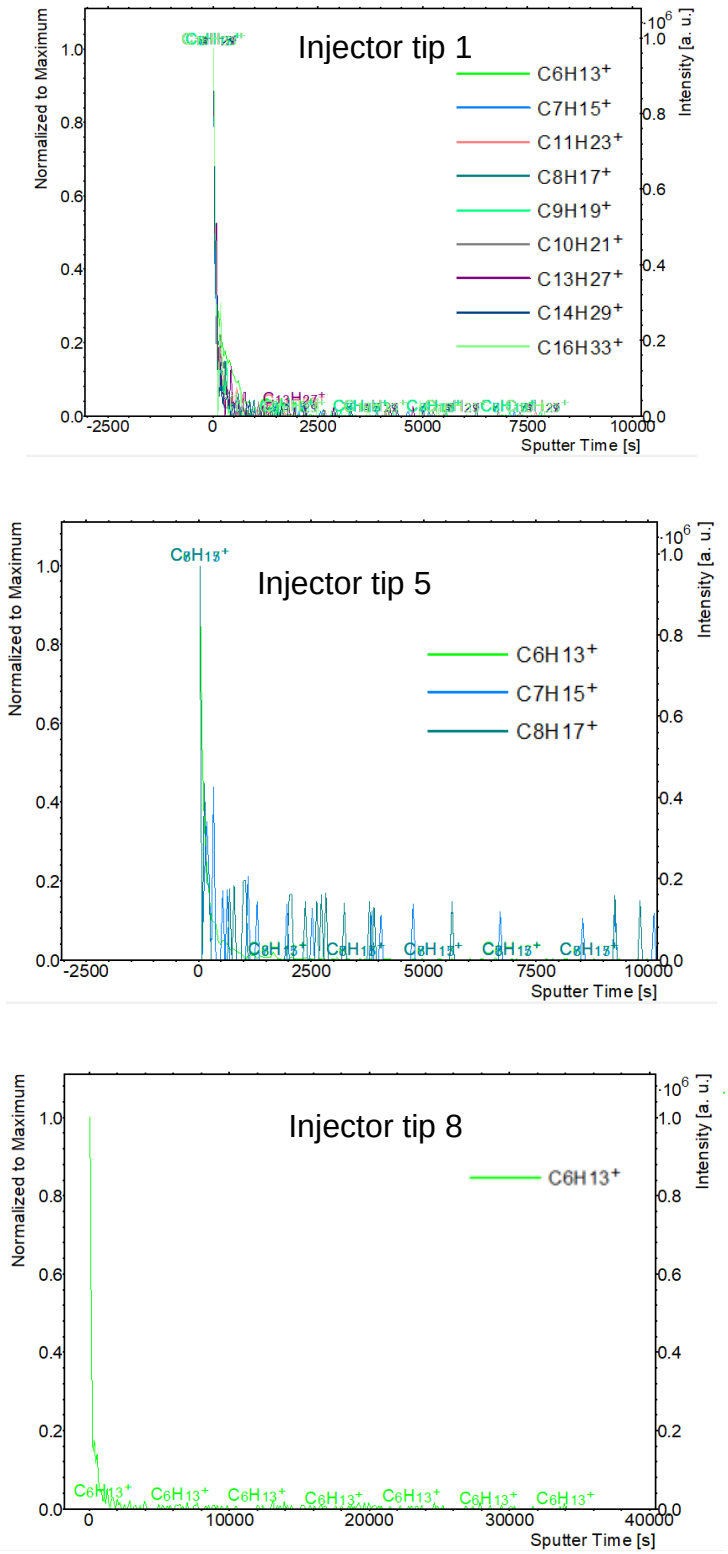
Supplementary figure S4.8*. Depth profile of polycyclic aromatic hydrocarbons in* ***(a)*** *Injector tip 1,* ***(b)*** *Injector tip 3,* ***(c)*** *Injector tip 4,* ***(d)*** *Injector tip 5,* ***(e)*** *Injector tip 6,* ***(f)*** *Injector tip 7,* ***(g)*** *Injector tip 8. Ions displayed are (in order of prevalence in the deposit* $C_7H_7^+$*, naphthalene (*$C_{10}H_8^+$*), coronene (*$C_{24}H_{12}^+$*), ovalene (*$C_{32}H_{14}^+$*) and hexabenzocoronene (*$C_{42}H_{18}^+$*).*

S4.9



Supplementary figure S4.9. *Depth profiles of 5-membered PAHs in* ***(a)*** *Injector 1,* ***(b)*** *Injector 3,* ***(c)*** *Injector 4,* ***(d)*** *Injector 5,* ***(e)*** *Injector 6,* ***(f)*** *Injector 7,* ***(g)*** *Injector 8. Fluorene ($C_{13}H_{10}^{+}$,), cyclopentapyrene ($C_{18}H_{10}$) benzofluoranthene ($C_{20}H_{12}$) and corannulene ($C_{20}H_{10}$).*

S4.10
(a)



Supplementary figure S4.10. *Depth profiles of species with an aliphatic content for species which contained ions with enough intensity to provide an informative depth profile.*

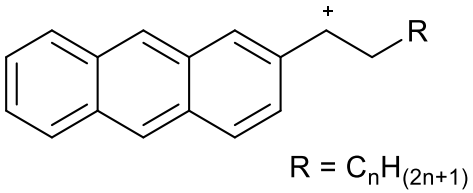
Supplementary table S4.11*: 3D OrbiSIMS accurate mass data for hydrocarbons with an aliphatic contribution identified in injector tip deposits. (a) Saturated hydrocarbons, (b) species with an aromatic portion with putative assignments. All ion peak tables were exported from Surface Lab software (IONTOF GmbH, version 7.1.b).*

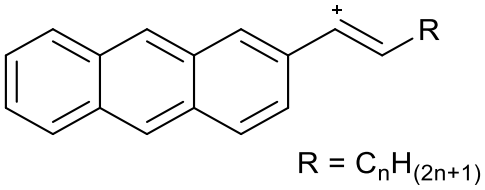
(a)

DBE = 0	Injector tip 1			Injector tip 2			Injector tip 5			Injector tip 8		
Assignment	Center Mass (u)	Deviation (ppm)	Area	Center Mass (u)	Deviation (ppm)	Area	Center Mass (u)	Deviation (ppm)	Area	Center Mass (u)	Deviation (ppm)	Area
C_6H_13+	85.101357	2.122838	749809.04	85.101397	2.591697	520115.87	85.101356	2.110708	360742.86	85.10136	2.155555	90294.38
C_7H_15+	99.116912	0.861387	50543.37	99.116951	1.248925	550369.03	99.116935	1.094524	16453.88			
C_8H_17+	113.132449	-0.246925	47467.83	113.132483	0.055611	542947.3	113.132475	-0.017477	17211.23			
C_9H_19+	127.148166	0.306492	54829.1	127.148144	0.132733	612927.87						
C_10H_21+	141.163834	0.40057	59568.13	141.163741	-0.257416	692567.65						
C_11H_23+	155.17948	0.340013	55623.57	155.17936	-0.432814	687630.37						
C_12H_25+	169.195153	0.449966	47177.68	169.19504	-0.221767	563652.12						
C_13H_27+	183.210912	1.005559	34290.37	183.210764	0.200537	519093.45						
C_14H_29+	197.226571	0.982382	32219.17	197.226424	0.234477	460484.38						
C_16H_33+	225.25761	-0.300503	20297.56	225.257687	0.040048	341267.53						
C_18H_37+	253.288776	-0.794989	9815.39	253.288941	-0.145126	220551.57						
C_21H_43+	295.33603	0.347652	6333.82	295.336029	0.342693	108209.86						
C_25H_51+	351.398296	-0.661624	4303.32	351.398593	0.185223	59168.75						

(b)

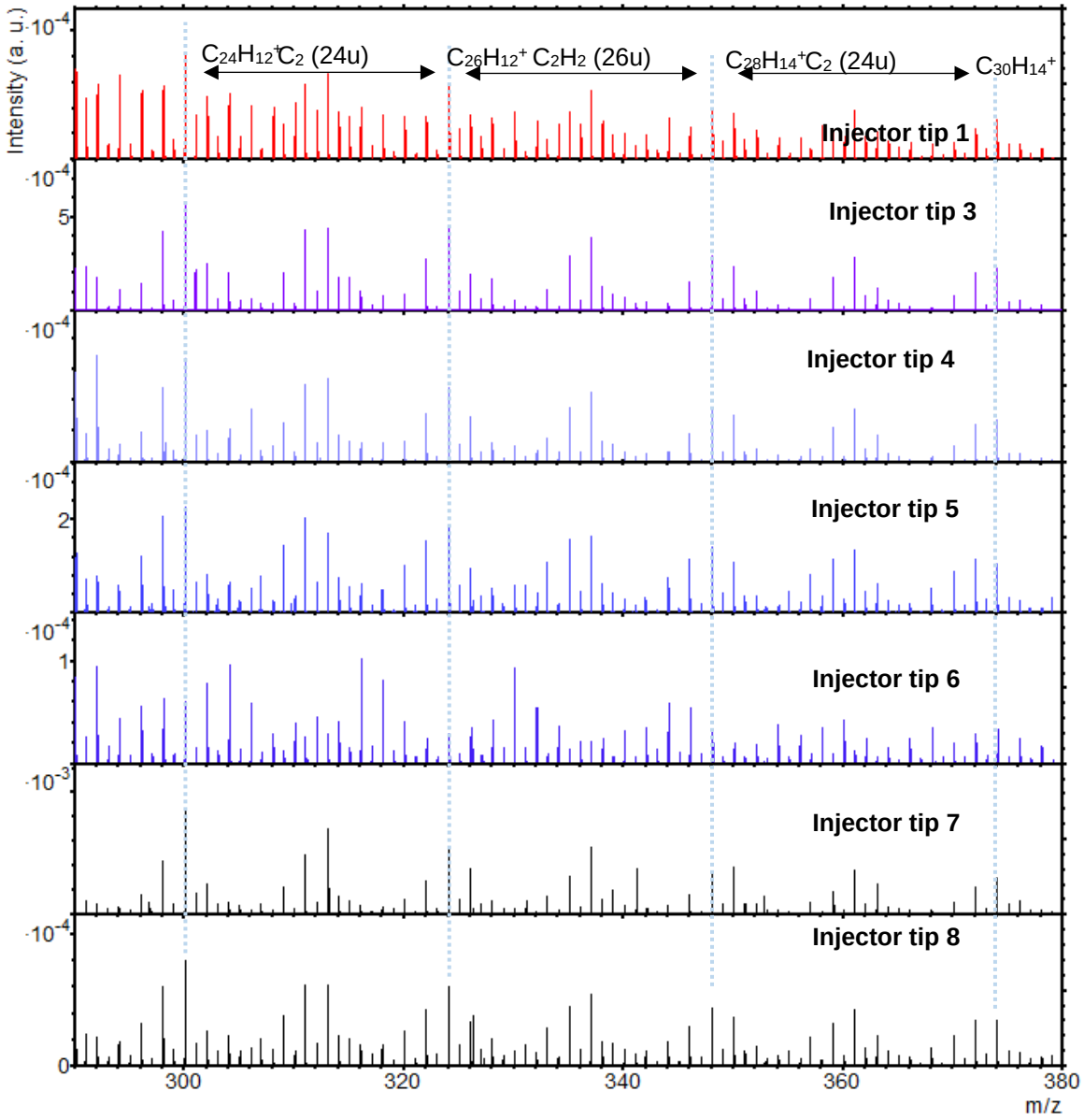
	Injector tip 1			
DBE = 10	Assignment	Center Mass (u)	Deviation (ppm)	Area
	C_17H_15+	219.116766	-0.27722	122739.98
	C_18H_17+	233.132374	-0.442115	10614.57
	C_39H_59+	527.461764	1.205452	5693.17
	C_41H_63+	555.492835	0.731157	7454.45
	C_46H_73+	625.570903	0.358158	11079.2
DBE = 11	Assignment	Center Mass (u)	Deviation (ppm)	Area
	C_17H_13+	217.101126	-0.233377	781418.24
	C_18H_15+	231.116775	-0.225365	113619.81
	C_19H_17+	245.132484	0.027457	37882.82
	C_20H_19+	259.148111	-0.063006	16549.84
	C_21H_21+	273.163774	-0.011466	31724.85
	C_22H_23+	287.179374	-0.184167	8732.67
	C_27H_33+	357.257685	0.021941	5289.19
	C_35H_49+	469.382855	-0.048915	4973.81



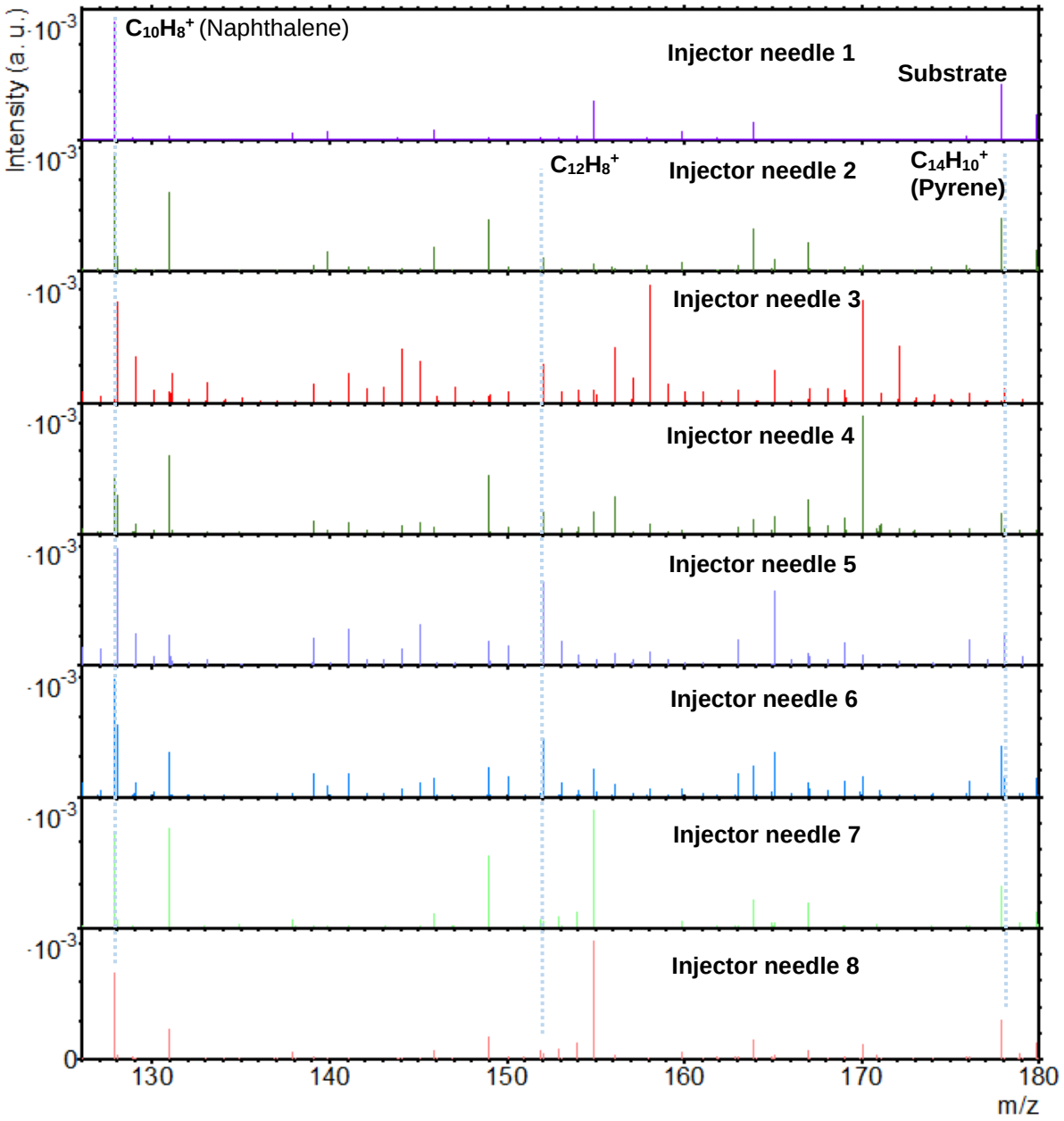


S4.12

(a)

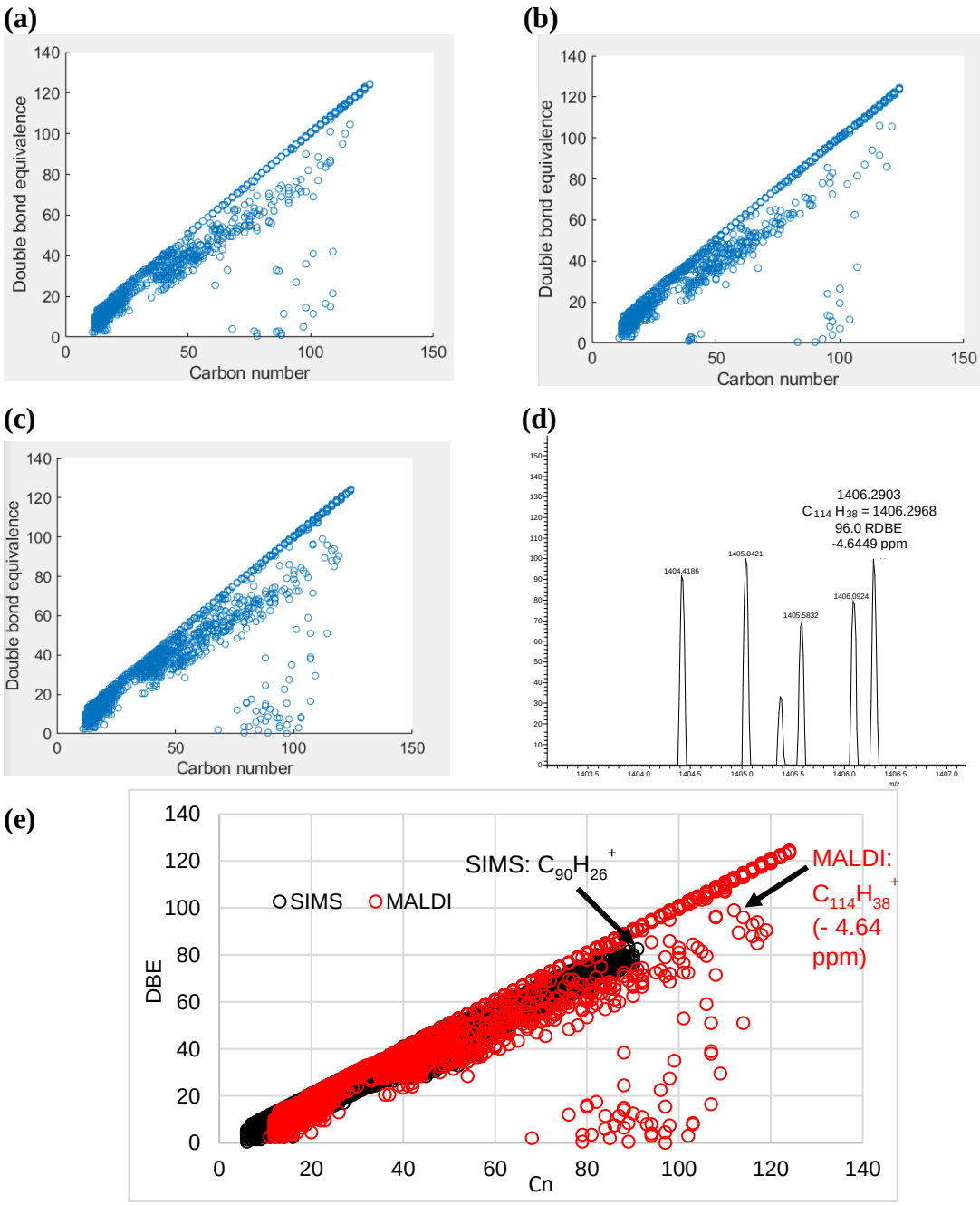

Intensity (a. u.)
$C_{24}H_{12}^{+}C_2$ (24u)
$C_{26}H_{12}^{+}$ C_2H_2 (26u)
$C_{28}H_{14}^{+}C_2$ (24u)
$C_{30}H_{14}^{+}$
Injector tip 1
Injector tip 3
Injector tip 4
Injector tip 5
Injector tip 6
Injector tip 7
Injector tip 8
300
320
340
360
380
m/z

(b)



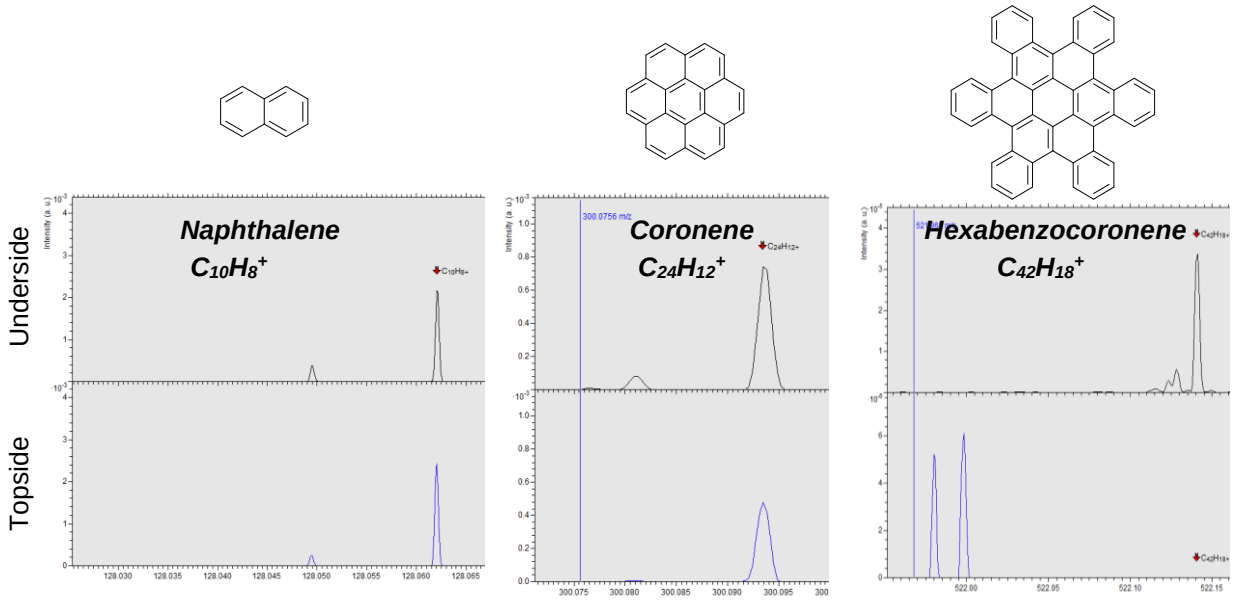
***Supplementary figure S4.12**: Illustrating the peak separation corresponding to alternate C_2H_2 and C_2 addition from 3D OrbiSIMS spectral fragmentation. **(a)** injector tip deposits, **(b)** injector needle deposits. Injector needle 1 did not show strongly ionizing peaks for PAHs above naphthalene ($C_{10}H_8^+$) AU, arbitrary units.*

S4.13



Supplementary figure S4.13. *(a – c) DBE v Cn of CH containing species (within a 6 ppm error range) from AP-MALDI analysis of injector tip deposit 5 using a TCNQ matrix for 3 analytical repeats. d) Spectral peak showing highest maximum mass PAH in MALDI data e) comparison of the SIMS and MALDI data with highest mass PAHs marked for each dataset.*

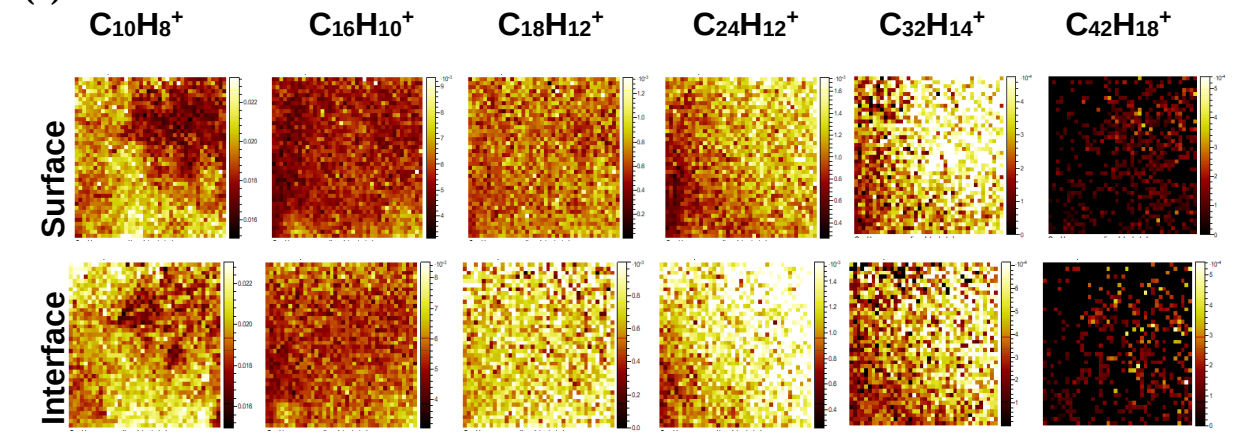
S4.14



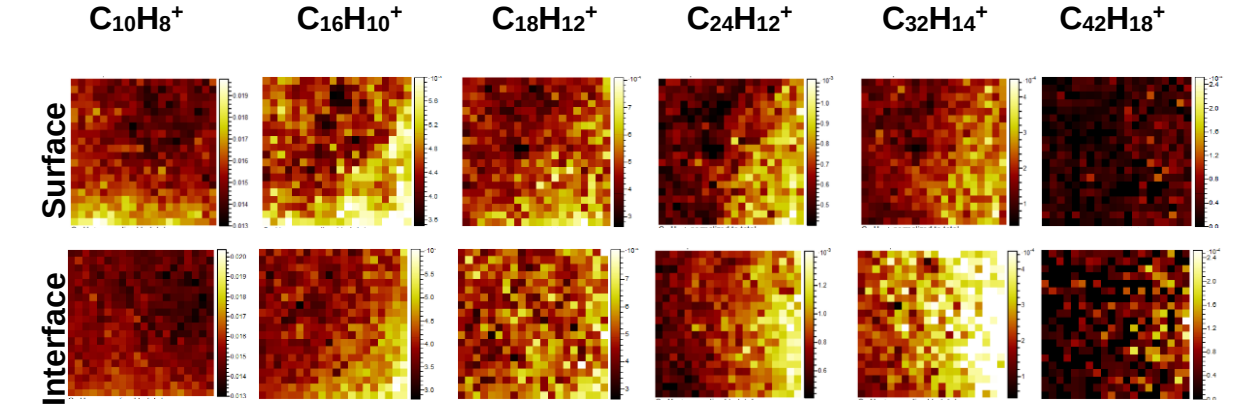
Supplementary figure S4.14. *3D OrbiSIMS spectra of 3 PAHs from the top and bottom side of a deposit scraping (30 scans), showing larger and more intense PAHs on the underside.*

S4.15

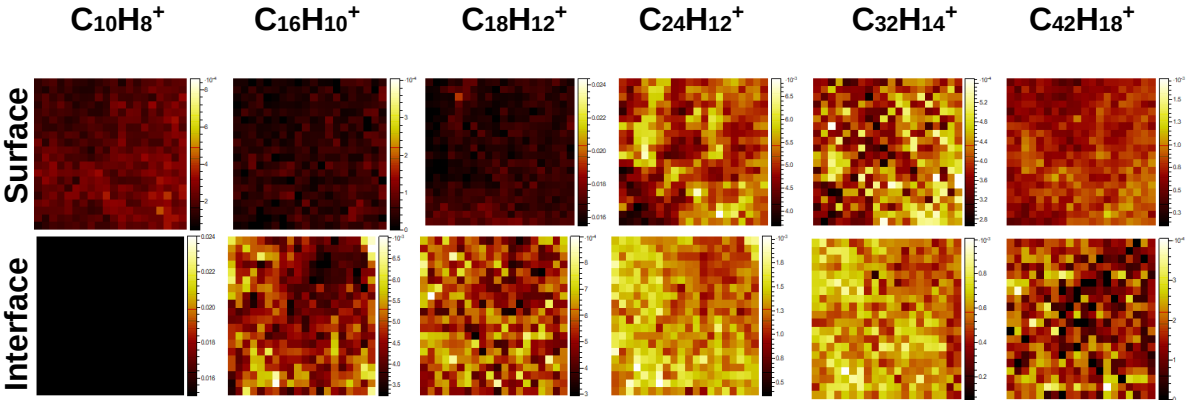
(a) i.



ii.

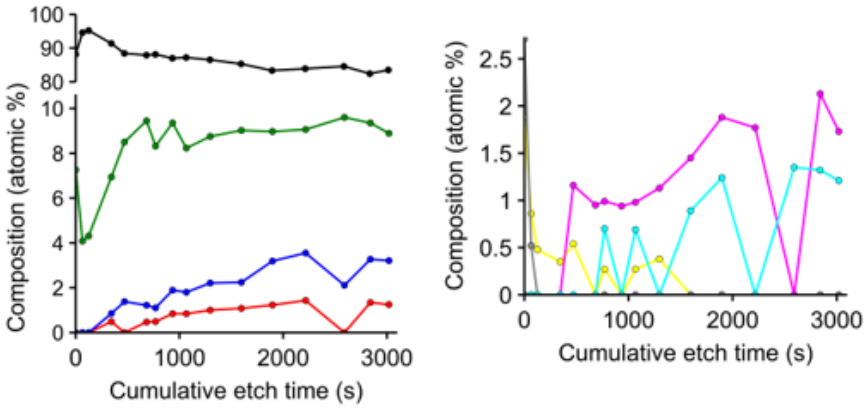


iii.



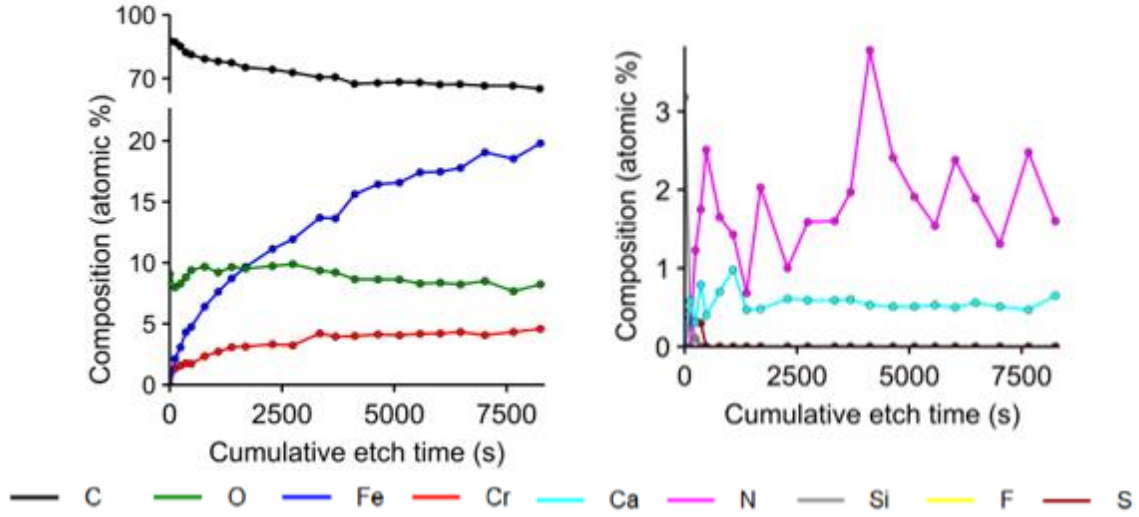
Supplementary figure S4.15. ***(a)*** *Chemical images (200 x 200 µm, normalized to the total ion count) of key ions taken at the surface (above) and at a lower deposit depth after sputtering (below).* ***i.*** *Injector tip 1 (sputter time = 510 s.* ***ii.*** *Injector tip 2 (sputter time = 2650 s.* ***iii.*** *Injector tip 3 (sputter time = 1850 s).*

S4.16
(a)



	Element and atomic percentage							
Cumulative etch time (s)	C 1s	O 1s	Fe 2p	Cr 2p	Ca 2p	S 2p	Si 2s	N 1s
0	87.74	9.08	0	0	0	0	3.18	0
120	87.15	7.98	2.13	1.33	0.58	0.37	0.46	0
240	85.12	8.28	3.07	1.57	0.31	0.32	0.1	1.23
360	82.29	8.8	4.31	1.76	0.79	0.3	0	1.75
480	81.23	9.39	4.74	1.72	0.4	0	0	2.51
780	79.21	9.68	6.41	2.34	0.7	0	0	1.65
1080	78.04	9.21	7.62	2.71	0.98	0	0	1.43
1380	77.4	9.65	8.72	3.08	0.47	0	0	0.68
1691	75.18	9.52	9.66	3.13	0.48	0	0	2.03
2291	74.21	9.73	11.13	3.32	0.61	0	0	1
2741	72.77	9.89	11.92	3.23	0.59	0	0	1.59
3341	70.56	9.36	13.69	4.21	0.59	0	0	1.6
3691	70.63	9.21	13.63	3.95	0.6	0	0	1.97
4121	67.43	8.65	15.62	4	0.53	0	0	3.78
4638	67.88	8.63	16.43	4.13	0.51	0	0	2.41
5117	68.32	8.62	16.57	4.06	0.51	0	0	1.91
5574	68.06	8.29	17.41	4.18	0.53	0	0	1.54
6024	67.11	8.36	17.46	4.2	0.5	0	0	2.38
6474	67.25	8.22	17.77	4.32	0.56	0	0	1.89
7019	66.56	8.5	19.05	4.07	0.51	0	0	1.31
7653	66.54	7.66	18.52	4.32	0.47	0	0	2.48
8253	65.15	8.23	19.79	4.58	0.65	0	0	1.6

(b)



Etch Time (s)	C158	O158	Fe158	Cr158	Ca158	S158	Si158	N158
0	87.74	9.08	0	0	0	0	3.18	0
120	87.15	7.98	2.13	1.33	0.58	0.37	0.46	0
240	85.12	8.28	3.07	1.57	0.31	0.32	0.1	1.23
360	82.29	8.8	4.31	1.76	0.79	0.3	0	1.75
480	81.23	9.39	4.74	1.72	0.4	0	0	2.51
780	79.21	9.68	6.41	2.34	0.7	0	0	1.65
1080	78.04	9.21	7.62	2.71	0.98	0	0	1.43
1380	77.4	9.65	8.72	3.08	0.47	0	0	0.68
1691	75.18	9.52	9.66	3.13	0.48	0	0	2.03
2291	74.21	9.73	11.13	3.32	0.61	0	0	1
2741	72.77	9.89	11.92	3.23	0.59	0	0	1.59
3341	70.56	9.36	13.69	4.21	0.59	0	0	1.6
3691	70.63	9.21	13.63	3.95	0.6	0	0	1.97
4121	67.43	8.65	15.62	4	0.53	0	0	3.78
4638	67.88	8.63	16.43	4.13	0.51	0	0	2.41
5117	68.32	8.62	16.57	4.06	0.51	0	0	1.91
5574	68.06	8.29	17.41	4.18	0.53	0	0	1.54
6024	67.11	8.36	17.46	4.2	0.5	0	0	2.38
6474	67.25	8.22	17.77	4.32	0.56	0	0	1.89
7019	66.56	8.5	19.05	4.07	0.51	0	0	1.31
7653	66.54	7.66	18.52	4.32	0.47	0	0	2.48
8253	65.15	8.23	19.79	4.58	0.65	0	0	1.6

Supplementary figure S4.16. *X-ray photoelectron spectroscopy elemental depth profile results using an* Ar_{500}^{+} *etching beam on (a), injector tip 1 and (b) injector tip 2.*

Supplementary table S4.17*. 3D OrbiSIMS ion table for nitrogen containing ions identified in* ***(a)*** *injector tip deposits* ***i.*** *injector tips 1-4,* ***ii.*** *Injector tips 5-8.* ***(b)*** *injector needle deposits All ion peak tables were exported from Surface Lab software (IONTOF GmbH, version 7.1.b). Deviation (ppm) refers to the difference between the observed and expected ion mass. The observed mass is measured as the center mass of the ion peak.*

(a) i.

Assignment	Injector tip 1			Injector tip 2			Injector tip 3			Injector tip 4		
Alkyl phenyl pyridine	Center Mass (u)	Deviation (ppm)	Area (Intensity)	Center Mass (u)	Deviation (ppm)	Area (Intensity)	Center Mass (u)	Deviation (ppm)	Area (Intensity)	Center Mass (u)	Deviation (ppm)	Area (Intensity)
C_12H_12N+	170.096511	0.498507	756476972.7	170.096382	-0.258774	2125402742	170.096231	-1.145983	719054730.9	170.096287	-0.816251	1703323931
C_13H_14N+	184.112229	0.829357	814005776.7	184.112104	0.154806	2004051970	184.111944	-0.715156	540500820	184.112007	-0.375943	2079875430
C_14H_16N+	198.127901	0.883809	532747793.8	198.127761	0.175291	932152860.2	198.12757	-0.784895	226801461.1	198.127628	-0.492281	1355005064
C_15H_18N+	212.14347	0.444577	239141572.7	212.14339	0.06393	304235090.5	212.143302	-0.350963	80326160.15	212.143338	-0.180226	562003332.3
C_16H_20N+	226.158977	-0.215925	90219871.04	226.158957	-0.30681	82484622.68	226.159024	-0.008516	23300378.78	226.159023	-0.014091	201954905.4
C_17H_22N+	240.17456	-0.483257	31045829.73	240.174571	-0.435648	23701271.64	240.174652	-0.100298	3443264.85	240.174665	-0.045176	58708024.22
Benzoquinoline												
C_9H_8N+	130.065191	0.501077	63579739.9	130.065132	0.05107	664401674.5	130.06504	-0.657868	113566957.6	130.065061	-0.494778	544263419.7
C_13H_10N+	180.080857	0.449847	96394302.94	180.080738	-0.208299	601226701.6	180.080574	-1.121618	241266795.8	180.080604	-0.952272	499572336.9
C_17H_12N+	230.096355	-0.308254	25731135.36	230.096434	0.035462	222112398.8	230.096457	0.134972	101548612.3	230.096444	0.076994	246884527.9
C_19H_12N+	254.096303	-0.484997	15979704.92	254.096365	-0.23934	167878516.9	254.096399	-0.10578	71136173.9	254.096371	-0.216779	114010522
C_23H_14N+	304.112045	-0.102498	4699548.36	304.112087	0.035305	49819119.05	304.11211	0.110598	19276497.48	304.112092	0.054196	28027983.43
C_25H_14N+	328.11215	0.224781	3308215.41	328.112189	0.345858	38889492.01	328.112193	0.356933	14593165.19	328.112179	0.313746	21198225.23
C_29H_16N+	378.12765	-0.201461	983772.9	378.127732	0.01659	12479313.49	378.127728	0.004962	2763353.05	378.127761	0.093615	4179549.4
C_31H_16N+	402.127644	-0.204412	735389.64	402.127748	0.05369	10523177.37	402.127722	-0.008569	2292424.21	402.127782	0.139673	3387187.88
C_35H_17N+	451.135537	-0.031428	114334.85	451.135651	0.220662	2383173.12	451.135587	0.07943	430924.27	451.135619	0.151457	722160.72
Alkyl quinoline												
C_10H_10N+	144.080845	0.481256	74220691.05	144.080751	-0.173888	629673627.5	144.080622	-1.069946	94479734.82	144.080656	-0.834386	771474216.1
C_11H_12N+	158.09648	0.343249	67050260.94	158.096373	-0.333695	301542081.4	158.096248	-1.12457	44234088.8	158.096284	-0.895181	665021237.9
C_12H_14N+	172.112067	-0.048795	33894545.68	172.111939	-0.793897	63849737.24	172.111847	-1.328902	6444577.96	172.111871	-1.18803	136015885.9
C_13H_16N+	186.127777	0.271985	9947215.89	186.127654	-0.383899	15408256.24	186.127573	-0.821654	815299.39	186.127611	-0.619876	20262679.09
Carbazole												
C_12H_10N+	168.08085	0.439041	164761068.1	168.080722	-0.322048	694638476.1	168.08057	-1.222109	330411933.1	168.080612	-0.972163	705144355.1
C_14H_12N+	194.096589	0.838526	82157736.21	194.096458	0.166582	418787465.8	194.096297	-0.664023	163130400.3	194.09632	-0.545144	346557909.7
C_20H_14N+	268.111957	-0.4418	10148034.48	268.112015	-0.227507	87892658.56	268.112073	-0.010727	37575276.97	268.112058	-0.067398	58152188.03

C_24H_16N+	318.127684	-0.133335	2611704.27	318.12773	0.011889	24565328.05	318.127755	0.092343	7424808.81	318.127752	0.08074	10850133.33
C_30H_20N+	394.158904	-0.308823	59041.85	394.159053	0.067567	984047.42	394.159052	0.065579	137200.22	394.159052	0.065961	199957.04

ii.

Assignment	Tip 5 (159)			Tip 6 (161)			Tip 7 (GM15)			Tip 8 (GM20)		
Alkyl phenyl pyridine	Center Mass (u)	Deviation (ppm)	Area (Intensity)	Center Mass (u)	Deviation (ppm)	Area (Intensity)	Center Mass (u)	Deviation (ppm)	Area (Intensity)	Center Mass (u)	Deviation (ppm)	Area (Intensity)
C_12H_12N+	170.09616	-1.564358	5196728487	170.095952	-2.788304	1997684036	170.096124	-1.777287	15551033.2	170.096167	-1.523339	2686935792
C_13H_14N+	184.111853	-1.208977	6536969746	184.111662	-2.247666	1343833612	184.111841	-1.27743	12778919.83	184.111871	-1.110751	3628249301
C_14H_16N+	198.127486	-1.209335	4325605324	198.12737	-1.797998	534613983	198.127467	-1.304837	5100404.21	198.127509	-1.095334	2376915008
C_15H_18N+	212.143208	-0.790566	1798055467	212.143141	-1.106284	188069403.7	212.14319	-0.876476	1695818.36	212.143229	-0.69414	993273682.9
C_16H_20N+	226.158868	-0.700654	607978348.8	226.15882	-0.91107	57339528.73	226.15889	-0.601894	491140.08	226.158866	-0.709262	331394654.2
C_17H_22N+	240.174422	-0.435648	201870765.2	240.174205	-1.959843	14348227.07	240.174516	-0.667462	107407.88	240.17439	-1.192499	97889945.55
Benzoquinoline												
C_9H_8N+	130.064971	-1.192605	578111287.5	130.064923	-1.557158	76553697.39	130.065015	-0.851358	101474357.2	130.064992	-1.028595	719985079.5
C_13H_10N+	180.080476	-1.665979	596574925.4	180.080463	-1.738122	72791635.18	180.080481	-1.634177	24754800.1	180.08053	-1.363394	828958570.9
C_17H_12N+	230.09623	-0.850152	232141948.6	230.09616	-1.155707	24949629.8	230.096285	-0.613252	21086795.76	230.09633	-0.417798	522811246.6
C_19H_12N+	254.096144	-1.108221	117455425.5	254.096044	-1.50426	7381411.5	254.096199	-0.893655	16631508.88	254.096178	-0.976083	240149664.3
C_23H_14N+	304.111918	-0.51987	29821635.63	304.111847	-0.753517	1631872.18	304.111943	-0.436945	5976649.53	304.111948	-0.419394	70318831.68
C_25H_14N+	328.112037	-0.117807	22789687.52	328.112045	-0.092728	932598.03	328.112053	-0.070644	5389444.3	328.112071	-0.01499	55107451.7
C_29H_16N+	378.127454	-0.720391	6336566.5	378.131476	9.917129	575902.1	378.127498	-0.601575	2734911.43	378.127515	-0.556636	23646556.13
C_31H_16N+	402.127431	-0.733701	5571040.21	402.131568	9.553538	389520.85	402.127482	-0.607737	2425068.55	402.127527	-0.495212	20243716.79
C_35H_17N+	451.135266	-0.630722	1342611.08	451.136048	1.102508	70362.35	451.13536	-0.42303	675568.72	451.135432	-0.262651	6024489.05
Alkyl quinoline												
C_10H_10N+	144.080545	-1.598046	930572876.3	144.080492	-1.96774	117787488.1	144.080592	-1.278696	104568185.3	144.080567	-1.448637	831074189.1
C_11H_12N+	158.096152	-1.731075	870101419.4	158.096038	-2.449847	89516993.62	158.096195	-1.458305	53789318.05	158.096165	-1.646969	505274847.6
C_12H_14N+	172.111703	-2.164953	247727955.6	172.111451	-3.630718	25371235.61	172.111759	-1.84022	10243595.09	172.111717	-2.086172	136486135.3
C_13H_16N+	186.127379	-1.865947	75274061.65	186.127059	-3.584664	5281477.73	186.127485	-1.29419	1844775.1	186.127394	-1.784002	32513020.3
Carbazole												
C_12H_10N+	168.080506	-1.606504	1350448460	168.080538	-1.412227	168868270	168.080483	-1.744282	15052246.2	168.080522	-1.510469	1217322210
C_14H_12N+	194.096166	-1.336027	435557046.6	194.096124	-1.55631	63067031.03	194.096186	-1.235079	13416109.56	194.096213	-1.094577	564754392.6

C_20H_14N+	268.111813	-0.981989	69209864.37	268.111593	-1.800201	5796362.98	268.111854	-0.828726	8080842.08	268.111818	-0.962554	154504142.9
C_24H_16N+	318.127503	-0.701422	16697097.68	318.127477	-0.781219	1523911.8	318.127537	-0.594723	3666300.33	318.127522	-0.642455	55601751
C_30H_20N+	394.158796	-0.584273	344220.01	394.159103	0.195481	51896.1	394.158825	-0.508856	286937.82	394.158843	-0.465621	3371079.25

(b) i.

Assignment	**Injector needle 1**			**Injector needle 2**			**Injector needle 3**			**Injector needle 4**		
Alkyl phenyl pyridine	Center Mass (u)	Deviation (ppm)	Area (Intensity)	Center Mass (u)	Deviation (ppm)	Area (Intensity)	Center Mass (u)	Deviation (ppm)	Area (Intensity)	Center Mass (u)	Deviation (ppm)	Area (Intensity)
C_12H_12N+	170.096203	-1.312168	2948608.28	170.096264	-0.954112	842358.27	170.096273	-0.901188	1093711.72	170.096263	-0.960003	9662485.84
C_13H_14N+	184.111938	-0.746771	7328028.69	184.111983	-0.501936	928981.41	184.111988	-0.478289	738338.2	184.111977	-0.537333	12928395.91
C_14H_16N+	198.127575	-0.76429	10153921.67	198.127605	-0.612498	498249.48	198.127621	-0.528443	438760.39	198.127598	-0.647315	8558795.69
C_15H_18N+	212.14334	-0.171508	7468490.47	212.143313	-0.29876	214805.13	212.143339	-0.172144	280816.5	212.143316	-0.284406	3894237.1
C_16H_20N+	226.159043	0.07659	3655397.11	226.159034	0.036622	87687.4	226.159055	0.126242	159390.38	226.158975	-0.227677	1580106.69
C_17H_22N+	240.174631	-0.188004	1392886.51	240.174736	0.251242	35653.09	240.174724	0.197538	62802.51	240.174599	-0.32078	529379.59
Benzoquinoline												
C_9H_8N+	130.065025	-0.774668	780859.15	130.065089	-0.279206	304770.09	130.065094	-0.243416	921117.68	130.065042	-0.643493	295635.81
C_13H_10N+	180.080522	-1.410001	413485.72	180.080592	-1.020355	251363.03	180.080625	-0.839667	680123.34	180.080567	-1.160369	271577.49
C_17H_12N+	230.096439	0.057105	1134653.08	230.096452	0.112926	88259.64	230.096491	0.28273	787533.7	230.096425	-0.005394	147247.6
C_19H_12N+	254.096378	-0.189888	85629.26	254.09634	-0.33927	35710.75	254.096437	0.042286	247203.22	254.096358	-0.265672	25921
C_23H_14N+	304.112096	0.06656	13707.36	x	x	x	304.112198	0.403081	61269.32	x	x	x
C_25H_14N+	x	x	x	x	x	x	328.112286	0.639643	36688.59	x	x	x
C_29H_16N+	x	x	x	x	x	x	x	x	x	x	x	x
C_31H_16N+	x	x	x	x	x	x	x	x	x	x	x	x
C_35H_17N+	x	x	x	x	x	x	x	x	x	x	x	x
Alkyl quinoline												
C_10H_10N+	144.080603	-1.197044	2716921.17	144.080667	-0.757102	369446.64	144.08068	-0.665259	1658561.16	144.080614	-1.122555	684873.66
C_11H_12N+	158.096233	-1.218944	3836676.23	158.096283	-0.90094	329102.03	158.096305	-0.765956	1449851.98	158.09623	-1.236105	964716.39
C_12H_14N+	172.111823	-1.468447	1794651.86	172.111867	-1.216315	107405.67	172.111898	-1.032169	445584.06	172.111821	-1.479955	500788.15
C_13H_16N+	186.127518	-1.117973	688712.54	186.127604	-0.655251	25210.58	186.127645	-0.436997	106358.25	186.127553	-0.930401	175463.72
Carbazole												

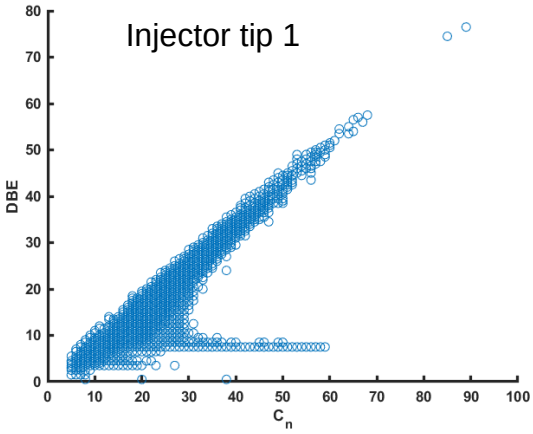
C_12H_10N+	168.080524	-1.495448	737507.54	168.080597	-1.061539	295215.68	168.080614	-0.964362	594314.5	168.080555	-1.310804	775103.13
C_14H_12N+	194.096244	-0.934857	493487.65	194.096326	-0.515498	178631.61	194.096351	-0.384326	463066.84	194.096281	-0.744935	256064.96
C_20H_14N+	268.112089	0.048789	52977.68	268.112172	0.360252	13653.45	268.112105	0.109683	114489.02	268.112069	-0.026765	15450.46
C_24H_16N+	318.127715	-0.033759	22791.9	x	x	x	318.127815	0.278978	37409.2	318.127696	-0.095068	2389.93
C_30H_20N+	x	x	x	x	x	x	x	x	x	x	x	x

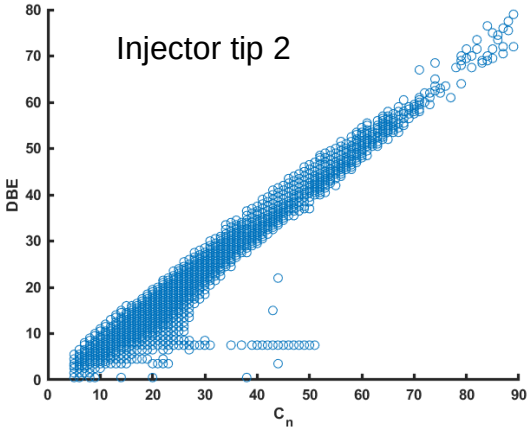
ii.

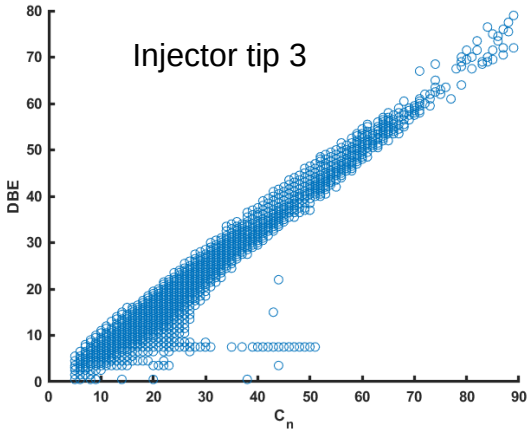
Assignment	Injector needle 5 (159)			Injector needle 6			Injector needle 7			Injector needle 8		
Alkyl phenyl pyridine	Center Mass (u)	Deviation (ppm)	Area (Intensity)	Center Mass (u)	Deviation (ppm)	Area (Intensity)	Center Mass (u)	Deviation (ppm)	Area (Intensity)	Center Mass (u)	Deviation (ppm)	Area (Intensity)
C_12H_12N+	170.096231	-1.144112	46360082.66	170.096202	-1.313197	1002722.86	170.096122	-1.788805	84291.58	170.096154	-1.596327	2808740.93
C_13H_14N+	184.111944	-0.71704	52522160.56	184.111911	-0.897591	768282.25	184.111799	-1.501502	78896.94	184.111857	-1.186918	4037296.75
C_14H_16N+	198.127558	-0.845727	33947407.65	198.127522	-1.02771	374424.93	198.127488	-1.199882	34000.76	198.127476	-1.261188	2550818.76
C_15H_18N+	212.143274	-0.480765	16118587.02	212.143246	-0.613591	172429.67	212.143187	-0.890564	13767.23	212.143217	-0.749733	1010975.53
C_16H_20N+	226.158971	-0.243906	7692459.45	226.158958	-0.302126	83044.77	x	x	x	226.158795	-1.02285	306271.26
C_17H_22N+	240.17459	-0.360116	3439496.48	240.174626	-0.207814	27711.3	x	x	x	240.174456	-0.914784	80135.17
Benzoquinoline												
C_9H_8N+	130.065043	-0.636211	6021337.9	130.065042	-0.642892	210097.66	130.065073	-0.402268	338984.73	130.064972	-1.185344	99871.06
C_13H_10N+	180.080536	-1.33077	3434370.74	180.080564	-1.17331	159714.3	180.0805	-1.531354	50389.09	180.080468	-1.709039	88846.08
C_17H_12N+	230.09641	-0.069355	2071942.43	230.096391	-0.151706	100855.1	230.096282	-0.625474	26217.5	230.096285	-0.613441	46916.71
C_19H_12N+	254.096339	-0.341327	818415.47	254.096318	-0.426014	31382.03	254.096182	-0.960188	17013.45	254.096233	-0.758836	19858.48
C_23H_14N+	304.112066	-0.033321	106124.58	x	x	x	304.111878	-0.649711	2546.59	304.111997	-0.260606	5925.76
C_25H_14N+	328.112165	0.272153	60480.04	x	x	x	x	x	x	328.112127	0.154354	5808.6
C_29H_16N+	378.12794	0.567113	13153.26	x	x	x	x	x	x	378.127529	-0.520734	2354.51
C_31H_16N+	402.127582	-0.358362	6719.22	x	x	x	x	x	x	402.127166	-1.393573	2701.61
C_35H_17N+	x	x	x	x	x	x	x	x	x	x	x	x
Alkyl quinoline												
C_10H_10N+	144.080629	-1.021873	24142326.55	144.080616	-1.110334	423310.59	144.080569	-1.433013	273902.78	144.080524	-1.744829	133461.91
C_11H_12N+	158.096255	-1.080069	52827343.08	158.096224	-1.279458	421704.85	158.096178	-1.564611	165386.73	158.096134	-1.843507	83271.5
C_12H_14N+	172.111861	-1.251098	26613194.54	172.111792	-1.651982	121829.29	172.111766	-1.801474	46731.72	172.11172	-2.065575	24902.97
C_13H_16N+	186.127527	-1.066407	5418008.26	186.127531	-1.048067	25548.79	186.127548	-0.956878	13950.27	186.127391	-1.798661	5091.31

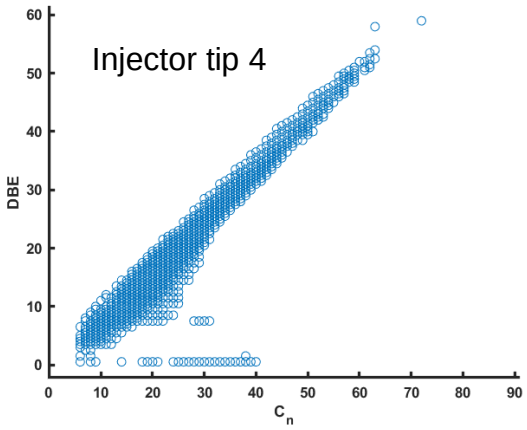
Carbazole												
C_12H_10N+	168.080541	-1.398396	7170195.36	168.080529	-1.469047	259392.07	168.080472	-1.8056	54348.5	168.080447	-1.954665	211099.21
C_14H_12N+	194.096259	-0.860822	3360288.61	194.096241	-0.951902	109160.52	194.096164	-1.347776	33342.67	194.096164	-1.349559	70292.22
C_20H_14N+	268.112017	-0.21873	544710.12	268.11197	-0.39349	10818.04	268.111879	-0.732454	6632.36	268.111823	-0.942145	7504.19
C_24H_16N+	318.127737	0.034968	72691.98	**x**	**x**	**x**	**x**	**x**	**x**	318.127507	-0.689765	2980.6
C_30H_20N+	**x**	**x**	**x**	**x**	**x**	**x**	**x**	**x**	**x**	**x**	**x**	**x**

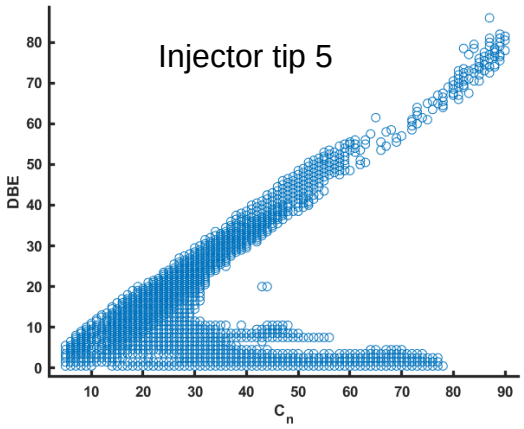
S4.18

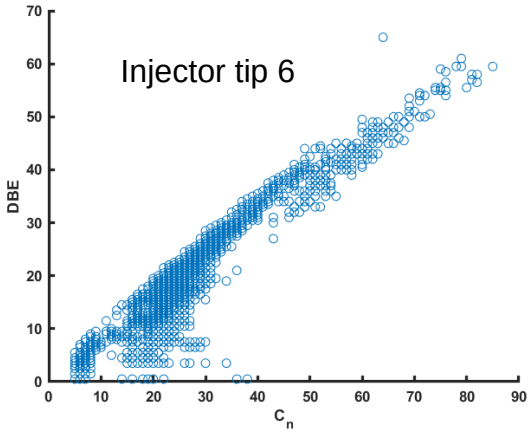

Injector tip 1
DBE
C n

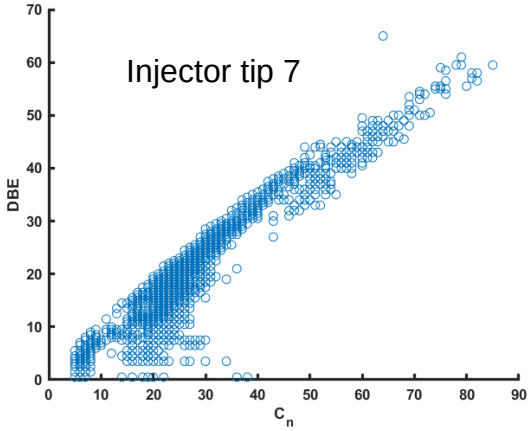

Injector tip 2
DBE
C n

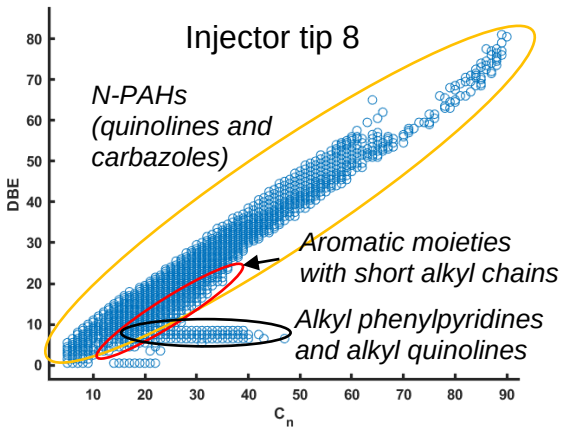

Injector tip 3
DBE
C n


Injector tip 4
DBE
C n


Injector tip 5
DBE
C n


Injector tip 6
DBE
C n


Injector tip 7
DBE
C n


Injector tip 8
N-PAHs
(quinolines and
carbazoles)
Aromatic moieties
with short alkyl chains
Alkyl phenylpyridines
and alkyl quinolines
DBE
C n

***Supplementary figure S4.18**. Plots of double bond equivalence (DBE) versus carbon number of all CHN_x species in injector tip deposits where x = 1, an annotated plot is given for injector tip 8 showing the discussed compound classes.*

S4.19

(a)

Parent ion	**Secondary fragments**				
C_13H_14N+	**Center Mass (u)**	**Formula**	**Mass Deviation (ppm)**	**Area (intensity)**	**Neutral loss**
	168.080649	C_12H_10N+	-0.753543	42350.3	[M – CH_3H]
	128.061995	C_10H_8+	-0.446183	8561.16	[M – C_2H_5CH]
	105.069934	C_8H_9+	0.541724	14708.87	[M – $C_2H_5C_5$]
	103.054342	C_8H_7+	1.121149	5371.65	[M – $C_2H_5(CH)_2C$]
	94.065323	C_6H_8N+	2.0937	7414.59	[M – $C_2H_5(CH)_5$ NH]
	91.054455	C_7H_7+	2.502575	94391.47	[M – $C_2H_5(CH)_2C_2$]
	79.054487	C_6H_7+	3.294923	13590.92	[M – $C_2H_5(CH)_2C_3$]

(b) i.

Parent ion	**Secondary fragments**				
C_9H_8N+	**Center Mass (u)**	**Assignment**	**Mass Deviation (ppm)**	**Area**	**Neutral loss**
(quinoline)	130.064977	C_9H_8N+	-1.146516	22753727.69	-
	128.049307	C_9H_6N+	-1.31343	111593.18	[M-2H]
	115.054166	C_9H_7+	-0.52368	273824.9	[M-NH]
	103.054248	C_8H_7+	0.205877	2627747.6	[M-CHN]
	102.046414	C_8H_6+	0.12502	158144.32	[M-CHN-H]

ii.

Parent ion	**Secondary fragments**				
C_13H_10N+	Center Mass (u)	Assignment	Mass Deviation (ppm)	Area	Neutral loss
(benzoquinoline)	180.080521	C_13H_10N+	-1.416637	39761353.48	-
	179.072739	C_13H_9N+	-1.180869	2947715.23	[M-H]
	178.06492	C_13H_8N+	-1.157576	2381097.57	[M-2H]
	166.064836	C_12H_8N+	-1.745838	426220.3	[M-CH-H]
	165.069597	C_13H_9+	-1.695639	673475.05	[M-NH]
	154.064831	C_11H_8N+	-1.911554	952140.22	[M-$(CH)_2$]
	141.057028	C_10H_7N+	-1.930894	70410.56	[M-$(CH)_3$]
	140.049225	C_10H_6N+	-1.789625	61834.59	[M-$(CH)_3$H]
	128.049302	C_9H_6N+	-1.357261	196864.25	[M-$(CH)_4$]
	108.080729	C_7H_10N+	-0.436517	391838.41	[M-C_6]
	107.072909	C_7H_9N+	-0.389194	33473.97	[M-C_6H]
	106.065114	C_7H_8N+	-0.108234	27742.09	[M-$(CH)_2C_4$]
	104.049475	C_7H_6N+	-0.003724	14044.94	[M-$(CH)_4C_2$]
	103.054259	C_8H_7+	0.311792	18846.28	[M-CHN$(CH)_2C_2$]
	94.065249	C_6H_8N+	1.309504	34306.33	[M-$(CH)_2C_5$]
	93.057445	C_6H_7N+	1.547004	13517.84	[M-$(CH)_3C_4$]

	91.054397	C_7H_7+	1.868241	13236.98	[M-CHN(CH)$_2$C$_3$]
	80.049744	C_5H_6N+	3.353475	13841.34	[M-(CH)$_4$C$_4$]

(c) i.

Parent ion	**Secondary fragments**				
C_12H_10N+					
(carbazole)	Center Mass (u)	Assignment	Mass Deviation (ppm)	Area	Neutral loss
	168.080359	C_12H_10N+	-2.479035	33951001.41	-
	167.072717	C_12H_9N+	-1.398117	42841238.99	[M-H]
	154.064838	C_11H_8N+	-1.864652	1127552.75	[M-(CH)H]
	152.061783	C_12H_8+	-1.770072	593252.96	[M-(NH)H]
	141.069614	C_11H_9+	-1.863438	4536790.34	[M-(CHN)]
	140.061805	C_11H_8+	-1.760533	2135647.44	[M-(CHN)H]
	139.054009	C_11H_7+	-1.561679	2952800.74	[M-(CHN)(2H)]
	115.054171	C_9H_7+	-0.480103	2342975.15	[M-(CHN)(CH)$_2$]
	89.038754	C_7H_5+	1.990212	201976.81	[M-(CHN)(CH)$_4$]

ii.

Parent ion	**Secondary fragments**				
C_16H_11N+	Center Mass (u)	Assignment	Mass Deviation (ppm)	Area	Neutral loss
(benzocarbazole)	217.08849	C_16H_11N+	-0.50958	98725.94	-
	165.069562	C_13H_9+	-1.905951	138381.59	[M-CHN(CH)C]
	176.061741	C_14H_8+	-1.765407	64654.65	[M-CHN(CH)H]
	177.056975	C_13H_7N+	-1.836766	43261.27	[M-(CH)$_3$H]
	166.06483	C_12H_8N+	-1.779945	15965.32	[M-(CH)$_3$C]
	163.053874	C_13H_7+	-2.164471	521241.66	[M-CHN(CH)$_2$H]
	152.061752	C_12H_8+	-1.974013	62202.34	[M-CHN(CH)$_2$C]
	150.046148	C_12H_6+	-1.68757	47538.7	[M-CHN(CH)$_3$H]
	140.049209	C_10H_6N+	-1.903593	64042.88	[M-(CH)$_5$C]
	139.053962	C_11H_7+	-1.90445	95349.13	[M-CHN(CH)$_3$C]
	128.061867	C_10H_8+	-1.444762	20497.63	[M-CHN(CH)$_2$C$_3$]

(d) i.

C_10H_10N+	Center Mass (u)	Assignment	Mass Deviation (ppm)	Area	Neutral loss
	144.080517	C_10H_10N+	-1.794899	14582916	-
	129.05711	C_9H_7N+	-1.479692	21409.31	[M-CH$_3$]
	130.064906	C_9H_8N+	-1.690158	807.16	[M-CH$_2$]
	129.069671	C_10H_9+	-1.592923	55590.72	[M-H]
	128.049278	C_9H_6N+	-1.540934	33959.2	[M-CH$_4$]
	117.069773	C_9H_9+	-0.885944	402844.14	[M-CH$_4$]
	116.049395	C_8H_6N+	-0.690452	219164.96	[M-C$_2$H$_4$]
	115.054158	C_9H_7+	-0.593446	448145.25	[M-CH$_3$]
	103.054231	C_8H_7+	0.041763	131747.92	[M-C$_2$H$_3$]

ii.

Parent ion	Secondary fragments				
C_11H_12N+	Center Mass (u)	Assignment	Mass Deviation (ppm)	Area	Neutral loss
	158.096181	C_11H_12N+	-1.547651	11802842.12	-
	143.072753	C_10H_9N+	-1.380619	2882915.86	[M-CH_3]
	130.064992	C_9H_8N+	-1.025907	1547264.03	[M-C_2H_4]

Supplementary figure S4.19*. MS/MS fragmentation data of different aromatic nitrogen moieties highlighted in* ***Table 1*** *in the main text.* ***(a)*** *alkyl phenyl pyridine,* $C_{13}H_{14}N^+$*,* ***(b)*** *quinolines i.* $C_9H_8N^+$*, ii.* $C_{13}H_{10}N^+$*.* ***(c)*** *carbazoles i.* $C_{12}H_{10}N^+$*, ii.* $C_{16}H_{11}N^+$*.* ***(d)*** *alkylated quinolines* ***i.*** $C_{10}H_{10}N^+$*, ii.* $C_{11}H_{12}N^+$*.*

S4.20

(a) i. DHB matrix

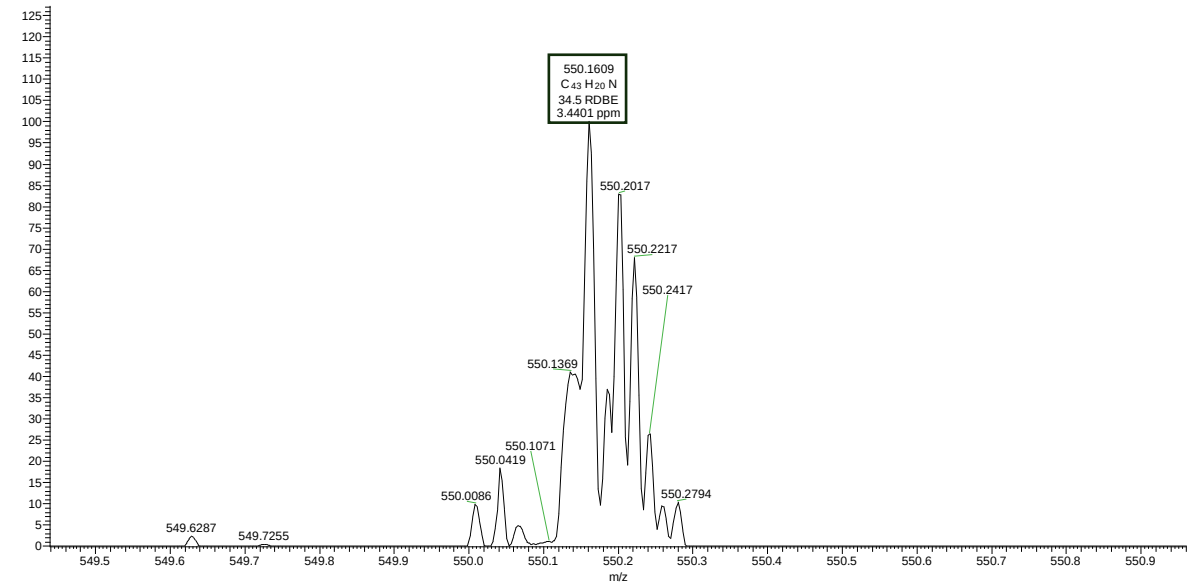
Compound class	Max. mass ion			
	3D OrbiSIMS	AP- MALDI repeat 1	AP-MALDI repeat 2	AP-MALDI repeat 3
Benzoquinoline	$C_{35}H_{18}N^+$ (-0.6 ppm)	$C_{25}H_{14}N^+$ (5.955 ppm)	$C_{25}H_{14}N^+$ (1.353 ppm)	$C_{25}H_{14}N^+$ (3.578 ppm)
Alkyl phenyl pyridine	$C_{59}H_{106}N^+$ (-1.1 ppm)	$C_{50}H_{88}N^+$ (-2.49 ppm)	$C_{22}H_{32}N^+$ (4.09 ppm)	$C_{55}H_{98}N^+$ (-2.37 ppm)
Carbazole	$C_{28}H_{18}N^+$ (-0.8 ppm)	$C_{28}H_{18}N^+$ (3.28 ppm)	$C_{26}H_{18}N$+ (1.63 ppm)	$C_{26}H_{18}N$+ (4.29 ppm)
Alkyl quinoline	$C_{43}H_{76}N^+$ (-0.5 ppm)	$C_{46}H_{82}N^+$ (-1.23 ppm)	$C_{20}H_{30}N^+$ (4.78 ppm)	$C_{46}H_{82}N^+$ (4.78 ppm)

ii. TCNQ matrix

Compound class	Max. mass ion			
	3D OrbiSIMS	AP-MALDI repeat 1	AP-MALDI repeat 2	AP-MALDI repeat 3
Benzoquinoline	$C_{35}H_{18}N^+$ (-0.6 ppm)	$C_{45}H_{22}N^+$ (5.955 ppm)	$C_{43}H_{20}N^+$ (3.598 ppm)	$C_{45}H_{22}N^+$ (4.54 ppm)
Alkyl phenyl pyridine	$C_{59}H_{106}N^+$ (-1.1 ppm)	$C_{30}H_{48}N^+$ (5.89 ppm)	$C_{29}H_{46}N^+$ (4.88 ppm)	$C_{29}H_{46}N^+$ (4.54 ppm)
Carbazole	$C_{28}H_{18}N^+$ (-0.8 ppm)	$C_{28}H_{18}N^+$ (-3.4 ppm)	$C_{28}H_{18}N$+ (-1.86 ppm)	$C_{28}H_{18}N$+ (-1.86 ppm)
Alkyl quinoline	$C_{43}H_{76}N^+$ (-0.5 ppm)	$C_{31}H_{52}N^+$ (3.17 ppm)	$C_{28}H_{46}N^+$ (4.45 ppm)	$C_{27}H_{44}N^+$ (6.1 ppm)

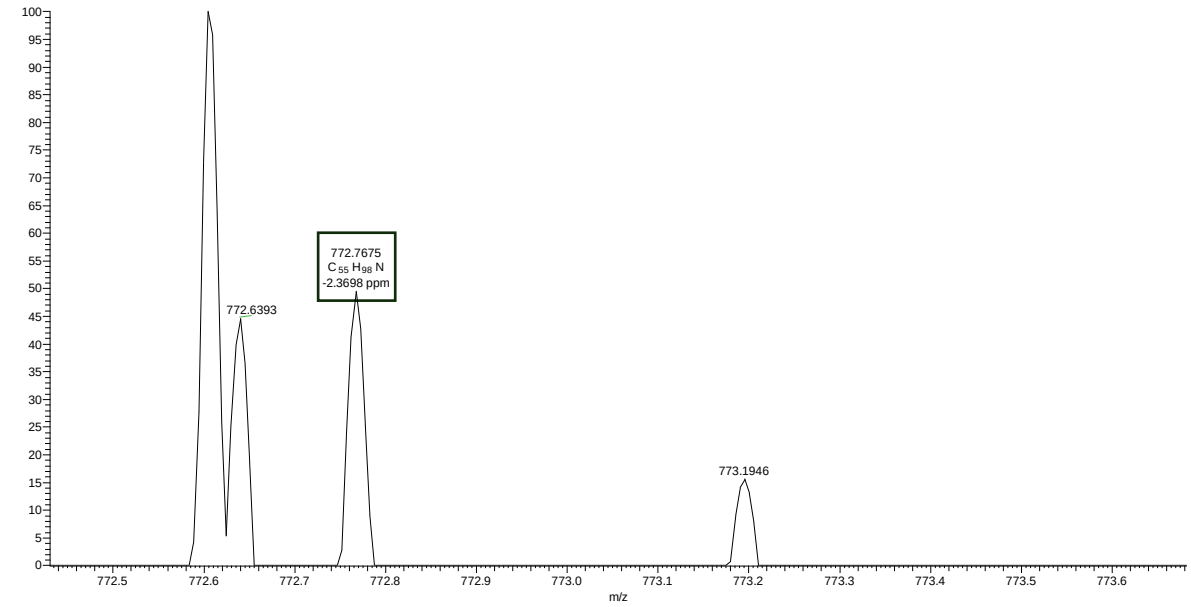
(b) i. Benzoquinolines

159+TCNQ13%(1) #6-225 RT: 0.09-1.43 AV: 220 NL: 5.42E2
T: FTMS + p MALDI Full ms [150.0000-1500.0000]

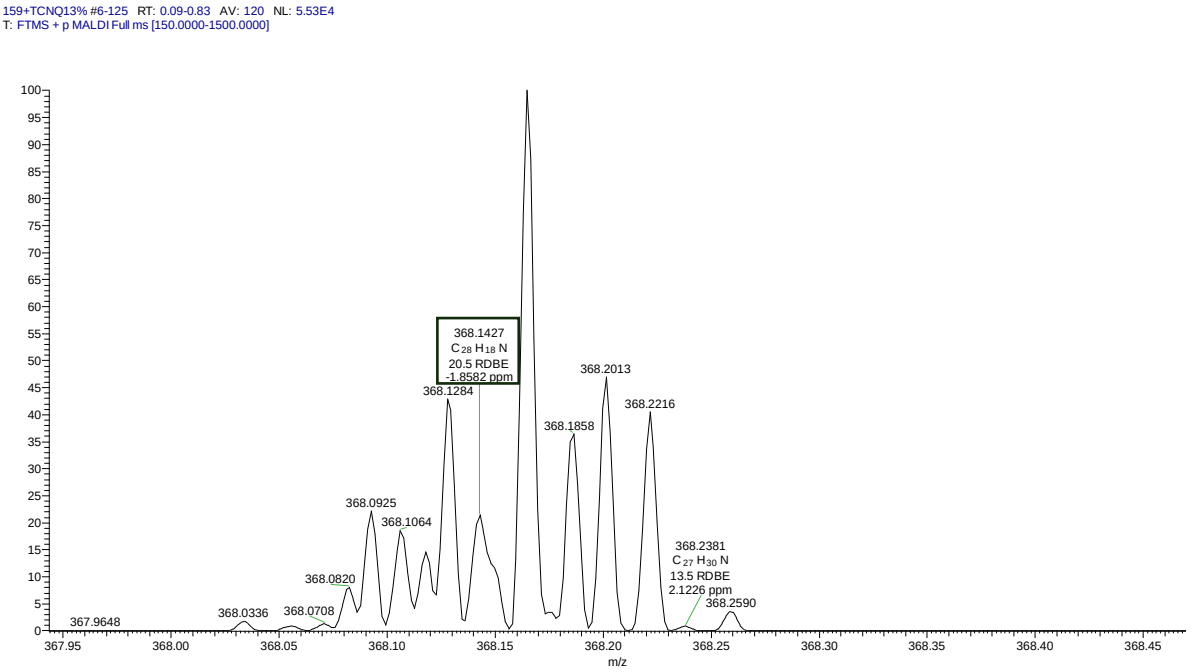


ii. Alkyl phenyl pyridines

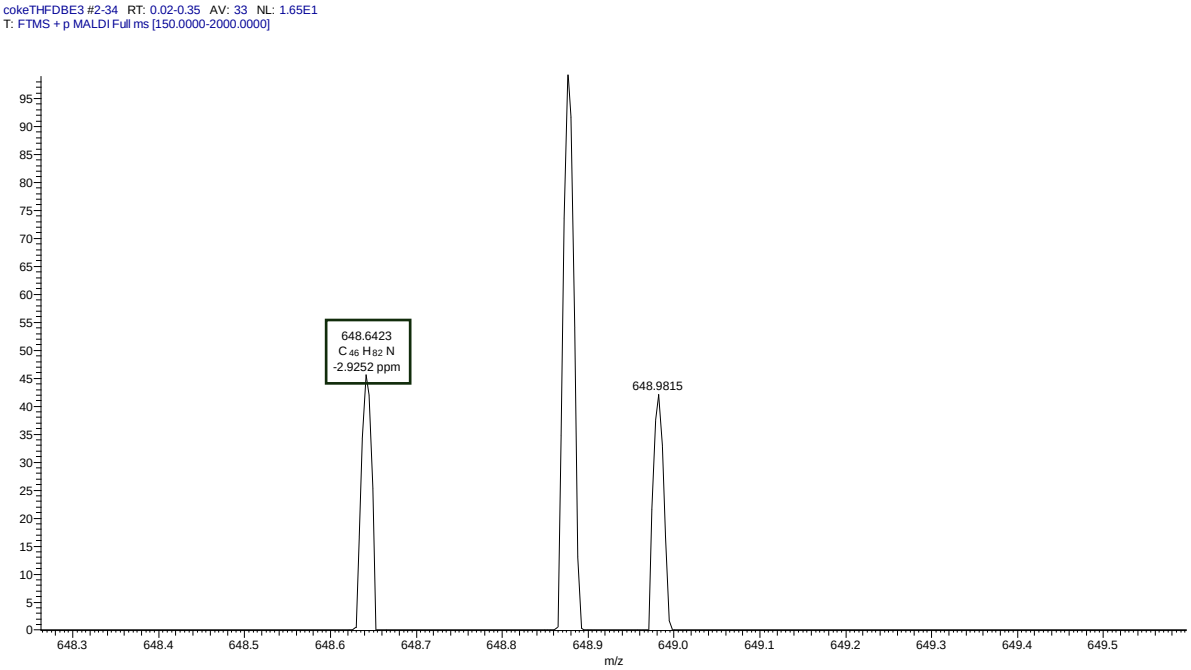
cokeTHFDBE3 #2-34 RT: 0.02-0.35 AV: 33 NL: 2.01E1
T: FTMS + p MALDI Full ms [150.0000-2000.0000]



iii. Carbazoles



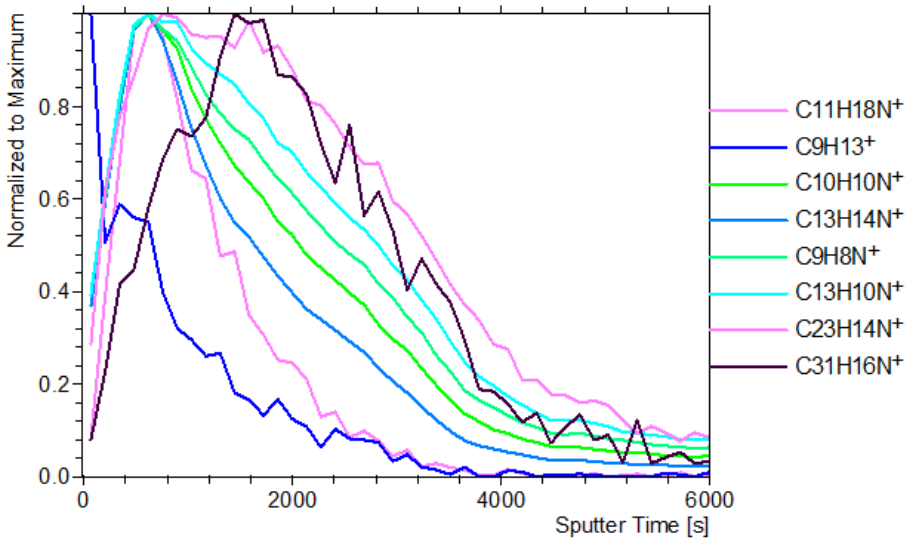
iv. Alkylated quinolines



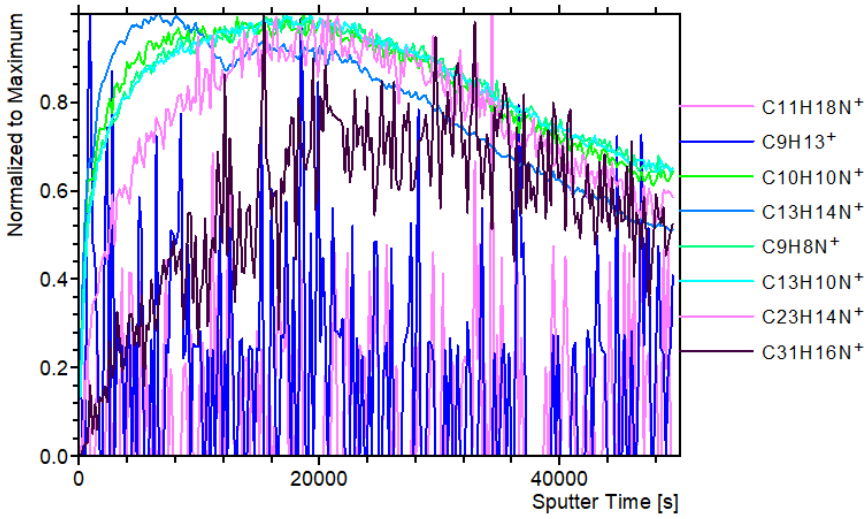
Supplementary figure S4.20. *(a) Table of maximum mass ions for each compound class annotated in the 3D OrbiSIMS and AP-MALDI MS repeat spectra from injector tip 5.* ***(b)*** *Raw AP-MALDI spectra using a TCNQ matrix showing peaks for maximum mass ions of each compound class from 'AP-MALDI dataset 2'.*

S4.21

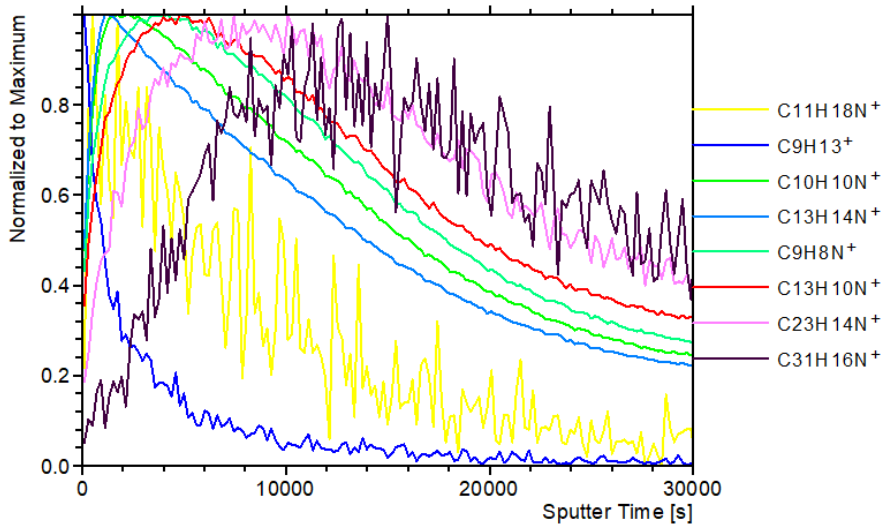
Injector tip 1



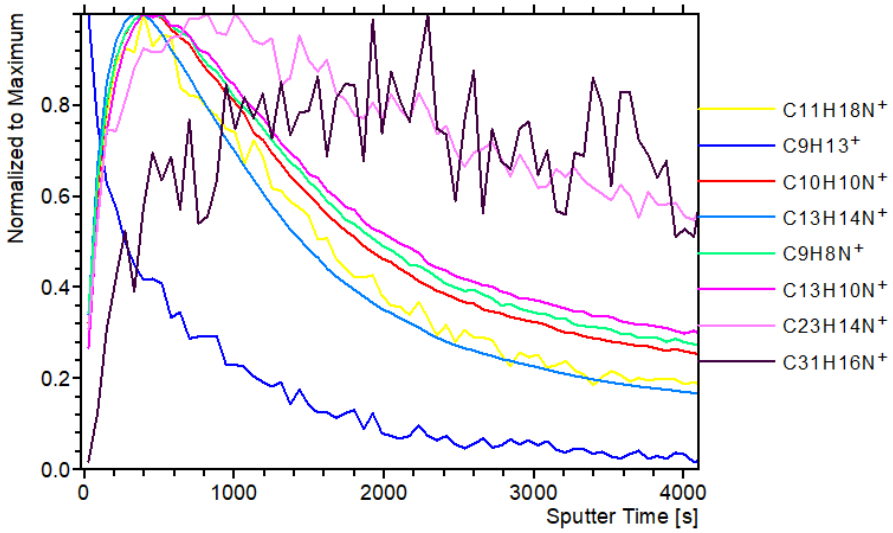
Injector tip 3



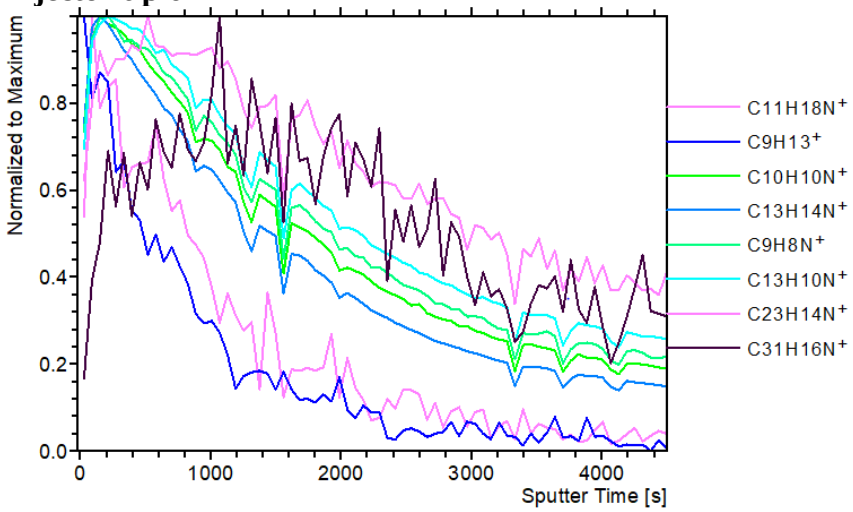
Injector tip 4



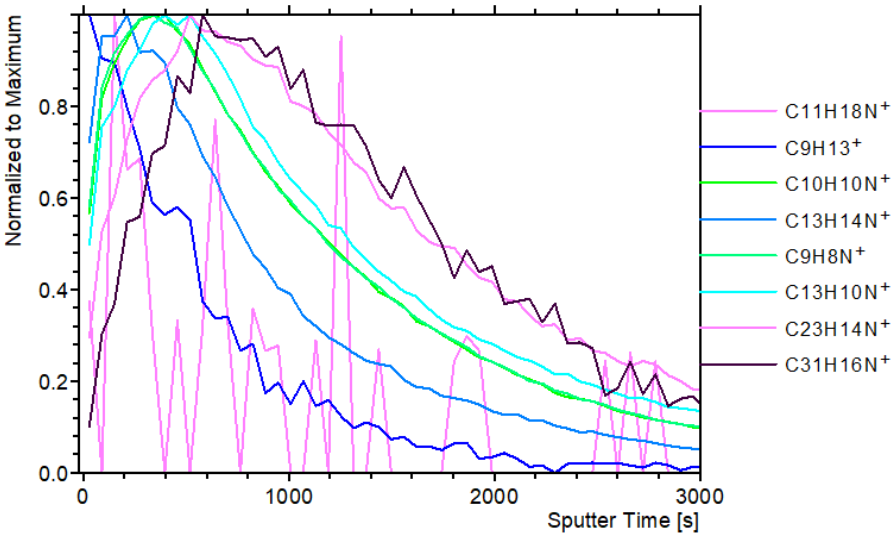
Injector tip 5



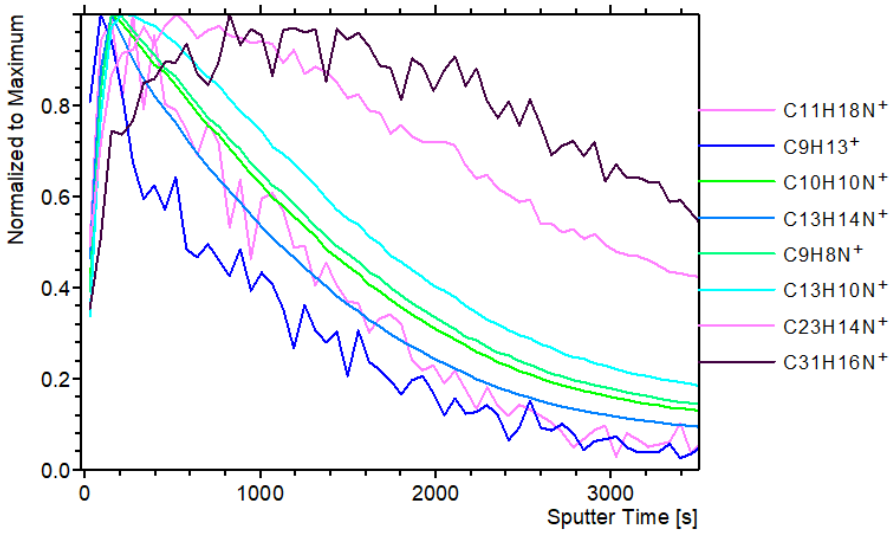
Injector tip 6



Injector tip 7



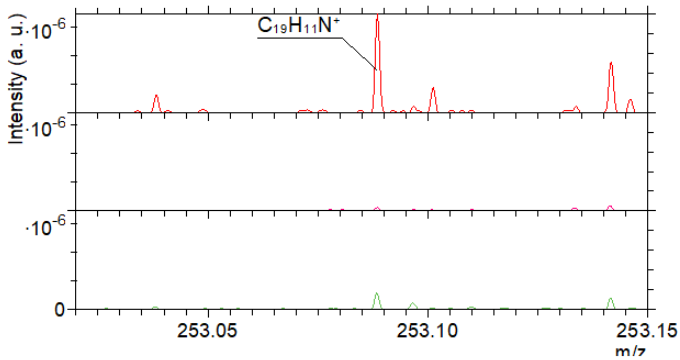
Injector tip 8



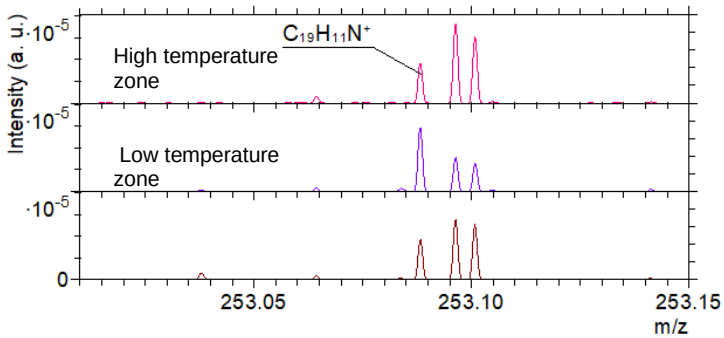
Supplementary figure S4.21*. 3D OrbiSIMS depth profiles of the highlighted nitrogen aromatic species in* ***Figure 4.2*** *for all injector tip deposits ions displayed are (in order of prevalence at depth).*

S4.22

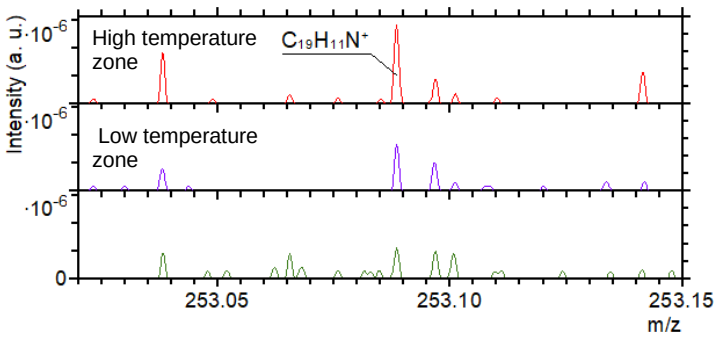
(a)



(b)



(c)



Supplementary figure S4.22. *3D OrbiSIMS spectra (normalized to total ion counts) of benzoquinoline ($C_{19}H_{11}N^+$) taken from different positions along (a) injector needle 1, (b) injector needle 2 and (c) injector needle 3.*

S4.23

(a)

C_7H_5O_3-	Centre Mass (u)	Assignment	Mass Deviation (ppm)	Area
	109.029453	C_6H_5O_2-	-0.459667	14619.49
	93.034421	C_6H_5O-	-1.799719	19606.87

(b)

C_8H_7O_3-	Centre Mass (u)	Assignment	Mass Deviation (ppm)	Area
	151.040012	C_8H_7O_3-	-0.36559	71818.67
	107.050281	C_7H_7O-	0.394903	45007.94
	122.037346	C_7H_6O_2-	0.150098	4178.69
	123.045164	C_7H_7O_2-	0.0883	8377.24
	123.008824	C_6H_3O_3-	0.456591	1634.14
	109.029552	C_6H_5O_2-	0.447403	1737.25

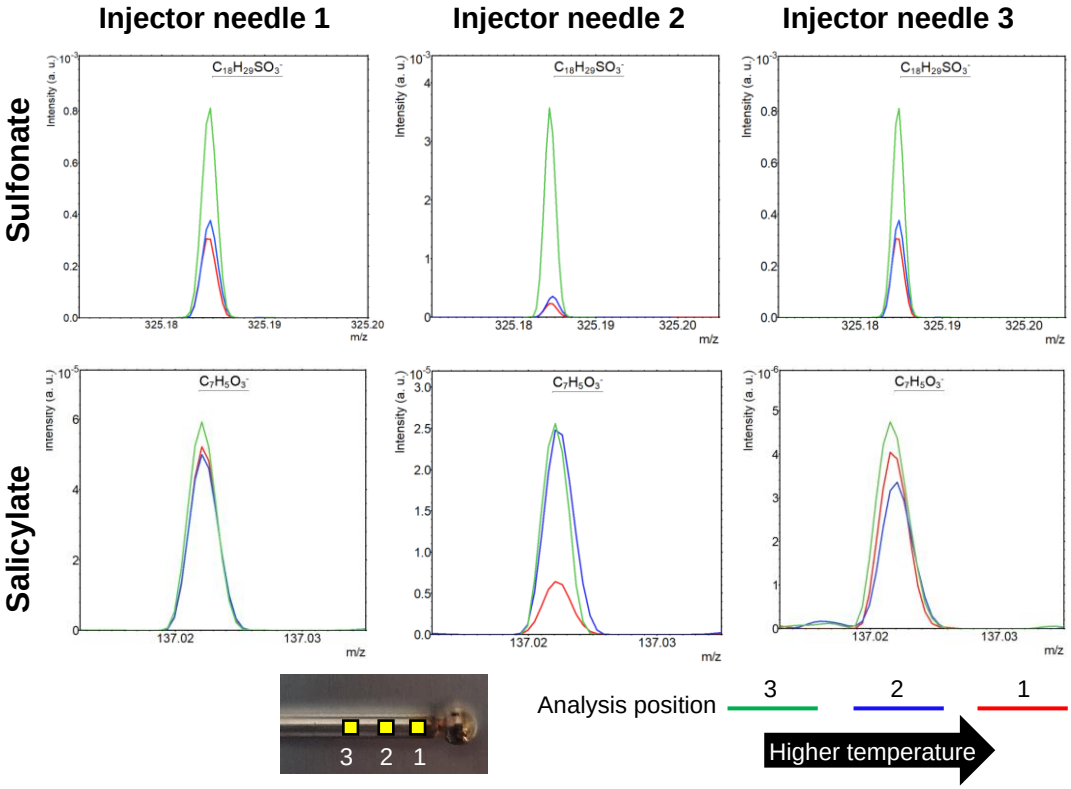
(c)

C_11H_7O_3-	Centre Mass (u)	Assignment	Mass Deviation (ppm)	Area
	187.040068	C_11H_7O_3-	0.001186	111752.82
	159.045115	C_10H_7O_2-	-0.237498	47219.63
	143.050163	C_10H_7O-	-0.530103	11727.89

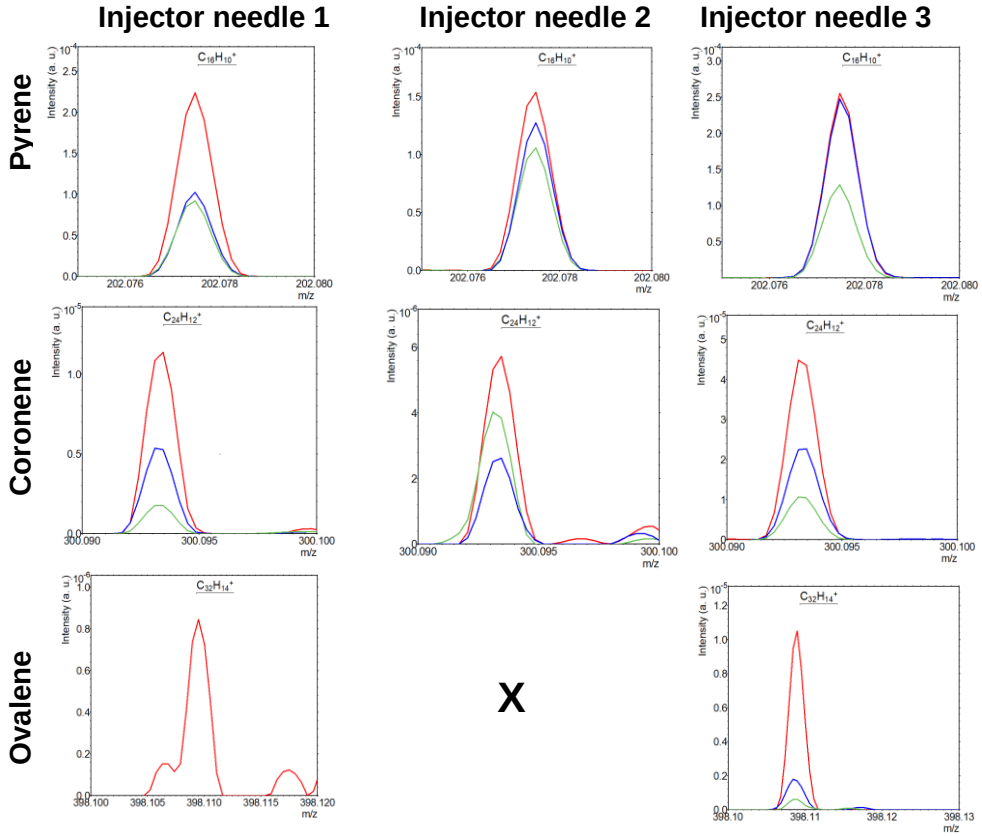
Supplementary figure S4.23*. MS/MS fragmentation for different salicylate types.* ***(a)*** *$C_7H_5O_3^-$ (with no alkyl chain),* ***(b)*** *$C_8H_7O_3^-$ (with alkyl chain length of 1).* ***(c)*** *$C_{11}H_7O_3^-$ (benzene fused salicylate).*

S4.24

(a)



(b)



Supplementary figure S4.24. *Normalized 3D OrbiSIMS spectral comparison of three different positions on injector needles 1, 2 and 3.* ***(a)*** *sulfonates and salicylates,* ***(b)*** *PAHs.*

Chapter 7

References:

1. Dabelstein, W., Reglitzky, A., Schütze, A. & Reders, K. Automotive Fuels. in *Ullmann's Encyclopedia of Industrial Chemistry* (American Cancer Society, 2007). doi:10.1002/14356007.a16_719.pub2.
2. Common-rail systems with piezo injectors. *Bosch Mobility Solutions* https://www.bosch-mobility-solutions.com/en/products-and-services/passenger-cars-and-light-commercial-vehicles/powertrain-systems/common-rail-system-piezo/.
3. Landia, A. Costs, not the environment, will drive switch to electric cars. *Financial Times* https://www.ft.com/content/c01f7a4a-38ed-11e8-8b98-2f31af407cc8 (2018).
4. BP. BP Energy Outlook 2019 edition.
5. Schöppe D, Greff A, Zhang H, Frenzel H, Rösel G, Achleitner E, et al. Requirements for Future Gasoline DI Systems and Respective Platform Solutions. in *Internationales Wiener Motoren symoposium* (2011).
6. Zhao, F., Lai, M.-C. & Harrington, D. L. Automotive spark-ignited direct-injection gasoline engines. *Prog Energy Combust Sci* **25**, 437–562 (1999).
7. Zimmerman, N., Wang, J. M., Jeong, C.-H., Wallace, J. S. & Evans, G. J. Assessing the Climate Trade-Offs of Gasoline Direct Injection Engines. *Environ Sci Technol* **50**, 8385–8392 (2016).
8. Graham, L. Chemical characterization of emissions from advanced technology light-duty vehicles. *Atmos Environ* **39**, 2385–2398 (2005).
9. Saliba, G. *et al.* Comparison of Gasoline Direct-Injection (GDI) and Port Fuel Injection (PFI) Vehicle Emissions: Emission Certification Standards, Cold-Start, Secondary Organic Aerosol Formation Potential, and Potential Climate Impacts. *Environ Sci Technol* **51**, 6542–6552 (2017).
10. Anderson, R. W., Brehob, D. D., Yang, J., Vallance, J. K. & Whiteaker, R. M. A new direct injection spark ignition (DISI) combustion system for low emissions. *FISITA-96* (1996).
11. Brehob, D. D., Fleming, J. E., Haghgooie, M. & Stein, R. A. Stratified-Charge Engine Fuel Economy and Emission Characteristics. in *International Fall Fuels and Lubricants Meeting and Exposition* (SAE International, 1998). doi:https://doi.org/10.4271/982704.
12. Wojik, K. & Fraidl, G. K. Engine and Vehicle Concepts for Low Consumption and Low Emission Passenger Cars. *FISITA-96, Paper* (1996).
13. Shimotani, K., Oikawa, K., Horada, O. & Kagawa, Y. Characteristics of gasoline in-cylinder direct injection engine. *JSAE Review* **17**, 267–272 (1996).
14. Karl, G., Kemmler, R., Bargende, M. & Abthoff, J. Analysis of a Direct Injected Gasoline Engine. in *International Congress & Exposition* (SAE International, 1997). doi:https://doi.org/10.4271/970624.
15. Guthrie, P. W. A Review of Fuel, Intake and Combustion System Deposit Issues Relevant to 4-Stroke Gasoline Direct Fuel Injection Engines. in *SAE 2001 World Congress* (SAE International, 2001). doi:https://doi.org/10.4271/2001-01-1202.

16. Badawy, T., Attar, M. A., Xu, H. & Ghafourian, A. Assessment of gasoline direct injector fouling effects on fuel injection, engine performance and emissions. *Appl Energy* **220**, 351–374 (2018).
17. Caprotti, R., Bhatti, N. & Balfour, G. Deposit Control in Modern Diesel Fuel Injection Systems. Preprint at https://doi.org/https://doi.org/10.4271/2010-01-2250 (2010).
18. Aradi, A. A., Imoehl, B., Avery, N. L., Wells, P. P. & Grosser, R. W. The Effect of Fuel Composition and Engine Operating Parameters on Injector Deposits in a High-Pressure Direct Injection Gasoline (DIG) Research Engine. in *International Fuels & Lubricants Meeting & Exposition* (SAE International, 1999). doi:https://doi.org/10.4271/1999-01-3690.
19. Lacey, P., Gail, S., Kientz, J. M., Milovanovic, N. & Gris, C. Internal Fuel Injector Deposits. *SAE Int J Fuels Lubr* **5**, 132–145 (2012).
20. Liaquat, A. M., Masjuki, H. H., Kalam, M. A. & Rizwanul Fattah, I. M. Impact of biodiesel blend on injector deposit formation. *Energy* **72**, 813–823 (2014).
21. Wang, C., Xu, H., Herreros, J. M., Wang, J. & Cracknell, R. Impact of fuel and injection system on particle emissions from a GDI engine. *Appl Energy* **132**, 178–191 (2014).
22. Barker, J. *et al.* The Investigation of the Structure and Origins of Gasoline Direct Injection (GDI) Deposits. *SAE Int J Fuels Lubr* **01**, (2019).
23. Barker, J. *et al.* Internal Injector Deposits (IDID). in *11th International Colloquium Fuels Conventional and Future Energy for automobiles* (2017).
24. Hoang, A. T. & Le, A. T. A review on deposit formation in the injector of diesel engines running on biodiesel. *Energy Sources, Part A: Recovery, Utilization, and Environmental Effects* **41**, 584–599 (2019).
25. Xu, H. *et al.* Fuel injector deposits in direct-injection spark-ignition engines. *Prog Energy Combust Sci* **50**, 63–80 (2015).
26. Pos, R., Cracknell, R. & Ganippa, L. Transient characteristics of diesel sprays from a deposit rich injector. *Fuel* **153**, 183–191 (2015).
27. Wen, Y. *et al.* The Impact of Injector Deposits on Spray and Particulate Emission of Advanced Gasoline Direct Injection Vehicle. in *SAE 2016 International Powertrains, Fuels & Lubricants Meeting* (SAE International, 2016). doi:https://doi.org/10.4271/2016-01-2284.
28. Henkel, S. *et al.* Injector Fouling and Its Impact on Engine Emissions and Spray Characteristics in Gasoline Direct Injection Engines. *SAE Int J Fuels Lubr* **10**, 287–295 (2017).
29. Jiang, C. *et al.* Effect of fuel injector deposit on spray characteristics, gaseous emissions and particulate matter in a gasoline direct injection engine. *Appl Energy* **203**, 390–402 (2017).
30. Bock, N., Jeon, J., Kittelson, D. & Northrop, W. F. Solid Particle Number and Mass Emissions from Lean and Stoichiometric Gasoline Direct Injection Engine Operation. in *WCX World Congress Experience* (SAE International, 2018). doi:https://doi.org/10.4271/2018-01-0359.
31. Berndorfer, A., Breuer, S., Piock, W. & von Bacho, P. Diffusion Combustion Phenomena in GDi Engines caused by Injection Process. in *SAE 2013 World Congress & Exhibition* (SAE International, 2013). doi:https://doi.org/10.4271/2013-01-0261.
32. Hoang, A. T. & Pham, V. V. Impact of Jatropha Oil on Engine Performance, Emission Characteristics, Deposit Formation, and Lubricating Oil Degradation. *Combustion Science and Technology* **191**, 504–519 (2019).

33. Xiao, J. *et al.* Experimental Study on the Effects of Nozzle Temperature on Internal Deposits of a Gasoline Direct Injector. *Energy & Fuels* **32**, 8978–8985 (2018).
34. Altin, O. & Eser, S. Carbon deposit formation from thermal stressing of petroleum fuels. *Am. Chem. Soc. Div. Fuel Chem.* **49**, (2004).
35. Joedicke, A., Krueger-Venus, J., Bohr, P., Cracknell, R. & Doyle, D. Understanding the Effect of DISI Injector Deposits on Vehicle Performance. in *SAE 2012 World Congress & Exhibition* (SAE International, 2012). doi:https://doi.org/10.4271/2012-01-0391.
36. Kinoshita, M., Saito, A., Matsushita, S., Shibata, H. & Niwa, Y. A Method for Suppressing Formation of Deposits on Fuel Injector for Direct Injection Gasoline Engine. in *International Fuels & Lubricants Meeting & Exposition* (SAE International, 1999). doi:https://doi.org/10.4271/1999-01-3656.
37. Xu, H. *et al.* Fuel injector deposits in direct-injection spark-ignition engines. *Prog Energy Combust Sci* **50**, 63–80 (2015).
38. Pradelle, F., Braga, S. L., Martins, A. R. F. A., Turkovics, F. & Pradelle, R. N. C. Gum Formation in Gasoline and Its Blends: A Review. *Energy & Fuels* **29**, 7753–7770 (2015).
39. Aradi, A. A., Colucci, W. J., Scull, H. M. & Openshaw, M. J. A Study of Fuel Additives for Direct Injection Gasoline (DIG) Injector Deposit Control. in *CEC/SAE Spring Fuels & Lubricants Meeting & Exposition* (SAE International, 2000). doi:https://doi.org/10.4271/2000-01-2020.
40. di Somma, I., Marotta, R., Andreozzi, R. & Caprio, V. Dicumyl Peroxide Thermal Decomposition in Cumene: Development of a Kinetic Model. *Ind Eng Chem Res* **51**, 7493–7499 (2012).
41. Barker, J., Cook, S. & Richards, P. Sodium Contamination of Diesel Fuel, its Interaction with Fuel Additives and the Resultant Effects on Filter Plugging and Injector Fouling. Preprint at https://doi.org/https://doi.org/10.4271/2013-01-2687 (2013).
42. McCormick, R. L., Alleman, T. L. & Janet, Y. *Sulfate Salts in Gasoline and Ethanol Fuels – Historical Perspective and Analysis of Available Data*. Sulfate Salts in Gasoline and%0AEthanol Fuels – Historical%0APerspective and Analysis of%0AAvailable Data (2017).
43. Dallanegra, R. & Caprotti, R. Chemical Composition of Ashless Polymeric Internal Diesel Injector Deposits. in *SAE 2014 International Powertrain, Fuels & Lubricants Meeting* (SAE International, 2014). doi:https://doi.org/10.4271/2014-01-2728.
44. Almena, M. D. C. *et al. Internal Diesel Injector Deposits: Sodium Carboxylates of C12 Succinic Acids and C16 and C18 Fatty Acids*. (2012).
45. Diaby, M., Sablier, M., le Negrate, A., el Fassi, M. & Bocquet, J. Understanding carbonaceous deposit formation resulting from engine oil degradation. *Carbon N Y* **47**, 355–366 (2009).
46. Ashida, T., Takei, Y. & Hosi, H. Effects of Fuel Properties on SIDI Fuel Injector Deposit. in *Spring Fuels & Lubricants Meeting & Exhibition* (SAE International, 2001). doi:https://doi.org/10.4271/2001-01-3694.
47. The Coordinating European Council for the Development of Performance Tests for Fuel Lubricants and Other Fluid. Direct Injection, Common Rail Diesel Engine Nozzle Coking Test. https://www.cectests.org/disptestdoc1.asp (2019).
48. Cardenas, D. *et al.* Internal Diesel Injector Deposits: Sodium Carboxylates of C12 Succinic Acids and C16 and C18 Fatty Acids. *SAE Technical Papers* **9**, (2012).

49. Lin, Y.-S. & Lin, H.-P. Spray characteristics of emulsified castor biodiesel on engine emissions and deposit formation. *Renew Energy* **36**, 3507–3516 (2011).
50. Reid, J. & Barker, J. *Understanding polyisobutylene succinimides (PIBSI) and internal diesel injector deposits*. (2013).
51. Feld, H. & Oberender, N. Characterization of Damaging Biodiesel Deposits and Biodiesel Samples by Infrared Spectroscopy (ATR-FTIR) and Mass Spectrometry (TOF-SIMS). Preprint at https://doi.org/https://doi.org/10.4271/2016-01-9078 (2016).
52. Berrios, M., Martín, M. A., Chica, A. F. & Martín, A. Storage effect in the quality of different methyl esters and blends with diesel. *Fuel* **91**, 119–125 (2012).
53. Barker, J. *et al.* The Application of New Approaches to the Analysis of Deposits from the Jet Fuel Thermal Oxidation Tester (JFTOT). Preprint at https://doi.org/https://doi.org/10.4271/2017-01-2293 (2017).
54. Xu, H. *et al.* Fuel injector deposits in direct-injection spark-ignition engines. *Prog Energy Combust Sci* **50**, 63–80 (2015).
55. Pickl, F., Russer, M., Hauenstein, M. & Wensing, M. Modelling and understanding deposit formation and reduction in combustion engines – Application to the concrete case of internal GDI injector deposit. *Fuel* **236**, 284–296 (2019).
56. Alves Fortunato, M., Starck, L., Takahashi, T., Ohmae, K. & Iida, Y. Oxidation Stability of Diesel/Biodiesel Blends: Impact of Fuels Physical-Chemical Properties over Ageing During Storage and Accelerated Oxidation. *SAE Int J Fuels Lubr* **2015-01–19**, (2015).
57. Christensen, E. *et al.* Experimental and theoretical study of oxidative stability of alkylated furans used as gasoline blend components. *Fuel* **212**, 576–585 (2018).
58. Venkataraman, R. & Eser, S. Characterization of deposits formed on diesel injectors in field test and from thermal oxidative degradation of n-hexadecane in a laboratory reactor. *Chem Cent J* **2**, 25 (2008).
59. Barker, J., Snape, C. & Scurr, D. Information on the Aromatic Structure of Internal Diesel Injector Deposits From Time of Flight Secondary Ion Mass Spectrometry (ToF-SIMS). in *SAE 2014 World Congress & Exhibition* (SAE International, 2014). doi:https://doi.org/10.4271/2014-01-1387.
60. Barker, J., Snape, C. & Scurr, D. A Novel Technique for Investigating the Characteristics and History of Deposits Formed Within High Pressure Fuel Injection Equipment. *SAE Int J Fuels Lubr* **5**, 1155–1164 (2012).
61. Barker, J. *et al.* The Characterisation of Diesel Internal Injector Deposits by Focused Ion-Beam Scanning Electron Microscopy (FIB-SEM), Transmission Electron Microscopy (TEM), Atomic Force Microscopy and Raman Spectroscopy. in *JSAE/SAE 2015 International Powertrains, Fuels & Lubricants Meeting* (SAE International, 2015). doi:https://doi.org/10.4271/2015-01-1826.
62. Goldstein 1939-, J. *Scanning electron microscopy and x-ray microanalysis / Joseph I. Goldstein ... [et al.]*. (New York : Kluwer Academic/Plenum Publishers, 2003).
63. Smith, A. & Williams, R. Linking the physical manifestation and performance effects of injector nozzle deposits in modern diesel engines. *SAE Int J Fuels Lubr* **8**, 344–357 (2015).
64. Lacey, P. *et al.* Fuel Quality and Diesel Injector Deposits. *SAE Int J Fuels Lubr* **5**, 1187–1198 (2012).
65. Hoang, A. T. & Pham, V. V. A study of emission characteristic, deposits, and lubrication oil degradation of a diesel engine running on preheated vegetable oil

and diesel oil. *Energy Sources, Part A: Recovery, Utilization, and Environmental Effects* **41**, 611–625 (2019).
66. Dearn, K. *et al.* An Investigation into the Characteristics of DISI Injector Deposits Using Advanced Analytical Methods. *SAE Int J Fuels Lubr* **7**, 771–782 (2014).
67. Paredes, A. M. *MICROSCOPY | Scanning Electron Microscopy*. (Elsevier Ltd, 2014). doi:10.1016/B978-0-12-384730-0.00215-9.
68. von Bacho, P. S., Sofianek, J. K., Galante-Fox, J. M. & McMahon, C. J. Engine Test for Accelerated Fuel Deposit Formation on Injectors Used in Gasoline Direct Injection Engines. in *SAE World Congress & Exhibition* (SAE International, 2009). doi:https://doi.org/10.4271/2009-01-1495.
69. Trobaugh, C. *et al.* Internal Diesel Injector Deposits: Theory and Investigations into Organic and Inorganic Based Deposits. *SAE Int J Fuels Lubr* **6**, 772–784 (2013).
70. Schwab, S. D. *et al.* Internal Injector Deposits in High-Pressure Common Rail Diesel Engines. *SAE Int J Fuels Lubr* **3**, 865–878 (2010).
71. Leedham, A., Caprotti, R., Graupner, O. & Klaua, T. *Impact of fuel additives on diesel injector deposits*. (2004).
72. D'Ambrosio, S. & Ferrari, A. Diesel Injector Coking: Optical-Chemical Analysis of Deposits and Influence on Injected Flow-Rate, Fuel Spray and Engine Performance. *J Eng Gas Turbine Power* **134**, 62801 (2012).
73. Vickerman, J. C. & Gilmore, I. S. *Surface Analysis: The Principal Techniques*. (Wiley, 2011).
74. Carlisle, H. W., Frew, R. W., Mills, J. R., Aradi, A. A. & Avery, N. L. The Effect of Fuel Composition and Additive Content on Injector Deposits and Performance of an Air-Assisted Direct Injection Spark Ignition (DISI) Research Engine. in *International Spring Fuels & Lubricants Meeting* (SAE International, 2001). doi:https://doi.org/10.4271/2001-01-2030.
75. Song, C., Eser, S., Schobert, H. H. & Hatcher, P. G. Pyrolytic degradation studies of a coal-derived and a petroleum-derived aviation jet fuel. *Energy & Fuels* **7**, 234–243 (1993).
76. de Graef, M. *Introduction to conventional transmission electron microscopy / Marc De Graef.* (Cambridge : Cambridge University Press, 2003).
77. Wo, H. *et al.* Morphology, composition, and structure of carbon deposits from diesel and biomass oil/diesel blends on a pintle-type fuel injector nozzle. *Tribol Int* **91**, 189–196 (2015).
78. Tanaka, A., Yamada, K., Omori, T., Bunne, S. & Hosokawa, K. Inner diesel injector deposit formation mechanism. *SAE Int J Fuels Lubr* **6**, 755–761 (2013).
79. Ullmann, J., Geduldig, M., Stutzenberger, H., Caprotti, R. & Balfour, G. Investigation into the Formation and Prevention of Internal Diesel Injector Deposits. in *SAE World Congress & Exhibition* (SAE International, 2008). doi:https://doi.org/10.4271/2008-01-0926.
80. Galante-Fox, J. & Bennett, J. Diesel injector internal deposits in High Pressure Common Rail diesel engines. *Fuel Systems for IC Engines* 157–166 (2012) doi:10.1533/9780857096043.5.157.
81. DoITPoMS. Raman Spectroscopy. *Cambridge University* https://www.doitpoms.ac.uk/tlplib/raman/printall.php.
82. Patel, M., Azanza Ricardo, C. L., Scardi, P. & Aswath, P. B. Morphology, structure and chemistry of extracted diesel soot—Part I: Transmission electron microscopy, Raman spectroscopy, X-ray photoelectron spectroscopy and synchrotron X-ray diffraction study. *Tribol Int* **52**, 29–39 (2012).

83. Perkin Elmer. *Thermogravimetric Analysis (TGA)*. http://www.perkinelmer.co.uk/CMSResources/Images/44-74556GDE_TGABeginnersGuide.pdf.
84. Eser, S., Venkataraman, R. & Altin, O. Utility of Temperature-Programmed Oxidation for Characterization of Carbonaceous Deposits from Heated Jet Fuel. *Ind Eng Chem Res* **45**, 8956–8962 (2006).
85. Barker, J., Richards, P., Pinch, D. & Cheeseman, B. Temperature Programmed Oxidation as a Technique for Understanding Diesel Fuel System Deposits. *SAE International Journal of Fuels and Lubricants* vol. 3 85–99 Preprint at https://doi.org/https://doi.org/10.4271/2010-01-1475 (2010).
86. Barker, J., Richards, P., Snape, C. & Meredith, W. A Novel Technique for Investigating the Nature and Origins of Deposits Formed in High Pressure Fuel Injection Equipment. Preprint at https://doi.org/https://doi.org/10.4271/2009-01-2637 (2009).
87. Barker, J., Reid, J., Snape, C., Scurr, D. & Meredith, W. Spectroscopic Studies of Internal Injector Deposits (IDID) Resulting from the Use of Non-Commercial Low Molecular Weight Polyisobutylenesuccinimide (PIBSI). Preprint at https://doi.org/https://doi.org/10.4271/2014-01-2720 (2014).
88. Martín, P. & Méndez, A. MECHANISMS OF GASOLINE DEPOSIT FORMATION IN ENGINE INDUCTION SYSTEMS. CHARACTERIZATION OF PRODUCT REACTION BETWEEN BENZOTHIOPHENE OXIDES WITH OLEFINS AND AROMATIC COMPOUNDS. *Pet Sci Technol* **15**, 409–427 (1997).
89. Martin, P. & Mendez, A. MECHANISMS OF GASOLINE DEPOSIT FORMATION IN ENGINE INDUCTION SYSTEMS, CHARACTERIZATION OF PRODUCT REACTION BETWEEN BENZOTHIOPHENE OXIDES AND BASIC NITROGEN AND NAPHTHENIC COMPOUNDS. *Pet Sci Technol* **16**, 611–626 (1998).
90. Dubey, M., Brison, J., Grainger, D. W. & Castner, D. G. Comparison of Bi1+, Bi3+ and C60+ primary ion sources for ToF-SIMS imaging of patterned protein samples. *Surface and Interface Analysis* **43**, 261–264 (2011).
91. Sanyova, J. *et al.* Unexpected Materials in a Rembrandt Painting Characterized by High Spatial Resolution Cluster-TOF-SIMS Imaging. *Anal Chem* **83**, 753–760 (2011).
92. Lehrle, R., Riches, J. & Wyszynski, M. The scope of laser—mass spectrometry and other mass spectrometric techniques for studying engine deposits and exhaust emissions. *J Anal Appl Pyrolysis* **26**, 1–20 (1993).
93. Lau, K., Junk, R., Klingbeil, S., Schümann, U. & Streibel, T. Analysis of Internal Common Rail Injector Deposits via Thermodesorption Photon Ionization Time of Flight Mass Spectrometry. *Energy & Fuels* **29**, 5625–5632 (2015).
94. Lin, L. *et al.* Types, principle, and characteristics of tandem high-resolution mass spectrometry and its applications. *RSC Adv* **5**, 107623–107636 (2015).
95. Delcorte, A., Bertrand, P. & Garrison, B. J. Collision Cascade and Sputtering Process in a Polymer. *J Phys Chem B* **105**, 9474–9486 (2001).
96. Nittler, L., Delcorte, A., Bertrand, P. & Migeon, H.-N. Insights into the yield enhancement and ion emission process in metal-assisted SIMS. *Surface and Interface Analysis* **45**, 18–21 (2013).
97. Kollmer, F. Cluster primary ion bombardment of organic materials. *Appl Surf Sci* **231–232**, 153–158 (2004).

98. Murray, P. T. & Rabalais, J. W. Ejection dynamics and electronic processes governing secondary particle emission in SIMS. *J Am Chem Soc* **103**, 1007–1013 (1981).
99. Mamyrin, B. A. Time-of-flight mass spectrometry (concepts, achievements, and prospects). *Int J Mass Spectrom* **206**, 251–266 (2001).
100. Shon, H. K., Yoon, S., Moon, J. H. & Lee, T. G. Improved mass resolution and mass accuracy in TOF-SIMS spectra and images using argon gas cluster ion beams. *Biointerphases* **11**, 02A321 (2016).
101. Juhasz, P., Vestal, M. L. & Martin, S. A. On the initial velocity of ions generated by matrix-assisted laser desorption ionization and its effect on the calibration of delayed extraction time-of-flight mass spectra. *J Am Soc Mass Spectrom* **8**, 209–217 (1997).
102. Mahoney, C. M. Cluster secondary ion mass spectrometry of polymers and related materials. *Mass Spectrom Rev* **29**, 247–293 (2010).
103. Seah, M. P. Universal Equation for Argon Gas Cluster Sputtering Yields. *The Journal of Physical Chemistry C* **117**, 12622–12632 (2013).
104. Seah, M. P., Havelund, R. & Gilmore, I. S. Universal Equation for Argon Cluster Size-Dependence of Secondary Ion Spectra in SIMS of Organic Materials. *The Journal of Physical Chemistry C* **118**, 12862–12872 (2014).
105. Seah, M. P. & Nunney, T. S. Sputtering yields of compounds using argon ions. *J Phys D Appl Phys* **43**, 253001 (2010).
106. Shard, A. G. *et al.* Argon cluster ion beams for organic depth profiling: results from a VAMAS interlaboratory study. *Anal Chem* **84**, 7865–7873 (2012).
107. ULVAC-PHI. INC. About Gas Cluster Ion Beams. https://www.ulvac-phi.com/en/surface-analysis/topics/gcib/.
108. Benninghoven, A. Analysis of Submonolayers on Silver by Negative Secondary Ion Emission. *physica status solidi (b)* **34**, K169–K171 (1969).
109. Hu, Q. *et al.* The Orbitrap: a new mass spectrometer. *Journal of Mass Spectrometry* **40**, 430–443 (2005).
110. Zubarev, R. A. & Makarov, A. Orbitrap Mass Spectrometry. *Anal Chem* **85**, 5288–5296 (2013).
111. G Marshall, A. *et al.* Mass resolution and mass accuracy: how much is enough? *Mass Spectrom (Tokyo)* **2**, S0009–S0009 (2013).
112. Thomas, M. J. *et al.* Petroleomic depth profiling of Staten Island salt marsh soil: 2ω detection FTICR MS offers a new solution for the analysis of environmental contaminants. *Science of The Total Environment* **662**, 852–862 (2019).
113. Hughey, C. A., Hendrickson, C. L., Rodgers, R. P. & Marshall, A. G. Elemental composition analysis of processed and unprocessed diesel fuel by electrospray ionization Fourier transform ion cyclotron resonance mass spectrometry. *Energy & Fuels* **15**, 1186–1193 (2001).
114. Rodgers, R. P., Blumer, E. N., Freitas, M. A. & Marshall, A. G. Jet fuel chemical composition, weathering, and identification as a contaminant at a remediation site, determined by Fourier transform ion cyclotron resonance mass spectrometry. *Anal Chem* **71**, 5171–5176 (1999).
115. Fernandez-Lima, F. A. *et al.* Petroleum crude oil characterization by IMS-MS and FTICR MS. *Anal Chem* **81**, 9941–9947 (2009).
116. F. Smith, D., C. Podgorski, D., P. Rodgers, R., T. Blakney, G. & L. Hendrickson, C. 21 Tesla FT-ICR Mass Spectrometer for Ultrahigh-Resolution Analysis of Complex Organic Mixtures. *Anal Chem* **90**, 2041–2047 (2018).

117. Barker, J., Langley, G. J. & Richards, P. *Insights into deposit formation in high pressure diesel fuel injection equipment*. (2010).
118. Kiss, A., Smith, D. F., Reschke, B. R., Powell, M. J. & Heeren, R. M. A. Top-down mass spectrometry imaging of intact proteins by laser ablation ESI FT-ICR MS. *Proteomics* **14**, 1283–1289 (2014).
119. Spraggins, J. M. *et al.* Next-generation technologies for spatial proteomics: Integrating ultra-high speed MALDI-TOF and high mass resolution MALDI FTICR imaging mass spectrometry for protein analysis. *Proteomics* **16**, 1678–1689 (2016).
120. Passarelli, M. K. *et al.* The 3D OrbiSIMS—label-free metabolic imaging with subcellular lateral resolution and high mass-resolving power. *Nat Methods* **14**, 1175 (2017).
121. Kotowska, A. M. *et al.* Protein identification by 3D OrbiSIMS to facilitate in situ imaging and depth profiling. *Nat Commun* **11**, 5832 (2020).
122. Starr, N. J. *et al.* Elucidating the molecular landscape of the stratum corneum. *Proceedings of the National Academy of Sciences* **119**, e2114380119 (2022).
123. Schaepe, K. *et al.* Imaging of Lipids in Native Human Bone Sections Using TOF–Secondary Ion Mass Spectrometry, Atmospheric Pressure Scanning Microprobe Matrix-Assisted Laser Desorption/Ionization Orbitrap Mass Spectrometry, and Orbitrap–Secondary Ion Mass Spectrometry. *Anal Chem* **90**, 8856–8864 (2018).
124. Bloomberg New Energy Finance. *Electric Vehicle Outlook*. (2019).
125. House of Commons: Business Energy and Industrial Strategy Committee. *Electric vehicles: driving the transition*. (2018).
126. Kalghatgi, G. Is it really the end of internal combustion engines and petroleum in transport? *Appl Energy* **225**, 965–974 (2018).
127. Moriarty, P. & Wang, S. J. Can Electric Vehicles Deliver Energy and Carbon Reductions? *Energy Procedia* **105**, 2983–2988 (2017).
128. Reitz, R. D. *et al.* IJER editorial: The future of the internal combustion engine. *International Journal of Engine Research* **21**, 3–10 (2019).
129. Moawad, A., Kim, N., Shidore, N. & Rousseau, A. *Assessment of Vehicle Sizing, Energy Consumption, and Cost through Large-Scale Simulation of Advanced Vehicle Technologies*. (2016).
130. Gabiña, G. *et al.* Performance of marine diesel engine in propulsion mode with a waste oil-based alternative fuel. *Fuel* **235**, 259–268 (2019).
131. Llamas, X. & Eriksson, L. Control-oriented modeling of two-stroke diesel engines with exhaust gas recirculation for marine applications. *Proceedings of the Institution of Mechanical Engineers, Part M: Journal of Engineering for the Maritime Environment* **233**, 551–574 (2018).
132. Behrendt, C. & Smith, A. A Study of Diesel Fuel Injector Deposit Effects on Power and Fuel Economy Performance. Preprint at https://doi.org/https://doi.org/10.4271/2017-01-0803 (2017).
133. Zhang, W., Ma, X., Xinhui, L. & Shuai, S. Impact of Fuel Properties on GDI Injector Deposit Formation and Particulate Matter Emissions. *SAE Technical Papers* **01**, (2020).
134. World Health Organization. Air Pollution. https://www.who.int/health-topics/air-pollution#tab=tab_1.
135. Edney, M. K., Barker, J., Reid, J., Scurr, D. J. & Snape, C. E. Recent Advances in the Analysis of GDI and Diesel Fuel Injector Deposits. *Fuel* **272**, (2020).

136. Technical Committee of Petroleum Additive Manufacturers in Europe. Fuel Additives: Uses and Benefits. *ATC Europe* https://www.atc-europe.org/public/Doc113 2013-11-20.pdf (2013).
137. Seah, M. P., Havelund, R. & Gilmore, I. S. Universal Equation for Argon Cluster Size-Dependence of Secondary Ion Spectra in SIMS of Organic Materials. *The Journal of Physical Chemistry C* **118**, 12862–12872 (2014).
138. Technical Committee of Petroleum Additive Manufacturers in Europe. *Lubricant Additives: Uses and Benefits*. (2016).
139. Nassar, A. M., Ahmed, N. S., El-shazly, R. I. & Abd el menem, Y. K. Preparation and evaluation of the mixtures of sulfonate and phenate as lube oil additives. *International Journal of Industrial Chemistry* **8**, 383–395 (2017).
140. Geng, Y. *et al.* Efficient synthesis of dodecylbenzene sulfonic acid in microreaction systems. *Chemical Engineering and Processing - Process Intensification* **149**, 107858 (2020).
141. Xie, W., Weng, L.-T., Ng, K. M., Chan, C. K. & Chan, C.-M. Defects of clean graphene and sputtered graphite surfaces characterized by time-of-flight secondary ion mass spectrometry and X-ray photoelectron spectroscopy. *Carbon N Y* **112**, 192–200 (2017).
142. Boot, M. D., Tian, M., Hensen, E. J. M. & Mani Sarathy, S. Impact of fuel molecular structure on auto-ignition behavior – Design rules for future high performance gasolines. *Prog Energy Combust Sci* **60**, 1–25 (2017).
143. Richter, H. & Howard, J. B. Formation of polycyclic aromatic hydrocarbons and their growth to soot—a review of chemical reaction pathways. *Prog Energy Combust Sci* **26**, 565–608 (2000).
144. National Research Council (US) Committee on Pyrene and Selected Analogues. *Polycyclic Aromatic Hydrocarbons: Evaluation of Sources and Effects*. (National Academies Press (US), 1983).
145. Zhang, W., Andersson, J. T., Räder, H. J. & Müllen, K. Molecular characterization of large polycyclic aromatic hydrocarbons in solid petroleum pitch and coal tar pitch by high resolution MALDI ToF MS and insights from ion mobility separation. *Carbon N Y* **95**, 672–680 (2015).
146. Roussak, O. V. & Gesser, H. D. *Applied Chemistry*. (Springer, Boston, MA, 2013). doi:https://doi.org/10.1007/978-1-4614-4262-2.
147. Treutler, C. P. O. Industrial use of plasma-deposited coatings for components of automotive fuel injection systems. *Surf Coat Technol* **200**, 1969–1975 (2005).
148. Boger, T., Glasson, T., Rose, D., Ingram-Ogunwumi, R. & Wu, H. Next Generation Gasoline Particulate Filters for Uncatalyzed Applications and Lowest Particulate Emissions. Preprint at https://doi.org/https://doi.org/10.4271/2021-01-0584 UI - 2021-01-0584 (2021).
149. Whitaker, P., Kapus, P., Ogris, M. & Hollerer, P. Measures to Reduce Particulate Emissions from Gasoline DI engines. *SAE Int J Engines* **4**, 1498–1512 (2011).
150. Yang, J. *et al.* Emissions from a flex fuel GDI vehicle operating on ethanol fuels show marked contrasts in chemical, physical and toxicological characteristics as a function of ethanol content. *Science of The Total Environment* **683**, 749–761 (2019).
151. Edney, M. K., Barker, J., Reid, J., Scurr, D. J. & Snape, C. E. Recent Advances in the Analysis of GDI and Diesel Fuel Injector Deposits. *Fuel* **272**, 117682 (2020).

152. Ding, H. *et al.* The Impact of GDI Injector Deposits on Engine Combustion and Emission. in *International Powertrains, Fuels & Lubricants Meeting* (SAE International, 2017). doi:https://doi.org/10.4271/2017-01-2248.
153. Beatrice, C. *et al.* Analysis of a Prototype High-Pressure "Hollow Cone Spray" Diesel Injector Performance in Optical and Metal Research Engines. Preprint at https://doi.org/https://doi.org/10.4271/2017-24-0073 UI - 2017-24-0073 (2017).
154. Edney, M. K. *et al.* Spatially Resolved Molecular Compositions of Insoluble Multilayer Deposits Responsible for Increased Pollution from Internal Combustion Engines. *ACS Appl Mater Interfaces* **12**, 51026–51035 (2020).
155. Abdallah, D. J. *et al.* Demistifying the Impact Diesel Fuel Bulk Composition PLays in Internal Injector Deposits with VASEtle. in *International Symposium on Stability, Handling and use of Liquid Fuels* (2017).
156. *Synthetics, Mineral Oils, and Bio-Based Lubricants*. *Synthetics, Mineral Oils, and Bio-Based Lubricants* (CRC Press, 2020). doi:10.1201/9781315158150.
157. XPS fitting. XPS reference pages. www.XPSFitting.com.
158. Pluskal, T., Uehara, T. & Yanagida, M. Highly Accurate Chemical Formula Prediction Tool Utilizing High-Resolution Mass Spectra, MS/MS Fragmentation, Heuristic Rules, and Isotope Pattern Matching. *Anal Chem* **84**, 4396–4403 (2012).
159. Pluskal, T., Castillo, S., Villar-Briones, A. & Orešič, M. MZmine 2: Modular framework for processing, visualizing, and analyzing mass spectrometry-based molecular profile data. *BMC Bioinformatics* **11**, 395 (2010).
160. Kind, T. & Fiehn, O. Seven Golden Rules for heuristic filtering of molecular formulas obtained by accurate mass spectrometry. *BMC Bioinformatics* **8**, 105 (2007).
161. Kew, W., Blackburn, J. W. T., Clarke, D. J. & Uhrín, D. Interactive van Krevelen diagrams – Advanced visualisation of mass spectrometry data of complex mixtures. *Rapid Communications in Mass Spectrometry* **31**, 658–662 (2017).
162. Marshall, A. G. & Rodgers, R. P. Petroleomics: Chemistry of the underworld. *Proceedings of the National Academy of Sciences* **105**, 18090 LP – 18095 (2008).
163. Rodgers, R. P., White, F. M., Hendrickson, C. L., Marshall, A. G. & Andersen, K. V. Resolution, elemental composition, and simultaneous monitoring by Fourier transform ion cyclotron resonance mass spectrometry of organosulfur species before and after diesel fuel processing. *Anal Chem* **70**, 4743–4750 (1998).
164. Gavard, R. *et al.* KairosMS: A New Solution for the Processing of Hyphenated Ultrahigh Resolution Mass Spectrometry Data. *Anal Chem* **92**, 3775–3786 (2020).
165. Green, F. M., Gilmore, I. S. & Seah, M. P. Mass Spectrometry and Informatics: Distribution of Molecules in the PubChem Database and General Requirements for Mass Accuracy in Surface Analysis. *Anal Chem* **83**, 3239–3243 (2011).
166. Trindade, G. F., Abel, M.-L. & Watts, J. F. simsMVA: A tool for multivariate analysis of ToF-SIMS datasets. *Chemometrics and Intelligent Laboratory Systems* **182**, 180–187 (2018).
167. Graham, D. J. & Castner, D. G. Multivariate Analysis of ToF-SIMS Data from Multicomponent Systems: The Why, When, and How. *Biointerphases* **7**, 49 (2012).
168. K. Edney, M. *et al.* Molecular Formula Prediction for Chemical Filtering of 3D OrbiSIMS Datasets. *Anal Chem* **94**, 4703–4711 (2022).

169. Edney, M. *et al.* Spatially Resolved Molecular Compositions of Insoluble Multilayer Deposits Responsible for Increased Pollution from Internal Combustion Engines. *ACS Appl Mater Interfaces* **12**, 51026–51035.
170. Treverton, J. A., Ball, J. & Fairlie, M. The reactions of oxidised aluminium surfaces with lubricant additives and related compounds. *Appl Surf Sci* **52**, 107–124 (1991).
171. Liebisch, G. *et al.* Update on LIPID MAPS classification, nomenclature, and shorthand notation for MS-derived lipid structures. *J Lipid Res* **61**, 1539–1555 (2020).
172. Ahmad, A. & Ahsan, H. Lipid-based formulations in cosmeceuticals and biopharmaceuticals. *Biomedical Dermatology* **4**, 12 (2020).
173. Ruffell, J. E., Farmer, T. J., Macquarrie, D. J. & Stark, M. S. The Autoxidation of Alkenyl Succinimides—Mimics for Polyisobutenyl Succinimide Dispersants. *Ind Eng Chem Res* **58**, 19649–19660 (2019).
174. Song, H., Xiao, J., Chen, Y. & Huang, Z. The effects of deposits on spray behaviors of a gasoline direct injector. *Fuel* **180**, 506–513 (2016).
175. Zhu, R., Hu, J., Bao, X., He, L. & Zu, L. Effects of aromatics, olefins and distillation temperatures (T50 & T90) on particle mass and number emissions from gasoline direct injection (GDI) vehicles. *Energy Policy* **101**, 185–193 (2017).
176. Teixeira, L. S. G. *et al.* The influence of Cu, Fe, Ni, Pb and Zn on gum formation in the Brazilian automotive gasoline. *Fuel Processing Technology* **88**, 73–76 (2007).
177. Slavchov, R. I., Mosbach, S., Kraft, M., Pearson, R. & Filip, S. v. An adsorption-precipitation model for the formation of injector external deposits in internal combustion engines. *Appl Energy* **228**, 1423–1438 (2018).
178. Slavchov, R. I. *et al.* The role of NO2 and NO in the mechanism of hydrocarbon degradation leading to carbonaceous deposits in engines. *Fuel* **267**, 117218 (2020).
179. Wang, N. *et al.* Molecular elucidating of an unusual growth mechanism for polycyclic aromatic hydrocarbons in confined space. *Nat Commun* **11**, 1079 (2020).
180. Taylor, R., Langley, G. J., Kroto, H. W. & Walton, D. R. M. Formation of C60 by pyrolysis of naphthalene. *Nature* **366**, 728–731 (1993).
181. Gover, R. K. E., Chamberlain, T. W., Sarre, P. J. & Khlobystov, A. N. Piecing Together Large Polycyclic Aromatic Hydrocarbons and Fullerenes: A Combined ChemTEM Imaging and MALDI-ToF Mass Spectrometry Approach. *Front Chem* **9**, (2021).
182. Reizer, E., Viskolcz, B. & Fiser, B. Formation and growth mechanisms of polycyclic aromatic hydrocarbons: A mini-review. *Chemosphere* **291**, 132793 (2022).
183. Matjacic, L. *et al.* OrbiSIMS metrology Part I: Optimisation of the target potential and collision cell pressure. *Surface and Interface Analysis* **n/a**, (2021).
184. Edney, M. K. *et al.* Molecular Formula Prediction for Chemical Filtering of 3D OrbiSIMS Datasets. *Anal Chem* **94**, 4703–4711 (2022).
185. Cha, E. *et al.* Ionization of Gas-Phase Polycyclic Aromatic Hydrocarbons in Electrospray Ionization Coupled with Gas Chromatography. *Anal Chem* **90**, 4203–4211 (2018).
186. Lien, G.-W., Chen, C.-Y. & Wu, C.-F. Analysis of polycyclic aromatic hydrocarbons by liquid chromatography/tandem mass spectrometry using

atmospheric pressure chemical ionization or electrospray ionization with tropylium post-column derivatization. *Rapid Communications in Mass Spectrometry* **21**, 3694–3700 (2007).
187. Kashiwa, K., Arai, M. & Kobayashi, Y. Study on PAHs and PM Formed by Benzene Pyrolysis. *SAE International Journal of Advances and Current Practices in Mobility* vol. 2 426–433 Preprint at (2019).
188. Parker, D. S. N., Kaiser, R. I., Troy, T. P. & Ahmed, M. Hydrogen Abstraction/Acetylene Addition Revealed. *Angewandte Chemie International Edition* **53**, 7740–7744 (2014).
189. Shukla, B. & Koshi, M. A novel route for PAH growth in HACA based mechanisms. *Combust Flame* **159**, 3589–3596 (2012).
190. McRae, C. *et al.* Use of Compound-Specific Stable Isotope Analysis to Source Anthropogenic Natural Gas-Derived Polycyclic Aromatic Hydrocarbons in a Lagoon Sediment. *Environ Sci Technol* **34**, 4684–4686 (2000).
191. Liu, L., Chen, S., Xu, H., Zhu, Q. & Ren, H. Effect of alkyl substituent for cyclohexane on pyrolysis towards sooting tendency from theoretical principle. *J Anal Appl Pyrolysis* **161**, 105386 (2022).
192. ANDERSON, R. C. Acetylene as an Intermediate in Combustion of Petroleum Hydrocarbons. in *LITERATURE OF THE COMBUSTION OF PETROLEUM* vol. 20 49–57 (AMERICAN CHEMICAL SOCIETY, 1958).
193. Shukla, B. & Koshi, M. A highly efficient growth mechanism of polycyclic aromatic hydrocarbons. *Physical Chemistry Chemical Physics* **12**, 2427–2437 (2010).
194. Miyayama, T., Sanada, N., Bryan, S. R., Hammond, J. S. & Suzuki, M. Removal of Ar+ beam-induced damaged layers from polyimide surfaces with argon gas cluster ion beams. *Surface and Interface Analysis* **42**, 1453–1457 (2010).
195. Yancey, D. F. & Reinhardt, C. Damage and repair of organic and inorganic surfaces by Ar+ ion and gas cluster ion beam sputtering. *J Electron Spectros Relat Phenomena* **231**, 104–108 (2019).
196. Snyder, L. R. & Buell, B. E. Nitrogen and oxygen compound types in petroleum. A general separation scheme. *Anal Chem* **40**, 1295–1302 (1968).
197. Robert Snyder, L. Petroleum nitrogen compounds and oxygen compounds. *Acc Chem Res* **3**, 290–299 (2002).
198. H. C. Prado, G., Rao, Y. & de Klerk, A. Nitrogen Removal from Oil: A Review. *Energy & Fuels* **31**, 14–36 (2016).
199. Speight, J. G. *The Chemistry and Technology of Petroleum, Fifth Edition*. (Taylor & Francis, 2014).
200. Rodríguez-Cabo, T. *et al.* Time-of-flight accurate mass spectrometry identification of quinoline alkaloids in honey. *Anal Bioanal Chem* **407**, 6159–6170 (2015).
201. Hallberg, A. & Martin, A. R. Mass spectral fragmentation patterns of heterocycles. VI. Carbazole and 1,8-dideuteriocarbazole. *J Heterocycl Chem* **21**, 837–840 (1984).
202. Parker, D. S. N. *et al.* GAS PHASE SYNTHESIS OF (ISO)QUINOLINE AND ITS ROLE IN THE FORMATION OF NUCLEOBASES IN THE INTAB - Nitrogen-substituted polycyclic aromatic hydrocarbons (NPAHs) have been proposed to play a key role in the astrochemical evolution of the interstellar mediu. *Astrophys J* **803**, 53 (2015).

203. Ricca, A., Bauschlicher, C. W. & Bakes, E. L. O. A Computational Study of the Mechanisms for the Incorporation of a Nitrogen Atom into Polycyclic Aromatic Hydrocarbons in the Titan Haze. *Icarus* **154**, 516–521 (2001).
204. Yao, T., Zhong, B.-J. & Luo, K. H. Compact Chemical Mechanism for Autoignition and Combustion of Methylcyclohexane under Engine Relevant Conditions. *Energy & Fuels* **31**, 11337–11347 (2017).
205. Ratkiewicz, A. Kinetics of the C–C bond beta scission reactions in alkyl radicals. *Physical Chemistry Chemical Physics* **13**, 15037–15046 (2011).
206. Tran, A., Abrrey Monreal, I., Moskovets, E., C. Aguilar, H. & W. Jones, J. Rapid Detection of Viral Envelope Lipids Using Lithium Adducts and AP-MALDI High-Resolution Mass Spectrometry. *J Am Soc Mass Spectrom* **32**, 2322–2333 (2021).
207. Lee, C. J. *et al.* Imaging mass spectrometry of fingermarks on brass bullet casings using sample rotation. *Analyst* **146**, 7563–7572 (2021).
208. Trindade, Gustavo F., M-L Abel, J. W. SIMSMVA: a tool for multivariate analysis of ToF-SIMS datasets. Preprint at (2018).
209. ASTM D4814 - 21 - Standard Specification for Automotive Spark-Ignition Engine Fuel.
210. Popczun, N. J., Breuer, L., Wucher, A. & Winograd, N. On the SIMS Ionization Probability of Organic Molecules. *J Am Soc Mass Spectrom* **28**, 1182–1191 (2017).